STUDY ON TENSILE, LOW CYCLE FATIGUE AND CREEP-FATIGUE INTERACTION BEHAVIOR OF SIMULATED MICROSTRUCTURES AND ACTUAL WELD JOINT OF P91 STEEL

By

K. MARIAPPAN
Enrollment No.: ENGG02201404008

Indira Gandhi Centre for Atomic Research, Kalpakkam

A thesis submitted to the
Board of Studies in Engineering Sciences
In partial fulfillment of requirements
for the Degree of

DOCTOR OF PHILOSOPHY

of

HOMI BHABHA NATIONAL INSTITUTE

August, 2021

Homi Bhabha National Institute

Recommendations of the Viva Voce Committee

As members of the Viva Voce Committee, we certify that we have read the dissertation prepared by **K. Mariappan** entitled "**Study on tensile, low cycle fatigue and creep-fatigue interaction behavior of simulated microstructures and actual weld joint of P91 steel**" and recommend that it may be accepted as fulfilling the thesis requirement for the award of Degree of Doctor of Philosophy.

Chairman – **Dr. B. P. C. Rao**	BPCRao	Date: 28/7/2021
Guide / Convener – **Dr. A. K. Bhaduri**	[signature]	Date: 28/7/2021
Examiner – **Prof. N. Narasaiah**	[signature]	Date: 28/7/21
Member 1– **Dr. Vani Shankar**	Vani Shankar	Date: 28.7.21
Member 2 – **Dr. S. Amirthapandian**	[signature]	Date: 28/7/21
Member 3 – **Prof. M. Kamaraj**	M. Kamaraj	Date: 28/7/2021

Final approval and acceptance of this thesis is contingent upon the candidate's submission of the final copies of the thesis to HBNI.

I/~~We~~ hereby certify that I/~~we~~ have read this thesis prepared under my/~~our~~ direction and recommend that it may be accepted as fulfilling the thesis requirement.

[signature]

Signature of Guide

Date: 28/7/2021

Place: IGCAR, Kalpakkam

STATEMENT BY AUTHOR

This dissertation has been submitted in partial fulfillment of requirements for an advanced degree at Homi Bhabha National Institute (HBNI) and is deposited in the Library to be made available to borrowers under rules of the HBNI.

Brief quotations from this dissertation are allowable without special permission, provided that accurate acknowledgement of source is made. Requests for permission for extended quotation from or reproduction of this manuscript in whole or in part may be granted by the Competent Authority of HBNI, when in his or her judgment the proposed use of the material is in the interests of scholarship. In all other instances, however, permission must be obtained from the author.

(K. Mariappan)

DECLARATION

I, hereby declare that the investigation presented in the thesis has been carried out by me. The work is original and has not been submitted earlier as a whole or in part for a degree / diploma at this or any other Institution / University.

(K. Mariappan)

List of Publications arising from the thesis

Journal

1. Comparative assessment of remnant tensile properties of modified 9Cr-1Mo steel under prior low cycle fatigue and creep-fatigue interaction loading, **K. Mariappan**, Vani Shankar, R. Sandhya, A. K. Bhaduri and K. Laha, International Journal of Fatigue, 2017, Volume 103, pp. 342-352.
2. Comparative evaluation of tensile properties of simulated heat affected zones of P91 steel weld joint, **K. Mariappan**, Vani Shankar and A. K. Bhaduri, Materials at High Temperatures, 2020, 37:2, 114-128.
3. Effect of microstructure and low cycle fatigue deformation on tensile properties of P91 steel, **K. Mariappan**, Vani Shankar and A. K. Bhaduri, Material Science Engineering & Technology (MAWE), 2020, 51:8, 1088–1099.
4. Effect of change in microstructures due to simulation temperatures on the low cycle fatigue behavior of P91 steel, **K. Mariappan**, Vani Shankar and A. K. Bhaduri, International Journal of Fatigue, 2020, Volume 140, 105847.

Conferences

1. Effect of strain amplitudes on fatigue behavior of simulated microstructures of HAZs of P91 steel weldment, **K. Mariappan**, Vani Shankar and A. K. Bhaduri, 3rd Int Conf and Exhibition on Fatigue, Durability and Fracture Mechanics & Symposium on Condition Assessment / Residual Life Assessment and Extension, Aug 2019, VTU, Jnana Sangama, Belagavi, Karnataka.
2. Effects of microstructures and cyclic loading on mechanical properties of simulated HAZs of P91 steel weldment, **K. Mariappan**, Vani Shankar and A. K. Bhaduri, Int Conf on Advanced Materials and Processes for Defence Applications —$ADMAT_{MatDef}$, Sep. 2019, DMRL-DRDO, Hyderabad, Telangana.

Awards

1. Best Oral presentation award in Int Conf on Advanced Materials and Processes for Defence Applications — $ADMAT_{MatDef}$, Sep. 2019, DMRL-DRDO, Hyderabad, Telangana.

K. Mariappan

DEDICATIONS

This thesis is dedicated to my mother (Late) Krishnammal

தெய்வத்தான் ஆகா தெனினும் முயற்சிதன்
மெய்வருத்தக் கூலி தரும்.
—திருவள்ளுவர்

"What if fate (or God) wills its failure and the object is not attained, the effort pays its own reward"

ACKNOWLEDGEMENTS

I owe to my guide **Dr. A. K. Bhaduri,** Director, Indira Gandhi Centre for Atomic Research for his constant inspiration, technical support and guidance during the entire period of this research.

I am indebted to **Dr. Vani Shankar,** SO/G, FSS, MDTD and Member, Doctoral Committee for her suggestion on the interesting title of the work. This work would not have accomplished without her mentoring, guiding and motivating. Her constant meticulous supervising has helped me to shape this thesis.

I am grateful to **Dr. M. Vasudevan,** Head, MDTD and **Dr. A. Nagesha,** Head, FSS, MDTD for critically reviewing the progress of this study and their commitment towards the corrections and suggestions in the thesis.

I sincerely acknowledge the timely support from **Dr. T. Jayakumar,** former Director, Metallurgy and Materials Group for his approval of registering of my PhD.

I am grateful to **Dr. Shaju K. Albert,** Director, Metallurgy and Materials Group and **Dr. R. Divakar,** Associate Director, MEG for their consistent encouragement throughout this work.

I am thankful to **Dr. S. Raju**, Associate Director, MCG and **Mrs. Vijaya Shanthi**, PMD for their support in the DSC analysis and **Dr. Amirtha Pandian,** Member, Doctoral Committee for TEM analysis.

I sincerely thank **Dr. M. Sai Baba** and **Dr. K. Velusamy,** Ex-Chairmen and **Dr. B.P.C. Rao**, Chairman and **Prof. M. Kamaraj**, IIT-M, Member, Doctoral Committee (DC) for their valuable suggestions during the DC meetings. I also thank **Dr. Anish Kumar**, Dean-Academic (Engineering Sciences), HBNI, IGCAR for his advice during documentation of the thesis.

I would like to express my extreme gratitude to **Dr. R. Sandhya**, former Head, FSS, MDTD and **Dr. K.B.S. Rao,** former Associate Director, MDCG for their motivation to pursue higher studies to enrich my career.

I am especially grateful to my colleagues **Dr. T. Sakthivel, Dr. V. David Vijayanand, Dr. E. Isaac Samuel, Dr. V. S. Srinivasan, Mr. Durga Prasada Rao Palaparti, Dr. G. V. Prasad Reddy, Mrs. N. Sreevidya, Dr. M. Divya, Mr. D. Manokaran, Mr. P. Vasantharaja, Dr. Saju T. Abraham and Dr. Pradyumna Kumar Parida** for many useful discussions and technical support during this study. I am indebted to **Mr. S. Sakthi** for his help on the design of sub-size specimen and making other engineering drawings. I would like to thank all my colleagues in Materials Development and Technology Division and IGCAR, who have directly or indirectly provided their support and motivation.

I am very grateful to my wife **Revathy**, daughter **Pon Karpagaa** and son **Kritna Senan** for their constant support, sacrifices and patience, without which it would not have been possible to complete this study.

K. Mariappan

CONTENTS

			Page No.
SUMMARY			xiv
LIST OF FIGURES			xvi
LIST OF TABLES			xxiii
NOMENCLATURE			xxv
ABBREVIATIONS			xxvi
CHAPTER 1: INTRODUCTION			
1.1	Background		1
1.2	Research objectives		5
1.3	Importance and application of the thesis		6
1.4	Organization of the thesis		6
CHAPTER 2: LITERATURE REVIEW			
2.1	Introduction		8
2.2	Material		8
	2.2.1	Development of 9-12% Cr-Mo steels	10
	2.2.2	Influence of alloying elements	12
	2.2.3	Physical metallurgy aspects of P91 steel	15
		2.2.3.1 Phase diagram	16
	2.2.4	Heat treatment	17
		2.2.4.1 Normalizing	17
		2.2.4.2 Tempering	18
		2.2.4.3 Typical microstructure	18
	2.2.5	Strengthening mechanisms	19
		2.2.5.1 Solid solution hardening	20
		2.2.5.2 Precipitation or dispersion hardening	20
		2.2.5.3 Dislocation hardening	21
		2.2.5.4 Boundary/sub-boundary hardening	21
	2.2.6	Microstructural degradation	21
		2.2.6.1 Precipitate coarsening (Ostwald ripening)	23
		2.2.6.2 Sub-grain coarsening	24
2.3	Tensile properties		25

2.3.1 Yield strength, σ_y 25
2.3.2 Ultimate tensile strength, σ_{TS} 26
2.3.3 Tensile ductility 27
2.3.4 Tensile deformation behavior of P91 steel 27
2.4 Fundamentals of fatigue 28
2.4.1 Two distinct domains of fatigue failure 28
2.4.2 Strain-controlled LCF testing 29
2.4.3 LCF strain-waveform 32
2.4.4 General parameters and procedures employed in LCF data analysis 32
2.4.5 Damage mechanisms in fatigue 36
2.4.6 Failure under conventional fatigue cycle 37
2.4.6.1 Fatigue crack initiation in ductile solids 37
2.4.6.2 Fatigue crack growth in ductile solids 38
2.4.6.3 Parameters influencing LCF properties at elevated temperatures 40
2.4.6.3.1 Slip character 40
2.4.6.3.2 Dynamic strain aging 41
2.4.6.3.3 Environment/oxidation 42
2.4.6.4 LCF behavior of ferritic alloys 44
2.5 Creep 46
2.5.1 Creep behavior of ferritic alloys 48
2.6 Fundamentals of creep-fatigue interaction 50
2.6.1 Types of waveforms 54
2.6.2 Environmental effect on creep-fatigue interaction 56
2.6.3 Creep-fatigue interaction behavior of ferritic alloys 57
2.7 Weld joint of ferritic steels 60
2.7.1 General information on welding 62
2.7.2 Microstructure evolution during fusion welding and post weld heat treatment 64
2.7.3 Hardness 66
2.7.4 Type IV failure location 67
2.7.4.1 Mechanism of Type IV cracking 69

2.7.5 Previous studies on LCF and CFI behavior of P91 weld joint 71

CHAPTER 3: EXPERIMENTAL METHODOLOGY

3.1 Introduction 74

3.2 Material composition and welding 74

3.3 Simulation of heat-affected zones through heat treatments 76

3.4 Mechanical tests 79

3.4.1 Matrix for tensile, LCF and CFI tests 79

3.4.2 Test specimen fabrication 81

3.4.3 Testing equipment 82

3.4.4 LCF test procedure 84

3.5 Metallography and hardness measurement 85

3.5.1 Optical microscopy (OM) 86

3.5.2 Transmission electron microscopy (TEM) 87

3.5.3 Field-emission scanning electron microscopy (FEGSEM) 87

3.5.3.1 Scanning electron microscopy (SEM) with Energy dispersive spectroscopy (EDS) 87

3.5.3.2 Electron back scattered diffraction (EBSD) examination 88

CHAPTER 4: INITIAL CHARACTERIZATION AND SIMULATION HEAT TREATMENTS VALIDATION

4.1 Introduction 89

4.2 Initial microstructure 89

4.2.1 Validation of HAZs microstructures simulation 92

4.2.1.1 Through grain size evaluation 92

4.2.1.2 Through precipitate size analysis 97

4.2.1.3 Through hardness characterization after PWHT 101

4.3 Initial characterization through EBSD analysis 102

4.4 Conclusions 118

CHAPTER 5: TENSILE PROPERTIES EVALUATION

5.1 Introduction 120

5.2 Monotonic tensile stress-strain behavior 120

5.3 Young's modulus (E) variation 123

5.4 Failure of the P91 steel weld joint due to monotonic tensile

deformation 126
5.5 Fractography 127
5.6 Hardness after tensile deformation 128
5.6.1 EBSD analysis on the microstructures of constituent regions of P91 steel weld joint 130
5.7 Deformation weighted/contribution factor analysis under tensile loading 133
5.8 Conclusions 136

CHAPTER 6: LOW CYCLE FATIGUE BEHAVIOR

6.1 Introduction 138
6.2 Cyclic stress response and stress-strain curves 138
6.3 Fatigue life 142
6.4 Hysteresis stress-strain behavior 147
6.5 Yield strengths and plastic strain accumulation under cyclic loading 149
6.6 Effect of microstructures and strain amplitudes on crack propagation behavior 151
6.7 Hardness and failure location of actual weld joint 161
6.8 Fracture analysis 164
6.9 Deformation mechanism analysis through EBSD technique 167
6.10 Deformation weighted/contribution factors analysis under LCF 171
6.11 Conclusions 173

CHAPTER 7: CREEP-FATIGUE INTERACTION BEHAVIOR

7.1 Introduction 176
7.2 Cyclic stress response curves and softening behavior 176
7.3 Fatigue life and fracture behavior 183
7.4 Crack propagation behavior 187
7.5 Hardness variation and failure location in the actual weld joint 190
7.6 Substructure evolution and property correlation 194
7.7 Optimization of weighted/contribution factors of each constituent region for estimating the fatigue life of actual weld joint 202
7.8 Prior creep-fatigue interaction damage on tensile properties of P91 steel base metal 204
7.9 Conclusions 211

CHAPTER 8: SUMMARY AND CONCLUSIONS 213
CHAPTER 9: FUTURE DIRECTIONS 218
REFERENCES 220

SUMMARY

Modified 9Cr-1Mo ferritic/martensitic steel also known as P91 steel has been chosen as the structural material for the steam generator components because of its combined better mechanical properties and resistance to environmental degradation. The temperature-sensitive microstructure of P91 steel gets modified during the weld thermal cycles; the highest temperature is reached by heat-affected zone (HAZ) that is closest to the weld metal. Hence within the narrow band of HAZ there is a complex variation of microstructures and mechanical properties. Frequent start-ups and shut-downs and constant load during the power generation lead to damage in the components either as the low cycle fatigue (LCF) or creep-fatigue interaction (CFI) mode. Thus, tensile properties, LCF and CFI behavior of high temperature structural components are important concern for design. Therefore, the present work aims to understand LCF and CFI behavior of each constituent region of the P91 steel weld joint in view of the progress of deformation and damage leading to the final failure of the microstructurally heterogeneous actual P91 steel weld joint at elevated temperature.

Towards this, the microstructures of coarse grain heat-affected zone (CGHAZ), fine grain heat-affected zone (FGHAZ) and inter-critical heat-affected zone (ICHAZ) were simulated through isothermal furnace heat treatments at 1473 K, 1208 K and 1138 K respectively. All simulated microstructures predominantly developed tempered martensite after oil quenching followed by tempering. Grain and precipitates sizes and hardness for each simulated microstructure of HAZ were compared with those of the actual weld joint to assure the accuracy of the simulation of microstructures through heat treatments. The LCF tests were performed on each constituent region and actual weld joint at the strain amplitudes range from ±0.25 to ±1.0% using triangular waveform. The CFI tests were carried out introducing

1, 10 and 30 min hold time at the peak tensile strain of ±0.6%. The tensile, LCF and CFI tests were carried out at a nominal strain rate of 3×10^{-3} s^{-1} and 823 K.

An increase in hardness at the ICHAZ in the weld joint was found after tensile deformation. The higher initial strain/work hardening behavior of soft ICHAZ attributes to the shifting of strain localization to the base metal, consequently failure at the base metal. It was found that not all the microstructures are equally responsible for the overall tensile behavior of the complex P91weld joint; the ICHAZ and the weld metal constitute the lower and upper bounds of the yield strengths respectively. Overall, the alloy exhibited continuous cyclic softening irrespective of the microstructures under both LCF and CFI conditions. Among all microstructural constituents of the weld joint, the weld metal exhibits the lowest fatigue life, followed by the ICHAZ and CGHAZ. However, the actual weld joint specimen failed at the interface between the ICHAZ and the base metal under LCF. Type IV mode of failure was identified to be operative under 30-minute tensile hold at 823 K. Factors such as grain size, mechanical strength of various phases (fine tempered martensites and over-tempered ferrite in ICHAZ), precipitate size (de-cohesion around coarsened carbides in ICHAZ), difference in the volume of microstructural regions in the actual weld joint, difference in plastic strain accommodation/accumulating capacity of individual microstructures and their evolution during fatigue deformation are identified for affecting cracking behavior and the resultant fatigue life. A common empirical relationship was established to estimate the fatigue life of actual weld joint using the sum of the product of weighted factors and the fatigue lives of the microstructural constituents of the P91 weld joint under LCF and CFI loadings.

List of Figures

Figure No.	Title	Page No.

CHAPTER 2

2.1	Chart showing the progressive development of Cr-Mo steels.	12
2.2	The austenitic loop in a 0.1%C steel, α being ferrite, γ being austenite and $(CrFe)_4C$ is the $M_{23}C_6$ carbide.	17
2.3	Typical initial tempered martensitic microstructure; (a) optical micrograph of P91 steel and (b) schematic representation of non-uniform precipitation states in 9-12% Cr steels.	19
2.4	Schematic illustration of pristine microstructure of P91 steel; (a) after tempering (internal interfaces and precipitates) and (b) evolution with exposure to elevated temperatures and external stress.	23
2.5	Schematic of Ostwald ripening mechanism.	24
2.6	The determination of the yield strength at 0.2% offset.	26
2.7	Stress-strain curves from tensile tests on Grade 91 steel. BMT and BML are base metal specimens in transverse and longitudinal directions, respectively.	28
2.8	Schematics of (a) heating and cooling the surface of a thick structure and (b) resulting hysteresis loop.	30
2.9	Schematic view of high-temperature fatigue problem showing physical stages in failure process in a typical notched component and relevant disciplines.	31
2.10	Typical waveforms for strain-controlled fatigue testing.	32
2.11	LCF parameters in the stress-strain hysteresis loop.	33
2.12	Schematic representation of the response of metals to cyclic strain.	34
2.13	Construction of cyclic stress-strain curve by joining tips of hysteresis loops. Points represents tips of stable hysteresis loops for a given strain amplitude.	35
2.14	Schematic of strain-life plots.	36
2.15	Cyclic deformation and fatigue damage. Sequence of events and classification of mechanisms.	38
2.16	Schematics of (a) fatigue crack propagation across a specimen indicating 3-stage of fatigue failure, (b) crack opening and crack-tip blunting and (c) crack closure and crack-tip re-sharpening.	39
2.17	Cyclic stress response curves of modified 9Cr-1Mo steel.	45

2.18 Normalized and tempered alloy showing elongated laths within the grains decorated with carbides and substructure ((a) and (b)) formation during fatigue cycling. 46

2.19 Schematic of typical creep curve showing three stages of creep. 47

2.20 Schematic of intergranular damage development. 48

2.21 Creep deformation and rupture results at different stress levels for P91 steel at 898 K. 49

2.22 Transgranular ductile fracture as observed in creep ruptured P91 steel specimen (a) before and (b) after etching with Nital solution (test condition: 151.5 MPa, 898 K). 50

2.23 Partitioning of typical cyclic hold hysteresis loop. 52

2.24 Schematic diagrams of failure modes during (a) continuous cycling, (b) creep and (c) simultaneous and (d) sequential creep-fatigue interactions conditions. 53

2.25 Typical waveforms of concurrent types of creep-fatigue interaction. 55

2.26 Influence of application of hold on the cyclic stress response of modified 9Cr-1Mo steel. 59

2.27 Transmission electron micrographs of P91 steel tested under 10-minute tensile hold; (a) carbides along initial lath boundaries (white arrows), (b) fine precipitates (V(C,N)) pinning dislocations, (c and d) carbides coagulation and coarsening. 60

2.28 Schematic representation of welded joint in 9–12% Cr ferritic steel. 63

2.29 The schematic of microstructures of P91 steel weld joint and corresponding phase fields (Fe-C binary phase diagram). The dashed line shows the carbon content of P91 steel. The optical micrographs of present study material's microstructures are superimposed at the corresponding temperatures. 65

2.30 Hardness profile of Grade 91 steel specimen; '0' being the center of the weld. 66

2.31 Classification of cracking in weld joints. 69

CHAPTER 3

3.1 Differential scanning calorimetry thermogram corresponding to the full heat-cool cycle for P91 steel at 10 $Kmin^{-1}$. 76

3.2 Schematic diagrams of thermal cycles during (a) actual welding and (b) furnace simulation of HAZs of P91 steel weld joint followed by tempering. 78

3.3 Test specimen details; (a) extraction of test specimen from weld pad and (b) geometry of cross-weld test specimen. 82

3.4	Servo-hydraulic fatigue test system; (a) schematic and (b) DARTEC make system used in MDTD, IGCAR, Kalpakkam. The insert is showing a spring-loaded axial-strain extensometer, placed on specimen ridges.	84
3.5	Strain-time waveforms; (a) triangular for LCF and (b) trapezoidal for CFI tests.	85

CHAPTER 4

4.1	Initial microstructure of P91 steel base metal in the normalized and subsequent PWHT condition; (a) optical, (b) TEM and (c) SEM micrographs and (d) EDS spectra comparison between matrix and precipitate.	90
4.2	Transmission electron micrographs of the initial microstructures of (a) weld metal and simulated (b) CGHAZ, (c) FGHAZ and (d) ICHAZ of P91 steel weld joint.	92
4.3	Optical micrographs of microstructures of actual weld joint (a) CGHAZ, (c) FGHAZ and (e) ICHAZ and simulated (b) CGHAZ, (d) FGHAZ and (f) ICHAZ.	94
4.4	Comparison of grain size distributions of simulated and actual weld joint microstructures; (a) CGHAZ, (b) FGHAZ and (c) ICHAZ and d) average PAG size of various microstructures of P91 steel weld joint.	96
4.5	Scanning electron micrographs of microstructures of (a) CGHAZ, (c) FGHAZ, (e) ICHAZ of actual weld joint and (b) CGHAZ, (d) FGHAZ and (f) ICHAZ of simulated P91 steel and (g) comparison between the HAZs′ precipitates and PAGs sizes of the simulated and the actual weld joint.	99
4.6	Hardness values comparison between the actual and simulated HAZs of the P91 steel weld joint.	102
4.7	Substructural analysis; (a-h) inverse pole figure (IPF) maps and (i) sub-grain size distributions plots; base metal, weld metal and actual and simulated HAZs after PWHT.	105
4.8	Grain boundary (a-h) misorientation maps and (i) distributions plots of base metal, weld metal, actual and simulated HAZ microstructures of P91 weld joint after PWHT.	109
4.9	Comparison of LAGBs distributions in simulated and actual weld joint microstructures of P91 steel.	110
4.10	Kernel average misorientation (a-h) maps and (i) distribution plots of base metal, weld metal, actual and simulated HAZ microstructures of P91 weld joint after PWHT.	114
4.11	Grain average misorientation (a-h) maps and (i) distribution plots of base metal, weld metal, actual and simulated HAZ microstructures of P91 weld	117

joint after PWHT.

CHAPTER 5

5.1 Monotonic tensile engineering stress-strain curves of base metal and simulated ICHAZ, FGHAZ and CGHAZ and weld metal and actual P91 steel weld joint at 823 K. 121

5.2 Tensile properties (yield strength and UTS and ductility in terms of elongation and reduction in area) of actual weld joint, weld metal, simulated CGHAZ, FGHAZ and ICHAZ and base metal of P91 steel tested at the strain rate of 3×10^{-3} s^{-1} and 823 K. 123

5.3 Microstructure dependent Young's modulus of P91 steel and its weld joint at 823 K. 125

5.4 Failed sample of P91 steel weld joint under monotonic tensile deformation at 823 K. Representatives magnified images of respective regions are overlapped. 126

5.5 Fractographs of the tensile tested specimens; (a) actual weld joint, (b) weld metal, simulated (c) CGHAZ, (d) FGHAZ and (e) ICHAZ and (f) base metal. 128

5.6 Comparison of propensity of hardness profiles of P91 actual weld joint after PWHT and tensile test. 129

5.7 Inverse pole figure (IPF) maps; (a) FGHAZ, (b) ICHAZ, (c) near fracture and (d) away from fracture of base metal of actual weld joint of P91 steel tensile deformed at the strain rate of 3×10^{-3} s^{-1} and 823 K. 131

5.8 Local misorientation (KAM) along with superimposed grain boundary maps; (a) FGHAZ, (b) ICHAZ and base metal (c) near fracture and (d) away from fracture; (e) local misorientation distributions plots of actual P91 steel weld joint after tensile deformation at 823 K. Scan step size: 0.05 μm. 132

5.9 Deformation weighted/contribution factors from each constituent region of P91 weld joint. 136

CHAPTER 6

6.1 Cyclic stress response curves of base metal, weld metal, simulated microstructures of HAZ and actual weld joint of P91 steel at the strain amplitudes of (a) ±0.25%, (b) ±0.4%, (c) ±0.6% and (d) ±1.0% and at 823 K. 140

6.2 Log-log cyclic stress-strain plots of base metal, simulated HAZs, weld metal and actual weld joint of P91 steel. 142

6.3 Fatigue life variations across the microstructures of P91 steel weld joint; (a) at the strain amplitudes ranges between ±0.25% and ±1.0% and (b) Coffin-Manson plots at 823 K 143

6.4	Low cycle fatigue hysteresis loops of weld metal, simulated CGHAZ, FGHAZ and ICHAZ and base metal and actual weld joint of P91 steel at ±0.6% and 823 K.	149
6.5	Variations of (a) cyclic yield strength and (b) cyclic plastic strain accumulation with the progressive cyclic deformation under LCF condition.	150
6.6	Cracks propagations; (a) weld metal, simulated (b) CGHAZ, (c) FGHAZ and (d) ICHAZ and (e) base metal of P91 steel at ±0.25% and 823 K.	154
6.7	Crack propagation; (a) weld metal, (b) and (c) CGHAZ, (d) FGHAZ, (e) ICHAZ, and (f) base metal of P91 steel weld joint during LCF deformation at ±0.6% and 823 K.	156
6.8	Crack propagation detail in CGHAZ; (a) inverse pole figure (IPF) map, (b) grain boundary misorientation map and (c) KAM map with grain boundary misorientation distribution.	158
6.9	Frequency distribution of cracks; (a) length and (b) width in weld metal, CGHAZ, FGHAZ, ICHAZ and base metal under LCF condition at 823 K.	159
6.10	Region-wise cracks distributions; (a) length and (b) width in the actual weld joint and (c) comparison of total number of cracks in the simulated and weld metal microstructures and microstructures of the actual P91 steel weld joint after the LCF test.	161
6.11	Comparison of hardness profiles across the P91 steel weld joint after PWHT and LCF test.	162
6.12	Longitudinal image of failed sample of P91 steel weld joint subjected to LCF loading at 823 K; representative magnified images of weld metal, HAZs, and base metal are indicated.	163
6.13	Fracture surfaces of (a) weld metal, (b) CGHAZ, (c) FGHAZ, (d) ICHAZ, (e) base metal and (f) actual weld joint; (g) the bar charts of striations sizes with standard deviations for different microstructures of P91 steel after LCF deformation at ±0.6% and 823 K.	166
6.14	Substructural analysis; (a-e) IPF maps of various microstructural regions of P91 steel weld joint and (f) sub-grain size distribution after LCF test at 823 K.	168
6.15	Substructural analysis; (a-e) KAM maps and (f) local misorientation (KAM) distribution map of various microstructural regions of P91 steel weld joint after LCF test at 823 K.	170
6.16	Microstructure dependent weighted factor/weld strength reduction factors of P91 steel.	172

6.17 Comparison of predicted and experimental fatigue lives of P91 weld joint under LCF condition at 823 K. 173

CHAPTER 7

7.1 Cyclic stress response curves of base metal and simulated CGHAZ, FGHAZ and ICHAZ and actual weld joint of P91 steel tested under CFI condition; (a) 1 MTH, (b) 10 MTH and (c) 30 MTH. 178

7.2 Scanning electron micrographs of simulated (a) CGHAZ, (b) FGHAZ and (c) ICHAZ under 30MTH-CFI at 823 K. 180

7.3 Plots of (a) precipitate sizes distribution and (b) comparison between average precipitate sizes of simulated CGHAZ, FGHAZ and ICHAZ under CFI and tempering conditions. 181

7.4 Comparison of variations of (a) cyclic yield strengths and (b) plastic strain accumulations with the progressive fatigue damage under LCF and 30MTH-CFI conditions at 823 K. 183

7.5 Hold time effect on (a) fatigue life and (b) dwell sensitivity and (c) correlation between fatigue life and stress relaxation of simulated microstructures and actual weld joint of P91 steel at 823 K. 185

7.6 Fracture surface morphologies of the simulated microstructures of (a) CGHAZ, (b) FGHAZ and (c) ICHAZ of P91 steel under 30MTH-CFI condition at 823 K. 187

7.7 Optical micrographs of simulated (a) CGHAZ, (b) FGHAZ and (c) ICHAZ and (d) base metal and under 30MTH-CFI condition at 823 K. 189

7.8 Cracks distributions under 30 MTH at 823 K; (a) length and (b) width. 190

7.9 Variation of hardness profiles across the weld joint microstructures after PWHT and LCF and CFI tests. 191

7.10 Collaged optical micrograph of actual weld joint of P91 steel failed under 30MTH-CFI condition at 823 K. 193

7.11 Cracks distributions; (a) length and (b) width and (c) comparison of total number of cracks in the actual weld joint tested under LCF and CFI conditions at 823 K. 194

7.12 Grain boundary misorientations maps of (a and b) base metal and simulated (c and d) CGHAZ, (e and f) FGHAZ and (g and h) ICHAZ after PWHT (left) and 30MTH-CFI deformation (right) at 823 K. 197

7.13 Plots of (a) substructures sizes and (b) grain boundary misorientations distributions. 198

7.14	Microstructural changes in terms of substructured, recrystallization and deformed fractions in the specimens of (a) base metal, simulated (b) CGHAZ, (c) FGHAZ and (d) ICHAZ of P91 steel weld joint tested under 30MTH-CFI condition at 823 K.	199
7.15	Fatigue lives variations with the microstructural changes in the simulated CGHAZ, FGHAZ and ICHAZ and base metal of P91 steel weld joint tested under 30MTH-CFI condition at 823 K.	200
7.16	Plots of (a) fatigue life weighted/contribution factors for individual mirostructural region, (b) predicted CFI lives of weld metal and comparison of fatigue lives between predicted and experimental results (c) LCF and (d) CFI at 823 K.	203
7.17	Change in tensile properties; (a) yield strength, (b) tensile strength, (c) total elongation and (d) uniform elongation of P91 steel base metal due to fatigue damage at 873 K.	206
7.18	Correlation between yield strength changes and stress relaxation during the progressive of CFI deformation at 873 K.	207
7.19	Inverse pole figure maps of the specimens after (a) normalizing and tempering and fatigue deformation up to (b) 5%, (c) 30% and (d) 50% of fatigue life and (e) plot of sub-grain size evolution with the progressive fatigue damage under CFI condition at 873 K. Step size is 0.2 µm.	209
7.20	Oxidation in P91 steel base metal subject to fatigue loadings up to (a) 10%, (b) 30% and (c) 50% of fatigue life and (d) surface roughness versus fatigue cycles under CFI condition at 873 K.	210

List of Tables

Table No.	Title	Page No.
	CHAPTER 2	
2.1	Details of precipitates in P91 steel	19
2.2	Typical waveforms used in creep-fatigue interaction tests	55
	CHAPTER 3	
3.1	Chemical composition of P91 steel base and weld filler material	75
3.2	Welding parameters employed for GTAW	75
3.3	Critical temperatures of P91 steel at the heating rate of 10 $Kmin^{-1}$	77
3.4	Test matrix	80
	CHAPTER 4	
4.1	Grain sizes comparison between the simulated and actual weld joint HAZs of P91 steel	97
4.2	Average PAG and precipitate sizes in the HAZs of simulated and actual weld joint of P91 steel.	99
4.3	Sub-grain size analyses in the base metal, weld metal, simulated and actual CGHAZ, FGHAZ, ICHAZ of P91 weld joint in PWHT condition	106
4.4	Grain boundary analyses in the base metal, weld metal, simulated and actual CGHAZ, FGHAZ and ICHAZ of P91 weld joint after PWHT	109
4.5	GAM analyses; base metal, weld metal and simulated and actual CGHAZ, FGHAZ, ICHAZ of P91 weld joint after PWHT	118
	CHAPTER 5	
5.1	Hardness values and tensile properties of individual microstructures of P91 steel weld joint. Actual weld joint tensile parameters are given for comparison	125
	CHAPTER 6	
6.1	Low cycle fatigue parameters of P91 steel at 823 K	146
6.2	Constants in Coffin-Manson and Basquin and cyclic stress-strain relationships for different microstructures of P91 steel weld joint	147
6.3	Comparison of EBSD results associated with microstructural changes in simulated microstructures of HAZ of P91 steel weld joint after PWHT and LCF test	170

CHAPTER 7

7.1	Comparison of EBSD results associated with microstructural changes in simulated microstructures of P91 steel HAZ after PWHT and LCF and CFI tests	201
7.2	Weighted/contribution factors indicating the amount of contribution of the individual microstructural region for the fatigue lives of P91 weld joint under LCF and CFI conditions at 823 K	204

NOMENCLATURE

σ_y	Yield Strength
σ_{TS}	Tensile Strength/Ultimate Tensile Strength
σ_w	Working Stress
σ_a	Alternating Stress
A_f	Cross-Sectional Area of Specimen at Fracture
E	Young’s Modulus
$\Delta\sigma$	Stress Range
σ_{max}	Peak Tensile Stress
σ_{min}	Peak Compressive Stress
$\Delta\varepsilon_t$	Total Strain Range
$\Delta\varepsilon_p$	Plastic Strain Range
$\Delta\varepsilon_e$	Elastic Strain Range
$\Delta\sigma/2$	Stress Amplitude
$(\Delta\sigma/2)_{max}$	Peak Tensile Stress Amplitude
$\Delta\varepsilon/2$	Total Strain Amplitude
$\Delta\varepsilon_p/2$	Plastic Strain Amplitude
$\Delta\varepsilon_e/2$	Elastic Strain Amplitude
K'	Cyclic Strength Coefficient
n'	Cyclic Strain-Hardening Exponent
ε'_f	Fatigue Ductility Coefficient
c	Fatigue Ductility Exponent
σ'_f	Fatigue Strength Coefficient
b	Fatigue Strength Exponent
ε_o	Instantaneous Strain
$2N_f$	Number of Strain Reversals to Failure

ABBREVIATIONS

ASME	American Society of Mechanical Engineers
ASTM	American Society for Testing and Materials
BCC	Body Centered Cubic
BCT	Body Centered Tetragonal
BM	Base Metal
CFI	Creep-Fatigue Interaction
CGHAZ	Coarse Grain Heat-Affected Zone
CMTW	Cold Metal Transfer Weld
CSR	Cyclic Stress Response
CSSC	Cyclic Stress-Strain Curve
CW	Cross Weld
DP	Dual Phase
DSA	Dynamic Strain Aging
DSC	Differential Scanning Calorimetry
EBSD	Electron Back Scattered Diffraction
EDS	Energy Dispersive Spectroscopy
FBR	Fast Breeder Reactor
FCAW	Flux Cored Arc Welding
FCC	Face Centered Cubic
FCP	Fatigue Crack Propagation
FEGSEM	Field Emission Gun Scanning Electron Microscope
FGHAZ	Fine Grain Heat-Affected Zone
GAM	Grain Average Misorientation
GND	Geometrically Necessary Dislocation
GTAW	Gas Tungsten Arc Welding
HAGBs	High Angle Grain Boundaries
HAZ	Heat-Affected Zone
HCF	High Cycle Fatigue
HRTEM	High Resolution Transmission Electron Microscope
IGHAZ	Inter-Critical Heat-Affected Zone
IPF	Inverse Pole Figure

KAM	Kernel Average Misorientation
LAGBs	Low Angle Grain Boundaries
LCF	Low Cycle Fatigue
LMFBR	Liquid Metal Fast Breeder Reactor
LVDT	Linear Variable Differential Transformer
MMAW	Manual Metal Arc Welding
OM	Optical Microscope
PAG	Prior Austenite Grain
PAGBs	Prior Austenite Grain Boundaries
PFBR	Prototype Fast Breeder Reactor
PWHT	Post Weld Heat Treatment
SCC	Stress Corrosion Cracking
SEM	Scanning Electron Microscope
SFE	Stacking Fault Energy
SFR	Sodium-Cooled Fast Reactor
SG	Steam Generator
SMAW	Submerged Metal Arc Welding
TEM	Transmission Electron Microscopy
TIG	Tungsten Inert Gas
TMF	Thermomechanical Fatigue
UTS	Ultimate Tensile Strength
WF	Weighted/Contribution Factor
WJ	Weld Joint
WM	Weld Metal
YS	Yield Strength

CHAPTER 1 INTRODUCTION

1.1 BACKGROUND

Modified 9Cr-1Mo ferritic/martensitic steel also known as P91 steel has been chosen as the structural material for the steam generator components of prototype fast breeder reactor (PFBR) in INDIA. The present design of PFBR is being reassessed based on the manufacturing experiences gained with a focus on improved economics and enhanced safety. The PFBR's pool type design with 500MWe power and two-loop concept is retained for future FBRs also. In the loop, the heat removed by primary sodium is transferred to the secondary sodium through intermediate heat exchanger. The heat is then transferred to steam-water system through steam generator (SG). From worldwide operating experience of sodium cooled FBRs, it is seen that reliable performance of steam generators, wherein sodium and high-pressure water/steam are separated by a thin wall boundary is very crucial from plant safety point of view. Thus, the reliability of the components in the SGs is of paramount importance for the success of sodium cooled FBRs.

The selection of P91 steel in power plants for headers in steam generators and tubing for heat transport systems is because of its high thermal conductivity, low coefficient of thermal expansion, superior creep strength as compared to other conventional structural materials [1–3], resistance to stress corrosion cracking [4] and good weldability [5–7]. The steel is a modified version of plain 9Cr-1Mo (P9) steel with the controlled addition of strong carbide and carbonitride formers like Vanadium (V), Niobium (Nb) and Nitrogen. The steel derives its high temperature strength from complex microstructures, which exhibit a high dislocation density and consist of lath and sub-boundaries decorated with secondary precipitates of $M_{23}C_6$, and MX type precipitates such as Nb-V carbonitride evenly distributed in the matrix. The small inter-particle spacing of MX type precipitates, their large volume fraction and resistance against coarsening are together responsible for the enhanced creep strength of P91 steel. As primary precipitates, the Nb and V rich carbides restrict grain growth during normalizing and obstruct the movement of dislocations that delay plastic deformation [8,9]. Steam generators are complex large structures that are made in parts and integrated by welding techniques. During welding, the temperature-sensitive microstructure of P91 steel gets modified up to various extents depending upon the temperature it is exposed to during the weld thermal cycles; the highest temperature is reached by heat-affected zone (HAZ) that is closest to the weld metal. Hence within the narrow band of HAZ there is a complex variation of microstructures and mechanical properties. During service, such a variation of microstructures and associated mechanical properties could lead to uncertainties in the performance of components if complete understanding based on simulating service conditions through laboratory experiments is not developed.

The tensile properties of base metal are often used in the design consideration of the weld joints in the structural components. Few experimental based studies have been carried out on the tensile behavior of the weld joint of ferritic/martensitic/Dual-Phase (DP) steels [10–13]. Notably, only a few studies have focused on the characterization of mechanical properties of individual microstructures of different regions of P91 steel weld joint [14–16]. As fabrication of SG involves numerous weld joints, it is important to evaluate the basic tensile properties of the weld joint and also develop an understanding on how each constituent region would contribute towards the overall tensile behavior of actual P91 steel weld joint.

The steam generator components are often subjected to repeated cyclic deformation due to temperature gradients that occur upon heating and cooling during start-ups and shut-downs of the power plants. This leads to low cycle fatigue (LCF) damage in the components. Hence LCF properties assume importance in the safe life design approach of steam generator components of power plants. P91 steels exhibit a tempered martensitic microstructure, which is intended to be stable over long periods of service [17,18]. The low cycle fatigue behavior of P91 steel base metal has been elaborately investigated by many researchers, in the normalized and tempered condition in both air and vacuum environments [19–27]. Under continuous cyclic loading, the steel is known to exhibits extensive cyclic softening behavior because of microstructural instability, which results in deterioration of fatigue life [28–30]**.** The increase in temperature decreases the fatigue life of the steel. At higher temperatures, the fatigue deformation behavior and life of the P91 steel are affected by the time dependent processes, like dynamic strain aging, oxidation, creep etc. The occurrence of dynamic strain aging in this steel has been reported at the temperature range of 573-773 K [31] and 773-873 K [23] at a nominal strain rate, 3×10^{-3} s^{-1}. The negative strain rate sensitivity of fatigue life and negative temperature dependence of half-life plastic strain amplitude are some of the typical manifestations of dynamic strain aging process in steel [31]. Effects of mechanical processes such as hot forging and rolling on the fatigue behavior of the steel have been studied by Ebi and McEvily [19]. The authors [19] also reported that the presence of relatively coarser grain size, which aids the early fatigue crack initiation and lowering the fatigue life of hot forged steel as compared to finer-grained hot rolled material at 811 K.

Exclusive reports on the LCF behavior of P91 steel weld joints are elusive rather the LCF data have been mostly documented in the research articles among the results of the creep-fatigue interaction studies of the weld joint [32–35]. Vani Shankar et al. [32,36] have observed lower cyclic stress response curve for the P91 steel weld joint than the base metal due to the presence of soft heat-affected zone in the weld joint. The authors [32] have also observed the change in failure location of the weld joint in a complex manner with the varying testing parameters. A study by Farragher et al. [35] used cyclic viscoplasticity model for isotropic softening and non-linear kinematic hardening to characterize the cyclic viscoplasticity behavior of the weld metal and HAZ at higher temperatures. This is one of the few theoretical studies using multi-scale model to predict cyclic behavior of P91 steel under LCF and thermomechanical fatigue conditions by using substructures, lath and precipitate size as input parameters [37,38]. An experimental validation and the study of fatigue behavior of each constituent region of the actual weld joint would be indispensable towards advancing the understanding on the underlying micro mechanisms of fatigue deformation in P91 weld joint and provide an insight for improving the welding technology in order to enhance the life of the welded component made out of P91 steel.

It has been observed, in general, that the creep strength of the cross-weld (weld joint) specimen is inferior to the base metal specimen of P91 steel. Many premature failures during high temperature service have occurred at the weld joints and have been identified to have occurred in a narrow inter-critical region of the HAZ in P91 steel. They are termed as Type IV failures [39–43]. A steady state operation in between the start-up and shut-down for the power generation at elevated temperature introduces creep, resulting in creep–fatigue interaction (CFI) condition. The P91 steel is also prone to oxidation. Thus, CFI along with oxidation can accelerate the kinetics of damage accumulation and consequently reduce the components life. Hence, reliable CFI test data is required for meticulous consideration of CFI and oxidation, which in turn is vital for sound design practices. Whereas the creep performance of weld joints of P91 steel is much better understood, the fatigue and CFI behavior of the weld joints are not well established. In the past two decades significant amount of investigations have been carried out on the CFI behavior of P91 steel base metal and weld joint [27,44,45]. However, it has been found that the failure location of the weld joint changes in a complex manner with the changes in testing parameters [36]. Hence there is a need to understand, how individual microstructural constituent of the weld joint contributes to the deformation and damage evolution of the actual weld joint under CFI condition.

In view of the above, it is necessary to understand the monotonic, continuous cyclic and creep-fatigue interaction behavior of all the contributing microstructures of the HAZs so as to be able to correlate with the overall mechanical behaviour of the actual P91 steel weld joint. The study also includes the microstructural characterization and hardness determination for the validation of simulation of the HAZ microstructures through heat treatments. This work has been organized to conduct detailed investigation on the P91 steel, to understand LCF and CFI behavior of each constituent region of the P91 steel weld joint in view of the progress of deformation and damage leading to the final failure of the microstructurally heterogeneous actual P91 steel weld joint at elevated temperature.

1.2 RESEARCH OBJECTIVES

The primary goal of the thesis is to be able to predict the fatigue behavior of the actual weld joint by studying the fatigue properties of the constituents' microstructures. Towards this, the microstructures of HAZ of the weld joint were simulated through heat treatments and tensile, LCF and CFI tests were performed on the simulated microstructures and the actual weld joint. Thereafter the tensile and cyclic properties so determined on the simulated microstructures were compared with the actual weld joint that were tested under the same experimental conditions.

Detailed microstructural characterization of base metal, simulated HAZs, weld metal and the actual weld joint of P91 steel in both before and after the monotonic tensile, LCF and CFI tests conditions was performed using electron microscopy techniques to understand in-depth of the underlying deformation mechanisms operative under various test conditions. Quantification of the microstructural changes and relation between the resulting mechanical properties could be established, based on which empirical relationships could be developed to predict the monotonic, LCF and CFI properties of actual weld joint from the constituent microstructures so generated.

1.3 IMPORTANCE AND APPLICATION OF THE THESIS

The components from P91 steel are generally fabricated with fusion welding processes. Fusion welding of P91 steel creates a microstructure gradient across the weld joint (which is difficult to remove by post-weld heat treatment). In-service P91 weld joint in the structural components typically undergo complex loadings at elevated temperatures leading to complex time dependencies that vary considerably with temperature, strain, etc. Understanding the LCF behavior and estimating the deformation weighted/contribution factor of each constituent region of P91 steel weld joint could provide important inputs for welding technology development. Particularly, the study on the heat-affected zone, which is a weaker in the microstructural constituents of weld joint would be more crucial. Therefore, for sound design considerations under those conditions, a thorough understanding of the tensile, fatigue and CFI deformation mechanisms is required. The acquired knowledge can greatly help in designing and fabricating better elevated temperature structural components that can provide improved performance under complex loading conditions. Knowledge of the mechanisms involved will also aid in the selection of appropriate inspection intervals and minimizing the risk of catastrophic structural failures and their subsequent economic consequences and danger to human safety.

1.4 ORGANIZATION OF THE THESIS

The Chapter 1 deals with the introduction for the present investigation, which covers the brief background and objective of the work. The Chapter 2 provides literature review on the study material and its physical and mechanical metallurgy aspects and fundamentals of the various elevated temperature deformation and damage mechanisms, namely tensile, fatigue, CFI for a given material under different loading conditions. This is followed by the Chapter 3 that describes on the topic under experimental; test material, P91 steel, typical heat treatments adopted for the simulation of HAZs and test matrix for tensile, fatigue and creep-fatigue and various microscopy analysis. The Chapter 4 deals with the initial characterization of all microstructural constituents of P91 steel weld joint, using optical and scanning electron microscopy and electron backscattered diffraction techniques. The Chapter also describes the validation of the generation of microstructures of HAZ through heat treatments with grain and precipitate sizes analysis and hardness comparison.

The tensile properties of simulated HAZs and base metal and weld metal of P91 steel weld joint are discussed in Chapter 5. Estimation of yield strength of P91 steel weld joint through substituting deformation weighted/contribution factors of all microstructural constituents in an empirical relationship is presented in this Chapter. This is followed by Chapter 6 in which the LCF behavior of simulated HAZs and base metal and weld metal at various strain amplitudes and 823 K are described. Derivation of fatigue life weighted/contribution factors from each constituent region of weld joint to estimate the fatigue life of actual weld joint is described in this Chapter. The Chapter 7 discusses the creep-fatigue behavior of weld metal, simulated microstructures of HAZ and base metal and the actual weld joint of P91 steel under tensile hold for various time periods. In this Chapter, the effect of prior creep-fatigue damage on the tensile properties of P91 base metal is evaluated. In the Chapter 8, summary of the work and conclusions are presented. Based on the observations and conclusions from the current study, scope for the further investigation is recommended in Chapter 9.

CHAPTER 2 LITERATURE REVIEW

2.1 INTRODUCTION

The present chapter trades in with the literature associated with the physical metallurgy aspects, mechanical properties and low cycle fatigue and creep-fatigue interaction behavior of the current study material, P91 steel. The steel has been selected as the material for the steam generators components of the Prototype Fast Breeder Reactor (PFBR), which has been commissioned at Indira Gandhi Centre for Atomic Research (IGCAR), Kalpakkam, Tamil Nadu, India. The basis of the selection of the steel for the application in the steam generators, the evolution of the Cr-Mo ferritic/martensitic steel, the effect of alloying elements added, microstructural changes due to tempering temperature and strengthening mechanism of the steel are briefly discussed in Section 2.2. In Section 2.3 the basic mechanical properties such as hardness and tensile properties are discussed. The general principles of fatigue, major classification in the fatigue, microstructural damage evolution during low cycle fatigue (LCF) deformation and factors involving LCF properties of the steel at elevated temperature are discussed in Section 2.4. The creep behavior of ferritic steel is discussed in Section 2.5. This is followed by Section 2.6, which deals with the fundamentals of creep-fatigue interaction (CFI) and types of CFI loadings. Literature pertaining to the weld joint of ferritic steels, microstructural evolution during welding and the importance of studies on the simulated microstructures of the P91 steel weld joint is dealt in Section 2.7.

2.2 MATERIAL

Materials selected for the steam generator of the sodium-cooled fast reactor (SFR) should have better mechanical properties like creep, fatigue and creep-fatigue interaction and resistance to carbon loss in the material through leaching, which causes a reduction in strength and resistance to stress corrosion cracking (SCC) during the high-temperature service in sodium and water atmosphere [46]. In view of the austenitic alloys that have poor resistance to aqueous SCC, ferritic steels are the most preferred materials for SG applications. Modified 9Cr–1Mo (P91) ferritic steel exhibits higher creep strength than that of many ferritic steels due to the stability of its microstructure even at prolonged high-temperature service [47,48]**.** This is one of the main aspects, which favors the selection of modified 9Cr–1Mo steel for steam generator components in SFRs. The selection of proper material and subsequent optimization in the design and fabrication ensure the high integrity of components of steam generators. The steam generator parts such as tube, shell, and thick-section tube sheet/plate are fabricated through welding using mono-metallic material because using single structural material improves the reliability of the welds [49].

In general, the P91 steel is used in the heat-treated condition includes normalizing and tempering that result in tempered martensite structure. The controlled addition of strong carbide formers such as vanadium, niobium, and nitrogen gives rise to grain boundaries precipitation of extremely stable MX-type (M-vanadium and niobium) carbonitride particles on tempering and during high-temperature service exposure that contribute to the high creep strength [50]. In actual structures fabricated by welding, a high percentage of failures occur in the heat-affected zone [42,51]. Since ferritic/martensitic steels are heat treatable and the microstructures are temperature sensitive the weld joint consists of varying microstructures having different mechanical properties. The high heat generated during fusion welding attributes to grain coarsening and the phase changes leading to the severe changes in microstructures [52].

2.2.1 Development of 9-12% Cr-Mo steels

The series of Chromium-Molybdenum ferritic/martensitic steels is a significant set of alloys and has been built-up as structural materials for high-temperature applications in the chemical, petrochemical and conventional coal-fired and nuclear power plants. The selection of materials for structural components for high-temperature applications is primarily based on high-temperature mechanical properties in addition to their compatibility with the service environment. A brief retrospection of the evolution of Cr-Mo steel up to modified 9Cr-1Mo steel and further development to its present state is discussed below.

The development of 9-12% chromium steels was begun with the manufacture of 12%Cr steel alloyed with 2-5% Mo in 1912 by Krupp and Mannesmann, primarily, for steam turbine blades [53,54]**.** In the 1920s, the Cr-Mo steels slowly started to find applications in conventional electricity generation plants. In the subsequent decades, the 2.25%Cr-1%Mo steel (P22/T22 steel) was gradually developed and is still widely used in thermal power and chemical processing plants, and steam generators of LMFBRs [55]. Increased operating temperature at or above 823K and/or the aggressive environment in the oil processing industry demanded the materials with chromium content higher than 2¼ Cr (5-12% Cr) [56]. Of these, 5Cr-0.5Mo finds an application in the Oil industry. The 9Cr-1Mo (T9/P9) type of steel, possessing higher corrosion resistance in the oxidation environment compared to 2.25%Cr-1%Mo steel, was initially developed in the 1930s for use in gas turbine engineering, aerospace industries, chemical and petrochemical plants, conventional and nuclear electrical power plants [57]. At present in the gas turbines and boilers and turbines in steam power plants the high-chromium ferritic/martensitic steels are predominantly used. This steel was started to be used in the late 1960s in the nuclear power program such as for the advanced gas-cooled reactor and experimental fast reactor and in both the atmospheres the steel exhibited excellent performance at elevated temperatures up to 823 K. Although the creep strength of 9Cr-lMo steel was enough for the conditions in which it was used, it was considered to increase the creep strength without any adverse effect on the other attractive properties. This has subsequently led to further development of 9%Cr heat-treatable steels with lower carbon (0.1% max.) contents, to have the combination of high temperature creep, oxidation and corrosion resistance. These steels include the initial modification in the plain 9Cr-lMo steel by the addition of stable carbide formers, like V, Nb, N (9Cr-1Mo-V-Nb known as P91 or T91) [1,58].

The continuous modification in altering the amount of Mo and the addition of W brought in new chemical composition such as 9Cr-0.5Mo-1.8W-V-Nb, which is designated as T92 or P92. Further to improve the creep strengths and steam corrosion resistance of the steel developed, optimization of alloying elements like Mo and addition of boron (B) and copper (Cu) was carried out in the 1990s [2,59,60]. The inferior steam oxidation resistance and low thermodynamic stability of the strengthening precipitates restrict the use of the P92 ferritic-martensitic steel at about 893 K [61].

The development of highly heat-resisting construction materials has been focused in view to maintain the resources and reducing the CO_2 emissions by an increase in the efficiency of energy conversion systems. The high chromium (9-12 wt%) steels are used in the most modern steam power plants, whereas austenitic steels still find applications, particularly in superheaters and reheaters. An improvement in efficiency to about 50% shall be achieved provided with the necessary increase of steam parameters to ~ 923 K/30 MPa [61,62].

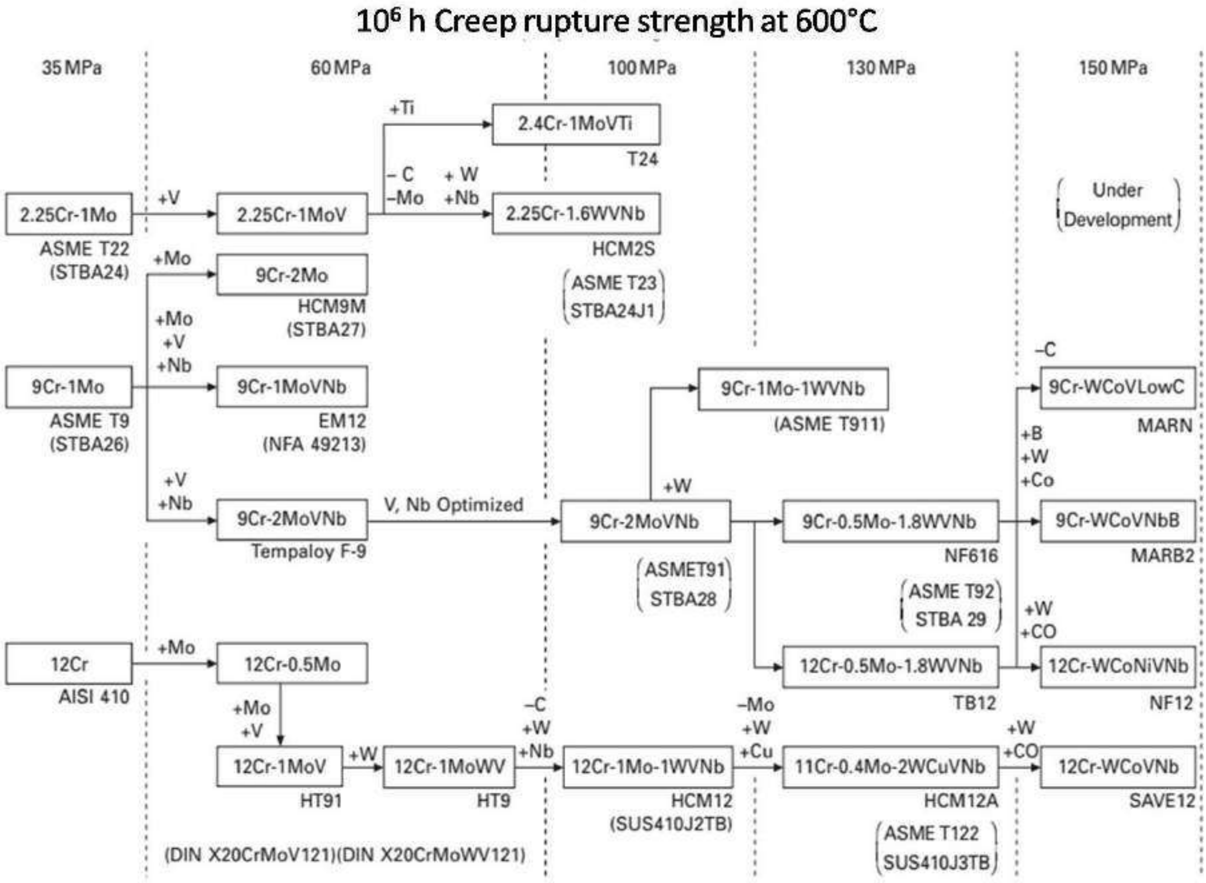

Fig. 2.1 Chart showing the progressive development of Cr-Mo steels [63].

Because of its inadequate creep strength and low resistance to steam oxidation due to the relatively lesser chromium content, the perception of 9-12 wt% chromium ferritic-martensitic steels appears to hit technological restrictions [63]. The even distribution of fine carbide and carbonitrides particles give rise to the stability of the microstructure, which in turn provides the significant creep strength of these materials. The development process of the Cr-1Mo steels to its present state is given in Fig. 2.1 [63].

2.2.2 Influence of alloying elements

The chemical elements composition of any alloy has an important effect on the phase transformation and the sequence of secondary precipitates formation due to heat treatments.

Similarly, the metallurgical optimization and/or new additions have resulted in better materials with improved properties in 9-12% Cr martensitic/ferritic steels [64,65]**.** The individual effect of a given element on the behavior of alloy is generally indeterminable due to the interaction of inter-element that depends on its quantity and the existence of other alloying elements and related kinetics [64,66–68]**.** Hence, alloying elements are typically chosen concerning their contribution that is observed to be either beneficial or detrimental to existing properties. The addition of most elements stabilizes certain phases or precipitates that are beneficial to long-term creep rupture strength and suppress some detrimental phases. Few elements are added to increase solid solution strengthening, improve the steam oxidation and corrosion resistance properties. The influences of alloying elements added in the P91 steel are described in the followings.

Carbon (C): It is the main alloying element in steel and has a large effect on steel properties. Carbon stabilizes austenite relatively better due to its greater solubility although it tends to occupy the interstitial sites in both austenite and ferrite phases. Besides, C in the form of carbides causes the secondary hardening of grade P91 steel [69]. It has been observed that an increase in C content (up to ~ 0.8%) generally increases hardness and tensile strength while decreasing the ductility, impact energy and weldability of this material [70,71].

Chromium (Cr): Cr is a strong ferrite stabilizer. It chemically reacts with carbon and strongly promotes the formation of carbides [72,73]. Tempering typically forms the carbides rich in Cr (for example, $M_{23}C_6$ and M_7C_3) and improves the steel's hardenability, creep strength and steam oxidation and corrosion resistance properties [65].

Molybdenum (Mo): It serves to stabilize the ferrite phase, M_2X and $M_{23}C_6$ precipitates in addition to promoting carbide formation in steels [74,75]. Molybdenum improves the corrosion resistance by increasing the grain-coarsening temperature of austenite. It also decreases the propensity of steels towards temper brittleness and improves their abrasion resistance [65].

Vanadium (V): It raises the grain-coarsening temperature of austenite and promotes the formation of fine grains. Moreover, V stabilizes the ferrite phase and increases the tendency towards formation of fine V-rich carbides, nitrides and carbonitrides (of the MX type) with C and N and subsequently improves the long-term creep rupture strength of steels [76,77]. It is also known to resist tempering, increase hardenability (when dissolved) and to provide marked secondary hardening effect.

Niobium (Nb): It also stabilizes the ferrite phase, similar to V. Niobium carbides and carbonitrides precipitates are very stable even at high temperatures and improves the creep strength of 9-12% Cr steels [78]. The addition of even small amounts of Nb is to retard the recrystallization of austenite phase that promotes the fine grain microstructure, which significantly increases the yield strength of steel [79,80].

Nitrogen (N): It is also an austenite stabilizer akin to C. Nitrogen too occupies interstitial sites in the Fe lattice. Higher amounts N tends to stabilize the fine MX type precipitates of 9-12% Cr steels and hence to achieve improved creep strengths [81].

Nickel (Ni): Being an austenite stabilizer it is commonly added to prevent the formation of δ-ferrite, and also to increase the toughness and strength of ferritic/martensitic steels [65]. In large quantities, it highly assists (along with Cr) in improving the oxidation and corrosion resistance in these steels. On the other hand, it also accelerates the coarsening of precipitates causing the lowering of creep strength of the steel.

Silicon (Si): It is added to assist in the formation of protective silicon dioxide (SiO_2) surface layers that provide better corrosion resistance [82]. Silicon stabilizes ferrite and also accelerates the precipitation and coarsening of the Laves phase, which influences the kinetics of carbide precipitation [83–85]. Addition of large quantities promotes the δ-ferrite formation and hence other austenite stabilizers are often added to counteract this adverse effect [69].

Manganese (Mn): Presence of Mn is mostly affecting the creep strength of P91 steel, however, it is usually added in small quantities to improve their hot working properties while marginally increasing strength, ductility and hardenability [79].

Copper(Cu): Cu is added to effectively slow down the formation of detrimental phases such as δ-ferrite [53]. The low solubility of Cu in the ferritic phase attributes to the formation of Cu-rich precipitates, which provides nucleation sites for Laves phase formation [80].

Boron (B): It improves the creep strength of 9Cr steel [86]. The preferential segregation of B along PAGBs and lath boundaries and partial replacement of C in $M_{23}C_6$ carbides efficiently slows down the carbides coarsening rate. It also retards the recovery of the dislocation and delays the grain growth during creep exposure [87]. Boron content should be strictly controlled (<0.001wt%) to decrease the formation of BN, which has an adverse effect [88].

2.2.3 Physical metallurgy aspects of P91 steel

As the development of the 9-12%Cr steels have made them increasingly more complex, an understanding of the fundamental principles of their physical concepts is important. The enhancements made in the 9-12%Cr steels have been achieved by small but important changes in the composition. These changes include the addition of relatively small amounts of elements like V, Nb, N, W and B. The main effects of these elements concern the precipitates they form. The aim of the end product would be to obtain a tempered martensitic microstructure with a fine distribution of precipitates.

2.2.3.1 Phase diagram

The addition of chromium to the iron-carbon system has important consequences not only on the corrosion resistance but also on the resulting microstructure and hence the attainable mechanical properties. Examination of the schematic pseudo-equilibrium phase diagram for the Fe-Cr-0.1%C system (Fig. 2.2) reveals that the steel with 9%Cr exists in one of the several sub-liquidus phase fields depending on temperature [89,90]: high temperature δ-ferrite + austenite; austenite; low temperature α-ferrite (pro-eutectoid) + austenite + primary carbides; and low temperature α-ferrite + primary carbides. The extent of any phase-field present in a particular alloy is dependent on its composition, which can be viewed in terms of a net chromium equivalent derived from the combined effect of ferrite and austenite stabilizing elements [91]. One such equation with composition in wt.% is given as:

Net Cr equivalent = (%Cr) + 6(%Si) + 4(%Mo) + 1.5(%W) + 11(%V) + 5(%Nb) + 12(%Al soluble) − 8(%Ti) − 40(%C) − 2(%Mn) − 4(%Ni) − 2(%Co) − 30(%N) − (%Cu).

Although N has a large coefficient, its absolute concentration level is usually an order of magnitude lower than C, therefore resulting in only a small effect. Increasing the Cr equivalent for example by increasing the Mo content or addition of V and Nb (both mechanism), will tend to shift the alloy in a duplex phase region beyond the austenite loop solvus. Study in plain 9Cr-1Mo steels have shown that low levels of δ-ferrite are formed inter granularly and are beneficial in inhibiting prior austenite grain growth [92,93]. A wide range of cooling rates leads to the formation of martensite [94,95].

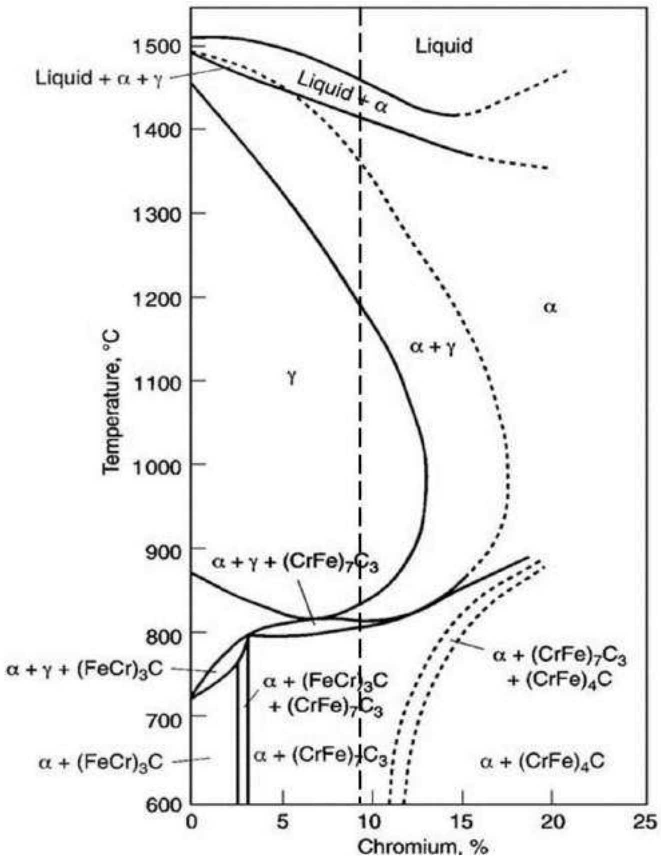

Fig. 2.2 The austenitic loop in a 0.1%C steel, α being ferrite, γ being austenite and $(CrFe)_4C$ is the $M_{23}C_6$ carbide [96].

2.2.4 Heat treatment

2.2.4.1 Normalizing

The typical heat treatment of 9-12%Cr steels involves normalizing, followed by tempering. The normalizing is generally performed at around 1323 K (inside the 'γ' austenitic loop, Fig. 2.2), typically for about 1-2 hours [97,98]. This should be adequate to dissolve most of the carbides and nitrides, and obtain a fully austenitic microstructure. The persistent ferrite at this time is commonly identified as δ-ferrite. The air cooling to room temperature generates fully martensitic structure in the steel (provided fixing the normalizing temperature to avoid the formation of δ-ferrite), with a high dislocation density. As the steel with the martensitic structure is hard and brittle, it is necessary to soften it by tempering.

2.2.4.2 Tempering

Tempering is carried out in order to obtain optimized toughness by reducing the brittleness of martensite that formed during normalizing and subsequent air cooling. The tempering temperature is generally fixed in the range between 953-1053 K, depending on the properties required [97,99]. The tempering heat treatment should take place at a temperature below the AC_1 temperature to avoid transformation to austenite. The formation of austenite will result in fresh martensite on cooling, which is undesired from a toughness standpoint. A longer tempering time at higher temperatures will result in lower hardness but increased toughness [64].

2.2.4.3 Typical microstructure

The Fig. 2.3(a) and (b) depict tempered martensitic microstructure in the P91 steel after normalizing and tempering and a schematic representation of dispersal precipitate states in martensitic 9-12%Cr steels respectively [45,100]. The typical microstructure of Cr-Mo steel consists of packets and blocks inside the prior austenite grains and elongated sub-grains with lath morphology inside each block. The Fig. 2.3(b) is a representative of P91 steel post-heat treatment, where the effect of tempering causes the precipitates to mostly reside along the substructure interfaces and the coarse carbonitrides are non-uniformly distributed within the different sub-grains. This microstructure contains plenty of heterogeneities besides prior austenite grain boundaries, including martensitic lath boundaries and a high dislocation density [101]. The PAG and sub-grain boundaries are stabilized by extensive $M_{23}C_6$ and M_7C_3 secondary-phase carbides (average size of ~ 100 nm), where M represents Cr, Fe and Mo and C represent carbon [50,56,102]. The homogeneous precipitation of finely dispersed Nb/V carbonitrides of the type MX (average size of ~50 nm) in ferrite as additional strengthening agents inside the matrix of P91 steel [103]. These precipitates can have a spherical Nb(C, N) center with plate-like ellipsoidal V-rich wings emanating from the sides (see Table 2.1) [104]. All these precipitates are relatively stable and effective obstacles against dislocation motion, increasing the elevated temperature strength of this steel.

Table 2.1 Details of precipitates in P91 steel [104] (underlined elements in the precipitates composition formula have the main contribution in the primary strengthening).

Precipitate	Formula	Morphology	Remark
$M_{23}C_6$	($\underline{Cr}$, Fe, Mo)$_{23}C_6$	Coarse	Precipitate during tempering
MX	($\underline{V}$, Nb) (C,N)	Fine & Ellipsoidal	
MX	($\underline{Nb}$, V) (C,N)	Fine & Spheroidal	Undissolved during austenitization

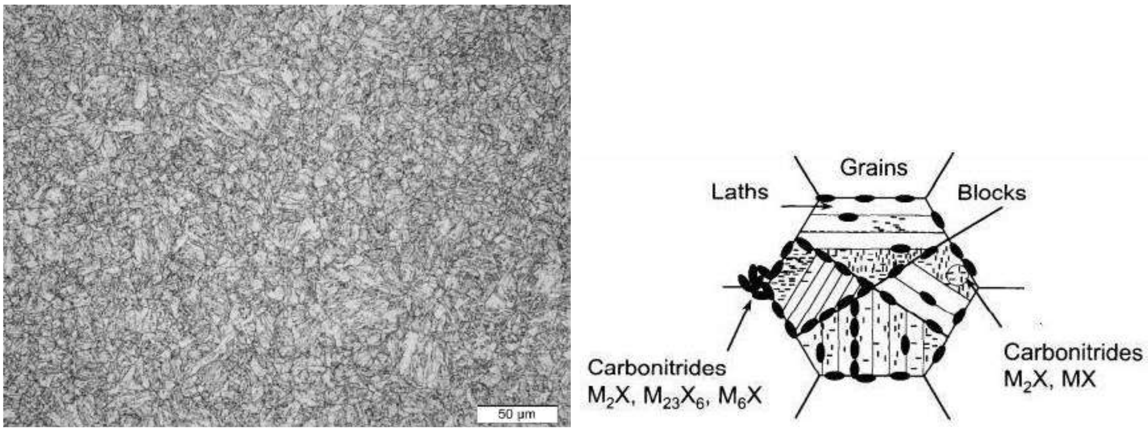

(a) (b)

Fig. 2.3 Typical initial tempered martensitic microstructure; (a) optical micrograph of P91 steel [45] and (b) schematic representation of non-uniform precipitation states in 9-12% Cr steels [100].

2.2.5 Strengthening mechanisms

Strengthening means the ability of a material to resist plastic deformation caused by dislocation movement. Creep-rupture strength of a material is defined as the stress at which it ruptures (fails) in a given time at an elevated temperature and is typically a combination of various strengthening mechanisms operating at the discrete microstructural scales. For P91 steel, the strengthening is obtained due to solid solution hardening, precipitation or dispersion hardening, dislocation hardening and boundary/sub boundary hardening [105,106]. Summary of different strengthening mechanisms are presented below.

2.2.5.1 Solid solution hardening

The addition of an alloying element (solute) introduces substitutional or interstitial point defects in the microstructural matrix (solvent) that induces localized crystallographic aberrations in the material. These tensile/compressive lattice distortions produce an additional strengthening effect – known as solid solution hardening – by hampering the movement of the dislocations that interact with the stress field of solute [107]. Substitutional solute atoms such as Mo have much larger atomic radii than Fe and hence, they are effective solid solution strengthening elements for P91 steel.

2.2.5.2 Precipitation or dispersion hardening

Additional creep rupture strengthening apart from substitutional point defects is provided with the clusters of precipitates, which constitute regions of a different phase in steels. Preferential nucleation of metal carbides/carbonitrides such as $M_{23}C_6$, M_7C_3, MX, etc., and intermetallic compounds like Laves phase especially at the vicinity of grain boundaries offer considerable precipitation hardening in these steels [108]. The minimum stress that required to penetrate a dislocation between these precipitates is described by several mechanisms such as the Orowan mechanism [64]. It has also been reported that the strengthening effect of solid solution and dispersion hardening mechanism is practically so inter-dependent that an additive rule does not generally hold good [106,109,110].

2.2.5.3 Dislocation hardening

Linear defects such as dislocations with high density (~ 1-10 $\times 10^{14}$ m^{-2}) even after tempering [111], provide effective strengthening in P91 steel due to their reduced mean free paths – the distance traveled by a free dislocation before it collides another one in its motion – at ambient temperatures only. However, the reduced activation energies for dislocation motion at elevated temperatures subdue their contribution to long-term strengthening.

2.2.5.4 Boundary/sub-boundary hardening

The laths and blocks, which are often considered as elongated sub-grains in the ferritic/ martensitic microstructure of P91 steel hinder the motion of dislocation along their boundaries. Hence, such kind of additional strengthening effect is common in these steels [106]. Further the fine carbonitride precipitates can stabilize the free dislocations in the matrix and the sub-grain structure to achieve enhanced dislocation and sub-boundary hardening, respectively against recovery [77,112].

Prolonged exposure to elevated temperature under constant stress and cyclic strain conditions significantly drop the precipitation and dislocation strengthening effects in P91 steel. These phenomena, further, accelerate microstructure evolution, which causes a loss of sub-boundary hardening [113]. Thus, all of these individual strengthening mechanisms are interrelated and make effective contributions to the overall material's strength.

2.2.6 Microstructural degradation

In general, the internal microstructure in material continuously and gradually changes when subjected to external loading at elevated temperatures. Mostly, the properties of materials are degraded due to this microstructural evolution with time and hence this needs to be considered for sound design practices [114,115]. If an accumulated damage reaches or exceeds critical levels, catastrophic failure ensues that may lead to human and/or economic loss.

As in the foregoing discussion, the matrix of ferritic/martensitic steels contains various internal interfaces including PAG boundaries, lath boundaries, sub-grain and block boundaries, and a very high dislocation density before tempering. Besides, the matrix and the boundaries are decorated with the different kinds of precipitates like $M_{23}C_6$ carbides and MX carbonitrides [116,117].

After tempering, the dislocation density decreases and the boundaries between the PAG, block and lath exist at thermodynamic equilibrium (Fig. 2.4(a)). However, when the component made of this material is exposed to elevated temperature (up to 923 K) and stress in-service, the material gradually responds by microstructural evolution as shown in Fig. 2.4(b). These conditions considerably decrease the material′s strength due to the coarsening of precipitates and intermetallic compounds ($M_{23}C_6$, Laves phase), coarsening of sub-grains and precipitation of undesirable phases (Z-phase, δ-ferrite), the creep rupture strength reduces considerably under these conditions [118–122]. A brief overview of these aspects of microstructural evolution is given below.

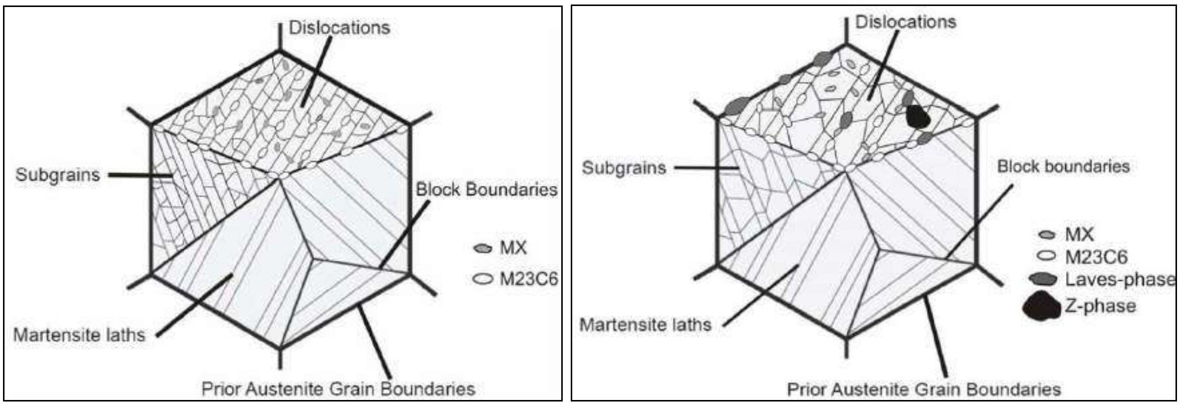

(a) (b)

Fig. 2.4 Schematic illustration of pristine microstructure of P91 steel; (a) after tempering (internal interfaces and precipitates) and (b) evolution with exposure to elevated temperatures and external stress [44].

2.2.6.1 Precipitate coarsening (Ostwald ripening)

The coarsening of carbides precipitates during service at elevated temperature greatly degrades the creep strength of P91 steel. It has been reported that the strength of P91 steel is derived from precipitation hardening, thus controlling the average size of precipitates in solid solution has important implications [85,86]. There are three stages of precipitates coarsening in a solid solution – nucleation and/or growth of the more stable phase in the metastable solid solution followed by coarsening or ripening of this phase. Ostwald proposed that the large carbide particles grow at the expense of less-stable smaller ones to reduce the interfacial energy of the material [123,124] and the near-equilibrium values of the volume fractions of the phases cause the coarsening of precipitates, as shown in Fig. 2.5. Thus, the total thermodynamic free energy of the system is decreased with an increase in the average size of large particles.

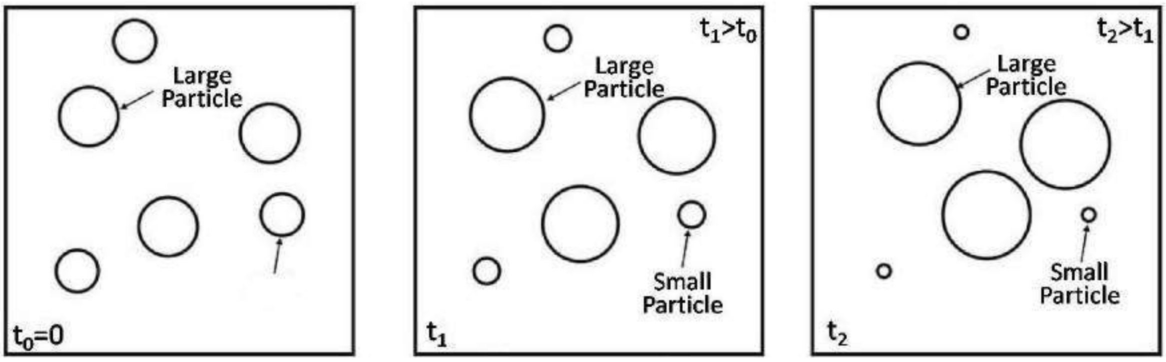

Fig. 2.5 Schematic of Ostwald ripening mechanism [125].

2.2.6.2 Sub-grain coarsening

The precipitation of solute atoms and recovery of dislocation cell structure due to tempering leads to the formation of a sub-grain structure, that is characterized by frequency distributions of boundary misorientations and spacing [126,127]. The sub-grains, in general, share their boundaries with PAGs, martensite lath blocks of similar orientation and martensite laths and other sub-grains within the laths [128]. It has been reported [129] that the PAG and block boundaries are of the high-angle type with misorientations generally >15°, whereas the martensite laths and sub-grains within the laths have comparatively low-angle boundaries characterized by lower misorientations (<15°). Thus, high-angle boundaries tend to interrupt the lattice coherency of adjacent crystals, whereas low-angle boundaries form planar dislocation networks. Although these high-angle boundaries provide considerable resistance to the motion of sustained dislocation, they however allow grains to share a common boundary to relatively sliding and thereby aid for atomic diffusion through the interface. The initial size of the sub-grain that also corresponds to the width of martensitic laths and blocks in tempered martensite is most commonly 0.4 µm [122,126]. As is the case in most structural applications of these steels, sub-grain coarsening occurs during the deformation with the time component in the applied load. It has been reported [121], that the reduction in creep rupture strength is only due to the forced sub-grain coarsening within relatively short periods with insignificant changes in the precipitate structure. It was further noticed that when the maximum stress in laboratory experiments is adequately low, the sub-grains size grows fast towards that of instantaneous stress-dependent steady-state sub-grains, with accumulating inelastic strain. Such a phenomenon of the sub-grain coarsening is also shown to increase by an order of magnitude in the minimum creep rate regime [121]. On the other hand, the authors [130] have reported that the sub-grain boundaries migrate to accommodate dynamic dislocation recovery during creep deformation.

2.3 TENSILE PROPERTIES

Tensile properties are composed of the reaction of the materials to resist when forces are applied in tension. Tensile properties such as yield strength, ultimate tensile strength (UTS), % elongation, % area of reduction are the basic and essential parameters that are considered for the choice of structural materials for engineering applications.

2.3.1 Yield strength, σ_y

The stress corresponding to the intersection of the monotonic tensile engineering stress-strain curve and the 0.2% offset line is known as the yield strength of the material. Generally, the yield strength is determined by drawing a straight line at 0.2% offset or 0.2% total strain parallel to the slope of the linear section of the monotonic tensile stress-strain curve as illustrated in Fig. 2.6. The yield strength, which designates the start of plastic deformation, is regarded to be crucial for the design of engineering structural components, where the factor of safety is generally applied as given in equation 2.1. It is worth noting that for engineering designs, the ultimate tensile strength, σ_{TS}, can also be substituted by the value of yield strength. Factors of safety depend on various issues such as the applied load's accuracy, evaluation of degradation, and the effects of failed structures on the fatality, financial loss, etc. Pressure vessels utilize safety factors of 3−4.

$$\sigma_w = \frac{\sigma_y}{\text{Safety Factor}} \cdot \frac{\sigma_{TS}}{\text{Safety Factor}} \qquad \text{----(2.1)}$$

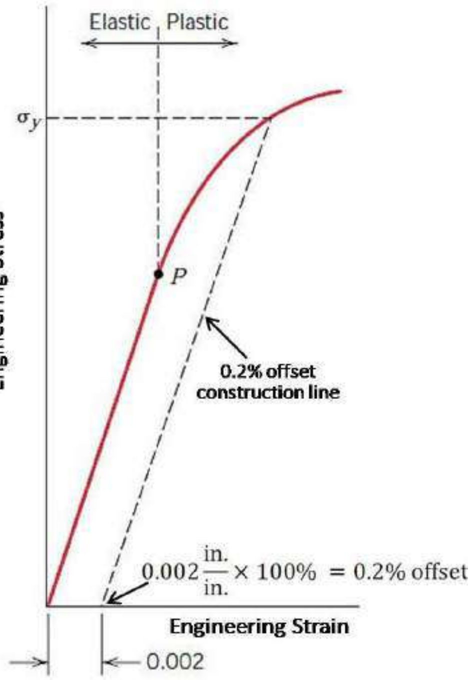

Fig. 2.6 The determination of the yield strength at 0.2% offset [131].

2.3.2 Ultimate tensile strength, σ_{TS}

The ultimate tensile strength or tensile strength (UTS, σ_{TS}) of the material indicates the maximum load that the material can withstand before necking occurs [132]. The necking can be identified through a local decrease in specimen cross-sectional area usually observed in the middle of the gage portion.

$$\sigma_{TS} = \frac{P_{max}}{A_0} \qquad \text{----(2.2)}$$

2.3.3 Tensile ductility

Tensile ductility is the measure of the deformation that the material can withstand before the material is completely fractured. It is also important that the material should have enough ductility to undergo deformation and avoid catastrophic failure of the component. The percentage of elongation and/or percentage of reduction in area are used for representing the ductility of a material with a definite gage dimension. The ductility can be calculated from the following equations;

$$\%\mathrm{Elongation} = \frac{\Delta L}{L_0} \times 100 \qquad \text{----(2.3)}$$

$$\%\mathrm{RA} = \frac{A_f - A_0}{A_0} \times 100 = \frac{\Delta A}{A_0} \times 100 \qquad \text{----(2.4)}$$

where A_f is the cross-sectional area of specimen at fracture [133].

2.3.4 Tensile deformation behavior of P91 steel

Monotonic tensile stress-strain curves of base metal and flux-cored arc welded (FCAW) weld metal of P91 steel at room temperature and 923 K are presented in Fig. 2.7. The steel exhibits typical tensile stress-strain curves with less difference between the yield strength and tensile strength, unlike the austenitic alloys. The yield strength of Grade 91 at room temperature was 500 MPa and at 923 K was 225 MPa [45]. The yield strength of the weld metal is higher than the base metal. During the test, the stroke (thus strain) rate has been increased after yielding to pull the sample to failure.

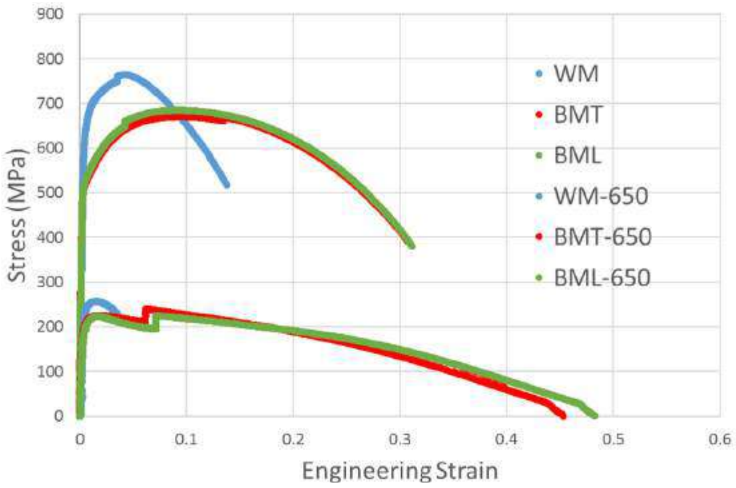

Fig. 2.7 Stress-strain curves from tensile tests on Grade 91 steel. BMT and BML are base metal specimens in transverse and longitudinal directions, respectively [45].

2.4 FUNDAMENTALS OF FATIGUE

Instead of pure monotonic loads, engineering structural components are often subjected to cyclic loads that can vary periodically or non-periodically over time. Under such loading condition, alternate stresses/strains are induced in a material which can cause progressive structural damage and lead to fatigue failure. Fatigue is defined as the process of localized degradation of materials under cyclic or alternate loads [134]. Even though fatigue failures are most common in the aerospace industry, it is estimated that 85-90% of the structural failures takes place under the influence of cyclic loadings [134].

2.4.1 Two distinct domains of fatigue failure

Low cycle fatigue or high strain fatigue refers to stress or strain cyclic loading in the dominantly plastic deformation regime, where the stress-strain relationship is not linear, i.e., Hook’s law is not valid. High stress or strain cyclic loading result in lower cyclic life. Therefore, the low cycle fatigue alternatively is defined in terms of failure in a lower number of cycles, i.e., $<10^4$. Low cycle fatigue loading stems from mechanical and thermal stresses that arise due to start-up and shut- down, variations in operating conditions and temperature gradient across the thickness. On the other hand, high cycle fatigue (HCF) or low strain fatigue refers to cyclic loading well within the elastic regime and hence higher cyclic life, i.e., $>10^4$.

Resistance to deformation under low cycle fatigue and thermal fatigue conditions is a principal requirement in the selection and use of materials for structures operating at high temperatures. The industries of aircraft, automotive and generating of power use higher temperature cycles and stress levels to improve the efficiency of fuel. Temperature fluctuations and flow-induced vibrations during the power plant operation generate fatigue loads. In a high temperature-engineering component such as a turbine rotor or a pressure vessel having internal pressure, localized plastic strains are generated by loading, at points of stress concentration such as notch [135]. It is presumed that a temperature gradient exists in the notch region. Regardless of the mode of loading, i.e., cyclic strain or stress-controlled, the plastic region near the root experiences a total strain-controlled situation dictated by a much larger surrounding mass of elastic material.

2.4.2 Strain-controlled LCF testing

Low cycle fatigue arising from thermal transients essentially occurs during strain-controlled cyclic deformation as the region of surface/subsurface is under constraints imposed by the remaining volume of the component**.** Figure 2.8 illustrates such a situation and the hysteresis loop generated as a result of thermal gradients in a thick section component [136]. As shown in Fig. 2.8(a)**,** if a hot fluid suddenly impinges at A, the surface at A undergoes compression as it tries to expand opposite to the restraining surrounding structure, yielding along OQ (Fig. 2.8(b)). As the flow of heat is slow towards the core, minimizing the temperature gradient across the system, the surface undergoes tension due to the bulk of the system expands, approximately isothermally along QR. Residual stress relaxes along RR′ during steady-state operation. When the fluid suddenly cools/shut-off, surface layers (at A) undergo tension as the contraction is attempted and afterward, as the full system cools, the surrounding metal taking the yielded section A into compression. Repetition of heating and cooling cycle again from point-P results in a closed hysteresis loop. It is important to note that the component undergoes strain within limits, called strain-controlled deformation, for a fixed temperature interval imposed on the component. Also, creep damage occurs during stress relaxation along RR’. Many high temperature components, therefore, have to be designed not only against creep and fatigue but also against CFI failure. In general, it has been found that small cracks do initiate very early in the total life of a laboratory specimen and that LCF is primarily a crack propagation phenomenon. That is, most of the total fatigue life is spent in propagating a micro-crack to a critical size.

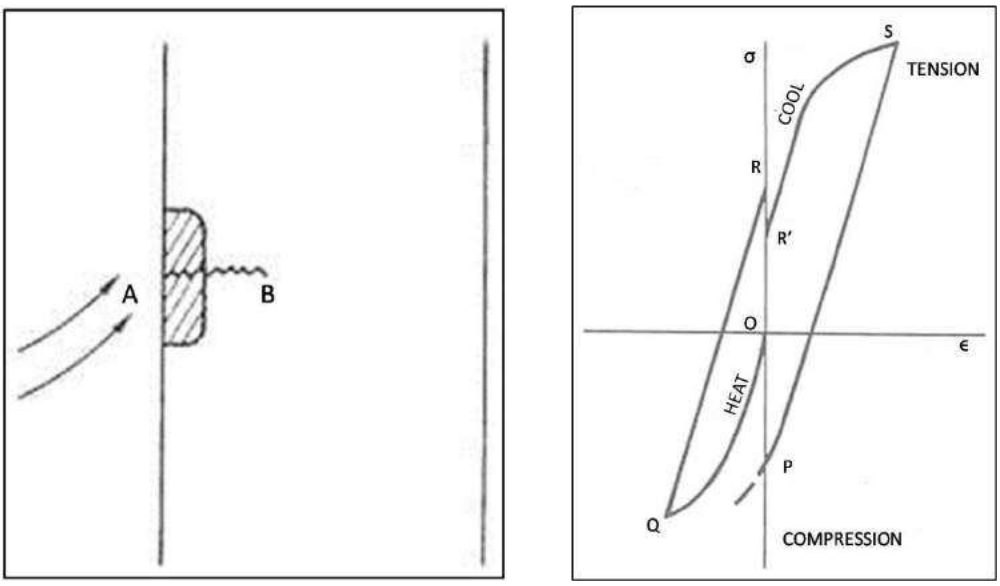

(a) (b)

Fig. 2.8 Schematics of (a) heating and cooling the surface of a thick structure and (b) resulting hysteresis loop [136].

Low cycle fatigue process can be envisaged to take place as in the following stages (Fig. 2.9): i) nucleation and premature crack growth in the vicinity of the plastic zone evolved at the stress concentration site (e.g., notch root); ii) stable crack's propagation within the plastic zone; iii) the crack propagation through the elastic zone, the plastic zone is generated with crack advance, up to the resultant structure failure, either abrupt fracture, leakage or by additional fluctuation or deformation [137]. Regardless of the external mode of loading, (stress or strain-controlled) the plastic region near the stress concentration site experiences a total strain-controlled situation dictated by the much larger surrounding mass of elastic material. Therefore, strain-controlled high temperature LCF tests on smooth specimens are used in evaluating the crack initiation fatigue life of the component.

In isothermal low cycle fatigue tests and thermo-mechanical fatigue (TMF) tests, the specimen is imagined to represent the surface layers (of the real component) undergoing reversed yield. The LCF tests are conducted to acquire the design data and to investigate the cyclic deformation and fracture mechanisms in the material.

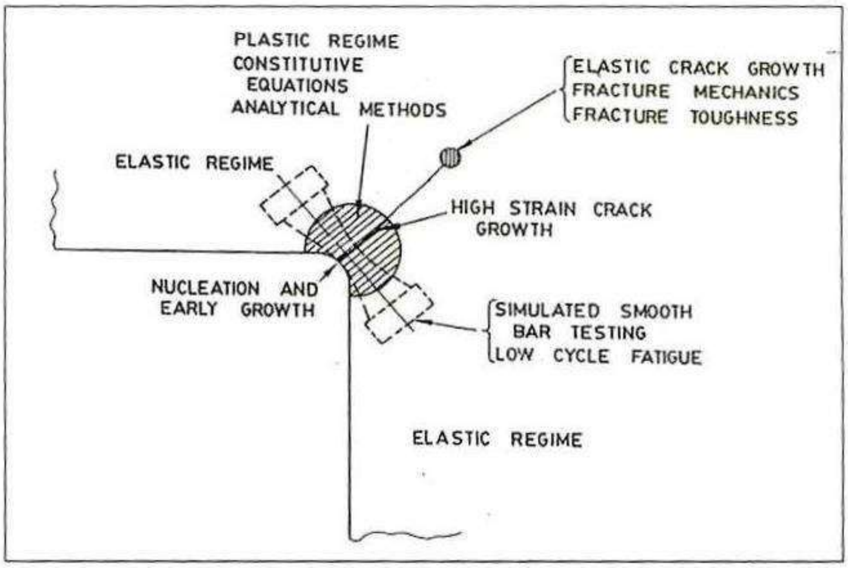

Fig. 2.9 Schematic view of high-temperature fatigue problem showing physical stages in failure process in a typical notched component and relevant disciplines [137].

2.4.3 LCF strain-waveform

Though there are sophisticated testing types of equipment that are capable of reproducing the complex σ-ε-T cycles, they are expensive. Therefore, the component behavior in a laboratory test is represented by replacing thermal strains by mechanical strain, introduced and controlled under isothermal conditions. Figure 2.10 shows typical waveforms used in LCF testing discussed in the previous section.

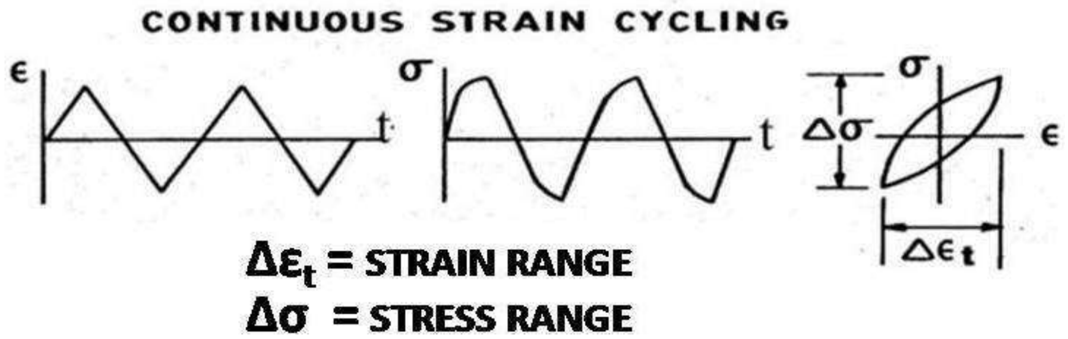

Fig. 2.10 Typical waveforms for strain-controlled fatigue testing.

2.4.4 General parameters and procedures employed in LCF data analysis

A schematic illustration of a stress-strain hysteresis loop in a fully reversed and symmetrical condition of the LCF regime is given in Fig. 2.11. The peak tensile (σ_{max}) and compressive (σ_{min}) stress values are measured as the height above and below the zero stress respectively. The stress range ($\Delta\sigma$) is defined as the difference between the peak tensile and compressive stresses in the hysteresis loop. The x-axis end to end distance is measured as the strain range ($\Delta\varepsilon_t$) and is composed of elastic and plastic components. The width of the hysteresis loop at zero stress is the plastic strain range ($\Delta\varepsilon_p$). The slope of the curve in the elastic portion of the load reversal regime is equal to the modulus of elasticity (E) of the material. The total elastic strain ($\Delta\varepsilon_e$) is given by $\Delta\sigma/E$, which is calculated as the difference between the total strain and the total plastic strain.

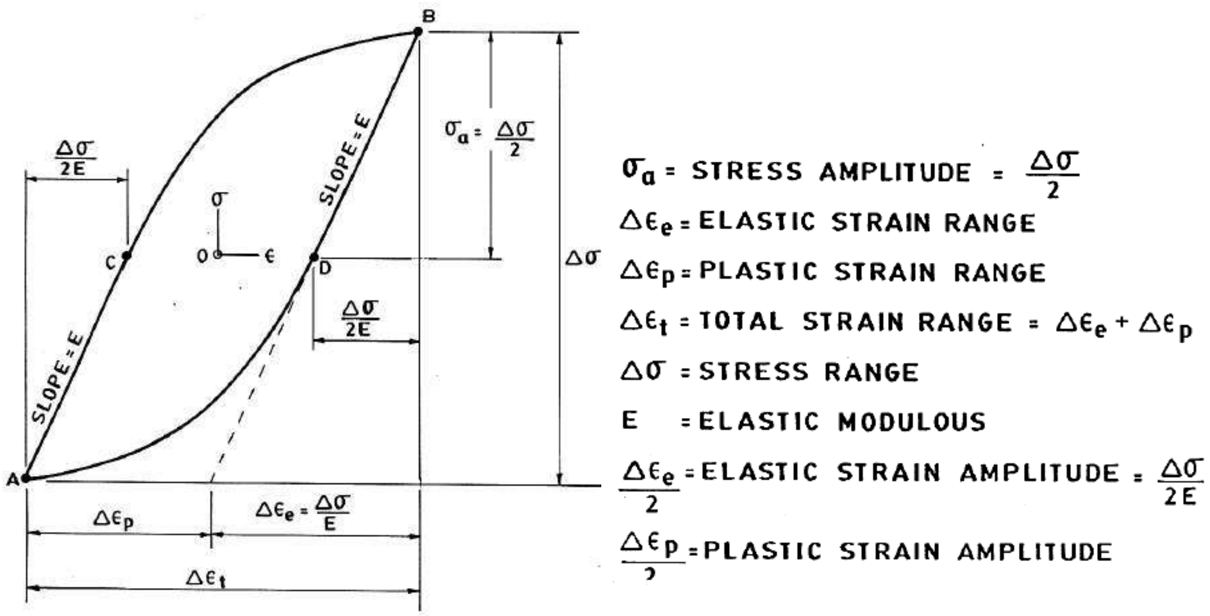

Fig. 2.11 LCF parameters in the stress-strain hysteresis loop.

The variable stress is recorded and plotted as a function of the number of cycles. A schematic representation of the cyclic stress response (CSR) curve for a material tested under strain control mode is presented in Fig. 2.12. During fatigue testing under total strain control, the stress to enforce the strain limit in successive cycles increases or decreases or remains constant. The alloys, which are initially hard (for e.g., FCC materials in cold worked and BCC materials with martensitic morphology conditions), soften during cycling whereas materials that are initially soft (annealed condition) harden during cycling. It has been suggested by authors [133,138] that when the ultimate strength to yield strength ratio is greater than 1.4, materials cyclically harden whereas those with a ratio of less than 1.4, cyclically soften.

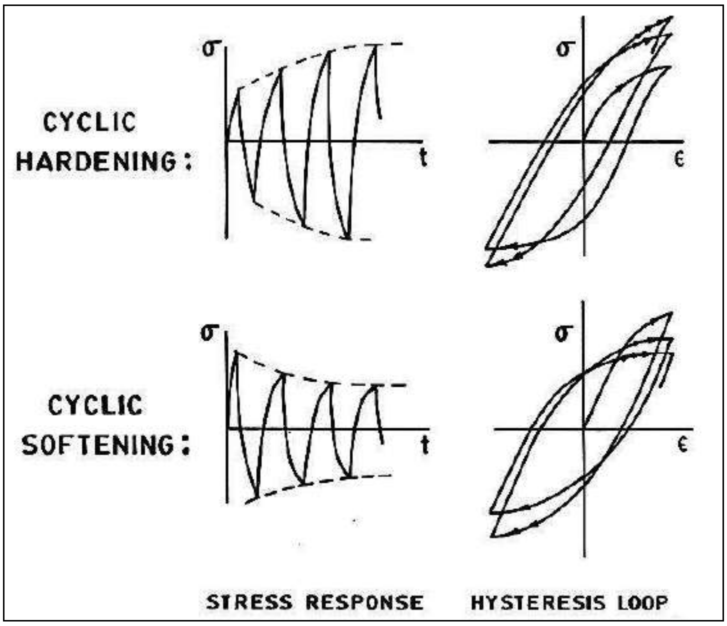

Fig. 2.12 Schematic representation of the response of metals to cyclic strain.

The cyclic stress-strain curve (CSSC) is drawn by connecting the peak tensile stresses of stable stress-strain loops of the same set of samples subject to fatigue tests at different strain amplitudes. A schematic illustration of this method can be seen in Fig. 2.13. Under conditions, where no saturation is attained the stress value is taken as the peak stress in a cycle corresponding to half-life [139]. The power-law relation, as shown in equation 2.5, represents the cyclic stress-strain curve.

$$\frac{\Delta\sigma}{2} = K'\left(\frac{\Delta\varepsilon_p}{2}\right)^{n'} \qquad \text{----(2.5)}$$

where, $\Delta\sigma/2$: cyclic stress amplitude at half life;

K' : cyclic strength coefficient;

$\Delta\varepsilon_p/2$: plastic strain amplitude at half life and

n' : cyclic strain-hardening exponent.

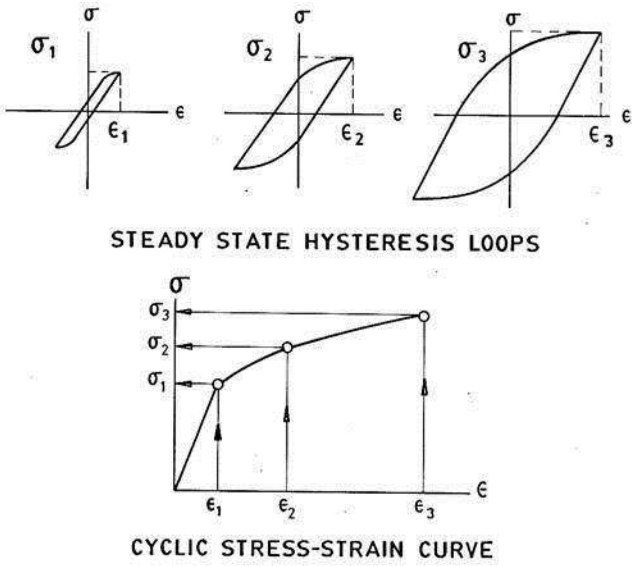

Fig. 2.13 Construction of cyclic stress-strain curve by joining tips of hysteresis loops. Points represents tips of stable hysteresis loops for a given strain amplitude.

The slope (n') can be evaluated from the log-log plot of stress amplitude versus strain amplitude. By plotting elastic and plastic strain amplitudes as a function of reversals to failure the fatigue life plots are obtained. These are known as Basquin [140] and Coffin-Manson [141,142] relations respectively. The relations are,

$$\frac{\Delta\varepsilon_p}{2} = \varepsilon_f'(2N_f)^c \quad \text{(Coffin-Manson)} \qquad \text{----(2.6)}$$

$$\frac{\Delta\varepsilon_e}{2} = \frac{\sigma_f'}{E}(2N_f)^b \quad \text{(Basquin)} \qquad \text{----(2.7)}$$

Where, $\Delta\varepsilon_p/2$: plastic strain amplitude at half life

ε'_f : fatigue ductility coefficient

c : fatigue ductility exponent

$\Delta\varepsilon_e/2$: elastic strain amplitude at half life

σ'_f : fatigue strength coefficient

E : elastic modulus

b : fatigue strength exponent and

$2N_f$: number of strain reversals to failure

On a double logarithmic scale, these equations have a linear variation as shown in Fig. 2.14. The curved line in Fig. 2.14 indicates the relationship of total strain amplitude-life, which obtained from the summation of Coffin-Manson and Basquin plots. Further, it is observed from the figure that at high strain, the plastic strain component dominates, whereas the elastic component is predominant at low strain. This observation leads to the understanding that a material having high ductility is preferred in the high strain or creep-fatigue region, whereas high strength materials are desirable in the high cycle fatigue regime. The intersection of Basquin and Coffin-Manson plots is considered as the transition between HCF and LCF regime with life corresponding to the intersection point defined as the transition fatigue life.

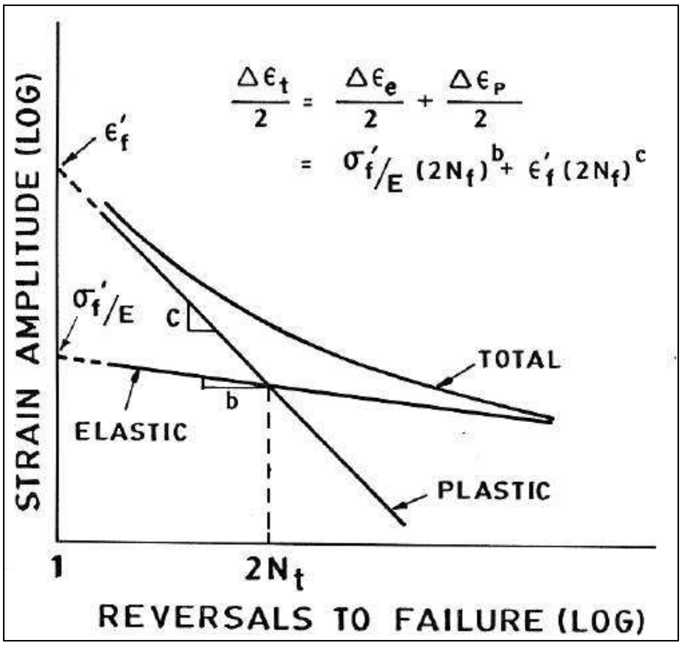

Fig. 2.14 Schematic of strain-life plots.

2.4.5 Damage mechanisms in fatigue

It has become widely accepted that fatigue damage is the result of repeated localized cyclic plastic microstrains (in the range $10^{-5} - 10^{-2}$). The different stages of the fatigue process are summarized in Fig. 2.15. They can be divided into the initial regime of cyclic deformation during which microstructural changes occur more or less homogeneously throughout the bulk and into the later regime of fatigue damage, which usually emanates from some form of strain localization and subsequent micro-crack initiation at or near the surface, and then spreads by crack propagation in a localized fashion into the bulk [143]. The saturation regime occupies a major part of fatigue life and hence steady-state values of the stress and (plastic) strain amplitudes are used as rough constant average values over the entire fatigue life. Cyclic hardening/softening depends on the metallurgical condition (cold worked/annealed) of material.

2.4.6 Failure under conventional fatigue cycle

In general, the fatigue-failure processes under faster strain rate cycling at elevated temperature and ambient temperature are similar. The final failure of the specimen takes place in the sequence of initiation (usually at the surface) and growth of one or more cracks until specimen separation occurs.

2.4.6.1 Fatigue crack initiation in ductile solids

Wood first proposed the origin of fatigue cracks in high purity metals and alloys and postulated that slip irreversibility of shear displacements along slip bands during cyclic straining leads to net slip [144]. This results in intrusions and extrusions, at sites where slip bands emerge at the free surface, which act as micro-notches and associated stress concentration promotes additional slip and fatigue crack nucleation. Slip irreversibility has been ascribed to dislocation annihilation within the slip bands, the formation of dislocation-jogs, nodes or locks, oxidation of slip steps, etc. Fatigue failure also initiates at the microscopic geometrical discontinuities such as grain and twin boundaries, inclusions, etc.

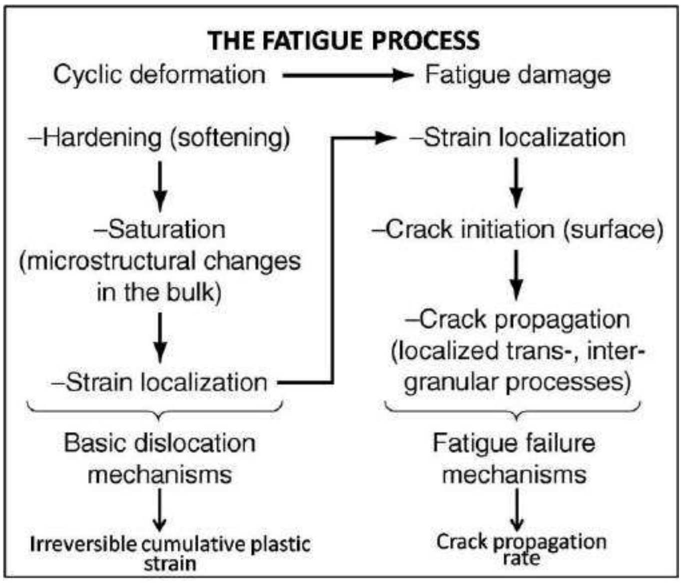

Fig. 2.15 Cyclic deformation and fatigue damage. Sequence of events and classification of mechanisms [143].

2.4.6.2 Fatigue crack growth in ductile solids

Fatigue crack growth occurs in three stages, as shown in Fig. 2.16(a). In stage I, cyclic crack growth occurs by single shear (on a plane of maximum shear, in the primary slip system) through the localized deformation zone at the crack tip, where the micro-crack and its surrounding plastic zone are confined to few grain diameters. This single slip mechanism results in a zigzag crack path, with the crack being oriented at about 45º to the applied stress/stain axis. Stage I fracture surface exhibits a faceted profile. In Stage II, crack growth occurs by simultaneous or alternating flow along with two-slip systems. This duplex slip mechanism results in a transition of crack from a plane of maximum shear to the plane normal to the principal stress, i.e., planar crack path normal to the far-field axis. Fracture surfaces exhibit crack marks known as fatigue striations, which are visual record of the crack front location during the propagation of the crack. One of the models for striation formation in the air is the plastic blunting process (Laird’s model) and applies to a wide variety of ductile materials including polymers.

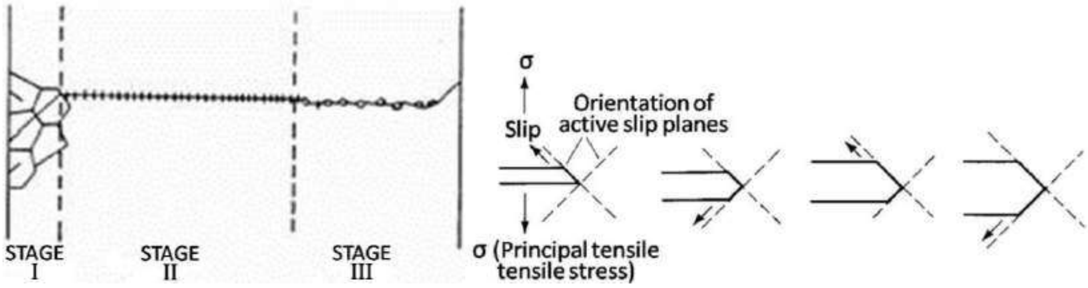

(a) (b)

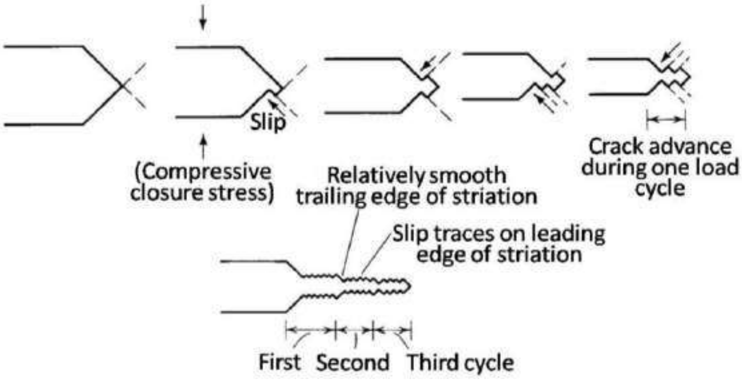

(c)

Fig. 2.16 Schematics of (a) fatigue crack propagation across a specimen indicating 3-stage of fatigue failure, (b) crack opening and crack-tip blunting and (c) crack closure and crack-tip re-sharpening [145].

The slips on the alternating slip planes open the crack during the tensile portion of cyclic straining, as illustrated in Fig. 2.16(b). While slip continues, the crack widens and the tip blunts at the peak tensile strain, but during the reverse of strain cycles towards compression the crack tip is re-sharpened through the partial slip reversal, Fig. 2.16(c). The crack closure does not weld, because of instantaneous oxidation (that induces slip irreversibility) of the new slip surfaces created during crack-opening displacement [145]. Stage II fatigue crack propagates stably until the local crack-tip deformation is of the order of material inhomogeneities and then static fracture contributes to the crack advance and leads to final fracture, as shown in Fig. 2.16(c).

2.4.6.3 Parameters influencing LCF properties at elevated temperatures

With an increase in temperature, several time-dependent phenomena such as substructural recovery, creep and environment and dynamic strain aging (DSA) occur with the fatigue process. These time-dependent effects may operate either independently or in combination in a synergistic way resulting in premature fatigue failure. In general, cyclically induced changes are increased at higher temperatures due to the fatigue enhanced time-dependent mechanisms.

2.4.6.3.1 Slip character

Slip character is a measure of the amount of dislocations dispersion during plastic deformation [146–148]. This concept is widely used to elucidate the cyclic stress response and the mode of cracking and fatigue failure. The stacking fault energy (SFE) plays a major role in the stability of the dislocation substructure, which is strongly influenced by dislocation mobility in a material. The material with high SFE exhibits easy cross slip due to large dislocation mobility, whereas low SFE materials show limited cross slip. Thus, the extent of cyclic hardening or softening of some materials differs from others. Cyclically softening is also reported in the certain solution annealed alloys, which is due to mutual annihilation and thermally activated rearrangement of dislocations at higher temperatures, which results in a decreased total dislocation density and a low energy dislocation configuration.

The addition of solutes to metal generally causes a reduction in the stacking fault energy in the alloy system, which promotes planar slip. However, at elevated temperatures, the reduced tendency for a cross slip in solid solution alloys due to a decrease in stacking fault energy is counterbalanced by the temperature-dependent increase in the stacking fault energy. Uniformly distributed nonplanar dislocation arrangements, cells and sub-grains in the substructure and a general surface wrinkling are the common features for wavy slip materials. The high SFE, incoherent precipitates, large strains, high temperature and low strain rate promote the cross slip deformation [148]. It has been suggested that conditions favorable to planar slip in the alloy produce better fatigue resistance than wavy slip [149]. This view is supported by experiments conducted on copper and copper-aluminium alloys [150,151] and on nitrogen added austenitic stainless steels [152]. The enhanced LCF resistance of planar slip alloys is gained by a combination of delayed crack initiation and reduced rate of crack propagation due to a high amount of slip reversibility.

2.4.6.3.2 Dynamic strain aging

In certain strain-rate and temperature regimes of deformation, solute atoms in an alloy exert drag forces on the mobile dislocations limiting the dislocation velocity. When sufficient dislocations are affected, the applied strain rate will no longer be realized by the existing population of mobile dislocations. The stress will then rise until new dislocations are created or existing dislocations are rescued from solute atmospheres. In either case, very fast-moving dislocations free of solute atmospheres will be formed in the region where this process occurs first, giving rise to inhomogeneous plastic flow and a stress drop followed by the repetition of the same process elsewhere. This phenomenon is termed as Dynamic Strain Aging (DSA).

In general, the increase in test temperature and reducing strain rate/frequency of cycling lower fatigue life. Fatigue and fracture behavior under such conditions are owing to the interaction between the cyclic deformation and either one or more of the time-associated processes, for e.g., creep, DSA, oxidation, change in the slip mode and other microstructural instabilities. However, under such test conditions even when creep and oxidation effects are minimal, degradation in fatigue life is still observed. It is then shown that dynamic strain aging interacts with fatigue and leads to a reduction in fatigue life. Various manifestations of DSA during LCF include [153]**:**

i) Serrations in the stress-strain hysteresis loops

ii) High normalized cyclic hardening ($(\Delta\sigma/2)_{max}$ / $(\Delta\sigma/2)_1$), where $(\Delta\sigma/2)_1$ is the tensile stress amplitude of first cycle and $(\Delta\sigma/2)_{max}$ is the highest tensile stress amplitude in the cyclic stress response curve, and the high cyclic hardening ratio with slow strain rate.

iii) Higher number of cycles to achieve $(\Delta\sigma/2)_{max}$ with slower strain rate.

iv) Decrease in plastic strain range with increase in temperature and low strain rate, for an applied total strain range.

v) Negative strain rate and positive temperature dependences of stress response.

A comparison of the results of LCF with tensile deformation, made by KBS Rao et al.[154] showed that serrated flows exhibited for a wider range of temperature under LCF condition than monotonic tensile deformation. Especially, under LCF the serrations occurred at lower temperatures due to the improved diffusion of solute atoms assisted by non-equilibrium vacancies generated during strain cycling. The occurrence of dynamic strain aging has been observed in modified 9Cr-1Mo ferritic steel between 573-773 [31] and 773-873 K [23] under LCF condition. The increase in temperature decreases the half-life plastic strain amplitude. Such negative temperature sensitivity of plastic strain amplitude at half-life is one of the typical manifestations of DSA under LCF [155].

2.4.6.3.3 Environment/oxidation

The effects of the environment on fatigue properties are assessed from comparative evaluation of test results in air, vacuum or inert atmosphere. Coffin [156] reported that the temperature dependence of LCF resistance of the material, A286, in air atmosphere vanishes in vacuum and the enhanced fatigue life in vacuum was associated with the sluggish transgranular crack propagation compared to lower fatigue life due to intergranular fracture in air.

It is generally observed that ferritic steels, austenitic steels and nickel base superalloys exhibit superior LCF resistance in vacuum or an inert atmosphere than in air environment [22,137,157–160]**.** However, the oxygen-bearing environment is not always detrimental. Gell and Leverant [148,161,162] observed oxidation strengthening effect and higher fatigue life of Mar M-200 at 1200 K in air compared to vacuum. The beneficial effect of oxidation has been ascribed to the increasing crack tip radius and blunting during the compressive half cycle of stage II crack growth [148].

The deleterious effect of oxidation during LCF results in both the early crack initiation and rapid crack propagation in the air environment. The most plausible explanation for oxide influence in crack nucleation is the repeated film rupture model proposed by Coffin [163] that allows a continuous disruption of a surface brittle film with cyclic strain. Kschinka and Stubbins [157] have noticed the delayed crack initiation in 2¼Cr-1Mo steel under vacuum compared to air. Ebi and Mc Evily [19] observed a large number of completely oxidized surface cracks in air with a more or less smooth surface, while the tests in vacuum exhibited free of surface cracks and numerous rumpling in the surface in modified 9Cr-1Mo steel. They reported that the lower fatigue life of the steel in air compared to in vacuum is due to early crack initiation, which is promoted due to early rupture of surface oxides; a weak barrier to slip. The crack growth rate in air consists of a mechanical component, i.e., crack growth in a vacuum and an environmental component. The environmental component depends on the type of oxidation reaction at the crack tip. At elevated temperatures and high plastic strains, oxidation directly contributes to cyclic growth by strain-enhanced oxidation and subsequent metal loss [163–167] or by diffusion of oxygen ahead of the crack-tip [163]. Haigh et al. [164] has expounded the theory of continuous cracking of oxide films at a crack tip. They assumed that each cycle of oxidation is parabolic, which is interrupted prematurely by oxide cracking. The fresh surface is exposed to further oxidation and cracking, resulting in a high oxidation rate. Haigh et al. [164] also proposed that the environmental contribution to fatigue crack growth is entirely due to the metal being removed by the oxidation reaction. Further, it has been envisaged that the low frequency will promote higher oxidation, more metal removal and higher crack growth rate [165–168]**.** The higher crack growth rate in air compared to vacuum in plain 9Cr-1Mo steel has been reported recently by Cotterill and Knott [166]. The temperature dependence of crack growth rate in air was not observed in vacuum. An analogy between fatigue crack tip oxidation and erosion-corrosion damage was made.

2.4.6.4 LCF behavior of ferritic alloys

Attempts have been made in the past to characterize the LCF behavior of modified 9Cr-1Mo steel [23,28,29,31]. Ebi and McEvily [19] have reported that the fine-grained hot-rolled alloy showed better fatigue performance than hot-forged larger grain size material at 811 K. The authors [19] also reported that the presence of relatively coarser grain size, which aids the early fatigue crack initiation and lowering the fatigue life of hot forged steel as compared to finer-grained hot rolled material. Nagesha et al. [23] and Mariappan et al. [31] have reported that the P91 steel exhibits significant decrease of fatigue life in the temperatures of DSA regime.

Vani Shankar et al. [28] and Glugoth et al. [29] explicitly studied the effect of temperature, strain amplitudes and various atmospheres on the LCF behavior of modified 9Cr-1Mo steel. In the previous study of the authors [169], it has been reported that the modified 9Cr-1Mo steel exhibits continuous cyclic softening, in general, followed by a rapid fall in the stress value at the end of the cyclic stress response curve due to the accelerated growth of macro-cracks (Fig. 2.17).

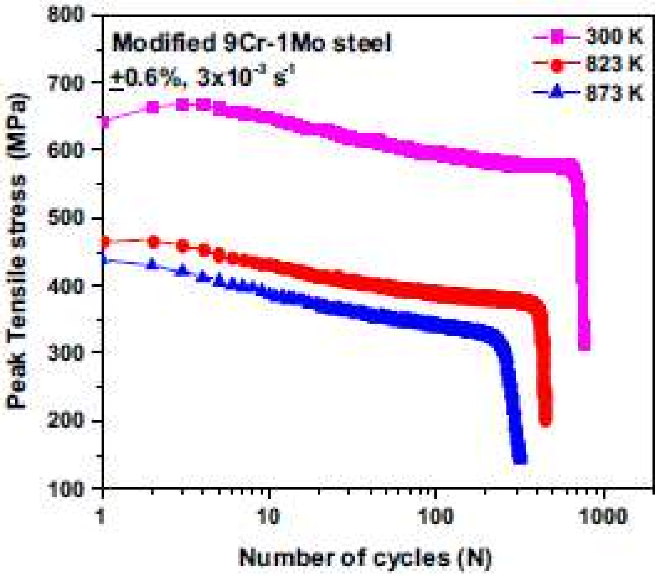

Fig. 2.17 Cyclic stress response curves of modified 9Cr-1Mo steel [169].

From TEM analysis (Fig. 2.18) on the microstructure of fatigue tested P91 steel, it is observed that the transformation of initial lath structure into cell structure with lower energy configuration occurs during fatigue deformation at high temperature [28]. Such microstructural recovery in the form of annihilation and rearrangement of dislocations causes the progressive cyclic softening as observed in modified 9Cr-1Mo steel (Fig. 2.17).

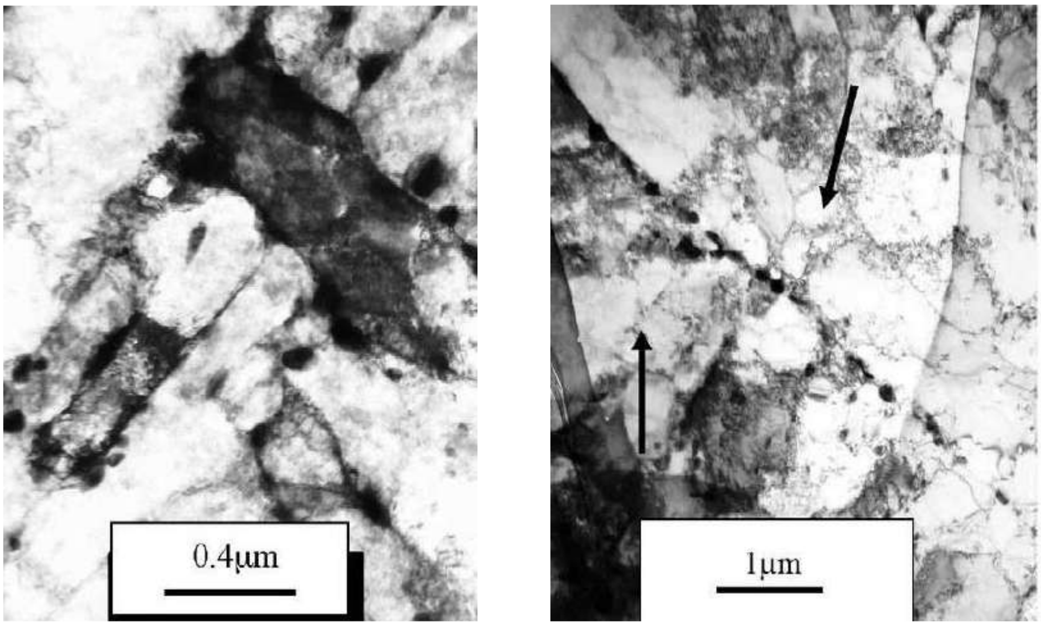

(a) (b)

Fig. 2.18 Normalized and tempered alloy showing elongated laths within the grains decorated with carbides and substructure ((a) and (b)) formation during fatigue cycling [28].

2.5 CREEP

Creep is defined as the time-dependent deformation that takes place on applying of steady load at elevated temperature. A typical shape of a creep curve is visualized in Fig. 2.19. As illustrated in Fig.2.19, one can observe an instantaneous strain, ε_o at the beginning of the curve, due to the application of load. Even though the initial sudden strain is not due to creep, it may account for a substantial fraction of the total allowable strain in components. Mostly, the creep strain is reported after subtracting the instantaneous strain from the total strain giving full credit to creep alone. In general, the creep curve is explained about its three principal stages. The primary creep designated as stage-I that means a state of reduction in creep rate. Primary creep is known as the transient creep in which the creep resistance of the material increases because of its own deformation (work hardening). The secondary creep, i.e., stage-II creep; in this region, the strain/work hardening and recovery processes are balancing each other and gives rise to a nearly constant creep. Hence, the secondary creep is also known as a steady-state creep. For the design purpose, the secondary creep rate is averaged out and used as a minimum creep rate. The stage-III creep or tertiary creep, the final region of the curve indicates an increase in the rate of creep cause eventually to specimen failure. The onset of tertiary creep occurs when the recovery process overcomes the hardening or due to intergranular cracks formation, which decreases the effective cross-sectional area causing necking. The rate of tertiary creep also often related to the following metallurgical changes; recrystallization, precipitates coarsening or diffusional changes in the phases that are present [133].

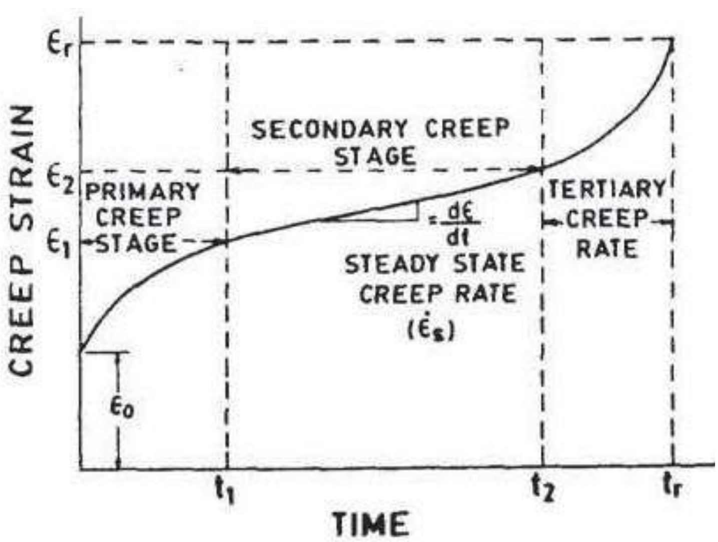

Fig. 2.19 Schematic of typical creep curve showing three stages of creep [135].

Generally, fracture mode due to creep is found as intergranular. The fracture includes nucleation of cavities at grain boundaries (intergranular), their growth and coalescence to form minor cracks followed by propagation of macro cracks and leads to final failure for an extensive loading duration (Fig. 2.20). The evolution of grain boundary (intergranular) creep damage occurs irrespective of the micro volumes of cavities. Independent of the mechanisms that are operating in connection with the nucleation of cavities and particularly growth, finally the linking of cavities starts to occur. The heterogeneity in the partial distribution of isolated cavities causes heterogeneity of further advanced form of creep damage, like above mentioned interlinked cavities and subsequent formation of intergranular micro-cracks.

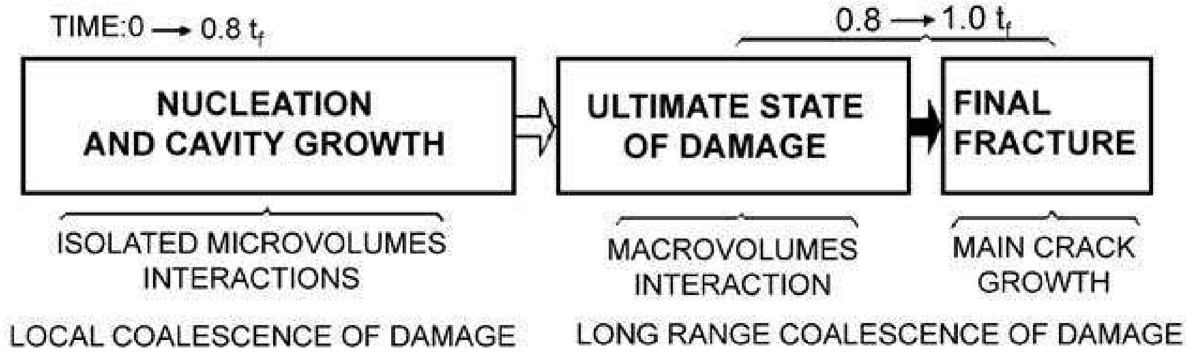

Fig. 2.20 Schematic of intergranular damage development [117].

In the nearest vicinity of specimen free surface, grain boundary creep damage appears first and the density of the boundaries damage fixes the onset of the location of the final stage of fracture. The long-range linking of damage causes extensive crack formation in the final stage. At this stage, the cracks from inside the creeping body merge with the surface cracks. This leads to final fracture due to the rapid linking of one of the potentially long surface cracks and forms a through crack, i.e., the fracture crack [117].

2.5.1 Creep behavior of ferritic alloys

In P91 steel, the microstructural evolution that contributes to an increase in creep rate at 873 K can be characterized by the following sequence of events: (i) dislocation density decreases as there are rearrangement and annihilation of excess transformation dislocations; (ii) finer equiaxed sub-grains develop from the former tempered martensitic microstructure; (iii) dissolution of the finely dispersed carbonitride precipitates (NbC, VC); (iv) redistribution of $M_{23}C_6$ carbides from stringers to a homogeneous distribution in ferrite and (v) coarsening of the $M_{23}C_6$ carbides and Nb and V carbonitrides and their interparticle spacing increases as well [117].

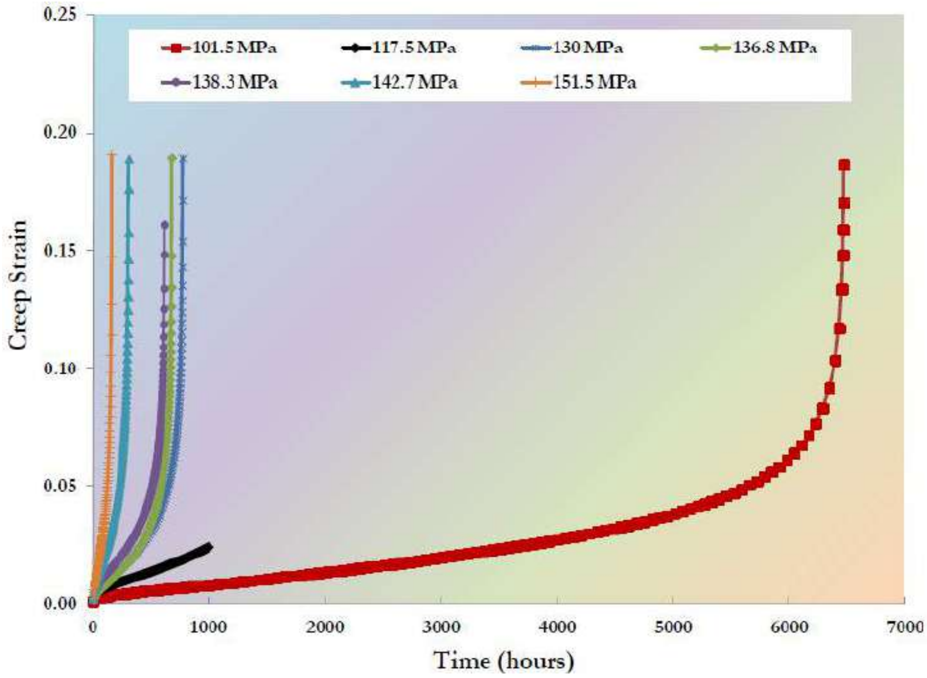

Fig. 2.21 Creep deformation and rupture results at different stress levels for P91 steel at 898 K [44].

The creep rupture ductility for P91 steel is high with the final longitudinal elongation changing between 16-19%. In general, the cumulative creep strain produced in the regimes of primary and secondary is lower compared to that in the third stage creep regime, i.e., tertiary creep, as depicted in Fig. 2.21. For any given test, because of localized necking at ~ 95% of the creep rupture time (t*), macro-cracking seems to have triggered superplastic behavior, delaying the event of rupture and contributing further to a rupture elongation. The superplastic behavior has also been observed in a similar study earlier for the ferritic/martensitic steels at elevated temperatures [117,170]. The metallographic investigation of ruptured specimens reveals the array of microvoids nucleate along certain crystallographic orientations towards the final rupture location, which indicates that the transgranular ductile fracture is the predominant failure mode during creep rupture (Fig. 2.22(a)). Notably, these arrays are mostly observed close to the inclusions in the material (precipitates and/or secondary phases, etc., see Fig. 2.22(b)).

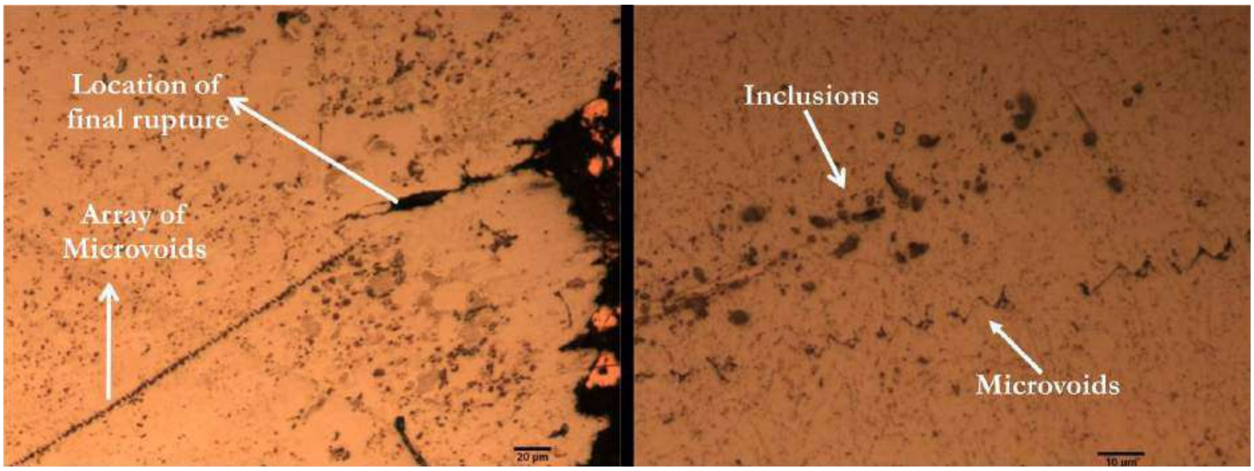

(a) (b)

Fig. 2.22 Transgranular ductile fracture as observed in creep ruptured P91 steel specimen (a) before and (b) after etching with Nital solution (test condition: 151.5 MPa, 898 K) [44].

2.6 FUNDAMENTALS OF CREEP-FATIGUE INTERACTION

Sharp thermal gradients are developed between the surface to the core of thick structural components operating at higher temperatures due to heating and cooling transients during start-ups and shut-downs. The repeated heating and cooling induce thermal stresses in the component provided thermal strain produced due to expansion/contraction is totally/partially restricted. Such thermal transients repetition leads to strain-controlled LCF damage in the components [171]. Besides, steady-state operation at elevated temperatures introduces creep, i.e., a major part of the application requires that a component undergoes constant loading for a period between the shut-downs of a power plant. The period for which the load is kept near-steady condition is known as dwell time. The dwell time sees some creep in the component if the combination of temperature and stress is maintained. Hence, the complex interactions between fatigue and creep processes introduce some multifaceted failure mechanisms within a high strain fatigue regime. The simulation of operating conditions of power equipment ranges from (a) strain control, simulating thermally induced stresses, to (b) load controlled, simulating constant centrifugal stresses. In the former, thermally induced stress decays with time owing to stress relaxation, whereas in the latter, constant centrifugal stress causes a steady-state loading [172].

Three types of damage modes such as competitive, additive and true interaction are established from the metallographic examples of power plant operation and laboratory testing under creep and fatigue interaction conditions. These damage modes are associated with the practical applications of the base load operation, fast start-up and shut-down procedures, slow start-up and shut-down procedures, etc. The damage due to creep-fatigue interaction is one of the most acute modes of structural failure in the design for elevated temperature. The terminology "creep-fatigue interaction" means to the condition in which the damage accumulation rate under combined loading varies from a linear combination of the damage rate generated by each loading component of creep and fatigue separately. Creep-fatigue interactions are majorly classified as "sequential" and "simultaneous" following the applied damage. In sequential interactions, the damage modes from the fatigue and creep are independent and one damage component follows other, but during simultaneous interactions both creep and fatigue damage modes exist in each stress/strain cycle [155]. Simultaneous interactions have been largely studied introducing hold periods at either tensile or compressive peak strain or both. During hold, stress relaxation occurs due to the conversion of elastic strain into plastic strain. The net effect is to methodically add a creep element in the cyclic loading under strain-controlled conditions. Creep-fatigue interactions are also investigated using slow–fast and fast–slow tests. In general, it has been well documented that the application of hold adversely affects the fatigue resistance at high temperature [173]**.**

During the initial stage of cyclic loading rapid stress relaxation occurs and in the later part, the relaxation rate continuously decreases [174]. In austenitic alloys, it has been reported that below a certain critical relaxation rate, grain boundary sliding is the basic mode of deformation and interacts with intra-granular damage that leads to sudden failure (Fig. 2.23) [175]. The failure mode may also change due to only grain boundary damage with the increase in creep component of the cycle through increasing the hold period or by reducing the strain rate [176]. The transition to intergranular failure can be explained by the interaction of the fatigue crack with grain boundary cavities. Further support for the above mechanism in the austenitic steels comes from the experimental study of the tensile hold being more detrimental compared to that of compressive hold [177,178] or hold times in both tension and compression [179]. Grain boundary cavities do not form under the compressive hold alone; as a result, the forgoing discussed mechanism does not apply. Under the synergistic hold, i.e., both tensile and compressive, the cavities that are formed due to tensile hold are sintered in the compressive hold, thus leading to a cancellation effect.

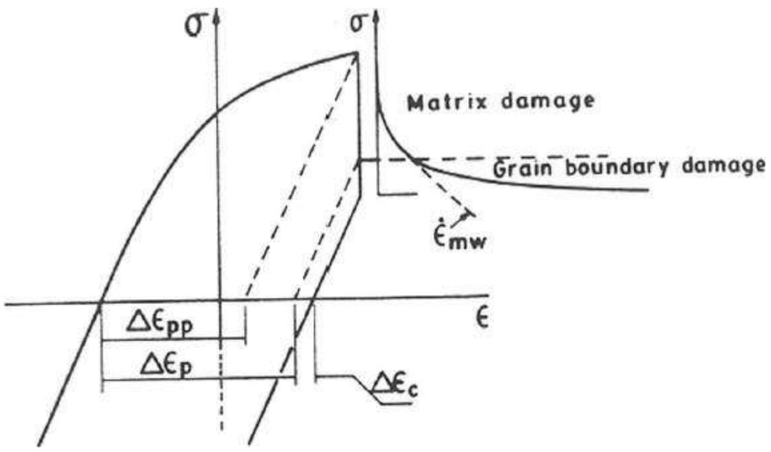

Fig. 2.23 Partitioning of typical cyclic hold hysteresis loop [175]**.**

The modes of failure are distinguished into the three different regimes (Fig. 2.24) and they are as follows:

(a) Fatigue dominated,

(b) Fatigue-creep interaction and

(c) Creep dominated.

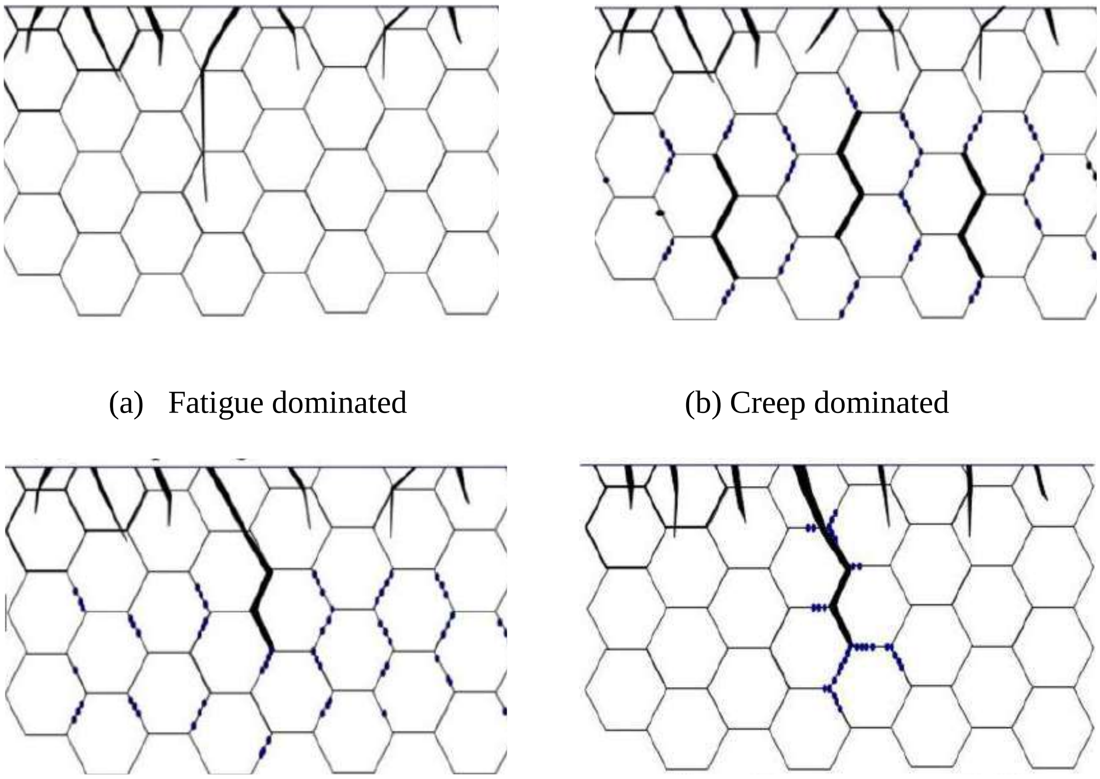

(a) Fatigue dominated (b) Creep dominated

(c) Fatigue-creep dominated (simultaneous) (d) Fatigue-creep dominated (sequential)

Fig. 2.24 Schematic diagrams of failure modes during (a) continuous cycling, (b) creep and (c) simultaneous and (d) sequential creep-fatigue interactions conditions [180].

Fatigue dominated failures occur only because of the growth of surface cracks through specimen without the cracks propagations through grain boundaries (Fig. 2.24(a)). However, under creep-fatigue interaction conditions, the synergistic damage is observed in the specimen with the formation of creep cavities plus surface fatigue damage. For longer hold times in simultaneous creep-fatigue interaction or material subject to the lesser fatigue damage sequentially crept to failure will have a crack path like as shown in Fig. 2.24(b). The damages from the fatigue and creep start separately and the possibility of real interaction depends upon the balance of them. Though, finally, the surface cracks due to fatigue interact with bulk damage due to creep, leading to the accelerated growth of crack causing the reduction in fatigue resistance under creep-fatigue interaction condition, Fig. 2.24(c). Due to such interaction, the failure occurred found a path of mixed (trans-granular plus inter-granular) mode. However, due to some test conditions, dominance from the creep component of the cycle is found, which causes intergranular failure because of the agglomeration of grain boundaries cavities as illustrated in Fig. 2.24(d), under such situations no interaction with the presence of fatigue damage. With the application of high stress for the sequential creep-fatigue deformation the prior cyclic deformation has an important adverse effect on rupture strength but is less influential on creep ductility due to particle/matrix decohesion. However grain boundary cavitation, which is predominant failure mechanism in the creep is observed in the test condition used lower stresses. Hence in the low stress creep-fatigue interaction damage, the influence of prior cyclic deformation on rupture strength is insignificant.

2.6.1 Types of waveforms

The waveform shapes and uses in studies are given in Table 2.2. Creep-fatigue interaction tests are conducted at a given strain amplitude and strain rate and temperature employing waveforms as shown in Fig. 2.25. Simultaneous creep-fatigue interaction tests are performed at a strain amplitude, strain rate and temperature of interest. Hold period of a given duration is introduced at peak tensile strain alone or compressive strain alone or tensile and compressive strains in a triangular waveform that is used for the LCF test. This phenomenon can also be simulated by employing a slow-fast waveform, equivalent to a tensile hold. A fast-slow waveform simulates a compression hold.

Table 2.2 Typical waveforms used in creep-fatigue interaction tests

	Waveforms	Remarks
1.	Hold period (tensile/compressive) at constant peak strain in trapezoidal waveforms.	Simulates the on-load service period of components in between start-ups and shut-downs, i.e., creep-fatigue interaction.
2.	Slow-fast and fast-slow strain rates in nonsymmetrical triangular waveforms.	Tensile strain rate is less than in the compressive part of the cycle in slow-fast waveform and converse is true for fast-slow waveform, i.e., creep-fatigue interaction.

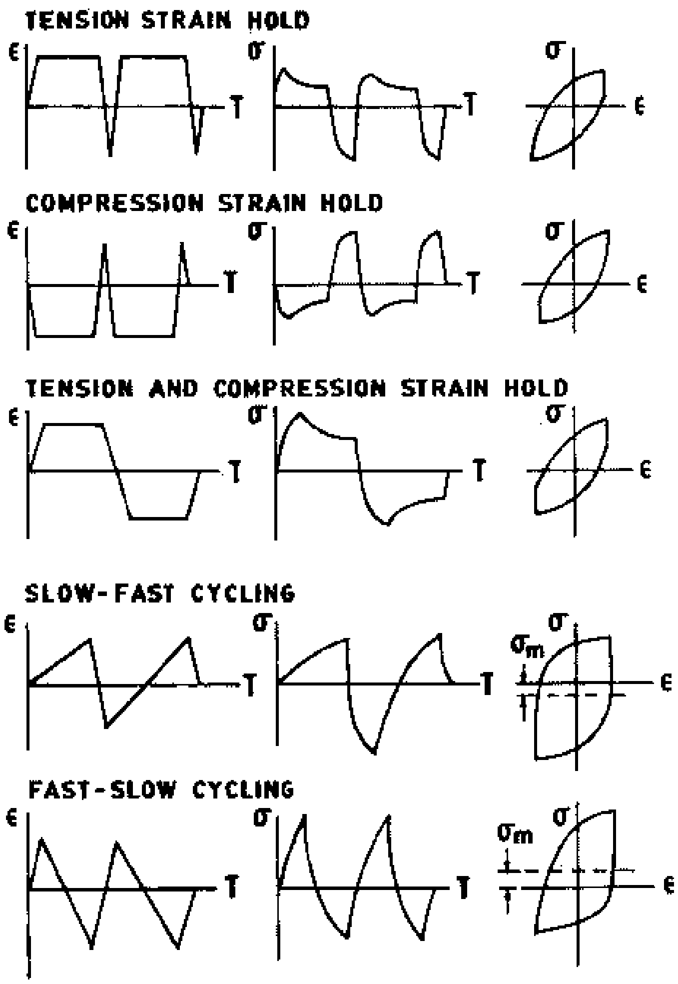

Fig. 2.25 Typical waveforms of concurrent types of creep-fatigue interaction [181].

2.6.2 Environmental effect on creep-fatigue interaction

Environmental effects can play an important role under certain testing conditions, and thus creep-fatigue interaction may be an incomplete descriptive term in these atmospheres. Some evidence from experiments supporting the imperative environment on fatigue behavior of austenitic alloys is summarized here. The results of the experiments related to the effect of the environment on the growth rate of fatigue cracks. For many austenitic steels [137,182,183], it was depicted that the crack growth rates under air atmosphere are faster than under vacuum or other inert atmosphere at elevated temperature. The sensitivity of the crack growth rate to the environment has been offered as evidence on the environment in temperature and frequency effects in LCF testing [182]**.** This explanation is applicable only if the elevated temperature fatigue lives are crack propagation controlled. It has also been reported that fatigue lives of stainless steel, aluminium alloy, and nickel base super alloy at the elevated temperature are similar at the same applied plastic strain range in vacuum [156]. Also, generally at elevated temperature, the failure modes of transgranular and intergranular have been observed in vacuum and air respectively. The intergranular failure material exhibited reduced fatigue life [156]. Further, under sequential creep-fatigue loading condition, the prior creep exposed (no detectable creep deformation) Rene 80 specimens exhibited a pronounced decrease in fatigue life [184]. However, after removal of a thin surface layer of the same material of creep exposed at an elevated temperature a significant improvement in fatigue life was found and was equal as of the heat-treated material [184]. Unlike the polycrystalline material the single-crystal Mar-M200 has depicted strengthening effect in the air atmospheric condition compared to the vacuum for fatigue life at elevated temperature [185]. It seems that there are two competing processes corresponding to the effect of oxidation. The increasing of crack tip radius and subsequent blunting of the crack during the compressive part of the cycle are the potential beneficial effect of oxidation

[162,185,186]. On the other hand, oxide formation at a crack tip will lead to a change in the composition of the matrix in the crack tip vicinity, which causes an accelerated crack growth rate [148,187,188]. Also, the presence of oxygen may act to embrittle grain boundaries [184].

2.6.3 Creep-fatigue interaction behavior of ferritic alloys

Several investigations so far discussed on creep-fatigue-environment interaction are associated with the austenitic. However, oxidation - one of the deleterious environmental effects can greatly influence the surface of ferritic steels at elevated temperature to cause oxidation assisted fatigue failure. Therefore, the importance of the environmental effect on the ferritic steel behavior under CFI conditions with the pieces of evidence of some experiments will be summarized here. As discussed earlier, the use of a detrimental environment assists to explain the effect of compressive hold that leads to more damaging in low chromium (2¼Cr-1Mo) ferritic steel [178,189,190]. Oxides form during the majority of the time in a cycle, i.e., in the hold period. During the subsequent tensile loading, a tensile strain equal to the total strain range is applied on the oxide scale [178,189–191]. This tensile strain in the oxide scale leads to the formation of circumferential cracks, which in turn be a potential site for the localized stress and strain concentrators and facilitate the earlier nucleation of fatigue cracks.

In the case of tensile hold creep-fatigue loading, the oxide scale in 2.25Cr-1Mo steel is observed to spall off [178,189,190]**.** The detrimental cracking found in the case of compressive hold is prevented due to the continuous spall-off of oxide during the tensile hold. Therefore, the above discussion holds an explanation for the reason why a compressive hold shows a severely damaging effect compared to a tensile hold [178,189,190]. The higher compressive dwell sensitivity was also observed in modified 9Cr-1Mo steel by Aoto et al. [192]. They also reported that in the case of a compressive hold the formation of oxide takes place during hold at the maximum compressive strain, where the tensile strain is zero. During the reversal of load after strain hold, the oxide layer at the crack tip experiences a considerable amount of deformation, which is almost equal to the total strain range. The inadequate thickness of the oxide layer is unable to resist the slip deformation at the crack tip due to the shortage of oxygen in the crack surface due to crack closure. Thus, in the compressive hold fatigue process, the slip deformation at the crack tip occurs easily and leads to the continuous crack growth. On the contrary, in the case of tensile hold, formation of thick oxide layer due to sufficient amount of oxygen in the crack surface assists to prevent slip deformation at the crack tip. Also, oxides formed in the tensile hold fill the crack and resists crack propagation. In modified 9Cr-1Mo, Vani Shankar et al. [193] and Kim and Weertman [158] have noticed that the environment played an important role in the dwell sensitivity of this steel. The steel exhibited compressive and tensile dwell sensitivities in air and vacuum respectively. In modified 9Cr-1Mo steel, the absent of tensile sensitivity is due to crack tip blunting due to the formation of thick oxide coating in the crack surface during a tensile hold in air, however, the crack tip remains sharp as they are closed during the compressive hold [194]. The phenomena such as creep and environmental degradation occur during hold time. On long holds, creep produces a detrimental effect on the fatigue life, whereas under short holds influence of creep become insignificant rather mostly the oxidation which generates a greater number of surface cracks decreases the fatigue life. After the hold, the cyclic straining during unloading in the tensile direction breaks the oxides and aids the oxygen to diffuse ahead of the crack tip promoting faster damage in the material. Therefore, the compressive dwell sensitivity is largely observed in this ferritic/martensitic steel.

The effect of application and duration of hold on the cyclic stress response of modified 9Cr-1Mo steel at the tensile and compressive strain peaks is shown in Fig. 2.26. As discussed earlier, as shown in Fig. 2.26, the substructural and precipitate coarsening and other typical metallurgical changes in the steel lead to continuous softening during the cyclic loading with or without hold. A secondary peak in the stress response of the material under continuous cycling is not observed under fatigue cycling with hold. Precipitation of fine VC particles at a temperature near to 873 K causes the pronounced secondary hardening in the later part of continuous cyclic loading. Further, the overall stress responses of the steel under strain-hold fatigue are lower than under without-hold cycling and an increase in the time of hold decreases the stress responses.

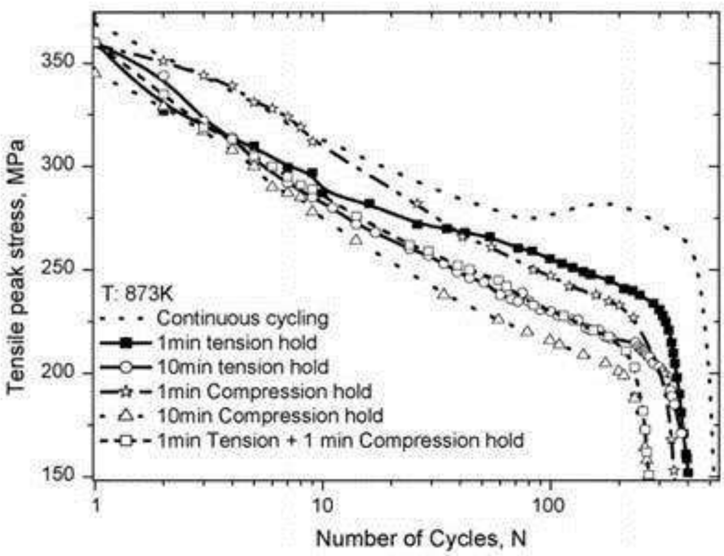

Fig. 2.26 Influence of application of hold on the cyclic stress response of modified 9Cr-1Mo steel [28].

Vani Shankar et al. [24] reported that the increase in hold time decreases fatigue life. The introduction of strain hold emphasized the cells/sub-grains formation. Creep-fatigue interaction experiments also enhance the carbides coarsening and change their morphologies resulting from a decrease in cyclic stress response. An increase in conversion of elastic strain into inelastic strain due to creep and oxidation during hold synergistically enhances the crack propagation. The Fig. 2.27(a)-(d) of the steel LCF tested with 10-minute strain hold show detailed observations made on the substructural evolution. The rearrangement and the position of the lath structure are indicated by the aligned carbides as shown in Fig. 2.27(a). These precipitates ($M_{23}C_6$) are comparatively coarser and found to be segregated carbides. The carbide particles are agglomerated with adjacent fine carbides and are substantially coarsened and become spherical or elliptical in shape (Fig. 2.27(c) and (d)). These substructural level changes have been associated with the occurrence of enunciated cyclic softening.

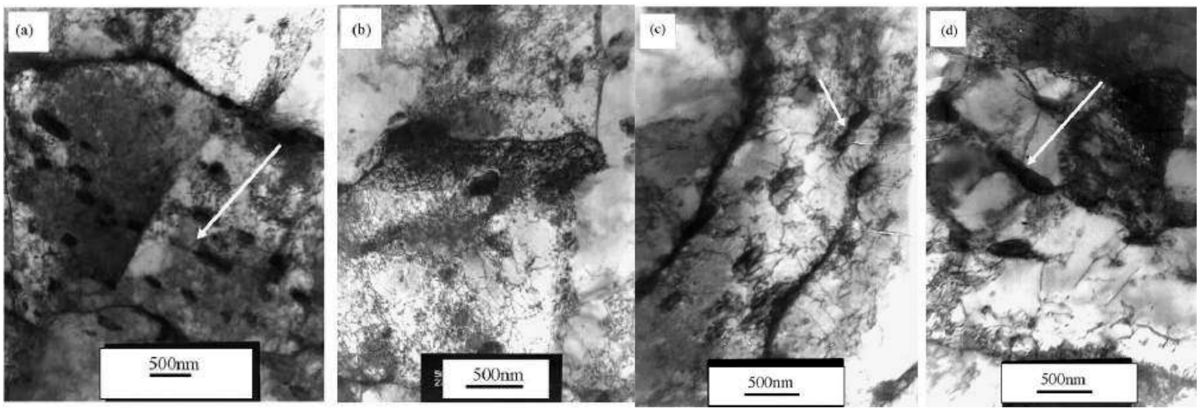

Fig. 2.27 Transmission electron micrographs of P91 steel tested under 10-minute tensile hold; (a) carbides along initial lath boundaries (white arrows), (b) fine precipitates (V(C,N)) pinning dislocations, (c and d) carbides coagulation and coarsening [24].

2.7 WELD JOINT OF FERRITIC STEELS

Fusion welding is necessary for the fabrication of large size steam headers and pipes components in steam generators of power plants. Steam headers i.e., joints at which several steam carrying pipes with large diameter converge, are considered as one of the most critical components as they are exposed to large fluctuations in temperature and pressure. Such highly expensive components are difficult to replace [195]. Butt and end cap welds as well as branch and stub welds are used for joining the thick section pipes of the steam generator. The welds frequently represent a weak link in a component, both microstructurally and mechanically, and they could form one of the potential sources of failure [196].

As was mentioned earlier, during welding significant changes in the microstructure of the steel, especially near the weld deposit takes place because of the temperature gradient across the weld. As a result, the steel weld joint ends up with three different zones, i.e., the weld metal, heat-affected zone and the unaffected base metal. The heat-affected zone typically comprises three principal and different microstructures: the coarse grain heat-affected zone (CGHAZ), the fine grain heat-affected zone (FGHAZ), and inter-critical heat-affected zone (ICHAZ). The hardness of the weld joints in the as-welded condition is high due to martensite formation during cooling after welding. Post weld heat treatment (PWHT) is essential for tempering the martensite formed during welding. The heat-affected zone(s) consists of complex microstructures closest to the weld metal zone has different mechanical properties compared to the base metal and weld metal. Even at a low-stress level, the material fails and the failure is termed as Type IV failure. This implicates that the soft zone and fine grain zone offer less creep resistance than the base metal [197,198]. Even though the reduction in creep strength of 9Cr-1Mo steel weld joints has been reported, many aspects including the exact failure location and the cause for creep strength reduction are not understood completely. In the recent experimental studies, the failure of the weld joint due to creep is generally characterized in the HAZ and such failure is termed as Type IV cracking. Further in the very recent past, detailed studies [71,199–202] have been carried out on creep performance of ferritic/martensitic steels at elevated temperatures. However, elaborate studies associated with the low cycle fatigue and creep-fatigue interaction behavior of microstructurally complex weld joint of P91 steel are still warranted. Particularly understanding the deformation gradient within the heat-affected zone under low cycle fatigue and creep-fatigue interaction conditions will give a better insight into the deformation mechanism of full weld joint under those conditions. Therefore, a brief review of the literature about the welding of ferritic/martensitic steels and microstructural changes due to that and previous studies on the mechanical properties, fatigue and creep-fatigue interaction behavior of P91 weld joint is discussed in this section.

2.7.1 General information on welding

The complex process involved in welding and subsequent heat treatment of this alloy could be attributable to several factors. The existence of large alloy content increases the hardenability of the material. The high hardenability character attributes to the formation of martensite in the weld and heat-affected zone even during a slow rate of cooling. However, the hardness of martensite is comparatively limited due to low carbon content. Therefore, the low carbon content in the modified 9Cr-1Mo steel contributes better weldability than the plain 9Cr-1Mo steel, which normally consists of high hardness due to high carbon content [203]. The choice of suitable welding technique for P91 steel depends on the position of welding, the thickness of the plate, composition of filler metal, flux and shielding gas and temperature and duration for PWHT. Some of the methods of welding that are widely used are as follows:

1) Gas tungsten arc welding (GTAW)

2) Submerged metal arc welding (SMAW)

3) Manual metal arc welding (MMAW)

4) Flux cored arc welding (FCAW)

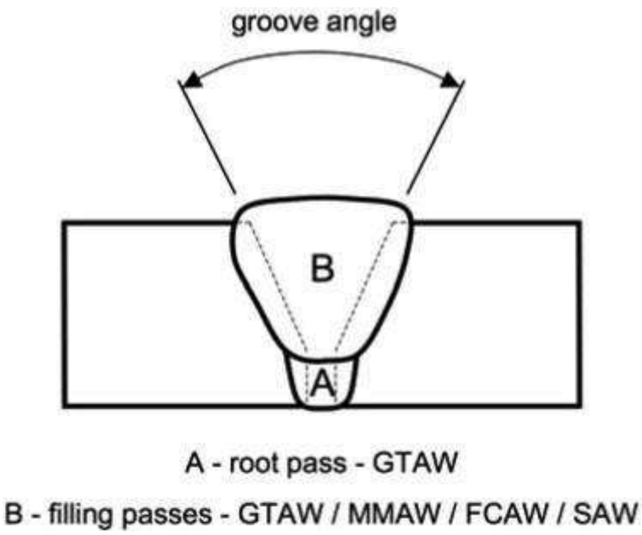

Fig. 2.28 Schematic representation of welded joint in 9–12% Cr ferritic steel [204]**.**

The weld metal hardness is higher for the GTAW process than the weld metal hardness obtained by SMAW as the HAZ hardness is lower for the GTAW welding process. A schematic diagram in Fig. 2.28 depicts a cross-section through of 9–12 Cr ferritic steel weld joint. The root pass is often completed using the gas tungsten arc welding technique. The root pass by which the welding commences needs stringent welding control because it undergoes compression strain during successive welding passes. High-quality weld deposits are obtained by employ of the GTAW process. But manual metal arc welding is frequently used in intricate joints, flux-cored arc welding and submerged arc welding are employed for high thick welds [205].

Equal creep strength of filler metals and parent materials is an important factor for welding the 9–12 Cr steels. Ideally, the toughness of them also matching at ambient temperatures, as the weld joint experiences transient stresses during shut down periods [206]. Though, it is apparent from the earlier reports that it would not be feasible for weld metals to meet both requirements at the same time [204,207]. While selecting the commercial filler metals and parent material with the match of creep strength, in order to enhance the toughness there is a propensity to contain higher amounts of manganese (0.6–0.7 wt.%) and nickel (0.4–0.6 wt.%) [208]. Higher toughness is achieved possibly due to reduced oxygen contents in the weld metal with the employ of the GTAW process compared to the uses of MMAW and FCAW processes [208]. In the context of Type IV phenomena, the information on the influences of heat input and preheat temperature on the weld creep performance is very much limited. Fixing of appropriate preheat temperature would assist to avoid cracking during cooling after welding [204,207]. Deposition of multiple beads and reducing the groove angle, which decreases the width of the HAZ are conducive to improve/enhance the toughness and creep strength of the weld joint respectively [209,210].

2.7.2 Microstructure evolution during fusion welding and post weld heat treatment

Grade 91 steel is typically welded with matching filler metal. Depending on the distance from the fusion boundary and the line separating weld metal from the parent or base material, the peak temperature of the weld thermal cycle will change creating a thermal gradient across the joint. The thermal gradient will cause corresponding microstructural gradients in the heat-affected zone. The differing microstructural regions of a fusion weld can be correlated to the iron-iron carbide (Fe-Fe_3C) phase diagram as depicted in Fig. 2.29. The fusion zone will contain fresh martensite after welding with large solidification grain boundaries. The as-welded fusion zone microstructure is depicted in Fig. 2.29. The heat-affected zone has further divided into three distinct microstructures, i.e., coarse grain, fine grain and inter-critical microstructures and they are briefly explained below [211,212].

Coarse grain zone (CGHAZ): The region closest to the fusion line exposed to the temperature well above AC_3 during welding of 9–12 Cr steels. The complete dissolution of carbides at this temperature leads to reduction in the impedance of grain growth. On cooling, the austenite formed at this temperature transforms to martensite.

Fine grain zone (FGHAZ): This zone is generated at the temperature range of lower than that of CGHAZ, but still above AC_3. The carbides that are only partially dissolved restrict the austenite grain growth in the 9–12 Cr steels. The austenite in the fine grain zone is transformed into martensite on cooling.

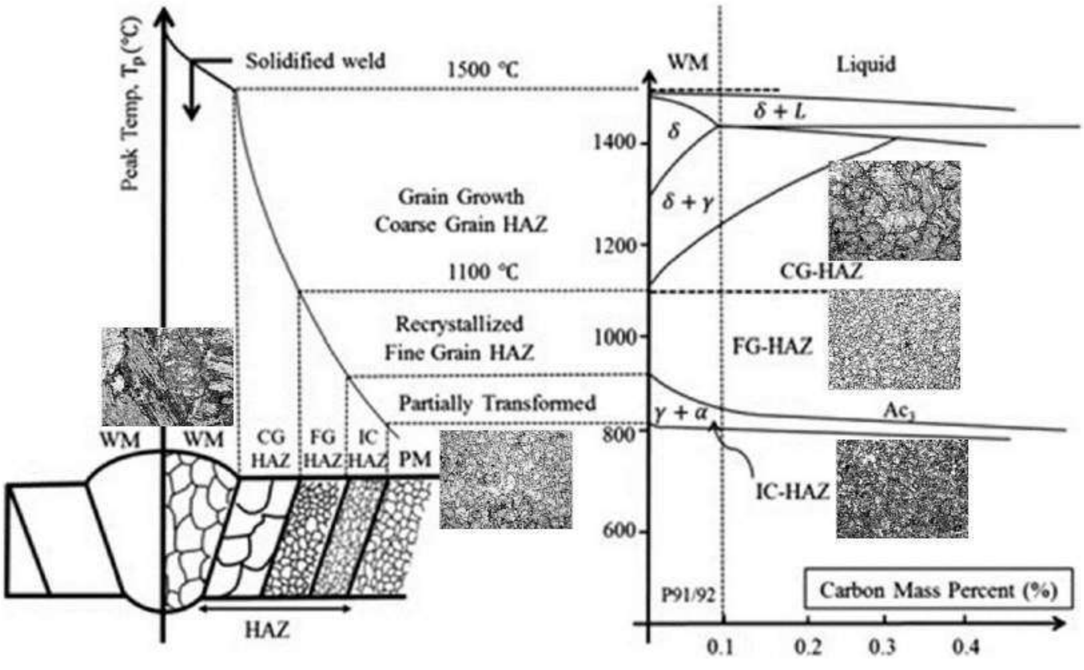

Fig. 2.29 The schematic of microstructures of P91 steel weld joint and corresponding phase fields (Fe-C binary phase diagram). The dashed line shows the carbon content of P91 steel [213]. The optical micrographs of present study material's microstructures are superimposed at the corresponding temperatures.

Inter-critical zone (ICHAZ): The zone well away from the fusion zone exposed to the peak temperature, $AC_1 < T_P > AC_3$, undergoes a partial transformation of austenite on heating. Nucleation of austenite occurs at the boundaries of prior austenite grain and martensite lath, whereas the untransformed microstructure remains as tempered martensite. The austenite (in 9–12 Cr steels) transforms into fresh martensite during cooling.

Post weld heat treatment (PWHT) is recommended on the welded grade 91 steel to temper the martensite formed on cooling subsequent to the welding and homogenize the microstructure gradient found across the HAZ. In the HAZ, the $M_{23}C_6$ carbides in the inter-critical region (ICHAZ) could coarsen since the precipitates did not completely dissolve in the welding process. The over-tempering of the ICHAZ could have attributed to the softening effect that observed as a dip in the hardness profile of the weld joint.

2.7.3 Hardness

Hardness is frequently used as a first-hand quality evaluation of base material, before and while in service. It provides the microstructural information about the presence of phases that gives the resistance to plastic deformation upon indentation. Such localized assessment to represent the bulk, further, linking the hardness values of various zones including HAZ to evaluate the overall performance of complex weld joint is not effective [214]. Hardness measurements made on polished samples will reveal changes quite well. The variation of hardness values from the base metal to base metal passed through sets of HAZ and middle fusion zone is depicted in Fig. 2.30. Higher hardness is observed in the fusion zone while a dip in the hardness values was observed in the HAZ region, particularly the lowest hardness region is ICHAZ, as shown in Fig. 2.30.

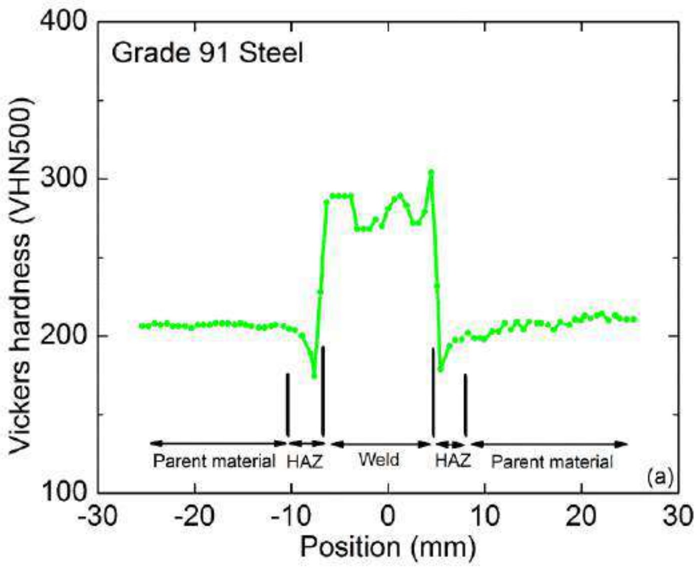

Fig. 2.30 Hardness profile of Grade 91 steel specimen; '0' being the center of the weld [215].

The presence of over-tempered martensite accompanying the α-ferrite phase and the microstructure comprises free of dislocation and precipitates could be the reason for lowering of hardness at the HAZ. It has been reported that a higher degree of plastic deformation takes place in the ferrite and austenite phases compared to the martensite phase [216]. During welding, the carbon migration generating soft areas in the HAZ and these areas are likely to be the potential sites for Type IV cracking. The lowest hardness of the HAZ is accredited to the decrease in dislocation density, precipitates coarsening, development of polygonized structure, rearrangement of lath martensite and precipitation that causes the decrease of solid solution strengthening [217,218].

The HAZ is considered the most creep-prone zone and is susceptible to Type IV cracking. It has been widely reported that Type IV cracking is the point of initiation of cracks in the HAZ. During creep, materials undergo recovery, recrystallization and grain growth resulting in the dynamic microstructure. The rate of transformation and localized concentration of δ-ferrite, austenite, α-ferrite, martensite and precipitates create ICHAZ, FGHAZ and CGHAZ. Inter-critical zone is of greater concern as it is the initiation point for Type IV cracking [65].

2.7.4 Type IV failure location

The classification of service cracking in weld joints devised by Schuller et al. [219] and Brear et al. [220] explains the cracking location associate with the weld and is depicted in Fig. 2.31. Types I–III cracks are developed, though occasionally due to long term creep-related, many times due to unsoundness in the joint fabrication or nonuniform solidification, presence of hydrogen, inappropriate reheat, temper embrittlement. The formation of Type IV cracking occurs at the edge of HAZ, adjacent to the base metal and is absolutely a cracking mechanism of creep that takes place during prolong loading. The identification of different subzones that generally exist in the HAZ microstructure would be useful to describe the location of Type IV cracks more accurately.

Most of the studies have documented that the Type IV cracking occurs at the edge of the HAZ just before the unaffected base metal. But some alternative reports have also stated that the accurate location of cracking varying between ICHAZ and FGHAZ. Hence, the location of Type IV cracking cannot be fixed at a definite HAZ microstructural region. The failure of a cross-weld sample has been observed either in the weld metal or HAZ or base metal depends upon the loading conditions. The creep strength of the weld metal of 9–12 Cr steels is comparable with the base metal, hence the failures occur either in the base metal or HAZ [204,207]**.** The tendency of Type IV failure associated with the applied stress is reported by Abe et al. [221]. The authors have compared weld metal, base metal and simulated FGHAZ against cross-weld rupture data for joints in P122 steel. Welds were made with electron beam welding, as well as with the gas tungsten arc process, using two different joint preparations. They have found the failure of the weld joints at the FGHAZ closest to the ICHAZ indicating Type IV cracking. The weld joints rupture times varying between those of the base metal and simulated FGHAZ. The weld joint creep rupture strength moves towards that of the base metal, for the applied stress just above 100 MPa, but it becomes nearly equal to that of the simulated FGHAZ at further low stress. The reports conclude that the concentration of creep deformation and eventual failure at the FGHAZ could be due to the recovery in the form of dislocation annihilation and coarsening of carbides that promote the heterogeneous coarse sub-grains formation during creep.

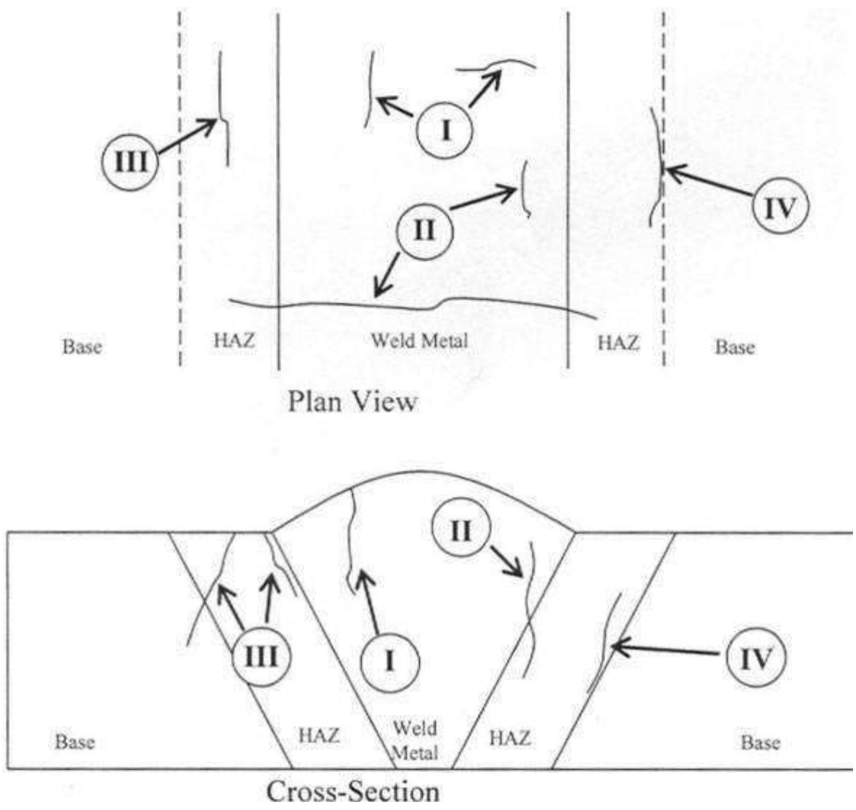

Fig. 2.31 Classification of cracking in weld joints from Brear et al. [220] according to Schuller et al. [219].

2.7.4.1 Mechanism of Type IV cracking

For the class of 9–12Cr steels, it seems that the microstructures of the FGHAZ and ICHAZ of the weld exhibit the poor creep strengths. The fine grain zone is generated with the temperatures just above the AC_3 i.e., inside the austenite phase field. But the temperature and time are inadequate to allow the carbides particles to totally dissolve. Therefore, the fine grains of austenite due to grain growth restriction from the undissolved carbides transform to martensite on cooling. During PWHT the carbides are coarsened without further precipitations. The dip in the hardness generally observed at ICHAZ, which consists of partially austenitized and remaining over-tempered martensite compared to the FGHAZ region. Among the simulated large volume homogenous HAZ microstructures, on higher stress application, the microstructure for the minimum creep strength coincides with the lowest hardness microstructure (ICHAZ). Even though, in the actual service conditions with the application of low stress, the FGHAZ showed minimum creep rupture life, while it displays higher hardness than ICHAZ across the weld joint. This denotes that the surface property such as hardness alone cannot be used to evaluate the Type IV vulnerability or Type IV location.

Abson et al. [222] stated that the over aging of precipitates in the inter-critical and fine grain regions of the HAZ was strongly associated with the Type IV failure. The repeated heating and cooling during multi-pass welding lead to a considerable amount of premature aging prior to the service and tempering of the HAZ region. The fine grain regions in the HAZ enhance localized diffusion and accelerate the growth of precipitates in service. The interface between coarsened precipitates and the matrix acts as a weak region, in which the creep accumulates strain in a continuous thin band of the HAZ, almost parallel to the fusion line. The localized accumulation of creep deformation causes the nucleation of voids and development of cracking and eventually to low ductility fracture.

Understanding the mechanism associated with the Type IV cracking is not simple, but is key to solving the problem effectively. As mentioned previously, the main microstructural factor accountable for poor creep behavior in the FGHAZ is the distribution of coarsened $M_{23}C_6$ precipitates. The tempered microstructure of base metal decorates the boundaries of PAG, lath and block mainly with the $M_{23}C_6$ precipitates that make up the martensitic structure. These precipitates provide grain boundary hardening and can obstruct the recovery and growth of sub-grains and prevent the movement of dislocation, more so than that associated with Orowan interaction [106]. The temperature range between 1173 and 1373 K attained during welding is associated with the formation of typical FGHAZ [43]. The rapid heating and cooling during welding allow re-austenitization at the peak temperatures with the incomplete dissolving of the boundary precipitates, despite the temperature being above the thermodynamic dissolution temperature for $M_{23}C_6$. This leads to the generation of microstructure that comprises of precipitates at the existing boundary positions and freshly formed boundaries without any such strengthening precipitates [87]. The new boundaries are considered weak, allowing recovery, sub-grain growth and softening to proceed more quickly [223,224]. Besides, the quick coarsening of the stable fine MX type precipitates at higher temperature service could also attribute to the reduction in the creep resistance in this location [225].

2.7.5 Previous studies on LCF and CFI behavior of P91 weld joint

As mentioned earlier that in the recent past, studies on the creep behavior of the weld joint of modified 9Cr-1Mo steel under long term creep conditions have been well established and extensively documented, and the Type IV failure is also well understood. However, there is comparatively less information available on the LCF and CFI behavior of the weld joints of this alloy at elevated temperatures. Especially research on the heterogeneous deformation contributions from the microstructurally functional HAZ for the overall weld joints deformation behavior under LCF and CFI conditions has not been conducted so far. Some of the recent investigations on the fatigue and creep-fatigue interactions behaviors of this alloy are discussed here.

Vani Shankar et al. [27] have carried out an elaborate study on LCF and CFI behavior of P91 steel weld joint at elevated temperatures. The study reported that the existence of inhomogeneous microstructure and the soft inter-critical zone attributed to lower cyclic stress response of the weld joint compared to the base metal. It has been observed that with a change in temperature and application of hold the failure location in the P91 steel weld joint also changes. The higher stress response at ambient temperature could cause the base metal failure, whereas, at elevated temperatures, the failure location is shifted to the soft ICHAZ under continuous cycling and compression hold. The failure location is shifted to the weld metal region of very close to the fusion line under a 10-minute tensile stain hold. The enhanced crack propagation due to the linkage of the sub-surface creep cavities due to strain localization in the soft region of the heat-affected zone lowers the fatigue life of the weld joint at higher temperatures.

Load-controlled fatigue and creep-fatigue experiments were conducted on cold metal transfer welded (CMTW) and flux-cored arc welded (FCAW) grade 91 steel weld joints and glebe simulated ICHAZ at 873 and 923 K by Payton [45]. The CMTW joint had a longer creep-fatigue life compared to the FCAW joint. The author reported that the fatigue lives of base metals of P92 and P122 steels at 873 K are nearly similar under LCF and CFI conditions. But under creep-fatigue interaction, the application of hold affect the fatigue life of weld metal and the HAZ of P122 by the factor of 2 to 4 compared to that of the LCF. The severe microstructural evolution is progressed in the weld metal and the HAZ during CFI deformation. The localized recovery of the lath structure in the form of sub-grain structure takes place in the weld metal rather than in the base metal. Such localized microstructural changes in the weld metal have been accredited to the comparatively intrinsic heterogeneity and the loose structure of the weld metal [226].

Besides some studies on the weld joint behavior under LCF and CFI conditions, understanding the mechanism contributions from each region of the weld joint, especially from the so-called weaker regions such as ICHAZ and FGHAZ is imperative to improve the fatigue performance of the actual weld joint during service at a higher temperature. Thus, the present study aims to determine the tensile, LCF and CFI behavior of all contributing microstructures of the HAZ to correlate with the overall mechanical behavior of the actual

P91 steel weld joint. Since the width of HAZ is few millimeters [32,227] with functionally graded microstructures, it is practically difficult to scoop out samples containing a single microstructure. To circumvent this, a powerful tool such as simulation of the different microstructures of HAZ through heat treatment was employed to produce a relatively larger volume and increased microstructural homogeneity compared to the corresponding microstructures of HAZ in the actual weld joint.

CHAPTER 3 EXPERIMENTAL METHODOLOGY

3.1 INTRODUCTION

Experimental details associated with material chemistry, heat treatments for homogenization of microstructure of mill-normalized and tempered material, simulation heat treatments to generate the heat-affected zone's microstructures, fabrication of tests specimen, hardness measurement, differential scanning calorimetry (DSC) for fixing the material critical temperatures and procedure for carrying out tensile, low cycle fatigue (LCF) and creep-fatigue interaction (CFI) experiments and microscopic investigation using optical microscope (OM), scanning (SEM) and transmission electron microscopes (TEM) and electron back scattered diffraction (EBSD) techniques are discussed in this Chapter.

3.2 MATERIAL COMPOSITION AND WELDING

The material for the present study is modified 9Cr-1Mo steel (P91 steel). The steel was obtained from M/s. Midhani Ltd., Hyderabad, India in the form of 30 mm thick plate and mill-normalized and tempered condition. The plate was cut into 12 mm × 12 mm × 75 mm size blanks and were subsequently normalized at 1313 K for 30 minutes and tempered at 1033 K for 1 h. The chemical composition of the base metal and the deposited filler wire are given in Table 3.1.

Table 3.1 Chemical composition of P91 steel base and weld filler material.

Element (wt.%)	C	Cr	Mo	V	Nb	Ni	Mn	Si	P	N	S	Fe
Base metal	0.11	9.3	0.99	0.25	0.1	0.14	0.46	0.32	0.020	0.068	0.008	Bal.
Filler wire	0.082	9.0	1.0	0.24	0.055	0.70	0.55	0.30	0.010	0.055	0.008	Bal.

The 30 mm thick plate was also sliced into two halves of 12 mm thick plates and joint employing gas tungsten arc welding (GTAW) process using modified 9Cr-1Mo filler wire. Soundness of the weld pad was checked with radiography and subsequently post weld heat treatment (PWHT) was carried out at 1033 K for 3 h. The welding conditions adopted are given in the Table 3.2.

Table 3.2 Welding parameters employed for GTAW

Parameters	**Parameters values**
Welding current	120−150 A (for each pass)
Voltage	20.0−25.0 V
Torch speed	25.0−30.0 mm/min
Electrode diameter	1.5 mm (root gap) 2.5 mm (remaining passes)
Heat input per pass	1.750 kJ/mm
Preheating, Inter-pass heating and Post bake-out heating temperature	563 K−573 K

3.3 SIMULATION OF HEAT-AFFECTED ZONES THROUGH HEAT TREATMENTS

Differential scanning calorimetry (DSC) study was carried out to affirm the critical temperatures of phase transformations at the heating rate of 10 $Kmin^{-1}$ and the results are given in Fig. 3.1 and Table 3.3. The AC_1 and AC_3 temperatures are identified at 1110 and 1176 K respectively. In the heating segment, the valleys (down peak) at 1015 and 1145 K in the calorimetric curve are associated with the Curie and tempered martensite to austenite transformations respectively. On the other hand, the peak at 659 K between the M_s (699 K) and M_f (609 K) in the cooling segment is associated with martensitic transformation of the steel cooled at 10 $Kmin^{-1}$. The transformation temperatures (AC_1 and AC_3) of P91 steel from this study is in good agreement with the other reported values obtained at heating rates between 20 $Kmin^{-1}$ and 3 $Kmin^{-1}$ [228,229]. Further the validity of the heat treatment cycles (soaking temperature-time-cooling rate combination for simulation of microstructures corresponding to HAZs of actual weld joint) was ensured through parameters such as prior austenite grain (PAG) size and hardness value comparison.

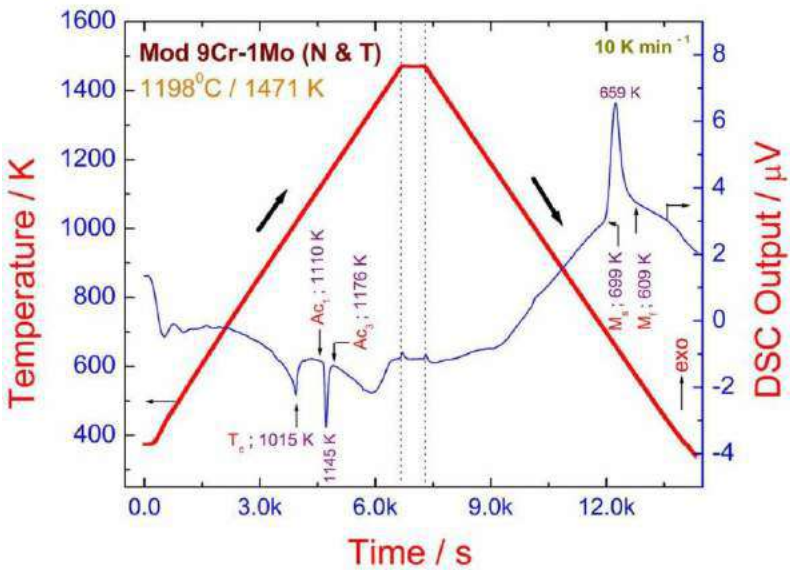

Fig. 3.1 Differential scanning calorimetry thermogram corresponding to the full heat-cool cycle for P91 steel at 10 $Kmin^{-1}$.

Table 3.3 Critical temperatures of P91 steel at the heating rate of 10 $Kmin^{-1}$

On-heating transformation temperature / *K (°C)*			Transformation temperature during cooling / *K (°C)*	
Critical temperature (T_c)	$\alpha \rightarrow \gamma$		Martensite Transformation	
	AC_1	AC_3	M_s	M_f
1015 (742)	1110 (837)	1176 (903)	699 (426)	609 (336)

Thermal cycles of actual welding and PWHT have been summarized in the form of schematic diagram as shown in Fig. 3.2(a). During actual welding, a linear heating rate is attained due to high heat input by depositing molten filler wire. The fast cooling in the actual welding process is attributed to the synergistic cooling effects from surrounding bulk parent metal and air atmosphere. As shown in Fig. 3.2(a) the welds cooling time at the end is prolonged due to the reduced temperature difference between the weld metal and the surrounding parent metal [230]. To simulate the microstructures of CGHAZ, FGHAZ and ICHAZ of P91 steel weld joint to as close as reasonably possible and keeping the experimental limitation into consideration, the steel blanks with the dimensions of 12 mm × 12 mm × 75 mm were subjected to the thermal cycle as shown in Fig. 3.2(b). Unlike the linear heating rate achieved in thermal cycle during actual welding, in the isothermal furnace heat treatment it can be seen (Fig. 3.2(b)) that the heating rate is rapid at the early stage and gradually decreases with time. The blanks were soaked for 5 min at the simulation temperatures; 1473 K (CGHAZ), 1208 K (FGHAZ) and 1138 K (ICHAZ) followed by oil cooling [14–16]**.** The oil cooling was chosen to nearly maintain the cooling rate of actual welding thermal cycle. The oil quenched blanks were tempered at 1033 K for 3 h (simulated PWHT).

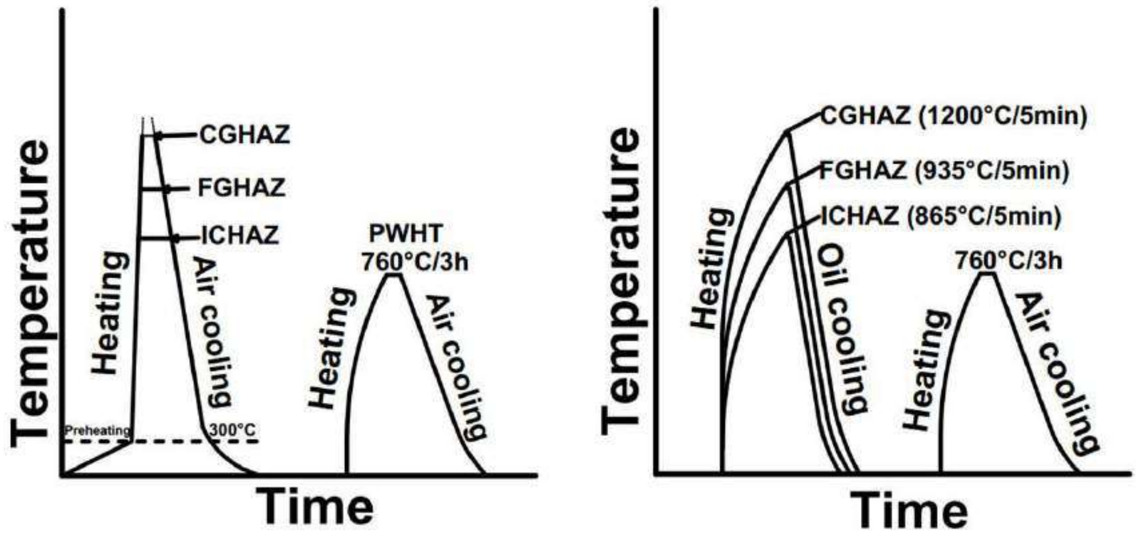

(a) (b)

Fig. 3.2 Schematic diagrams of thermal cycles during (a) actual welding and (b) furnace simulation of HAZs of P91 steel weld joint followed by tempering.

The tempering at 1033 K for 3 h was carried out on all samples heat treated at various soaking temperatures to replicate the PWHT condition. The American Society of Mechanical Engineers (ASME) Boiler and Pressure Vessel Code and ASME B31.1 stipulate PWHT at 977 K minimum and time as short as 15 min is mandatory. Post weld heat treatment at such a low temperature will not adequately temper the filler materials due to their higher nickel and manganese contents [231]. Post weld heat treatment should be conducted at optimum temperature of 1033 K by considering the entire microstructures across the P91 steel weld joint [7,232]. The alloy system responds slowly to tempering treatments because of excellent high temperature stability. As a result, the PWHT duration should never be less than two hours [233] even though the ASME codes allow PWHT from time as short as 15 min in thinner sections. Higher PWHT temperatures risk the chance of violating the lower transformation temperature, AC_1, which is as low as 1110 K. If the PWHT temperature is above the AC_1 temperature, austenite will start to form, which on-cooling will transform to fresh martensite. A reduction in toughness will be observed because of such untempered martensite [7]. Many researchers have reported that the PWHT at 1033 K for 3 h has significantly improved the mechanical properties of P91 steel weld joint [234–238].

3.4 MECHANICAL TESTS

3.4.1 Matrix for tensile, LCF and CFI tests

Strain rate controlled monotonic tensile tests were carried out using a ramp type waveform with the help of load-displacement data acquisition software. Low cycle fatigue tests were conducted applying strain amplitudes ranging from ±0.25% to ±1.0% using a triangular waveform. Creep-fatigue interaction tests were performed at a constant strain amplitude of ±0.6% with introducing hold periods of 1, 10 and 30 minutes at peak tensile strain in trapezoidal waveform. The above all types of tests were carried out at a constant strain rate of 3×10^{-3} s^{-1} and temperature of 823 K in a servo hydraulic testing machine equipped with a resistance heating furnace inbuilt with thermocouples. Specimen temperature was monitored using an external K-type thermocouple. The temperature variation along the gage length did not exceed ±1 K. The test matrix followed during the study is given in the Table 3.4.

The experimental data pertaining to creep, fatigue and creep-fatigue interaction in the temperature range of 773-873 K are essential for designing structural components for high temperature application [49]. In prototype fast breeder reactor (PFBR), the steam generator (SG) is fabricated using P91 steel. During operation of the PFBR the hot sodium enters the SG at 798 K and its temperature remains almost unaltered below the top thermal shield, which is also fabricated using P91 steel [239]. The temperature of sodium may increase up to 823 K in the event of pump failure during actual service. The RCC-MR (nuclear component installations) design code also prescribes 823 K as one of the temperatures for which the SG components have to be qualified with regard to creep and fatigue properties. Therefore, the LCF and CFI tests were carried out at the above temperature.

Table 3.4 Test matrix

Strain rate $3\times10^{-3}\ s^{-1}$ and temperature 823 K		
Material condition		Types of loading
Weld metal		1. Monotonic tensile tests up to failure.
Base metal		2. LCF tests up to failure at the strain amplitudes of ± 0.25, ± 0.4, ±0.6 and ±1.0%.
Simulated microstructure	ICHAZ	3. CFI tests up to failure introducing 1, 10 and 30 min at the tensile side of strain amplitude of ± 0.6%.
	FGHAZ	
	CGHAZ	
Actual weld joint		4. Interrupted tests on base metal up to 5, 10, 30 and 50% of total fatigue life under 30MTH-CFI.

Optimum strain amplitude (±0.6%) was employed in the CFI tests to understand the deformation mechanism due to fatigue in the CFI loading. Subjecting the materials to lower strain amplitude (±0.25%) would superimpose the influence of time dependent phenomena such as creep and oxidation on the deformation behavior. To circumvent this issue and based on earlier studies on ferritic/martensitic steels, the strain amplitude (±0.6%) was employed in the CFI tests [36,240,241]. To achieve the statistical validity of experimental data, minimum of three tests were planned in each of the six microstructural conditions (BM, ICHAZ, FGHAZ, CGHAZ, WM and WJ) at each strain amplitude in case of LCF and each hold time in case of CFI condition. Initially two sets of tests were conducted and the repeatability of the results was checked. If the test results are almost identical with respect to fatigue cycles and the cyclic stress response the third test was considered optional. Further, if the test results at various strain amplitudes satisfied the Coffin-Manson relation, test repetitions were avoided. Statistical compliance demanded 3-4 tests under some conditions. Therefore, the data given in the thesis are the representatives of the results obtained.

3.4.2 Test specimen fabrication

Non-standard cylindrical specimens with 6 mm diameter and 15 mm gauge length were fabricated from the rectangular blanks of base metal (BM) in the normalized and tempered condition, ICHAZ, FGHAZ, CGHAZ, weld metal and the actual weld joint of P91 steel. Test specimens were fabricated from the heat-treated rectangular blanks of 75 mm × 12 mm × 12 mm were cut from the weld plate in the directions as shown in Fig. 3.3(a). Considering the dimensions limitations of the gage length the test blanks for the cross-weld (weld joint) specimens were extracted from the weld pad as shown in Fig. 3.3(a). The weld joint specimen has been cautiously designed in such a way that all the constituent microstructures of the weld joint i.e., the weld metal region, the HAZ, and the base metal are almost evenly accommodated within the gage section as clearly depicted in Fig. 3.3(b). The specimen configuration used for tensile, LCF and CFI experiments is depicted in Fig. 3.3(b). The gauge section dimensions of the test specimen are of 15 mm (length) × 6 mm (diameter). The quality of surface finish can have a considerable effect on life to crack initiation during fatigue testing at ambient temperatures. Consequently, the specimen used in the present study was machined with a surface finish to a micron level ~0.4 μm that is confirmed by surface profilometer.

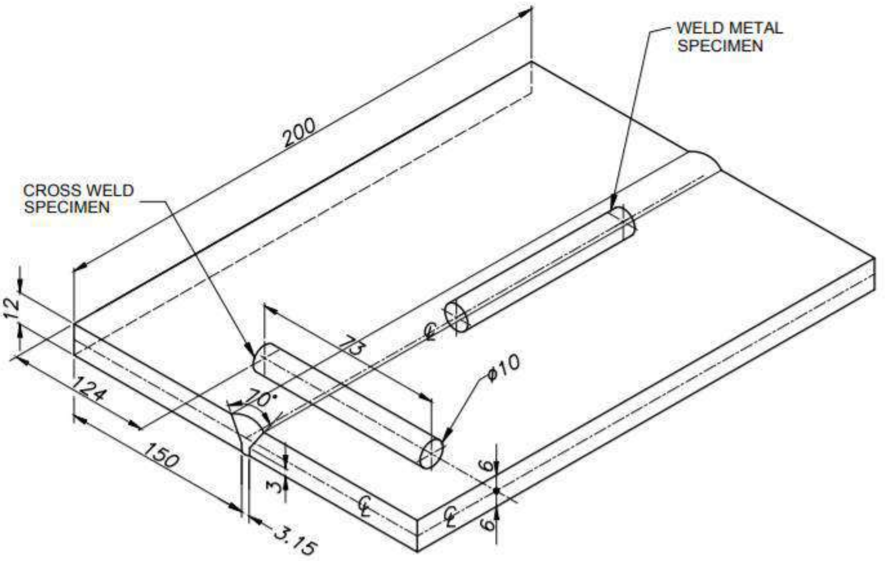

(a)

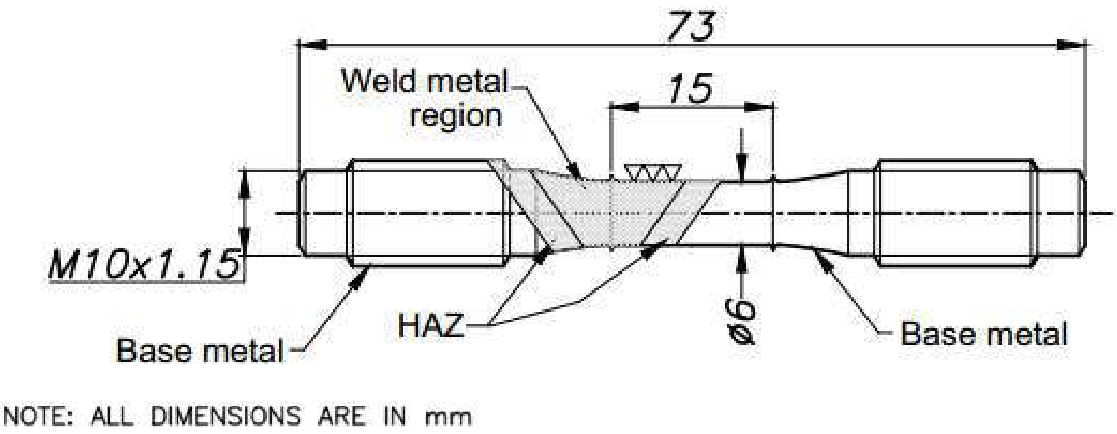

(b)

Fig. 3.3 Test specimen details; (a) extraction of test specimens from weld pad and (b) geometry of cross-weld test specimen.

3.4.3 Testing equipment

A schematic of the servo-hydraulic test system is shown in Fig. 3.4 (a). Total axial strain-controlled fatigue tests were carried out using a servo hydraulic low cycle fatigue system, equipped with a resistant heating furnace and the axial strain measurement was done using an averaging type extensometer fixed on to the ridges of the specimen.

The test system has hydraulic power pack from which the oil is pumped into the system through a servo valve. Servo valve controls the movement of actuator by controlling the flow rate of the oil to the actuator, according to the input signal (load or strain). The axial extensometer operates on LVDT principle, having a maximum measuring range of ±1.0 mm. The zero adjustment is made by means of each arm of the extensometer linearly. The test system consists of cylindrical shape heating unit, which is designed to heat specimens from 3 mm to 50 mm in diameter in the temperature range 473 to 1273 K. The furnace control module is designed to control the set temperature within $\pm$1 K. A photograph of DARTEC make servo-hydraulic fatigue testing machine used in this study is shown in Fig. 3.4(b).

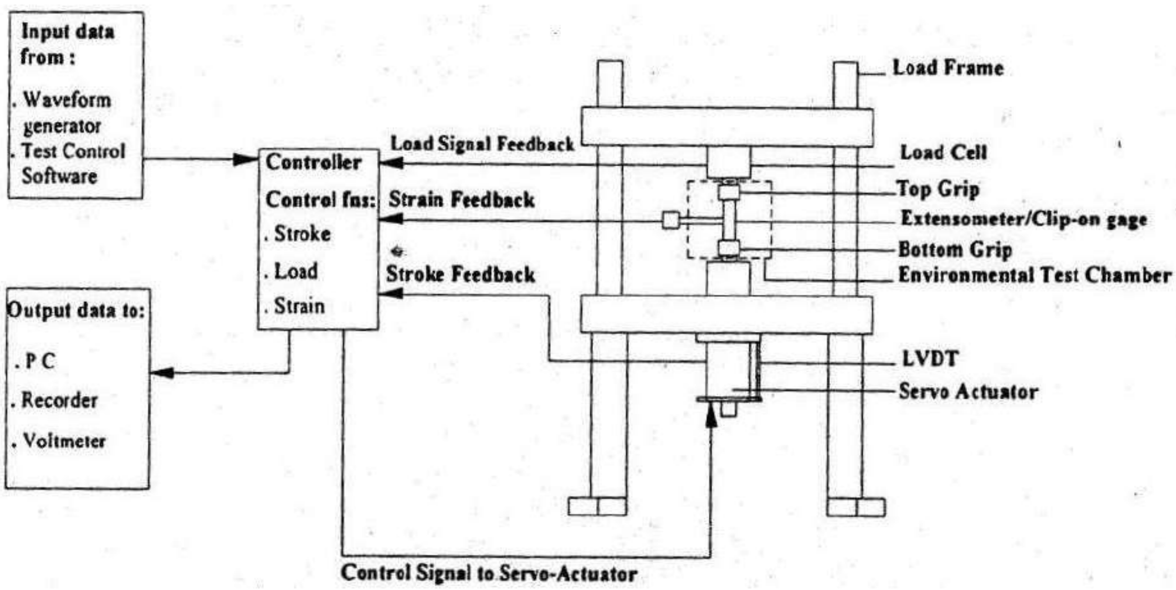

(a)

(b)

Fig. 3.4 Servo-hydraulic fatigue test system; (a) schematic and (b) DARTEC make system used in MDTD, IGCAR, Kalpakkam. The insert is showing a spring-loaded axial-strain extensometer, placed on specimen ridges.

3.4.4 LCF test procedure

The fully reversed axial strain-controlled LCF and CFI tests are performed as per the ASTM-E 606 and E 2714 respectively [242,243]. The specimen is initially mounted in the pull rods in the position control mode. The control is then transferred to load mode and the averaging type extensometers are fixed onto the specimen ridges having 15 mm gauge length. For high temperature testing, specimens are subsequently heated with the use of a resistance heating furnace. The heating of LCF specimen is performed under zero load condition. This procedure ensures the movement of actuator to compensate for thermal expansion of the specimen during heating. Once the set temperature is reached and stabilized, the thermal strain accumulated during heating is nullified and then the testing mode is changed to strain control. The test is then commenced with the inputs of test parameters.

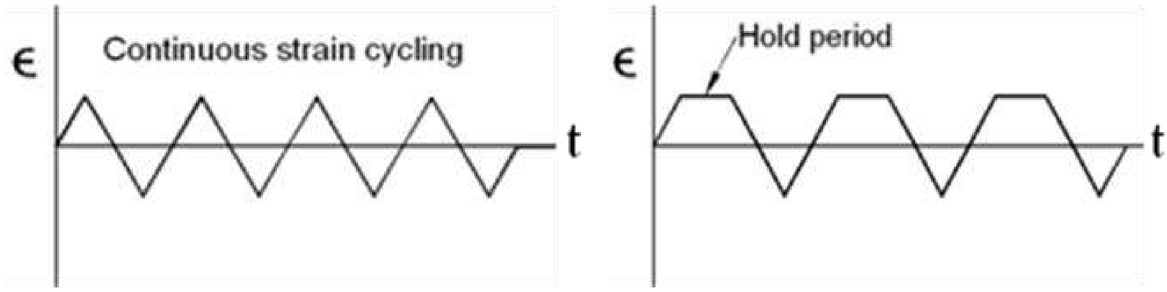

(a) (b)

Fig. 3.5 Strain-time waveforms; (a) triangular for LCF and (b) trapezoidal for CFI tests.

Continuous cycling LCF tests were conducted by employing a triangular waveform (Fig. 3.5). In the continuous cycling LCF tests, the strain rate was calculated using the equation,

$$\text{Strain rate} = 2 \times \Delta\varepsilon_t \times \upsilon \qquad \text{----(3.1)}$$

where, $\Delta\varepsilon_t$ ─ total strain range, and υ ─ frequency in Hz.

During testing, the stress-strain hysteresis loops were recorded at frequent intervals to determine the cycle dependent changes in stress and strain amplitude. A drop in the peak tensile stress by 40% with reference to the value corresponding to cyclic saturation was considered as the failure criterion for all the tests. The cyclic life was defined to be the number of cycles corresponding to a 20% reduction in peak tensile stress from the saturated stress value or the value corresponding to the cyclic number representing half the separation life [244].

3.5 METALLOGRAPHY AND HARDNESS MEASUREMENT

The microstructural characterization of the P91 steel base metal and weld joint as fabricated and subject to fatigue and creep-fatigue loading is important in modern power station construction. In these investigations, the samples of heat-affected zones recreated through heat treatments are elaborately used before and after tensile, fatigue and creep-fatigue tests. The results of the mechanical tests together with the qualitative and quantitative results of metallography are presented with the aim of correlating the deformation and damage with the evolving microstructures under monotonic and cyclic loadings. Special attention is paid to the understanding of contributions made from each microstructure of the HAZ to the overall mechanical behavior of the actual weld joint of P91 steel. Hardness measurement was carried out using Vickers micro-hardness tester at an applied load of 100 g and a dwell of 15 s at 0.1 mm interval in the specimen.

3.5.1 Optical microscopy (OM)

The grain size, crack propagation modes (transgranular or intergranular), extent of oxidation assisted cracking and crack number density that were observed in the samples of before and post-tests were studied. Small slices of steel blanks and longitudinal sections of the tested specimens were cut and mounted in a hot setting machine. The mounted specimens were ground using the SiC emery papers with the grit sizes of 400, 600, 800, 1000, 1200 and 2000. Subsequent to the grinding, the samples were further polished with the 6 µm, 3 µm, 1 µm and finally polished to the surface finish of 0.25 µm diamond suspension. The polished samples were etched by mechanical swabbing with the Vilella's reagent with composition of 1 g of picric acid + 5 ml conc. HCL + 100 ml ethyl alcohol. M/s. Carl Zeiss make optical microscope was used for optical examination. Both bright-field and dark-field images were captured under magnifications from X50 to X1000. Minimum 100 grains were taken up to quantify the average prior austenite grain size by linear intercept method using image analysis software, image J®. The software was also used for the determination of carbides sizes that were present at the grain boundaries.

3.5.2 Transmission electron microscopy (TEM)

Discs of 3 mm diameter and 0.25 mm thick samples were cut from the untested steel blanks and were mechanically thinned down to the metal foils of 50 μm thickness by silicon carbide paper (Grit-1200). Preparation of fine thin samples is very important to minimize magnetic aberrations in the TEM [245]. Subsequently the thin samples were electro polished in an electro jet thinning unit (electrolyte: 80% methanol + 20% perchloric acid, 20 V voltage and electrolyte bath temperature: 233 K) and were used for high resolution transmission electron microscopy (HRTEM) studies using Libra-200 FE operated at an accelerating voltage of 200 kV. The information limit of the TEM is 1.3 Å.

3.5.3 Field-emission scanning electron microscopy (FEGSEM)

Microstructure characterization of the HAZ specimens was conducted on a Zeiss-make SUPRA-55 model field emission scanning electron microscopy (FEGSEM). The FEGSEM is equipped with a secondary electron detector, an in-lens secondary electron detector, a backscattered electron detector, an energy dispersive spectroscopy detector, and forescatter detectors. Secondary electron detector and in-lens secondary electron detector were used for surface morphology analysis. The energy dispersive spectroscopy detector was used for chemical analysis. The electron backscatter diffraction detector was used for phase identification and crystal orientation measurement.

3.5.3.1 Scanning electron microscopy (SEM) with Energy dispersive spectroscopy (EDS)

Fractography analysis was conducted for the observation of crack initiation, striations, mode of failure (ductile and brittle) and oxidation that took place during mechanical testing. The EDS analyses were conducted on the samples using the X-Max 150 EDX system attached on the main equipment at 20 kV accelerating voltage and using 60 µm objective aperture at a work distance of 14 mm. The EDS data acquisition along with simultaneous crystal structure information was continuously obtained from Aztec 3.1 acquisition software provided by Oxford Instruments Nano-Analysis, UK.

3.5.3.2 Electron back scattered diffraction (EBSD) examination

Plane parallel flat surface of specimen was prepared by standard metallographic procedure used for optical microscopy in which polishing was carried out up to applying of 0.25 µm diamond suspension. This was followed by strain removal polishing using colloidal silica suspension with 0.04 µm size silica particles. Time for polishing with colloidal silica suspension was optimized at 45 minutes for the best results. The samples were ultrasonically cleaned by isopropyl alcohol and dried. Electron back scattered diffraction measurements were performed in a Zeiss make SUPRA 55 model field emission gun scanning electron microscope with an accelerating voltage of 20 kV, an aperture of 120 µm, keeping a nominal working distance of 16 mm, a tilt angle of 70°, sample–detector distance 178 mm and an indexing algorithm based on eight detected bands was utilized. Standardization of EBSD scan setting had to be carried out for obtaining large amounts of reliable data in a reasonable time for studying the deformation process. For all investigations, magnification of 2000X and 5000X scan step sizes of 0.1 µm and 0.05 µm (square grids) respectively. Aztec software was used for data collection and HKL-Channel 5^{TM} software was used for post processing of the data. Electron backscatter diffraction investigations were extensively used to clarify the deformation mechanisms taking place during tensile, fatigue and creep-fatigue interaction tests.

CHAPTER 4 INITIAL CHARACTERIZATION AND SIMULATION HEAT TREATMENTS VALIDATION

4.1 INTRODUCTION

The microstructures across the weld joints of 9% Cr martensitic P91 steel is quite complex. In the narrow width of the heat-affected zone, there is a wide variation in both microstructures and mechanical properties. A systematic microstructural investigation on different regions of the actual P91 weld joint is thus necessary to understand the evolution of damage in individual microstructural zones to be able to predict the performance and final failure of the weld joint under various mechanical test condition. In view of this, the current chapter is dedicated to the microstructural studies carried out on the initial base metal and various zones of the HAZ that were simulated through heat treatments. The microstructures obtained by simulated heat treatments are subsequently compared with the microstructures of actual weld joint using optical, scanning and electron microscopes.

4.2 INITIAL MICROSTRUCTURE

The optical micrograph as shown in Fig. 4.1(a), illustrates the initial microstructure of P91 steel in the normalized (1313 K/30 min) and tempered (1033 K/3 h) condition. The average prior austenite grain size was computed from approximately 100 grains and is found to be 14 µm with a standard deviation of ±4 µm. Figure 4.1(b) depicts that the initial microstructure of the base metal is composed of prior austenite grain boundaries (PAGBs), packet/block and lath boundaries, which are decorated with different types of carbide precipitates. Coarse $M_{23}C_6$ (M: Cr, Fe, Mo) type precipitates are nonuniformly distributed to different interfaces such as PAG, block, lath, and sub-grains boundaries while fine MX (M: V, Nb and X: C, N) type precipitates are dispersed uniformly in the matrix and on the dislocations. This observation is in good agreement with earlier reports [28,43,227]. The microstructure of P91 steel base metal (Fig. 4.1(c)) depicts various boundaries pinned with white precipitates of varying sizes. Comparison of EDS spectra obtained on both precipitates at the boundaries and the matrix vividly illustrates an enrichment of Cr and Mo and depletion of Fe elements in the precipitate region as opposed to the EDS obtained on the matrix (Fig. 4.1(d)). EDS mapping confirms that the precipitates at the boundaries are chromium rich $M_{23}C_6$.

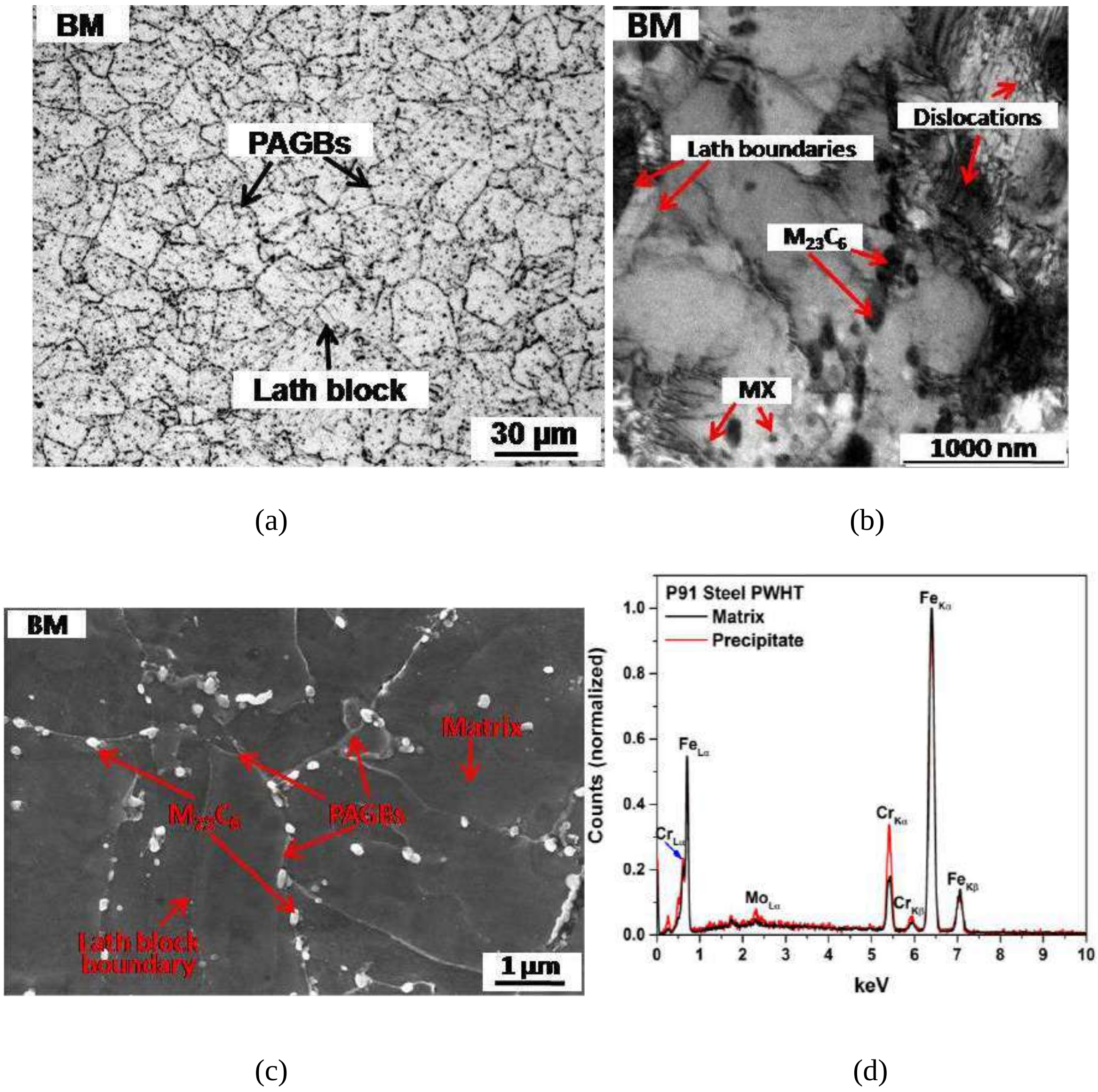

Fig. 4.1 Initial microstructure of P91 steel base metal in the normalized and subsequent PWHT condition; (a) optical, (b) TEM and (c) SEM micrographs and (d) EDS spectra comparison between matrix and precipitate.

The transmission electron micrographs of the initial microstructures of the weld metal, simulated CGHAZ, FGHAZ and ICHAZ are displayed in Fig. 4.2 (a)-(d). The weld metal is composed of a considerable amount of small sub-grains, high density of dislocations, and islands of delta ferrite, as shown in Fig. 4.2(a). The formation of sub-grains in the weld metal is due to the repeated heat/re-heat cycles experienced during the deposition of successive weld metals. The TEM micrograph of the weld metal shows some oxide inclusions and agrees with the observation made by Eggeler et al. [234]. Fine precipitates in the intralath regions, mostly covered by dislocations, are observed in the CGHAZ (Fig. 4.2(b)). The occurrence of equiaxed sub-grains and significant number of dislocations at the boundaries are typical of the FGHAZ microstructure. Sawada et al. [246] have also reported that the FGHAZ of the P91 steel weld joint is composed of fine martensitic lath structure and contains high dislocation density. The TEM image pertaining to the FGHAZ shows some evidences of pinning of dislocations by the MX types precipitates on the lath and sub-grain interiors. The ICHAZ, as shown in Fig. 4.2(d), consists of fresh martensites along with α ferrite that has the lath morphology. The ICHAZ has larger sub-grains than the base metal as can be observed by comparing Fig. 4.1(b) and 4.2(d).

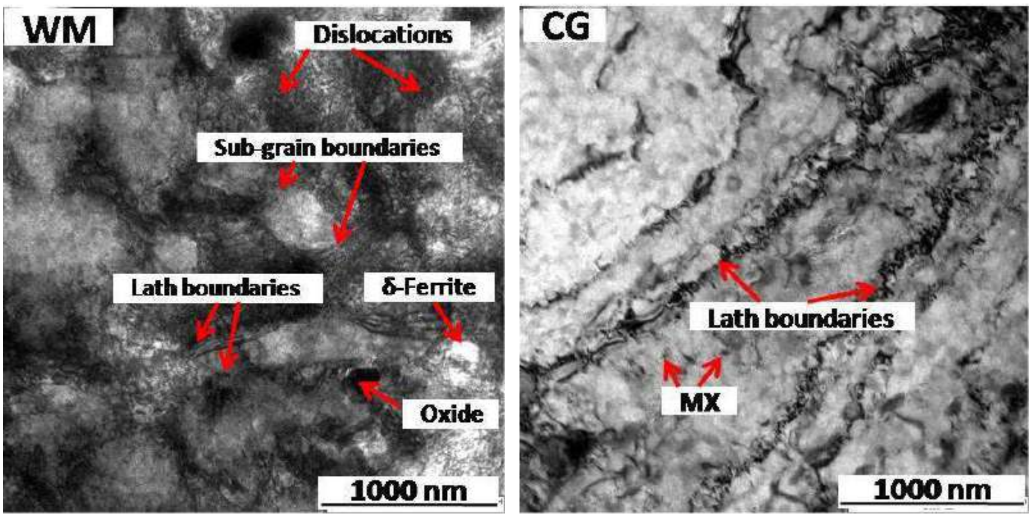

(a) (b)

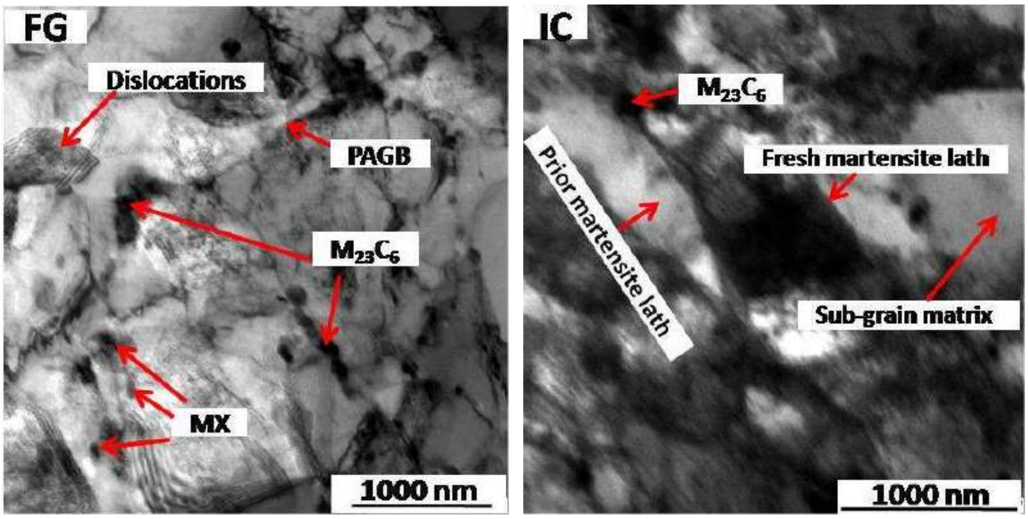

(c) (d)

Fig. 4.2 Transmission electron micrographs of the initial microstructures of (a) weld metal and simulated (b) CGHAZ, (c) FGHAZ and (d) ICHAZ of P91 steel weld joint.

4.2.1 Validation of HAZs microstructure simulation

4.2.1.1 Through grain size evaluation

It is well known that the microstructural features in the form of grain size, affect the mechanical properties of materials. For material such as P91 ferritic/martensitic steel in which the prior austenite grain is further partitioned into packets, blocks and sub-grains through various complex boundaries [50,170,247–249], apart from the PAGs, the substructures affect the mechanical properties. Scanning electron microscopy has been used especially in the present work to describe the substructures of various regions of HAZ and quantify the submicron size precipitates. While optical micrographs have been used to quantify the PAG sizes for all microstructural regions associated with P91 weld joint, EBSD analysis has been performed to understand the statistical substructural distribution and the underlying strains due to heat treatments and welding of the thermally sensitive P91 steel.

Optical micrographs of HAZs of the actual weld joint and the corresponding simulated HAZs are illustrated in Fig. 4.3(a)-(f). Coarse grain heat-affected zone forms at the adjoining base metal next to the molten weld pool. Figures 4.3(a) and (b) show the tempered martensitic laths within the coarse-equiaxed PAGs of the CGHAZ. At peak temperature, well above AC_3, the base metal transforms to CGHAZ due to the dissolution of former MX and $M_{23}C_6$ precipitates that were pinning various boundaries [250]. Re-precipitation of carbides take place along the PAG and lath boundaries near the fusion line in the parent metal during cooling and subsequent PWHT [251]. Hald [252] reported that the instantaneous growth of austenite grains is attributed to the drop of impeding action of dissolved precipitates at well beyond AC_3. Delta ferrite is expected to form during welding and subsequent cooling when the temperature reaches between 1673 K and the melting temperature of pure iron with reference to the Fe-C equilibrium diagram. Such high temperature was not reached during any of the simulation heat treatments in the present study and hence δ-ferrite was not observed for any of the simulated microstructures.

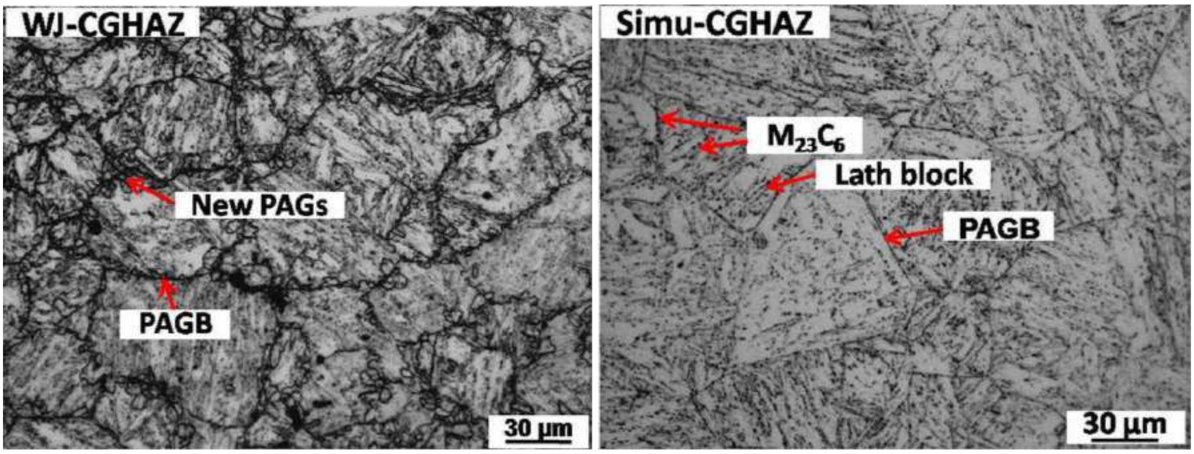

(a) (b)

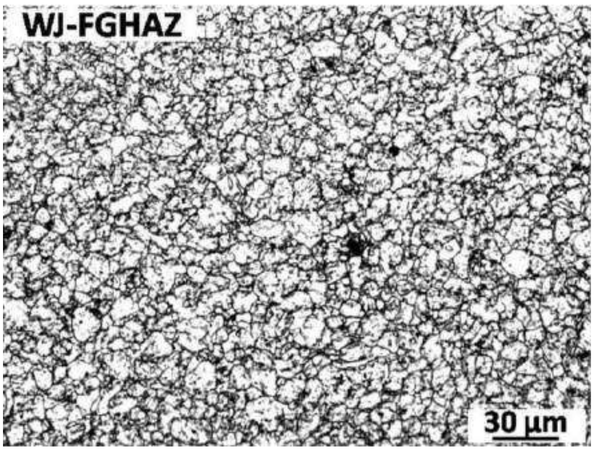

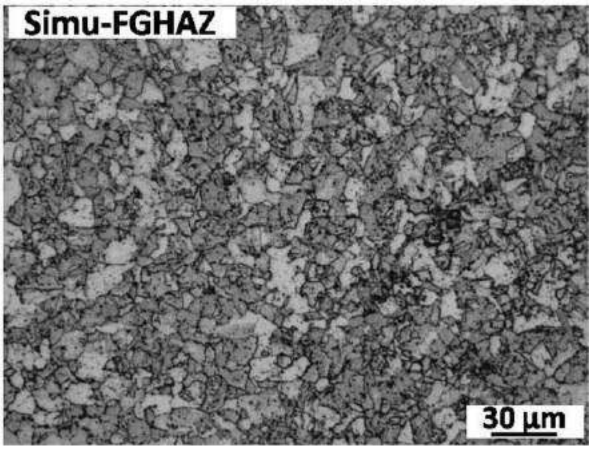

(c) (d)

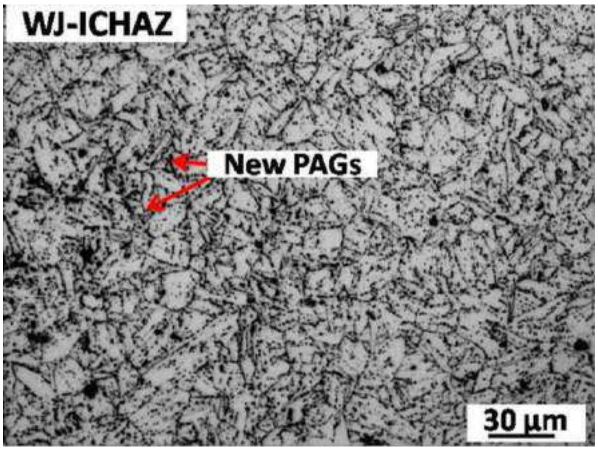

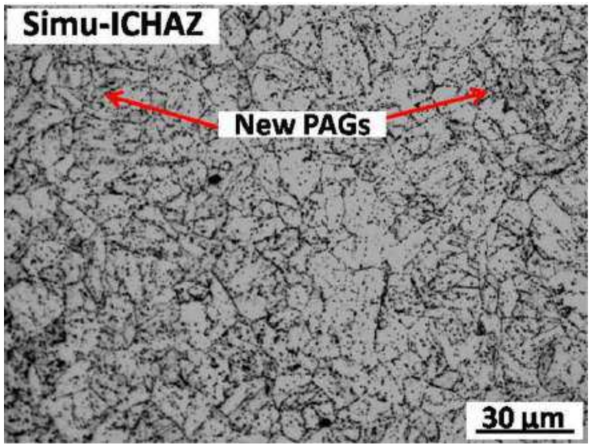

(e) (f)

Fig. 4.3 Optical micrographs of microstructures of actual weld joint (a) CGHAZ, (c) FGHAZ and (e) ICHAZ and simulated (b) CGHAZ, (d) FGHAZ and (f) ICHAZ.

The formation of FGHAZ microstructures during simulation or actual welding takes place at just above the AC_3 temperature (1208 K). The range of exposure temperature and the short dwell time during weld thermal cycles are believed to limit the grain growth (Fig. 4.3(c) and (d)) during martensite to austenite transformation [253,254]. It is apparent from the Fig. 4.3(e) and (f), that inter-critical heating during either isothermal heat treatment or actual welding lead to the partial transformation of tempered martensite into new fine austenite grains (shown using arrows) and unaffected α-ferrite [255]. Upon cooling, the new fine austenite transforms into fresh martensite. During subsequent PWHT the freshly formed martensite gets tempered and the unaffected α-ferrite gets over tempered. Repeated heating of prior cooled regions, particularly in the heat-affected zones takes place during multi-pass welding. Heat dissipation through the previously cooled region of the parent metal gives rise to the nucleation of new grains or precipitation reaction at the high energy regions such as PAGBs during actual welding [230,256]. These attribute to the thickening of PAGBs in the case of microstructures of the actual weld joint. Repeated nucleation of such tiny grains does not occur at the PAGBs in the case of simulated microstructures due to isothermal heating. Thus, the PAGBs of simulated microstructures are comparatively sharper and well defined than the corresponding microstructures of actual weld joint as shown in Fig. 4.3(a)-(f).

Grain size distribution for all the microstructures of HAZs of simulated and actual weld joint of P91 steel is displayed in Fig. 4.4. Prior austenite grain sizes of CGHAZ of both simulated and actual weld joint varied between 10 and 80 μm and many grains concentrated around 50 μm (Fig. 4.4(a)). The microstructure of FGHAZ (Fig. 4.4(b)) during heating through 1176−1373 K attained the average PAG sizes well within 10 μm with a maximum at ~7 μm. Single Gaussian distribution for all microstructures is seen except for the ICHAZ that displays a double Gaussian distribution of the prior austenite grain size. The double Gaussian distribution is attributed to the presence of over tempered coarse ferrites and fine and fresh tempered martensites. Prior austenite grain sizes varied from 4 to 18 μm with peaks at 8 μm and 14 μm for the ICHAZ microstructures (Fig. 4.4(c)). The average grain size of simulated HAZ is slightly larger than that of the actual weld joint due to the difference of the heat input rates of furnace heating and weld cycles respectively.

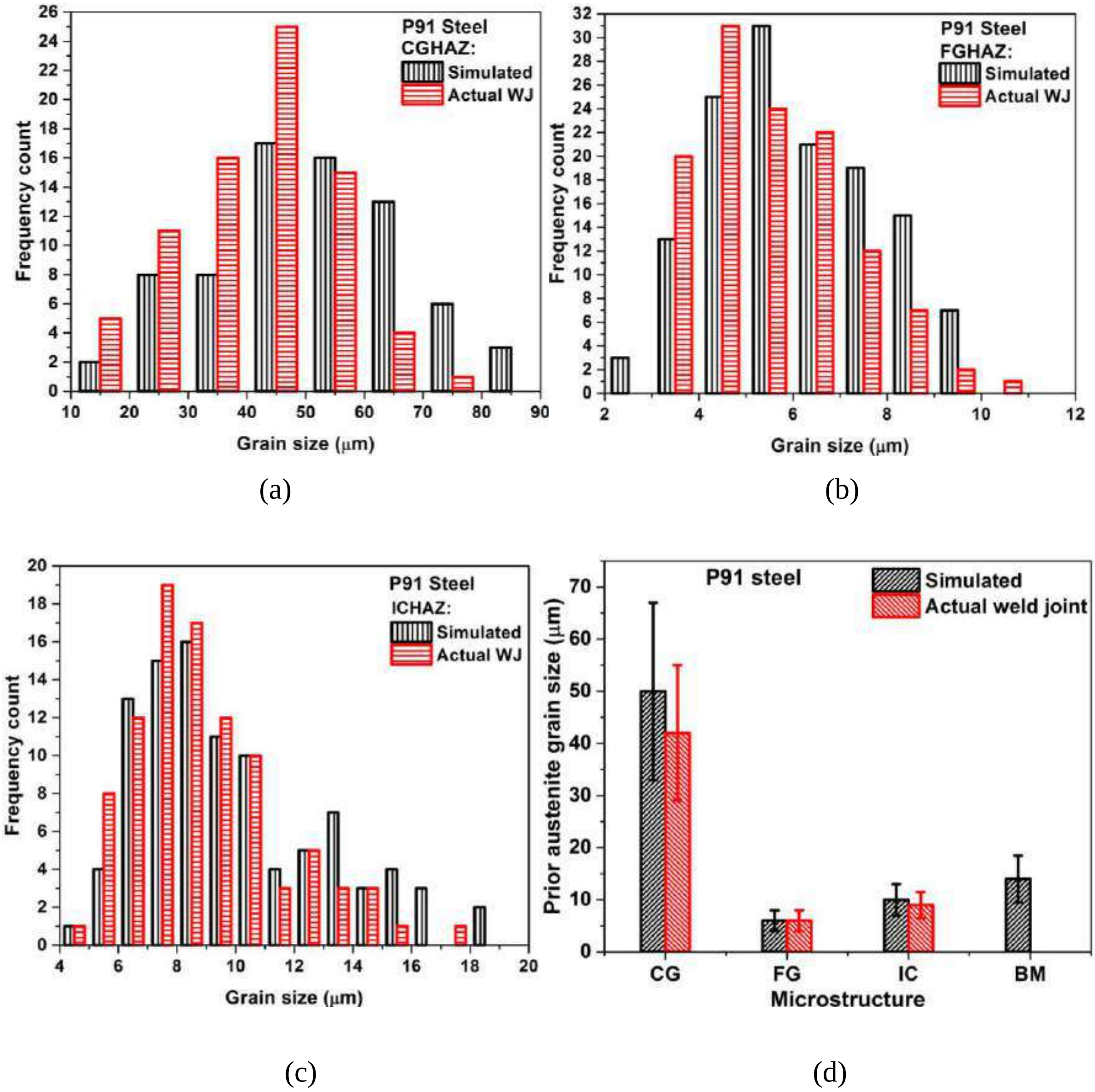

Fig. 4.4 Comparison of grain size distributions of simulated and actual weld joint microstructures; (a) CGHAZ, (b) FGHAZ and (c) ICHAZ and d) average PAG size of various microstructures of P91 steel weld joint.

Average PAG sizes measured for both simulated and actual weld joint HAZs are depicted in Fig. 4.4(d) along with standard deviations. The standard deviations are high for the CGHAZs of both simulated and actual weld joint compared to the microstructures of FGHAZ and ICHAZ. This is due to the sluggish dissolution/precipitation of primary carbides (NbC) that are responsible for restricting grain growth and pinning of grain boundaries [257]. Average prior austenite grain size measurements for the HAZs of simulated and actual weld joint are summarized in Table 4.1.

Table 4.1 Grain sizes comparison between the simulated and actual weld joint HAZs of P91 steel.

Microstructure	Simulated		Actual weld joint	
	Grain size (μm)	Standard Deviation (±μm)	Grain size (μm)	Standard Deviation (±μm)
CGHAZ	50	17	42	13
FGHAZ	6	2	6	2
ICHAZ	10	3	9	2.5
Base metal	14	4.5	14	4.5

4.2.1.2 Through precipitate size analysis

Scanning electron micrographs of simulated HAZs and the corresponding HAZs of actual weld joint are illustrated in Fig. 4.5(a)-(f). A range of 75-100 precipitates are taken up for measuring the average precipitate size in each HAZ. The average precipitate sizes of CGHAZ, FGHAZ and ICHAZ for both simulated and the actual weld joint are compared and depicted in Fig. 4.5(g). The precipitate sizes in all microstructures show large standard deviation because of their continuous formation and coarsening during PWHT. Both precipitate and grain sizes are comparable for the actual and simulated microstructures and the precipitate and the grain sizes are in the order of ICHAZ>FGHAZ>CGHAZ and CGHAZ>ICHAZ>FGHAZ respectively. The average grain and precipitate sizes of the various microstructures in the HAZs of the simulated and actual weld joint are given in Table 4.2.

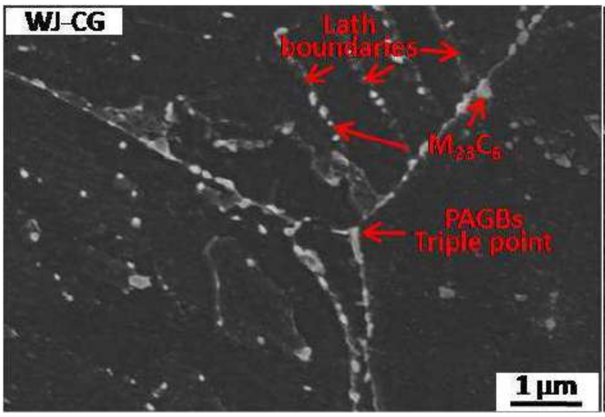
WJ-CG
Lath boundaries
M23C6
PAGBs Triple point
1 µm

(a)

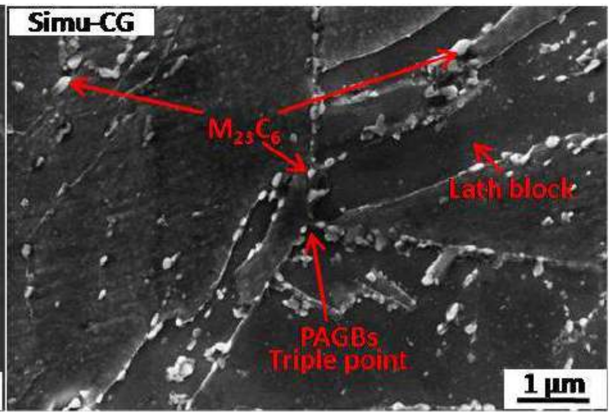
Simu-CG
M23C6
Lath block
PAGBs Triple point
1 µm

(b)

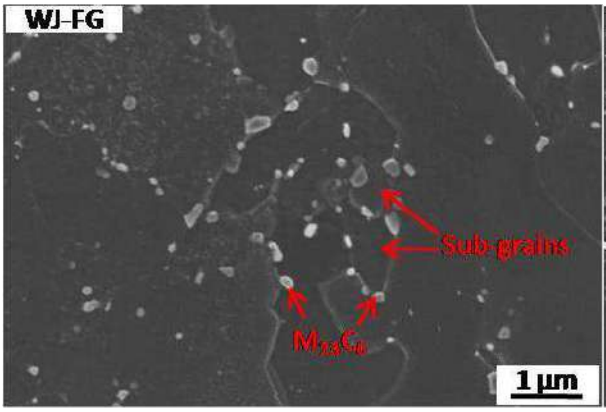
WJ-FG
Sub-grains
M23C6
1 µm

(c)

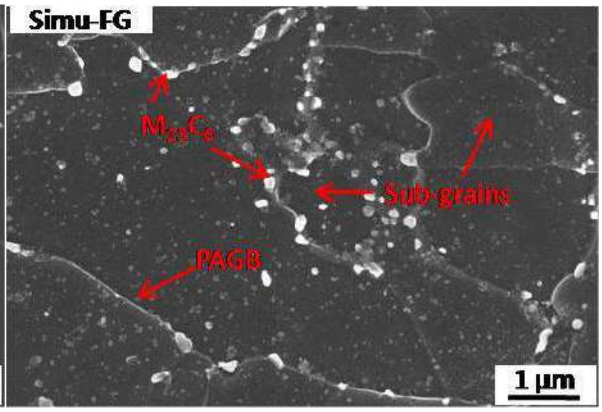
Simu-FG
M23C6
Sub-grains
PAGB
1 µm

(d)

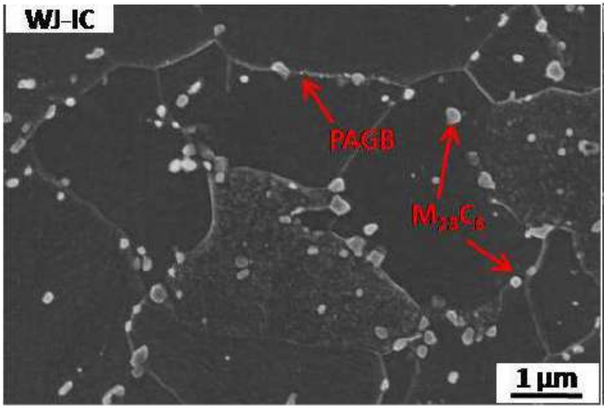
WJ-IC
PAGB
M23C6
1 µm

(e)

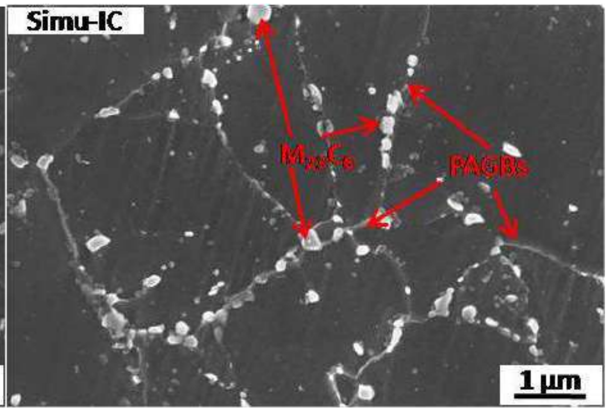
Simu-IC
M23C6
PAGBs
1 µm

(f)

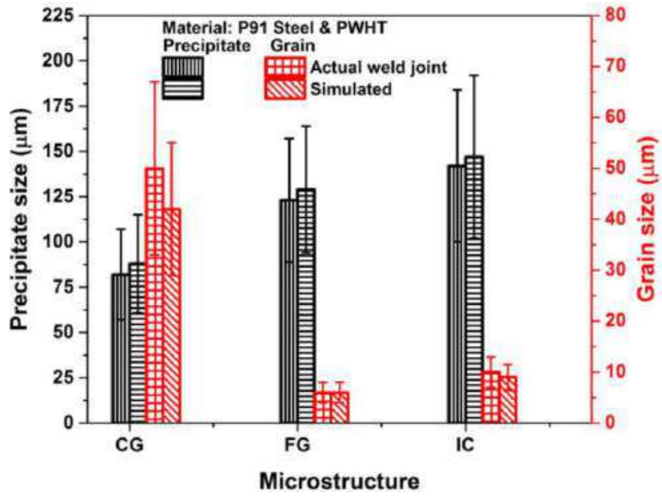

(g)

Fig. 4.5 Scanning electron micrographs of microstructures of (a) CGHAZ, (c) FGHAZ, (e) ICHAZ of actual weld joint and (b) CGHAZ, (d) FGHAZ and (f) ICHAZ of simulated P91 steel and (g) comparison between the HAZs′ precipitates and PAGs sizes of the simulated and the actual weld joint.

Table 4.2 Average PAG and precipitate sizes in the HAZs of simulated and actual weld joint of P91 steel.

Micro-structure	Simulated				Actual weld joint			
	Grain size (μm)	Standard Deviation (±μm)	Precipitate ($M_{23}C_6$) size (nm)	Standard Deviation (±nm)	Grain size (μm)	Standard Deviation (±μm)	Precipitate ($M_{23}C_6$) size (nm)	Standard Deviation (±nm)
CGHAZ	50	17	88	27	42	13	82	25
FGHAZ	6	2	129	35	6	2	123	34
ICHAZ	10	3	147	45	9	2	142	42

The region adjacent to the weld metal, which is exposed to the temperature range well above the AC_3 consists of coarse grained HAZ (CGHAZ) (Fig. 2.29). At this temperature range the tempered martensite transforms to austenite accompanied by a complete dissolution of carbides that also includes the primary MC type carbides that are responsible for pinning of the grain boundaries and restricting grain growth. Significant grain growth is a result of dissolution of some of the primary carbides resulting in prior austenite grains of ~45 μm average sizes in the CGHAZ (Fig. 4.5(a) and (b)). During the post-weld cooling and subsequent PWHT re-precipitation of various carbides occur and the larger $M_{23}C_6$ are discernible at various boundaries (Fig. 4.5(a) and (b)). Quenching from higher temperature introduces large number of defects that act as sites for precipitation of fine $M_{23}C_6$ in the region next to the weld metal pool i.e., CGHAZ of actual weld joint and the simulated microstructure. The average carbide sizes in the CGHAZs of actual weld joint and simulated conditions are 82 nm and 88 nm respectively, with the standard deviation approximately ±25 nm. The formation of microstructures of FGHAZ during actual welding or simulation heat treatment takes place at just above the AC_3 temperature (1208 K). The limitation of grain growth during martensite to austenite transformation is due to the lower exposure temperature range and the short dwell time during weld thermal cycles [250,254]. The $M_{23}C_6$ precipitates are also larger in FGHAZ than those observed in the CGHAZ. There are different views on the dissolution temperature of $M_{23}C_6$ carbides in P91 steel. Based on Thermocalc simulation by Cipolla et al. [258], $M_{23}C_6$ dissolves in austenite at temperatures > 1143 K, whereas the kinetics of dissolution is sufficiently slow under weld thermal cycles resulting in limited dissolution of carbides below 1373 K. As reported by MacLachlan et al. [259] that $M_{23}C_6$ completely dissolves at 1141 K , whereas results of Gaffard et al. [260] indicates that 1208 K may not be high enough to completely dissolve the $M_{23}C_6$ precipitates thereby resulting in comparatively coarser precipitates as also observed in the present study. Thus, the average sizes of these precipitates in the FGHAZs of actual and simulated are 123 nm and 129 nm (~±35 nm) respectively and the average grain size is 6 μm (±2) for both the simulated and actual weld joint. It is apparent from the Fig. 4.5(e) and (f), that inter-critical heating during either isothermal heat treatment or actual welding leads to partial transformation of tempered martensite into new fine austenite grains and unaffected α-ferrite without significant dissolution of $M_{23}C_6$ carbides [255]. Upon cooling, the new fine austenite transforms to fresh martensite and during subsequent PWHT the freshly formed martensite gets tempered and the α-ferrite becomes over tempered. The average grain sizes are 10 and 9 μm (~ ±3) for the ICHAZs of simulated and actual weld joint respectively (Fig. 4.5(e) and (f)). Tempering results in the coarsening of pre-existing carbides. The average precipitate sizes in the inter-critical zones of actual weld joint and simulated are 142 nm (±42 nm standard deviation) and 147 nm (±45 nm standard deviation) respectively.

4.2.1.3 Through hardness characterization after PWHT

Roughly, three layers with various hardness ranges can be divided, including base metal (unaffected region), HAZ, and a weld metal. The Fig. 4.6 displays variation in the hardness profile across the actual weld joint in the PWHT condition. In the figure, the hardness values of simulated HAZs are incorporated at the appropriate distances, matching with the corresponding zones in the actual weld joint after PWHT. It is found that the hardness value of FGHAZ reproduced through simulation heat treatment (soaking at 1208 K for 5 minutes) represents the FGHAZ of the actual weld joint at a distance of ~1.6 mm from CGHAZ in the hardness profile. The variation in the hardness values is observed due to gradient in the microstructures across the weld joint. In the HAZs, the CGHAZ exhibits the highest hardness value of 239 HV0.1 because of the strengthened matrix due to the dissolution of most of the primary carbides/nitrides at 1473K and above. Further, the dispersion of fine precipitates in the CGHAZ also increase the hardness through stabilizing the free dislocations [211,261]. A minimum (189 HV0.1) in the hardness profile of the actual weld joint has been attributed to the soft ICHAZ. The least value of hardness for ICHAZ as in the present case has also been reported in P91 steel elsewhere [16,262–264]. This has been accredited to the replacement of well-defined martensite laths (high dislocation density) with large over tempered soft ferrite (low dislocation density) and coarser $M_{23}C_6$ carbides (Fig. 4.2(d)) owing to inter-critical heating. Scanty areas of high dislocation density contrast from freshly formed laths (shown by arrows in Fig. 4.2(d)) due to the partial transformation of austenite during inter-critical heating are also visible. The FGHAZ and base metal showed hardness values of 199 HV0.1 and 207 HV0.1 respectively. The hardness values of simulated microstructures follow the same tendency of hardness profile of the actual weld joint (Fig. 4.6) thereby, complementing that the simulation heat treatments given are adequate to reproduce the microstructures of the actual weld joint.

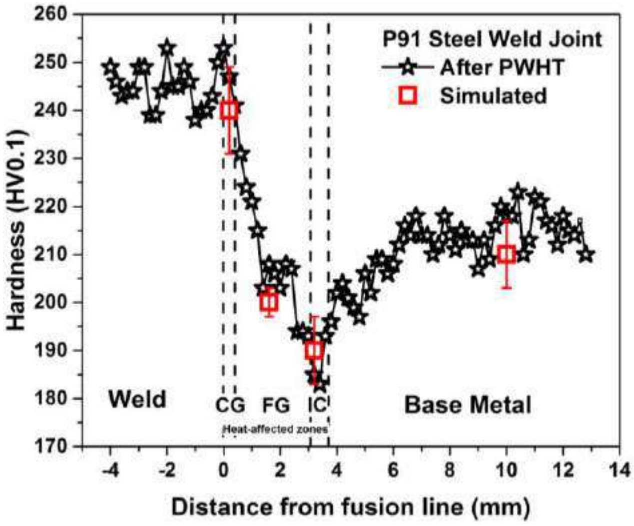

Fig. 4.6 Hardness values comparison between the actual and simulated HAZs of the P91 steel weld joint.

4.3 INITIAL CHARACTERIZATION THROUGH EBSD ANALYSIS

Electron backscattered diffraction technique is an ideal tool to visualize and quantify the submicron features such as sub-grain size, classification of grain boundaries and their statistical distribution, the strain distribution within the constituting substructures, phase fraction in Grade 91 steel. In the present work the inverse pole figure (IPF) maps have been used to show the substructural distribution within individual sample grains. Throughout, the scanning reference frame is chosen such that the Z-direction is normal to the plane of the map. Based on the crystal orientation, each scanned point is assigned a color from a predefined color code of a triangle. The apexes of the color legend triangle correspond to the planes of (001), (101) and (111) and shape of the triangle is based upon the standard stereographic projection cubic system. As the IPF maps show the individual grain orientation with respect to the standard projection, a point is assigned as a grain boundary if there is large orientation difference between the neighboring points. The GBs having misorientations in the range of 2-15º are classified as low angle grain boundaries (LAGBs) and those having misorientations greater than 15º are demarcated as high angle grain boundaries (HAGBs) [265]. The microstructures of the base metal, weld metal and actual and simulated CGHAZ, FGHAZ and ICHAZ of P91 steel weld joint after tempering (PWHT) are presented through IPF maps (Fig. 4.7(a)-(h)). The sub-grain size distribution of the simulated and actual microstructural constituents of weld joint is compared in Fig. 4.7(i).

The IPF clearly depicts partitioning of prior austenite grains into packets, blocks and martensite laths. Same orientation blocks are of the same color scheme and the martensite blocks are separated by high angle grain boundaries (compare Fig. 4.7(a) through (h) with Fig. 4.8(a) through (h) respectively). The substructure sizes were measured from the grain boundary maps using the line-intercept method. In the present study, the tempered martensite matrix has been treated as pure body-centered-cubic (BCC) iron since it is assumed that there is a small distortion in the lattice parameter 'c' because of the presence of low carbon content (~0.1 wt%) in the base metal. The local strain or deformation magnitude within grains was evaluated by calculating the kernel average misorientation (KAM) between the pixels/kernels in the tempered martensite P91 steel.

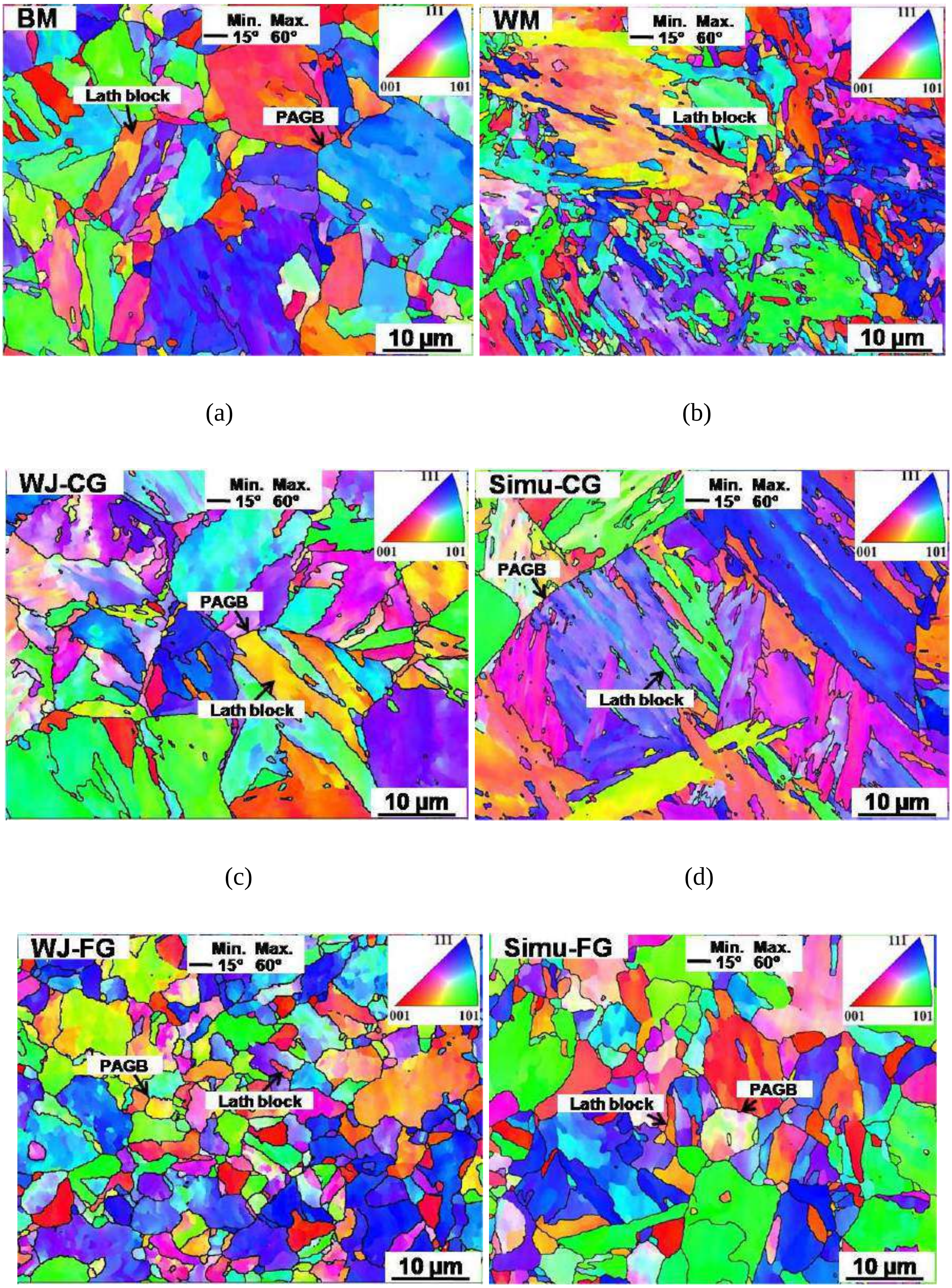
BM
Min. Max.
15° 60°
111
001
101
Lath block
PAGB
10 μm
WM
Min. Max.
15° 60°
111
001
101
Lath block
10 μm
WJ-CG
Min. Max.
15° 60°
111
001
101
PAGB
Lath block
10 μm
Simu-CG
Min. Max.
15° 60°
111
001
101
PAGB
Lath block
10 μm
WJ-FG
Min. Max.
15° 60°
111
001
101
PAGB
Lath block
10 μm
Simu-FG
Min. Max.
15° 60°
111
001
101
Lath block
PAGB
10 μm

(a) (b)

(c) (d)

(e) (f)

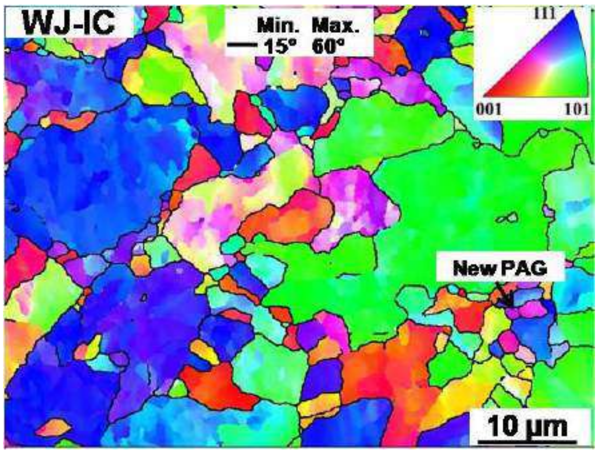

(g)

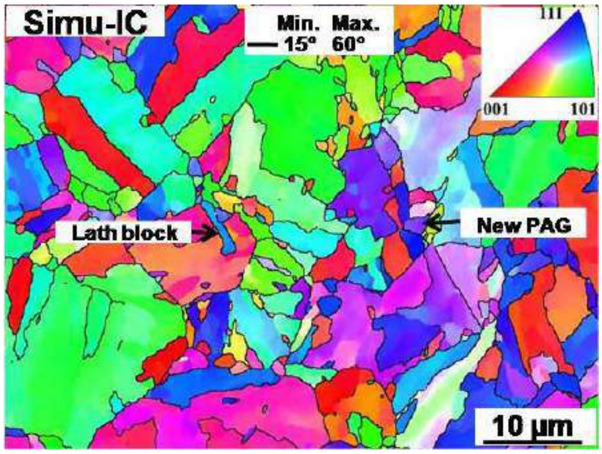

(h)

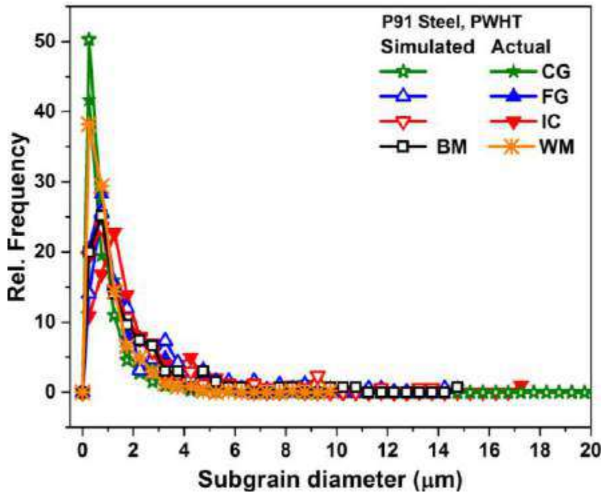

(i)

Fig. 4.7 Substructural analysis; (a-h) inverse pole figure (IPF) maps and (i) sub-grain size distributions plots; base metal, weld metal and actual and simulated HAZs after PWHT.

The weld metal and CGHAZ depict martensitic laths in PAGs (Fig. 4.7(b)-(d)). The CGHAZs of both simulated and actual weld joint and the weld metal exhibit the finest average substructure sizes ~1 µm, which is comparable to block sizes in the weld metal. Similar values for the microstructures after PWHT at 1033 K for 2 h are reported by Wang et al. [71]. Due to isothermal simulation heat treatment, the size of the lath blocks within the PAG of simulated CGHAZ are larger than the CGHAZ generated due to welding. In general, the lath block size seems to increase with the increase in PAG sizes [71].

The IPF map of ICHAZ microstructure depicts distribution of both fine and coarse grains with some of the martensite blocks having size of approximately 2 μm, also given in Table 4.3. This is in good agreement with the observation by Xinghua et al. [266]. The finer blocks within the small prior austenite grains formed during heating are the result of exposure to temperature between AC_1 and AC_3. Also, the visible large martensite packets and blocks correspond to the over tempered ferrite (Fig. 4.7(g) and (h)). These results are in line with the observations made by optical microscopy as well.

Table 4.3 Sub-grain size analyses in the base metal, weld metal, simulated and actual CGHAZ, FGHAZ, ICHAZ of P91 weld joint in PWHT condition.

Sub-grain parameter	Simulated				Actual weld joint			
	BM	CGHAZ	FGHAZ	ICHAZ	WM	CGHAZ	FGHAZ	ICHAZ
Grain size (μm)	1.94	0.98	2.15	2.12	0.98	1.33	1.57	2.10
Grain size SD (μm)	2.28	1.79	2.26	2.51	0.98	1.96	1.46	2.14

Based on the neighboring misorientations, the grain boundary maps of simulated and actual CGHAZ, FGHAZ and ICHAZ and base metal and weld metal of P91 weld joint are generated and the results are depicted in Fig. 4.8(a)-(h). Grain boundary distribution based on misorientation between neighboring pixels is compared for all microstructural regions in Fig. 4.8(i). In high Cr steels, prior austenite grain boundaries and martensitic packet/block boundaries are identified as high angle grain boundaries and the lath boundaries are recognized as low angle boundaries [71]. There is a significant difference in the grain boundary plots with the exposure temperature (Fig. 4.8). Though the overall prior austenite grain sizes are comparable for the corresponding microstructures of simulated and actual weld joint, the grain boundary distribution map shows that there is remarkable difference in the block size.

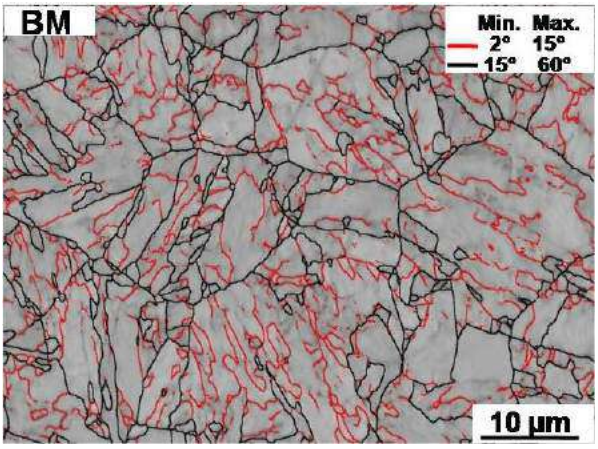

(a)

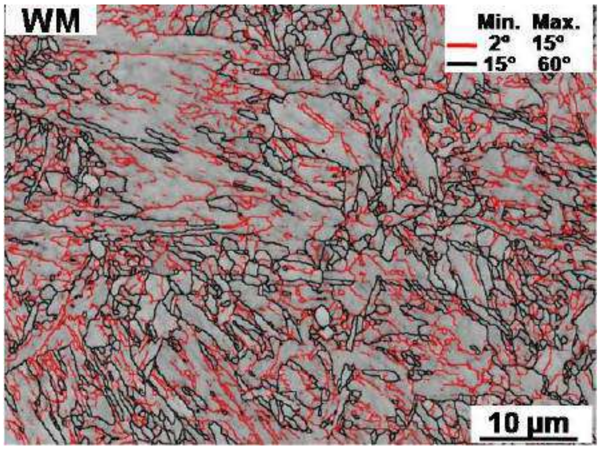

(b)

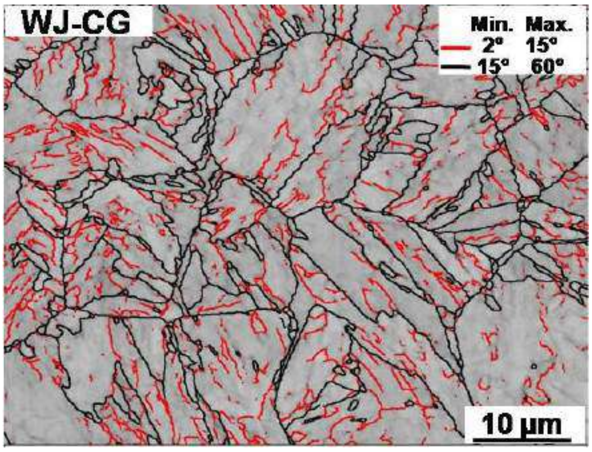

(c)

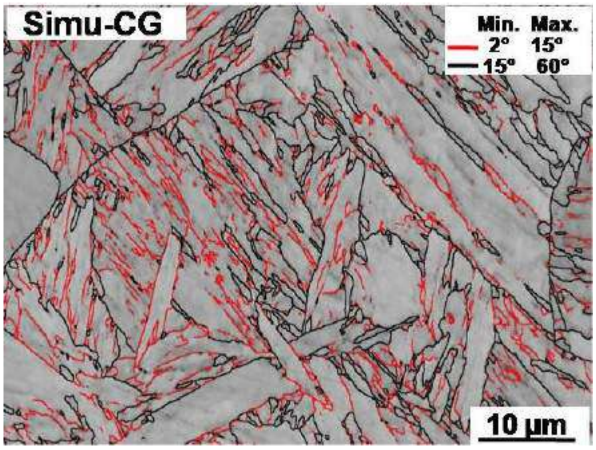

(d)

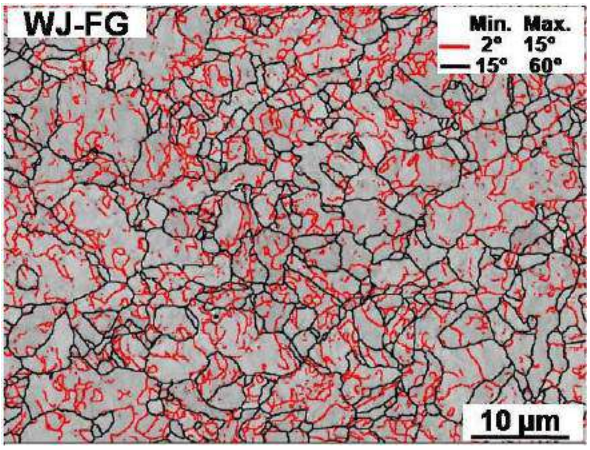
WJ-FG
Min. Max.
2° 15°
15° 60°
10 μm

(e)

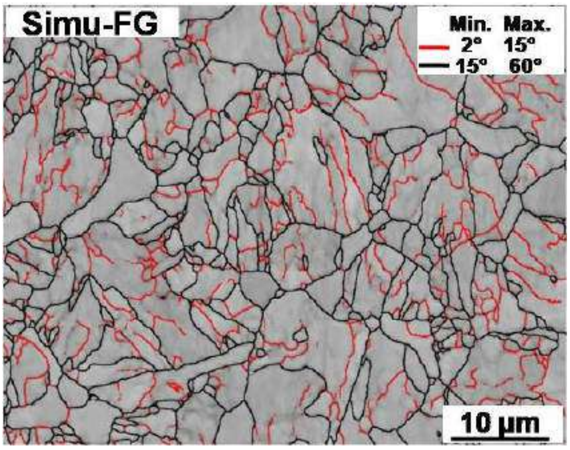
Simu-FG
Min. Max.
2° 15°
15° 60°
10 μm

(f)

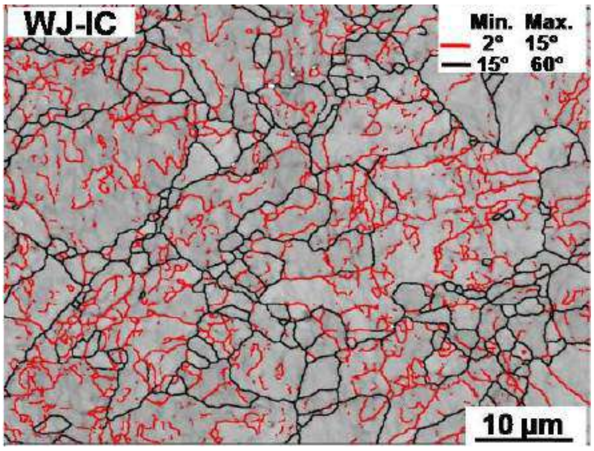
WJ-IC
Min. Max.
2° 15°
15° 60°
10 μm

(g)

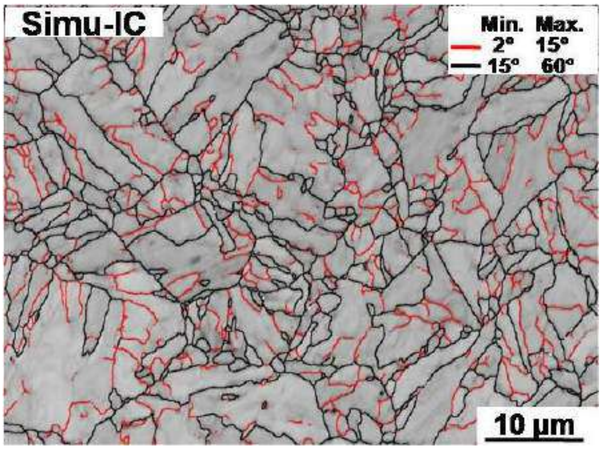
Simu-IC
Min. Max.
2° 15°
15° 60°
10 μm

(h)

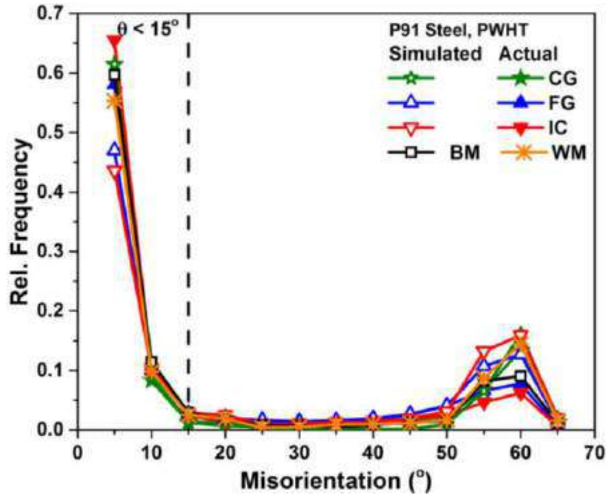

(i)

Fig. 4.8 Grain boundary (a-h) misorientation maps and (i) distribution plots of base metal, weld metal, actual and simulated HAZ microstructures of P91 weld joint after PWHT.

Table 4.4 Grain boundary analyses in the base metal, weld metal, simulated and actual CGHAZ, FGHAZ and ICHAZ of P91 weld joint after PWHT.

Grain boundaries fraction (%)	Simulated				Actual weld joint			
	BM	CG HAZ	FG HAZ	IC HAZ	WM	CG HAZ	FG HAZ	IC HAZ
LAGB	75.2	74.1	61.2	58.6	69.2	72.3	72.1	78.9
HAGB	24.8	25.9	39.8	41.4	30.8	27.7	27.9	21.1
Ratio (LAGB/ HAGB)	3.03	2.86	1.54	1.42	2.25	2.61	2.58	3.74

Comparisons of LAGBs and HAGBs in various microstructural conditions of P91 steel are given in Table 4.4. Since LAGBs comprise nearly 75% of the total grain boundaries, the same has been considered throughout the thesis to make a comparative microstructural assessment of both simulated and actual weld joint. Figure 4.9 depicts the total LAGB contribution in various microstructural conditions. Thus, LAGB contributions are 74%, 61%, 57% (simulated) and 72%, 72% and 79% (actual) for CG, FG and IC respectively. The

LAGB distributions for base metal and weld metal are 75% and 69% respectively. The LAGBs distributions in the CGHAZ microstructures of simulated and actual are not much different, whereas there is large difference between the FGHAZs of simulated and actual weld joint. Same is true for the simulated and actual ICHAZs. This may be explained as follows: exposure to elevated temperatures ensures complete transformation to austenite and subsequent transformation to martensite upon cooling for the CGHAZ. The ICHAZ, on the other hand, is associated with partial phase transformation. In FGHAZ also, though exposure to temperature above AC_3 ensures austenite formation, the temperature is still not high enough to complete dissolution of precipitates and thereby formation of finer grains. The shorter thermal exposure duration during welding results in greater LAGBs contribution in the ICHAZ and FGHAZ microstructures compared to the LAGBs in the corresponding simulated microstructures of isothermal heating. The larger substructure sizes for all the simulated microstructures compared to the corresponding zones of actual weld joint are also a result of the difference in the rate of heat exposures.

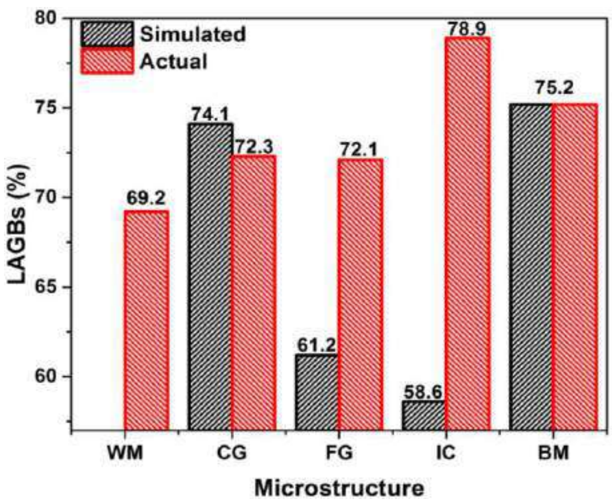

Fig. 4.9 Comparison of LAGBs distributions in simulated and actual weld joint microstructures of P91 steel.

Kernel average misorientation (KAM) is calculated as the misorientations between the center point of the kernel and all surrounding points in the kernel and averaged that gives the local misorientation value of the center point except those misorientation angle is > 2°. The KAM can be used as good approximation for dislocation density measurements. The KAM maps of simulated and actual microstructural zones of P91 weld joint are illustrated in Fig. 4.10(a)-(h). The KAM maps show an inhomogeneous strain distribution within the microstructures with some packets and blocks depicting larger strains as compared to the neighboring blocks. Quantification of KAM distribution for all microstructures was done and results are depicted in Fig. 4.10(i). It is seen from the figure that the actual and simulated CGHAZs exhibit same KAM value of 0.35°, whereas the FGHAZ and ICHAZ of simulated and actual weld joint and base metal and weld metal show the same KAM value of 0.25°. Larger strains are heterogeneously distributed within the grains of CGHAZs (Fig. 4.10(c) and (d)). The higher exposure temperature (>>AC_3) during simulation or welding caused solid solution hardening of matrix leading to the inhomogeneous strain distribution in CGHAZ. There is a significant difference between the tendencies of strain distributions of simulated and actual FGHAZ and ICHAZ. The higher frequency peak at lower KAM value of simulated FGHAZ may be due to the higher substructural recovery due to longer thermal exposure during simulation. The comparatively higher strain distribution in the actual FGHAZ is due to insufficient austenitizing temperature (1223 K)-time combination. The higher strain distribution in the vicinity of newly formed PAG is due to the partial martensitic transformation in ICHAZ (Fig. 4.10(h)) [71]. However, the over-tempered ferrites in the ICHAZ barely have these martensite blocks due to further tempering effect from the welding/heating thermal cycle. The higher local strain distributions in the comparatively soft microstructures of actual FGHAZ and ICHAZ (Fig. 4.10(e) and (g)) are due to the deformation constraint (existing residual stress even after PWHT) by the neighboring harder regions such as weld metal, CGHAZ and base metal during welding [267]. The homogenous microstructures (simulated FGHAZ and ICHAZ) produced due to simulation heat treatments do not have such mechanical strain heterogeneity.

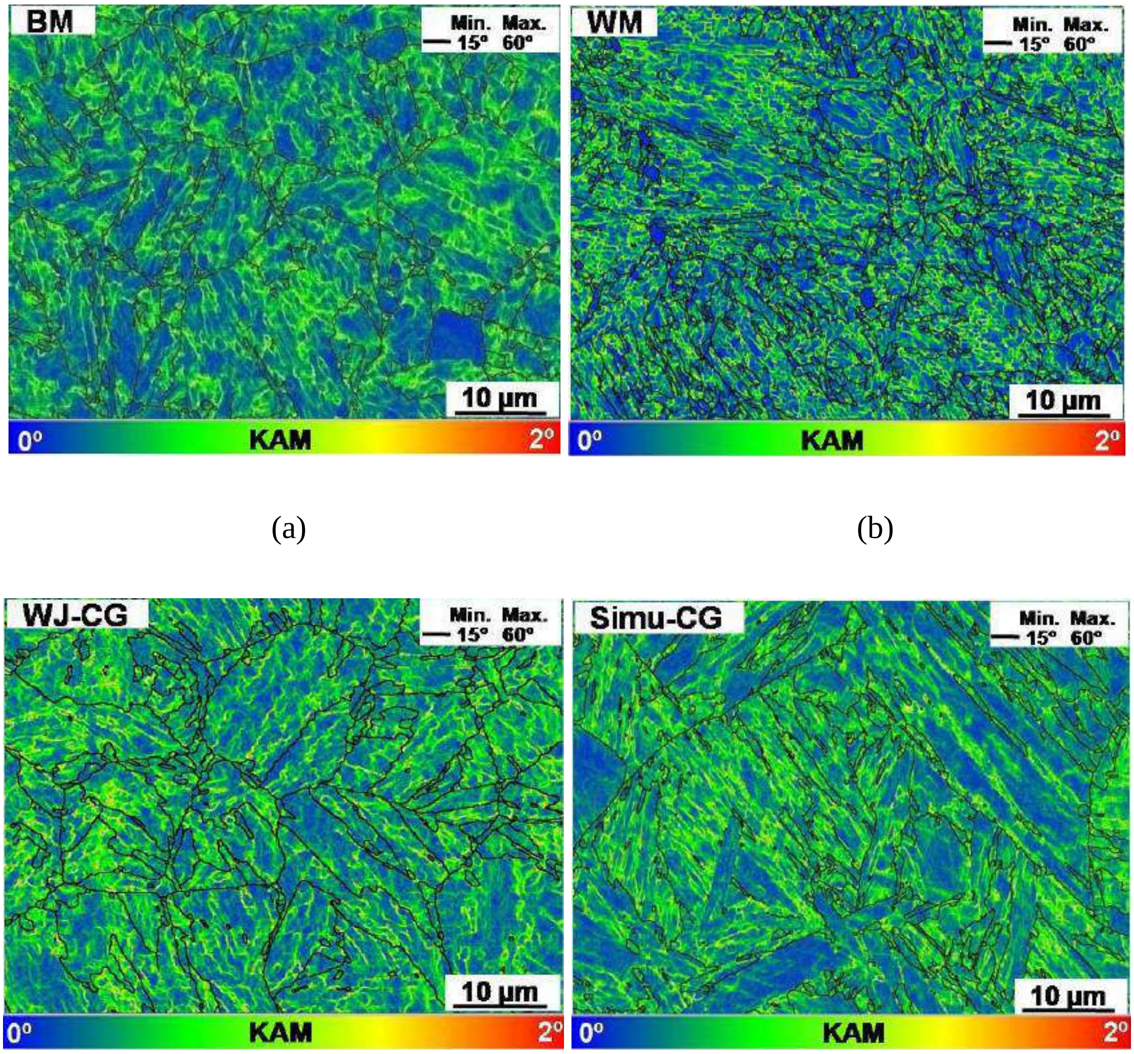

(a) (b)

(c) (d)

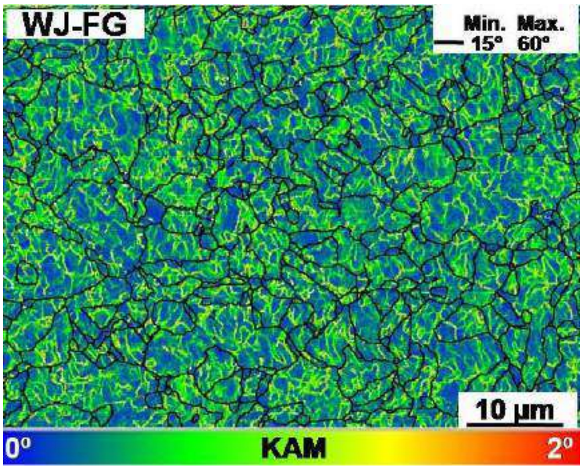
WJ-FG
Min. Max.
15° 60°
10 µm
0°
KAM
2°

(e)

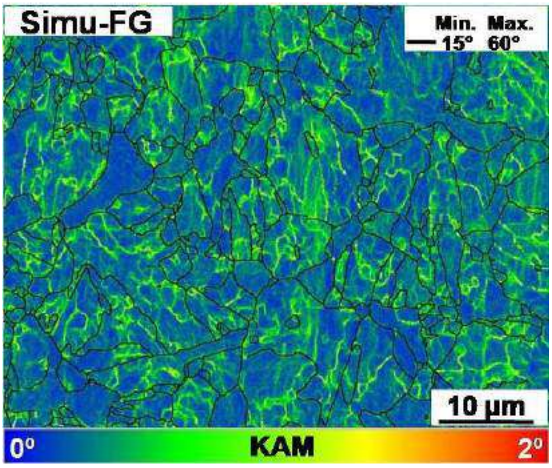
Simu-FG
Min. Max.
15° 60°
10 µm
0°
KAM
2°

(f)

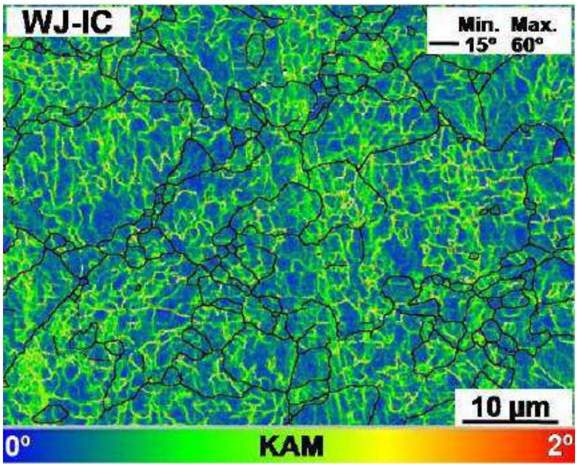
WJ-IC
Min. Max.
15° 60°
10 µm
0°
KAM
2°

(g)

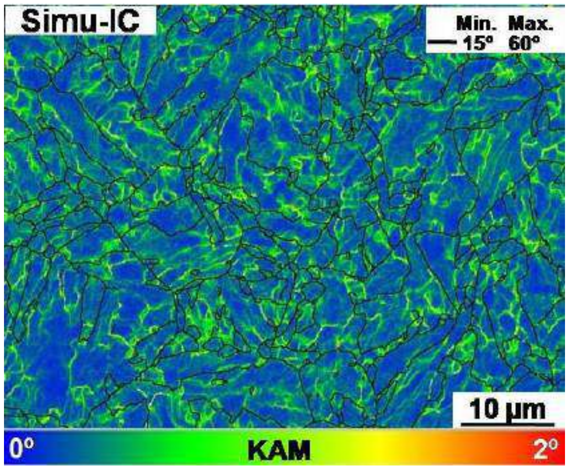
Simu-IC
Min. Max.
15° 60°
10 µm
0°
KAM
2°

(h)

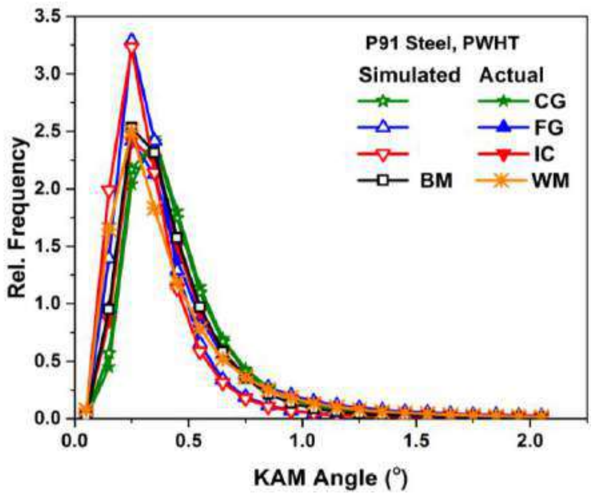

(i)

Fig. 4.10 Kernel average misorientation (a-h) maps and (i) distribution plots of base metal, weld metal, actual and simulated HAZ microstructures of P91 weld joint after PWHT.

The average misorientation between every adjacent pair of the measured pixels within each grain, which evaluates the local strain of the individual grain is known as the grain average misorientation (GAM) [268–270]. The angle of internal average misorientaion within the grain and average misorientation between sub-grains is measured to differentiate the grains. In this study, the local strain energy difference in the grains interiors are classified into recrystallized, substructured and deformed grains by GAM evaluation with a threshold of 1°.

The Fig. 4.11(a)-(h) show the degree of microstructural changes that would take place if the base metal is subjected to various heat treatments or welding. The GAM results are given in Table 4.5. The GAM maps indicate that all the majority of the microstructural regions are featured as substructure (with a relative area fraction of nearly 90% or more) which establishes that significant amount of recovery due to PWHT has occurred. The P91 steel base metal in the normalized and tempered (3 h) condition exhibits large area of substructured grains and a small fraction of recrystallized grains as well. The 3 h PWHT attributes to the significant substructural recovery. A relatively large distribution of fine recrystallized structures along the prior austenite grain boundaries in the fusion zone (Fig. 4.11(b)) is attributed to the formation of new austenite, which forms due to exposure to high temperature. There is also a similarity in the simulated ICHAZ and FGHAZ that show large fractions of recrystallized structures, which are attributed to the formation of new austenite grains. The difference between the fractions of the recrystallized grains of actual and simulated FGHAZ and ICHAZ are due to the difference in the thermal exposure time.

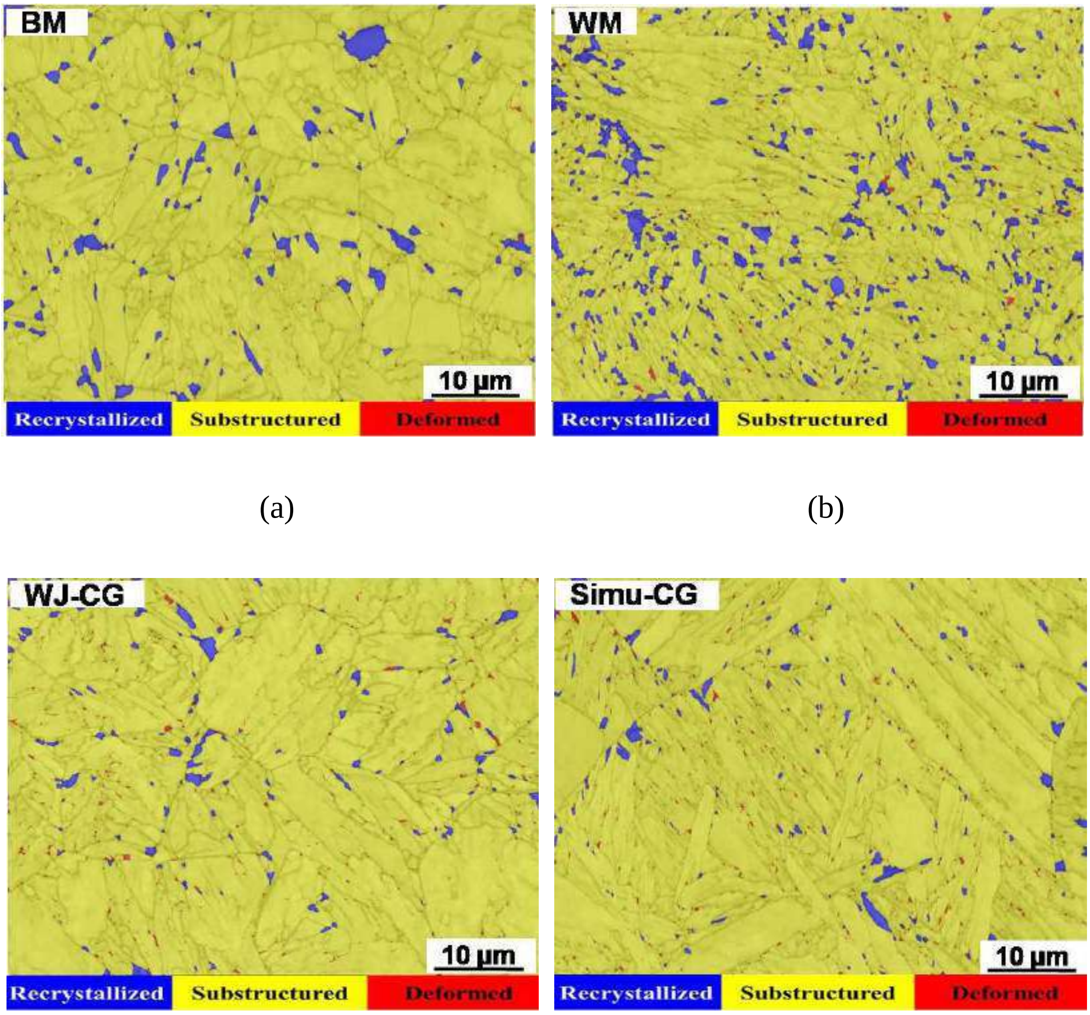

(a) (b)

(c) (d)

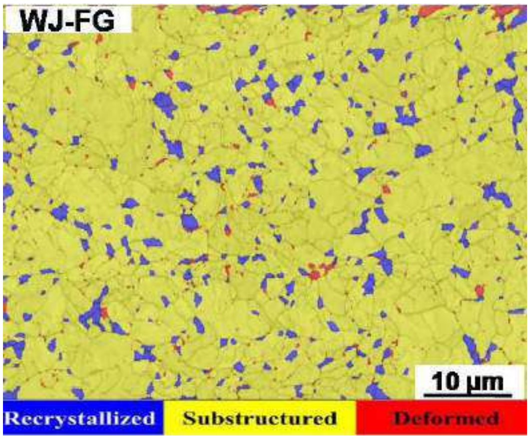
WJ-FG
10 µm
Recrystallized
Substructured
Deformed

(e)

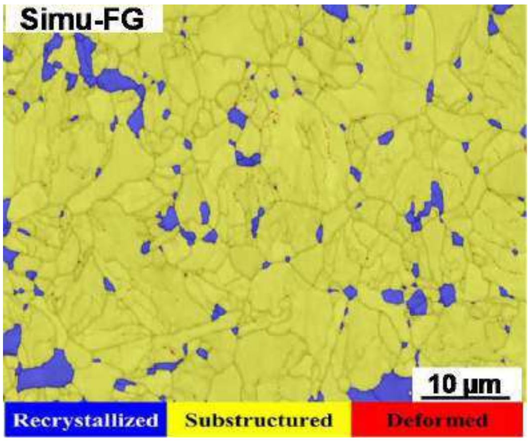
Simu-FG
10 µm
Recrystallized
Substructured
Deformed

(f)

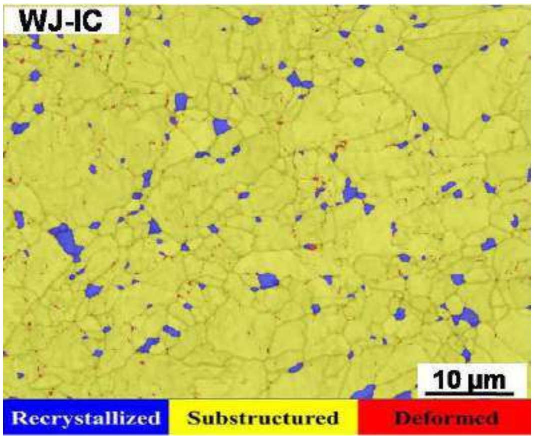
WJ-IC
10 µm
Recrystallized
Substructured
Deformed

(g)

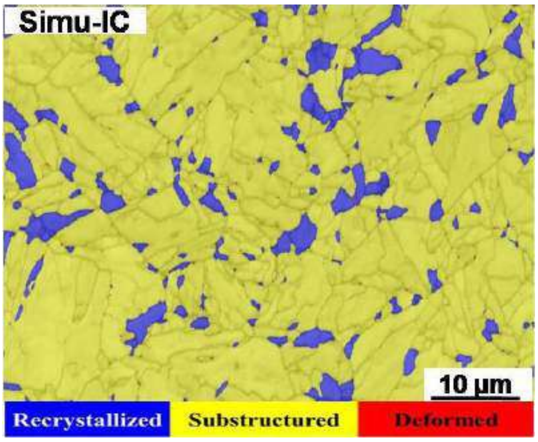
Simu-IC
10 µm
Recrystallized
Substructured
Deformed

(h)

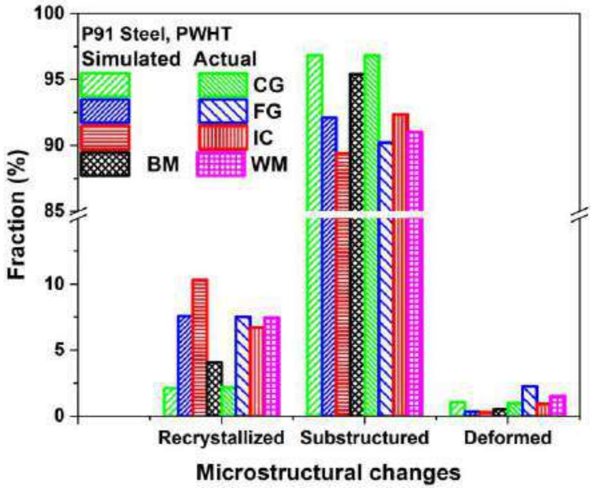

(i)

Fig. 4.11 Grain average misorientation (a-h) maps and (i) distribution plots of base metal, weld metal, actual and simulated HAZ microstructures of P91 weld joint after PWHT.

Grain average misorientation distribution is depicted in Fig. 4.11(i). In the FGHAZs the fraction of the substructured or partial-recrystallized grains is ~90% with nearly 7.5% recrystallized grains. Wang et al. [249] have reported similar observation on the fine grained heat-affected zone of P91 steel. The recrystallized fractions in the simulated and actual weld joint ICHAZs are about 10% and 6.7% respectively. The higher recrystallization in the simulated ICHAZ is due to the formation larger number of new PAGs, which are the potential sites for recrystallization.

Table 4.5 GAM analyses; base metal, weld metal and simulated and actual CGHAZ, FGHAZ, ICHAZ of P91 weld joint after PWHT.

Microstructural Changes (%)	Simulated				Actual weld joint			
	BM	CGHAZ	FGHAZ	ICHAZ	WM	CGHAZ	FGHAZ	ICHAZ
Recrystallized	4.09	2.11	7.57	10.31	7.46	2.19	7.52	6.73
Substructured	95.4	96.8	92.1	89.4	91.0	96.8	90.2	92.3
Deformed	0.51	1.07	0.33	0.29	1.54	1.01	2.28	0.97

4.4 CONCLUSIONS

1 A comparative study between simulated and actual weld joint made using prior austenite grain size and hardness determinations and differential scanning calorimetry method established that the temperatures of 1138 K, 1208 K and 1473 K were adequate to generate respective microstructures of ICHAZ, FGHAZ and CGHAZ of P91 steel weld joint.

2 The grain size, precipitate size and hardness analyses validate the simulations of microstructures of HAZ of P91 weld joint through heat treatments. An inverse relation between the precipitate sizes and the PAG sizes for the three principal microstructures of HAZ under both simulated and actual weld joint conditions exist.

3 Grain boundary partitioning based on misorientation established that LAGBs are the main contributors (nearly 75%) to the complex microstructure of P91 steel. Heat treatment in the form of furnace heating or actual welding greatly changes the LAGBs distribution. The LAGBs contributions are 74%, 61%, 57% (simulated) and 72%, 72% and 79% (actual) for CGHAZ, FGHAZ and ICHAZ respectively. The LAGBs for base metal and weld metal are 75% and 69% respectively. The higher amount of LAGBs

distribution in the HAZ microstructures of actual weld joint compared to the simulated HAZ is due to large temperature gradient across the weld joint HAZ during welding.

4 Partitioning of microstructure also established that blocks and packets with HAGBs character remained more stable as compared to the martensite laths with LAGBs character that underwent recovery.

5 Kernel average misorienation and GAM distributions analyses revealed that inhomegeneous strain distribution within the substructures are existed for all the microstructures of P91 steel weld joint. The higher local strain distributions in the comparatively soft FGHAZ and ICHAZ of actual weld joint are due to the deformation constraint (existing residual stress even after PWHT) by the neighboring harder regions such as weld metal, CGHAZ and base metal. The homogenous microstructures (simulated FGHAZ and ICHAZ) produced due to simulation heat treatments do not have such mechanical strain heterogeneity. The GAM analyses indicate that the majority of the microstructural changes are featured as substructure (with a relative area fraction of nearly 90% or more), which establishes that significant amount of recovery due to PWHT has occurred. The higher recrystallization in the simulated ICHAZ is due to the formation larger number of new PAGs, which are the potential sites for recrystallization.

CHAPTER 5 TENSILE PROPERTIES EVALUATION

5.1 INTRODUCTION

Welding of the temperature sensitive P91 steel significantly changes its microstructure and subsequently its mechanical properties such as hardness and monotonic tensile properties. The extent of changes in the hardness and tensile properties of the steel depends upon the temperature it is exposed to during the weld thermal cycles or simulation through heat treatment. The HAZ with the narrow band size is a complex variation of microstructure with varied tensile properties. The study includes the assessment of tensile properties such as yield strength, ultimate tensile strength and ductility and hardness changes across the weld due to monotonic tensile deformation. The Chapter concludes with establishing an empirical relationship for the deformation/damage contribution from each constituent region towards the overall tensile behaviour of actual weld joint.

5.2 MONOTONIC TENSILE STRESS−STRAIN BEHAVIOR

The engineering tensile stress-strain curves of various microstructures of weld metal, simulated CGHAZ, FGHAZ and ICHAZ and base metal and the actual weld joint are depicted in Fig. 5.1. The uniaxial macroscopic tensile stress-strain responses of the different microstructural regions consist of the onset of yielding subsequently, a short deviation from linearity with a steep work hardening response until the ultimate tensile strength is reached, then the slopes of all stress-strain curves fall till the final fracture with respect to the deformation accommodating capability of each zone. All the microstructurally different regions indifferently exhibit continuous yielding behavior and high yield strength to ultimate tensile strength ratio, which are typical characteristics of bcc metals consist of not so close-packed planes [133]. Through the curves, it is clear that the tensile stress-strain responses of the constituent regions of P91 weld joint are not the same. It is interesting to note that all the stress-strain curves of microstructures converge around 0.15 total strain. Below 0.15 total strain, the weld metal shows the upper bound, the FGHAZ and ICHAZ together forms the lower bound and the CGHAZ, base metal and weld joint curves are sandwiched between the tensile curves of those upper and lower bounds microstructures as shown in Fig. 5.1.

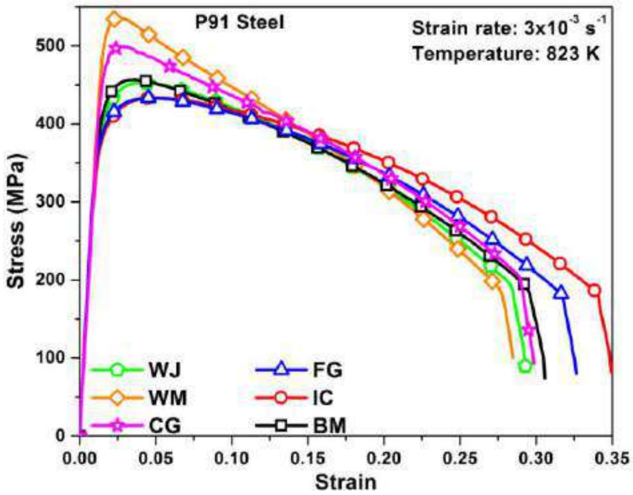

Fig. 5.1 Monotonic tensile engineering stress-strain curves of base metal and simulated ICHAZ, FGHAZ and CGHAZ and weld metal and actual P91 steel weld joint at 823 K.

The variation of 0.2% offset yield strength, UTS, total elongation and reduction in area for actual weld joint, weld metal, simulated CGHAZ, FGHAZ and ICHAZ and base metal of P91 steel is depicted in Fig. 5.2. The uniform elongation (2-5%) is substantially lower than the total elongation (~30%) due to the inherent lower work hardening capability of P91 steel, which is generic to bcc materials. But the yield strengths between the constituent regions are in the ranges of 350 MPa−500 MPa. Considering the minor differences in uniform/total elongation and a large variation in yield strength with nearly 150 MPa, it is indisputable that the tensile behavior of actual weld joint is dictated by the strength character rather than ductility. Due to higher enunciated changes in yield strength than UTS, and more/less similar uniform elongation for all microstructures, yield strength variation will be taken for the current discussion.

The order of yield strengths of various regions of weld joint is as follows: weld metal>CGHAZ>base metal>FGHAZ>ICHAZ. The reason for a large decrease in yield strength from CGHAZ to FGHAZ and ICHAZ is the exposure to lower temperatures that causes a decrease in the extent of dissolution of the MX type precipitates that is responsible for solid solution strengthening of the matrix. The yield strength of CGHAZ is greater than base metal as well. Exposure to a temperature, i.e., well above AC_3 results in a greater extent of dissolution of primary carbides, thereby implementing solid solution strengthening in CGHAZ. Thus, even though the CGHAZ has much larger PAG size than the base metal, greater solid solution strengthening results in higher yield strength of CGHAZ as compared to base metal. Also, a trivial difference between yield strengths of ICHAZ and FGHAZ as compared to the CGHAZ again confirms that the dual distribution of grain size (in ICHAZ) has not made the same effect that solid solution strengthening has made on the matrix of P91 steel. The hardness values and tensile properties of base metal, simulated microstructures and weld metal are evaluated and given in Table 5.1. The tensile properties of actual weld joint are also given in the Table 5.1 and the Fig.5.1 and 5.2 for comparison.

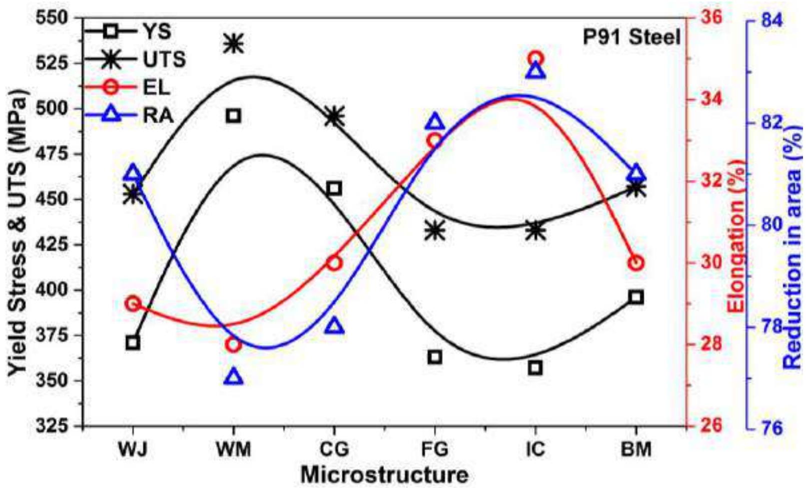

Fig. 5.2 Tensile properties (yield strength and UTS and ductility in terms of elongation and reduction in area) of actual weld joint, weld metal, simulated CGHAZ, FGHAZ and ICHAZ and base metal of P91 steel tested at the strain rate of 3×10^{-3} s^{-1} and 823 K.

5.3 YOUNG'S MODULUS (E) VARIATION

The values of the Young's modulus (E) of weld metal and simulated microstructures of HAZ and base metal are given in Table 5.1 and are graphically represented in Fig. 5.3. The prior heat treatment affects the modulus of elasticity of steel [133]. The modulus (E) values were obtained from the initial slope of first cycle hysteresis loops of various microstructures of HAZs of P91 steel subjected to total axial strain-control fatigue cycling. The modulus (E) value of each microstructure is an average of the values obtained at the strain amplitudes of ±0.25, ±0.4, ±0.6 and ±1.0% and at 823 K. Applying strain-controlled tensile deformation at a strain rate higher than 1×10^{-3} s^{-1} in a servo-hydraulic equipment gives more accurate elastic modulus value due to the removal of anelastic deformation, which generally occurs due to the elastic bending of lath boundaries in the tempered martensitic steel at slower strain rate and high temperature [271]. In this study, increase in Young's modulus (E) values are found with the increases in simulation temperatures. Among the microstructures of weld joint, weld metal region shows the highest Young's modulus, whereas among the HAZs, a maximum modulus (E) value is found for CGHAZ, and the least value of modulus (E) is observed for

ICHAZ. Soaking at very high temperature, i.e., well above AC_3 to generate the microstructure of CGHAZ gives rise to the complete dissolution of carbide precipitates in matrix. Elastic modulus increases linearly with an increase in solute in matrix [271].

Mostly precipitation due to aging at higher temperature plays a major role on the strengthening of austenitic alloy. Increase in internal friction by means of continuous locking between dense dislocations generated due to age hardening at higher temperature increases the elastic modulus (E) of Co-Ni based alloy [272]. Montecinos et al. [273] reported that the aging time influences the modulus of elasticity by means of precipitation process in the Cu-2Be alloy. The variation of the Young's modulus is similar to the changes observed in the yield strength (Fig. 5.2) and hardness (Fig. 4.6) values of the various microstructures reproduced through heat treatments at various simulation temperatures. The decrease in Young's modulus at the ICHAZ could be attributed to the attaining of inhomogeneous solid solution, i.e., partial austenitization due to rapid heating at inter-critical region and precipitates coarsening that developed during subsequent tempering at 1033 K for 3 h (simulated PWHT). The modulus (E) values of FGHAZ and ICHAZ given in Table 5.1 are in good agreement with the reported modulus values for simulated HAZs of P91 steel [10]. Dieter [133] has stated that the heat treatment and microstructures also change the E values.

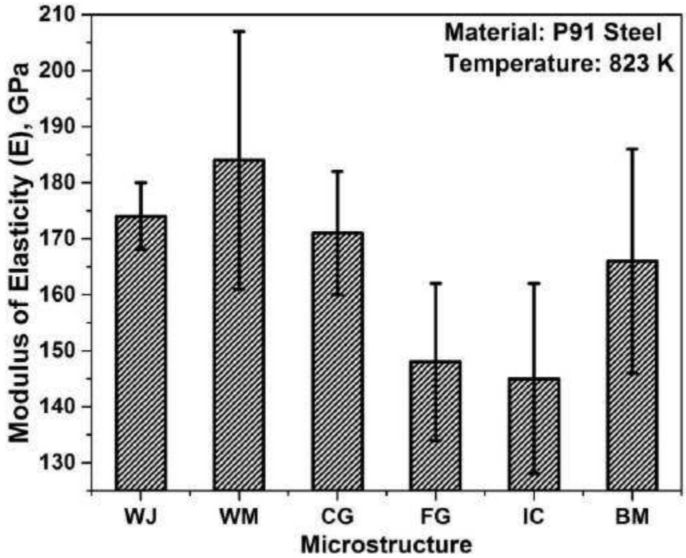

Fig. 5.3 Microstructure dependent Young's modulus of P91 steel and its weld joint at 823 K.

Table 5.1 Hardness values and tensile properties of individual microstructures of P91 steel weld joint. Actual weld joint tensile parameters are given for comparison.

Micro-structure	Uniform Elongation (%)	Total Elongation (%)	Reduction in Area (%)	Yield Strength (MPa)	UTS (MPa)	Hardness Hv0.1	E, GPa
Weld joint	4.2	29	81	371	453	--	175±5
Weld metal	2.5	28	77	496	536	244±9	185±20
CGHAZ (Simulated)	2.7	30	78	456	496	239±9	170±10
FGHAZ (Simulated)	4.4	33	82	363	433	199±3	150±15
ICHAZ (Simulated)	5	35	83	357	433	189±7	145±15
Base metal	3.6	30	81	396	457	207±7	165±20

5.4 FAILURE OF THE P91 STEEL WELD JOINT DUE TO MONOTONIC TENSILE DEFORMATION

The collaged optical micrographs of tensile failed P91 weld joint in the longitudinal/loading directions are depicted in Fig. 5.4. A few representative magnified images taken on each constituent region of the actual weld joint are also superimposed and their locations are indicated in the collaged micrographs. As discussed earlier, the ICHAZs of both simulated and actual weld joint exhibited the lowest hardness and the simulated ICHAZ also exhibited the lowest yield strength. However, under tensile deformation, the actual P91 weld joint failed in the base metal region that has higher hardness and yield strength than ICHAZ and FGHAZ. Base metal failures in the weld joints of DP600 steel and P91 and P92 steels have also been reported earlier under monotonic tensile deformation and higher creep stress conditions [12,274,275].

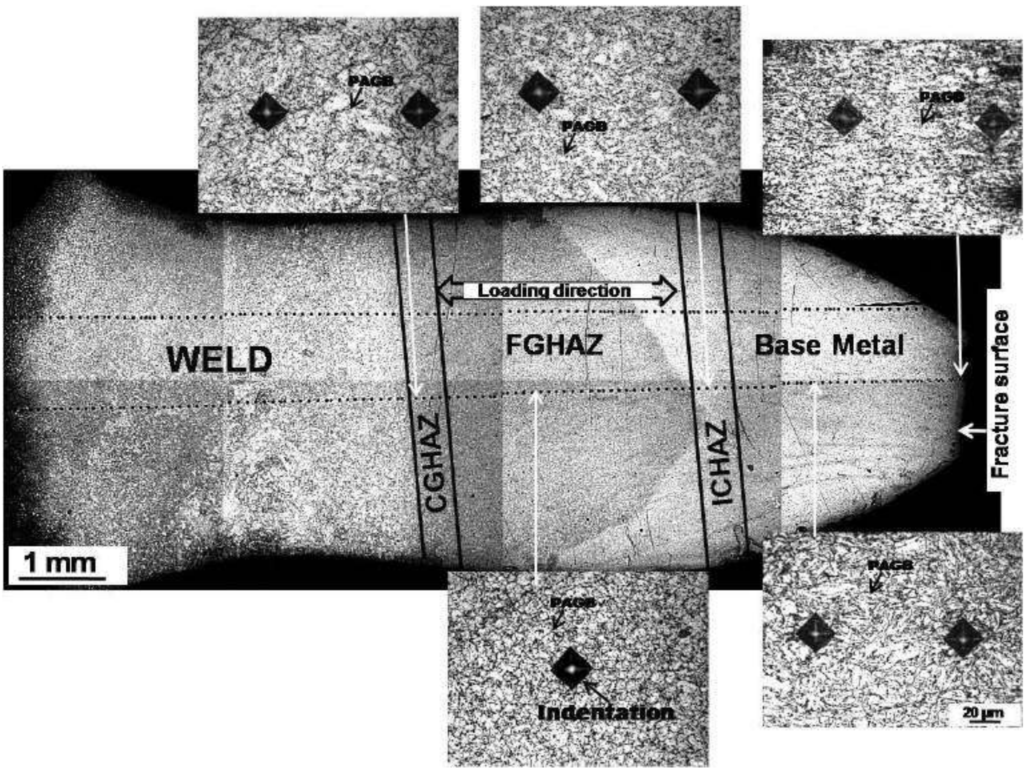

Fig. 5.4 Failed sample of P91 steel weld joint under monotonic tensile deformation at 823 K. Representatives magnified images of respective regions are overlapped.

5.5 FRACTOGRAPHY

Representative fractographs of the tensile tested specimens of actual weld joint, weld metal and simulated CGHAZ, FGHAZ and ICHAZ and the base metal of P91 steel are illustrated in Fig. 5.5(a)-(f). In general, the fracture surface morphologies of various microstructural regions indicate similar fracture behavior characteristics under monotonic tensile deformation. The presence of dimples on both actual weld joint and base metal represents typical ductile fracture. The CGHAZ fracture surface exhibits a mixed mode with a brittle dominating feature such as flat facet and some dimple appearing characteristic. Higher area fractions of the honey-comb like fracture surfaces are observed for both soft ICHAZ and FGHAZ.

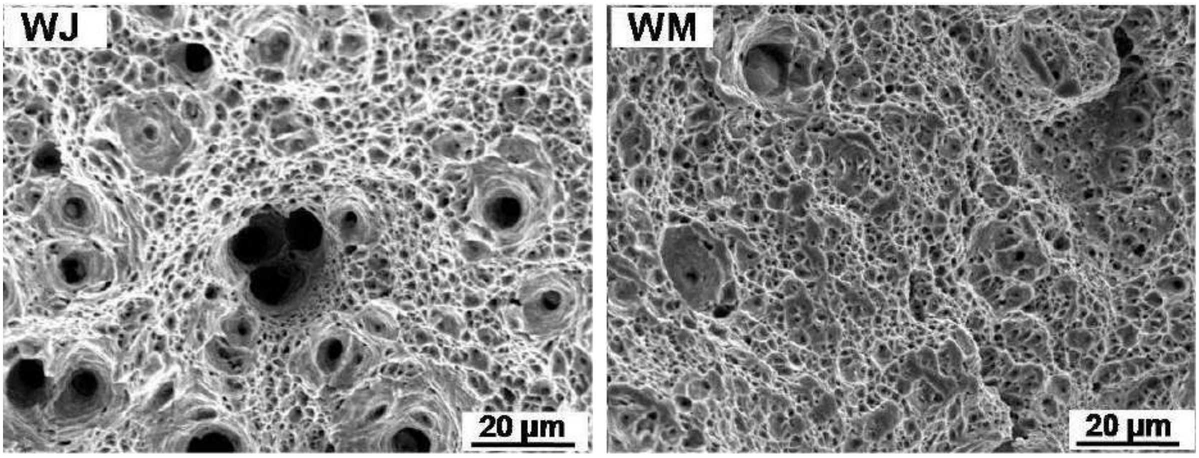

(a) (b)

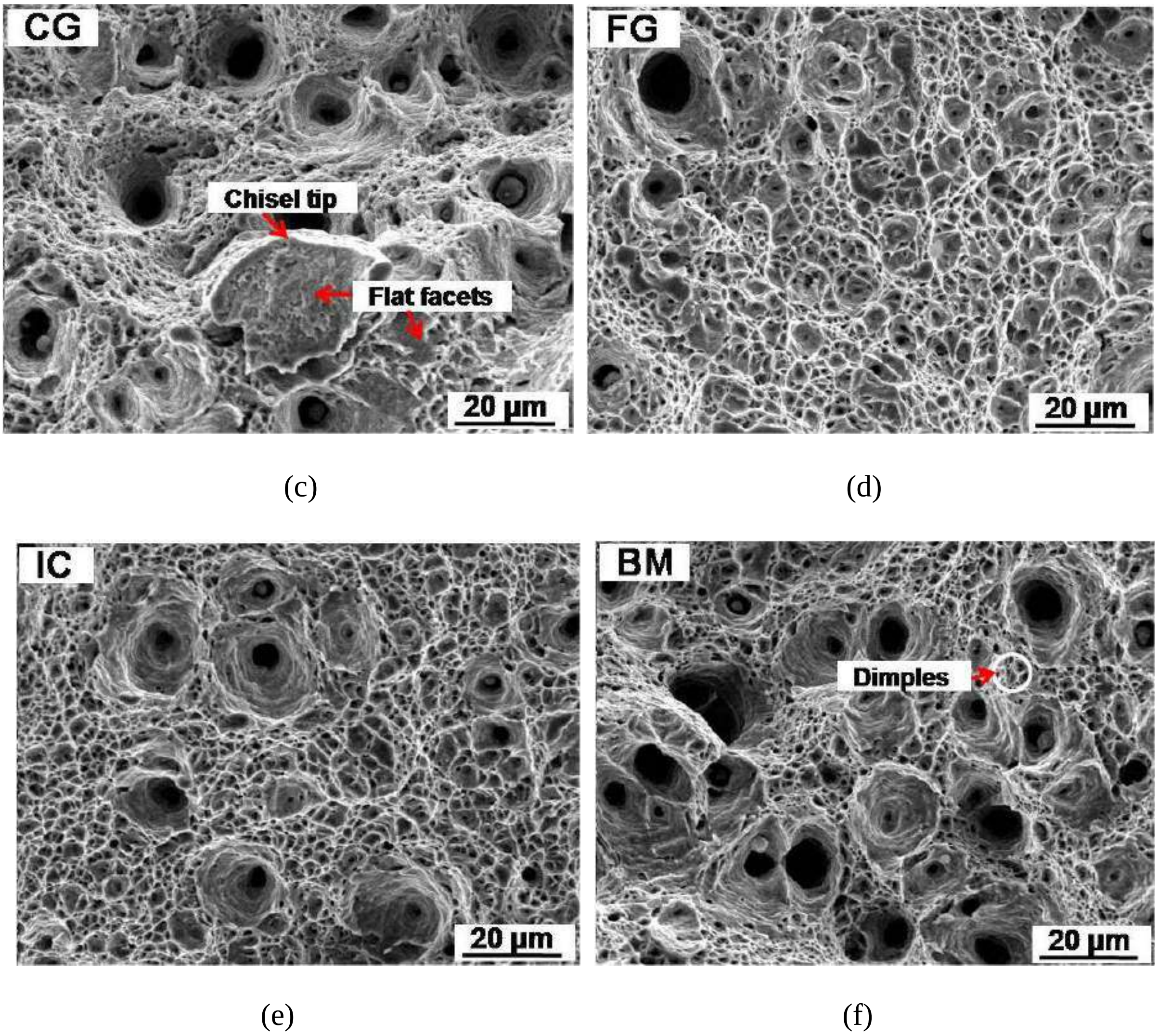

Fig. 5.5 Fractographs of the tensile tested specimens; (a) actual weld joint, (b) weld metal, simulated (c) CGHAZ, (d) FGHAZ and (e) ICHAZ and (f) base metal.

5.6 HARDNESS AFTER TENSILE DEFORMATION

The hardness distributions across the P91 steel weld joint after PWHT and tensile deformation are compared in Fig. 5.6. Similar trend is apparent in the most parts of the hardness profiles of the weld joint before (PWHT) and after tensile deformation. The comparison of hardness plots for the two conditions depicts the following: initially, sharp downward shift from weld metal to FGHAZ, increase in the hardness profile at the ICHAZ followed by sharp decrease of hardness of base metal. Further there is a sharp increase in the hardness near the fracture surface of tensile tested sample as compared to the PWHT untested sample.

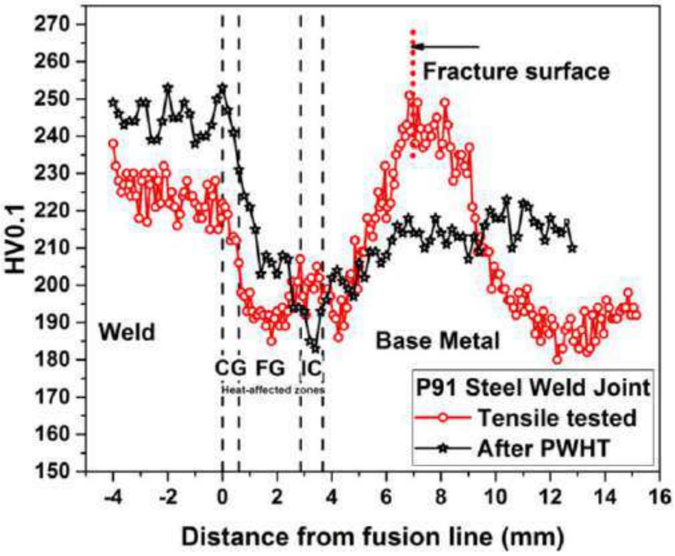

Fig. 5.6 Comparison of propensity of hardness profiles of P91 actual weld joint after PWHT and tensile test.

The softening behavior of the harder regions such as weld metal, CGHAZ and FGHAZ due to recovery in the form of dislocation annihilation during high temperature deformation could be the reason for the downward shift of hardness profile. The work hardening during tensile deformation has been accredited to the increase in the hardness of the initially soft ICHAZ. The base metal near the fracture region also shows severe hardening and strain localization. This implies that the shift of strain localization from soft ICHAZ/FGHAZ to the neighboring base metal is due to the strain hardening or work hardening of soft ICHAZ and the constraint/incompatibility of plastic strain distribution within the complex weld joint comprising of soft zones with the neighboring hard zones [12]. The larger volume (half of the gage portion volume of the specimen) fraction of the base metal in the actual weld joint is also the reason for the strain accommodation and subsequent strain localization. The stain/work hardening behavior of the ICHAZ during tensile deformation is due to the interactions between the unpinned geometrically necessary dislocations (GNDs) and the immobile dislocations in the ferrite interiors [11].

5.6.1 EBSD analysis on the microstructures of constituent regions of P91 steel weld joint

Electron back scattered diffraction analysis was carried out to identify the preferred deformation orientation planes and estimate the strain distribution across the various microstructures of the P91 weld joint subject to monotonic tensile deformation at 823 K. The inverse pole figure (IPF) maps for the various microstructural regions such as FGHAZ, ICHAZ and base metal of actual weld joint are depicted in Fig. 5.7(a)-(d). All the major groups of orientation variant pairs are observed in all microstrcutural regions. Figure 5.7(c) illustrates that the <100> plane deforms extensively than the other crystallographic planes.

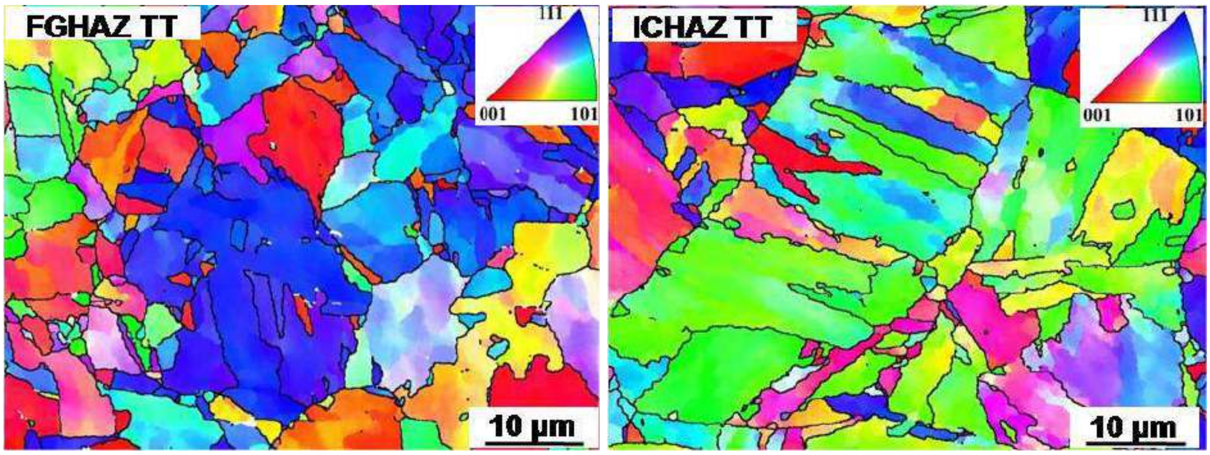

(a) (b)

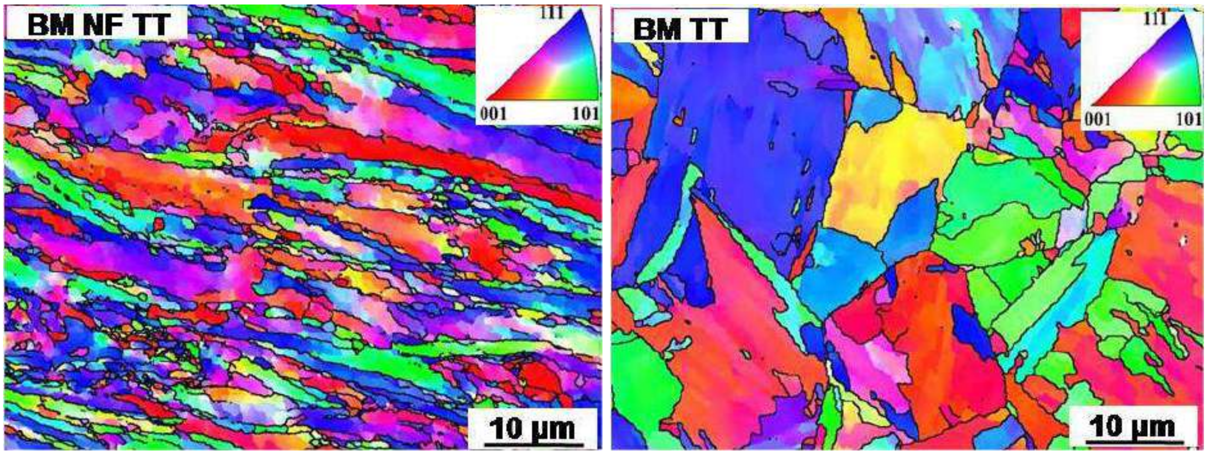

(c) (d)

Fig. 5.7 Inverse pole figure (IPF) maps; (a) FGHAZ, (b) ICHAZ, (c) near fracture and (d) away from fracture of base metal of actual weld joint of P91 steel tensile deformed at the strain rate of $3{\times}10^{-3}$ s^{-1} and 823 K.

Kernel average misorienation maps were extracted for the measure of localized strain accumulation generated by the geometrically necessary dislocations (GNDs). Kernel average misorientation is the arithmetic mean of the scalar misorientations between groups of pixels, or kernels, that measures the local strain levels of the grains [268]. Higher values of angle of misorientation indicate the occurrence of a higher density of GNDs. Therefore, to identify the localized strain gradients within the microstructure the KAM map can be used.

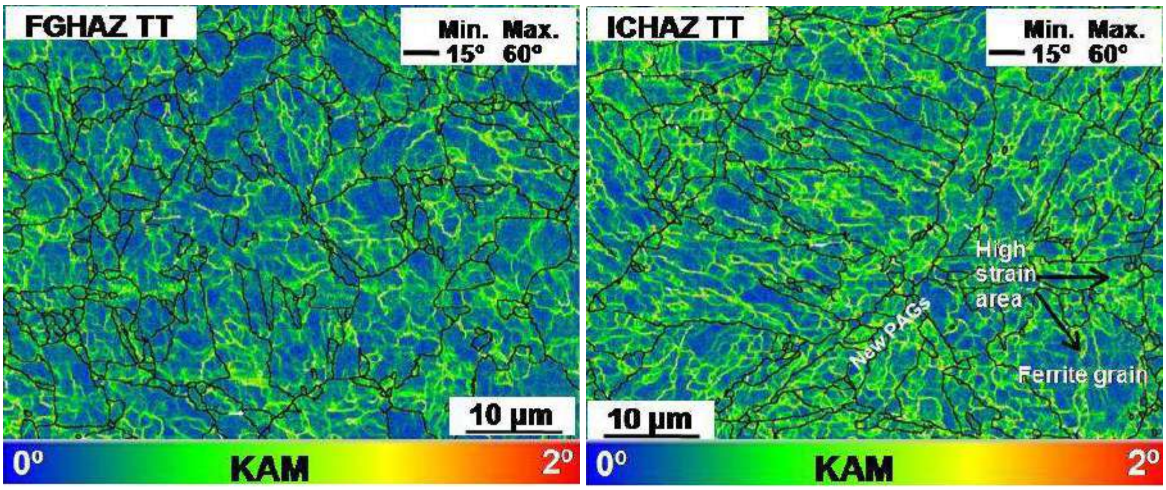

(a) (b)

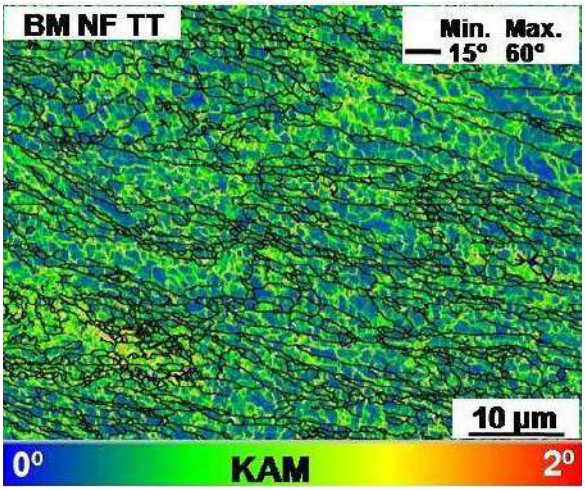

(c)

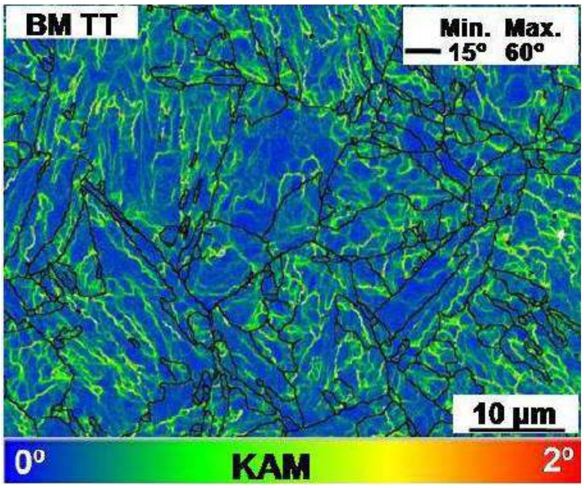

(d)

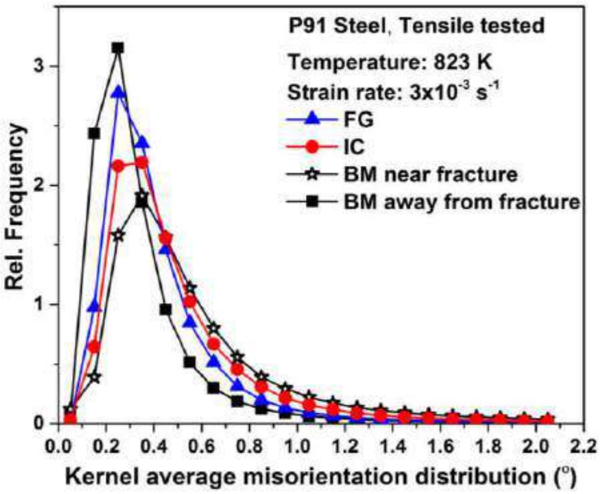

(e)

Fig. 5.8 Local misorientation (KAM) along with superimposed grain boundary maps; (a) FGHAZ, (b) ICHAZ and base metal (c) near fracture and (d) away from fracture; (e) local misorientation distributions plots of actual P91 steel weld joint after tensile deformation at 823 K. Scan step size: 0.05 µm.

Figure 5.8 illustrates the local misorientation (KAM) distributions in the three different regions of the P91 steel weld joint. The lowest deformation is indicated by blue color corresponding to misorientation of 0°, whereas the highest deformation is marked by red color, which denotes a misorientation of 2°. The substantial higher value of KAM for the

FGHAZ has been credited to the higher number of PAGs (Fig. 5.8(a)) since the grain boundaries are the sites for higher deformation [12]. Although the higher strain distribution is seen among the newly transformed martensite/PAGs, most of the existing ferrite grain interiors consist of a considerable amount of strain distribution in ICHAZ (Fig. 5.8(b)). The higher strain distribution in the interior of ferrite grains could be due to the interactions between the GNDs and the immobile dislocations, causing strain/work hardening during tensile deformation [11]. The KAM map of the near-fracture base metal showed higher values of misorientation angles near the PAG boundaries, particularly near the sub-boundaries formed due to localized higher deformation (Fig. 5.8(c)). The unaffected base metal exhibited the lowest misorientation (Fig. 5.8(d)).

The variations of the KAM values from FGHAZ to fracture surface follow a similar trend of the hardness variation of tensile tested P91 steel weld joint. The KAM values for FGHAZ, ICHAZ, base metal and near fracture base metal are 0.25, 0.35, 0.25 and 0.35 respectively. The hardness comparison of both before and after tensile deformation indicated the strain/work hardening of initially soft ICHAZ and softening of the initially hard microstructural zones of weld metal and CGHAZ. Thus, both EBSD and hardness values confirm that the strain/work hardening of the soft ICHAZ due to tensile straining and incompatibility of strain distribution across the weld joint leads to the base metal failure.

5.7 DEFORMATION WEIGHTED/CONTRIBUTION FACTOR ANALYSIS UNDER TENSILE LOADING

In this section deformation contribution from each constituent region and their subsequent effect on the yield strength of the actual weld joint is derived and presented. The weighted/contribution factor (WF) of individual zone in the tensile deformation is defined by the following equation (5.1)

$$\mathbf{WF_{ind\ zone}} = \frac{\mathbf{YS_{wj}}}{\mathbf{YS_{ind\ zone}}} \qquad \text{----(5.1)}$$

where,

YS_{wj} — yield strength of actual weld joint

$YS_{ind\ zone}$ — yield strength of individual zone (weld metal, CGHAZ, FGHAZ, ICHAZ and base metal)

$WF_{ind\ zone}$ — weighted factor of individual zone

As mentioned earlier yield strength is sensitive to heat treatment or monotonic loading. In view of this, the tensile deformation is characterized in terms of yield strength as weighted factor. Further, the material deformation behavior becomes localized after the UTS is reached and also after yielding other factors such as work hardening and dynamic strain aging (DSA) etc. effects are in active. Therefore, to achieve the reliability of data and avoid non-uniformity in the deformation, the yield strength parameter is used in the empirical equation. An empirical relationship with the weighted factors (a, b, c, d and e) of each constituent region is given in Eq. 5.2

$$\mathbf{YS_{wj}} = \boldsymbol{a}\mathbf{YS_{bm}} + \boldsymbol{b}\mathbf{YS}_{\boldsymbol{ic}} + \boldsymbol{c}\mathbf{YS_{fg}} + \boldsymbol{d}\mathbf{YS_{cg}} + \boldsymbol{e}\mathbf{YS_{wm}} \qquad \text{----(5.2)}$$

where a, b, c, d and e denote the weighted factors of base metal, inter-critical, fine grain and coarse grain heat-affected zones and weld metal respectively. The computed weighted factor of each constituent region is substituted in Eq. 5.2 and is rewritten below as

$$\mathbf{YS_{wj}} = \mathbf{0.94YS_{bm}} - \mathbf{1.04YS_{ic}} - \mathbf{1.02YS_{fg}} + \mathbf{0.8YS_{cg}} + \mathbf{0.75YS_{wm}} \qquad \text{----(5.3)}$$

Using the Eq. 5.3 it was found that the predicted yield strength value (395 MPa) is equal to the experimental value (395 MPa) of actual weld joint. This shows that the yield strengths of the constituent regions may be used to estimate the yield strength of actual weld joint. For weld metal, the yield strength of tempered cast material can be used. The negative sign is given (Eq. 5.2) for both weighted factors corresponding to the ICHAZ and FGHAZ as their yield strengths are lower than the actual weld joint.

A variation in the weighted factors of all constituent regions is displayed in Fig. 5.9. A unity line is drawn for the actual weld joint. The weighted/contribution factors above the unity line signify the damaging/deformation role made by individual microstructural zone and the factors below the line indicate the strengthening contribution. The plot of deformation weighted/contribution factor clearly indicates that both ICHAZ and FGHAZ microstructures contribute to the deformation whereas the base metal, weld metal and CGHAZ contribute to the strengthening of the weld joint. The deformation weighted/contribution factors of ICHAZ and FGHAZ are very close to the overall deformation behavior line corresponding to the actual weld joint i.e., the unity line. All damage weighted/contribution factors of CGHAZ and weld metal are comparatively far away from this line. This means that the overall tensile behavior of the actual weld joint is supposed to be dictated by the ICHAZ and FGHAZ. The failure of the actual weld joint also should occur in the soft ICHAZ or to some extent at the FGHAZ. But in the real case, as discussed earlier, the actual weld joint failed in the base metal region. With the comparatively faster strain rate the resulting failure may be due to the following factors; i) variation in the volume fraction of individual region in complex P91 weld joint, ii) inadequate time for deformation only due to microstructural changes. In general, higher strength material exhibits weak resistance at a faster rate of deformation, while the slower rate of deformation deteriorates the tensile strength of materials with soft microstructures. Therefore, at the present test conditions, 3×10^{-3} s^{-1} being comparatively faster strain rate, the failure of the weld joint occurs at the base metal, which is relatively a higher strength microstructure than the ICHAZ.

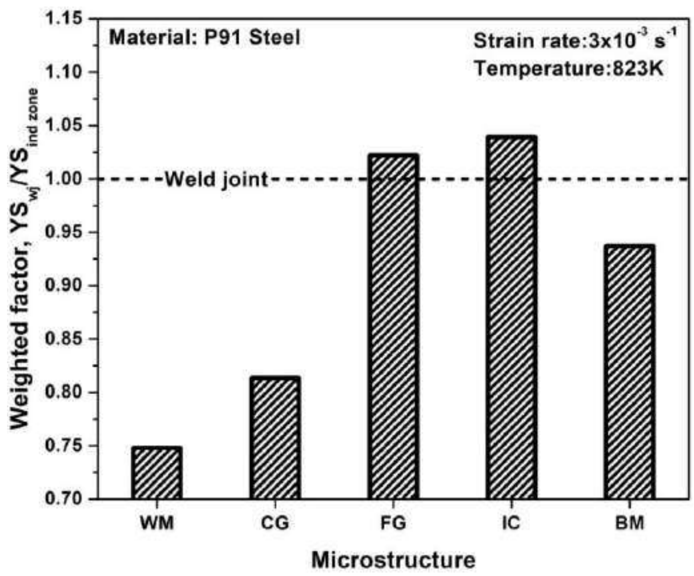

Fig. 5.9 Deformation weighted/contribution factors from each constituent region of P91 weld joint.

5.8 CONCLUSIONS

1 Significant variation (~150 MPa) in yield strengths and trivial difference in uniform elongations (2−5%) among the various constituent regions of P91 weld joint confirmed that strength dictated the tensile behavior of weld joint and not the ductility at a strain rate of 3×10^{-3} s^{-1} and temperature of 823 K.

2 Hardness measured across the weld joint before and after tensile test indicate that the strain/work hardening of initially soft ICHAZ and softening of initially harder microstructural regions such as CGHAZ and weld metal occur during tensile deformation. Among the simulated HAZ microstructures, the ICHAZ exhibited the lowest yield strength and hardness. However, the actual P91 weld joint failed in the base metal. The strain/work hardening of the soft ICHAZ and the strain incompatibility among the harder zones shifts the strain localization towards the base metal of the weld joint.

3 The higher local strain (KAM) distribution in the ICHAZ after tensile deformation compared to after PWHT confirms the occurrence of strain/work hardening during monotonic tensile deformation. The higher strain distribution in the ICHAZ could be due to numerous interactions between the dislocations, depending upon the local microstructure and stress states during tensile deformation.

4 From the estimation of deformation weighted/contribution factors of the simulated/individual microstructures, it was expected that the low strength and high ductility microstructure may contribute more for the failure in the case of actual P91 steel weld joint. But unlike the expected, the proposed failure criteria are deviated and the weld joint specimen failed at the base metal. This implies that the complexity in microstructure, strain accommodating capability and volume fractions of various regions and higher applied strain rate led to the failure of the weld joint at the relatively higher strength base metal rather than at soft inter-critical or FGHAZ.

5 The tensile behavior of P91 weld joint can be determined from the base metal as their strength and ductility are comparable at the strain rate of 10^{-3} s^{-1} at 823 K.

CHAPTER 6 LOW CYCLE FATIGUE BEHAVIOR

6.1 INTRODUCTION

Understanding the low cycle fatigue (LCF) behavior and estimating the weighted/contribution factor of each constituent region for the overall fatigue performance of P91 steel weld joint could provide important inputs for the development of welding technology. Particularly, the study on the heat-affected zones (HAZs), which are weaker in the microstructural constituents of weld joint would be more crucial. Microstructures of the three principal HAZs of weld joint were simulated through isothermal heat treatments in furnace at different soaking temperatures ranges from 1143 K to 1473 K, i.e., just above AC_1 and well above AC_3 respectively. In this chapter, the LCF behavior of each constituent region of weld joint is investigated and compared with the response of actual weld joint of P91 steel. Though the experiments have been carried out employing strain amplitudes ranges from ±0.25% to ±1.0% at a strain rate of 3×10^{-3} s^{-1} and 823 K under total axial strain control mode, in this Chapter detailed discussion pertaining to the results of ±0.6% strain amplitude is presented.

6.2 CYCLIC STRESS RESPONSE AND STRESS−STRAIN CURVES

Figure 6.1(a)-(d) depicts the cyclic stress response (CSR) of the actual weld joint, weld metal, CGHAZ, FGHAZ, ICHAZ and the base metal of P91 steel due to cyclic deformation at the strain amplitudes in the range between ±0.25% and ±1.0% at a strain rate of 3×10^{-3} s^{-1} and 823 K. In general, irrespective of the initial microstructural conditions, all test specimens exhibit continuous cyclic softening throughout the cyclic deformation at all strain amplitudes. Sudden load drops are observed at the end of the cyclic stress response curves, which are due to the propagations of macro cracks. The extensive substructural investigations at elevated temperatures have summarized that the deformation mechanisms such as coarsening of substructures in the form of dislocation annihilation, conversion of lath martensite into cell structure and precipitate coarsening are mainly responsible for the cyclic softening behavior of Chromium-Molybdenum steels [121,158]. Oxidation induced numerous microcracks formation in the surface and an associated reduction in the cyclic stress response during cyclic deformation is also reported [169].

The weld metal, simulated CGHAZ and FGHAZ and the base metal show rapid cyclic softening in the initial 10% of fatigue life from the first cycle onwards. A brief cyclic hardening (up to 3-5 cycles) is observed in the dual phase microstructural constituents such as ICHAZ and also in the weld joint, which also comprises of the ICHAZ in its complex geometry. Similar observations are reported in the dual phase steel [276,277]. Mediratta et al. [276] reported that the diffusion of carbon atoms into the plastically deformed region (ferrite) from the hard martensite during LCF loading causes a significant amount of cyclic hardening in dual-phase steel. The authors also stated that at higher strain amplitudes (±0.6%), the cyclic hardening occurs due to the dominant effect of interaction between carbon atoms and dislocations in the ferrite region than the formation of cellular structure from dislocations rearrangement in the martensite region, especially in the initial 5 to 10 cycles. S.K. Paul et al. [277] reported that the dual phase steel consists of 20-49% volume fraction of martensite exhibited cyclic hardening in the first few cycles due to the dislocation multiplication and entanglement in the ferrite region. The base metal and FGHAZ display near-saturation in the cyclic stress responses until the onset of the final load drop.

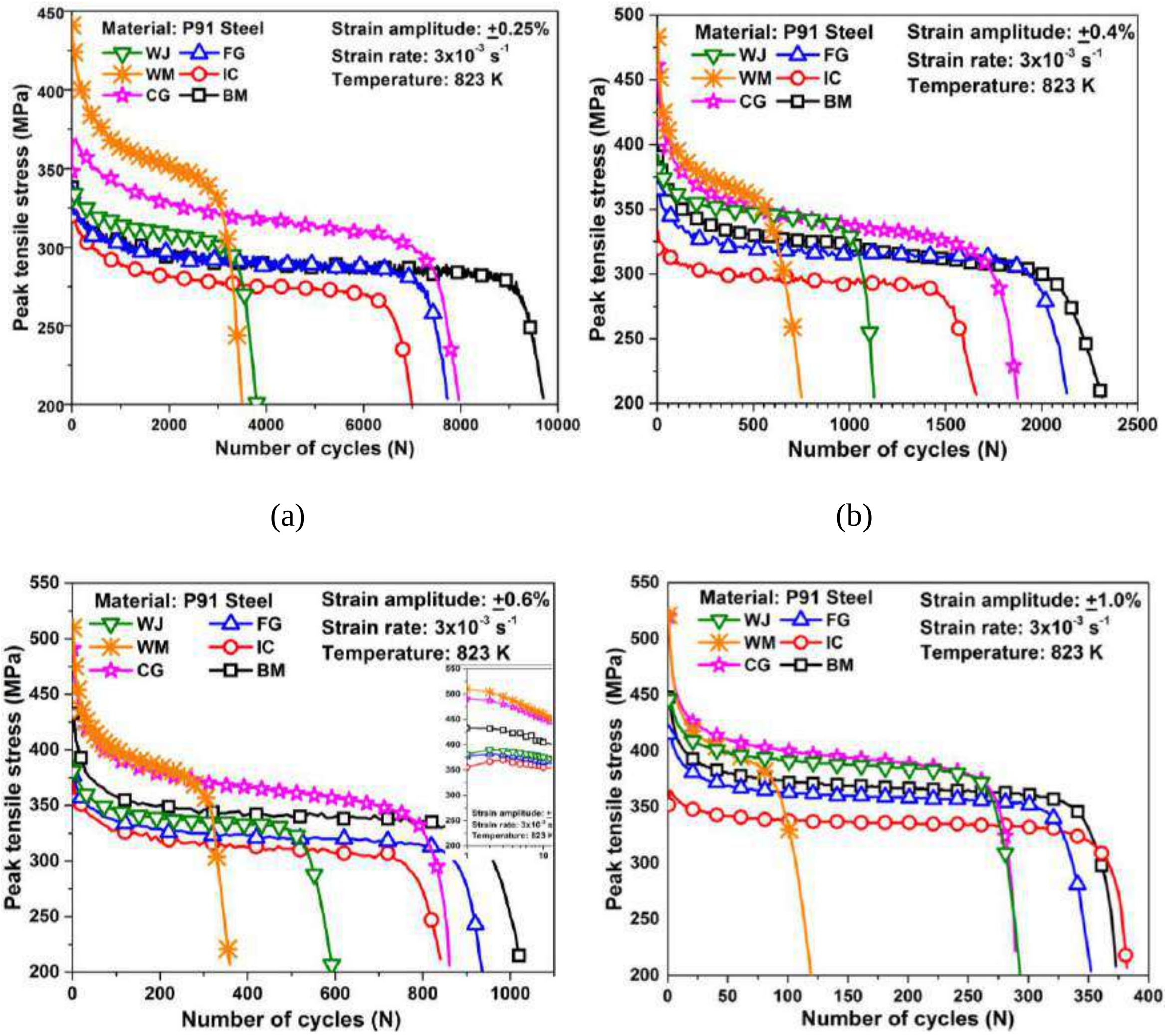

(a) (b)

(c) (d)

Fig. 6.1 Cyclic stress response curves of base metal, weld metal, simulated microstructures of HAZ and actual weld joint of P91 steel at the strain amplitudes of (a) ±0.25%, (b) ±0.4%, (c) ±0.6% and (d) ±1.0% and at 823 K.

Among the HAZs, the CGHAZ shows the highest cyclic stress response due to high solid solution strengthening, while the soft ICHAZ exhibits the lowest stress response among the all microstructural regions and the actual weld joint. At all strain amplitudes, the CSRs of weld metal and CGHAZ together form upper bound, whereas the CSR of ICHAZ constructs lower bound and the CSRs of the base metal, FGHAZ and actual weld joint are sandwiched between the upper and lower bounds. The rate of cyclic softening is found to be in the decreasing order for the microstructures of CGHAZ, base metal, FGHAZ and ICHAZ respectively. These observations reveal that the larger is the initial strength of a microstructure (solid solution strengthening is higher as the temperature of exposure is higher), greater shall be the rate of softening with cyclic loading. During fatigue cycling at elevated temperature, the conversion of initial lath structure with higher number of dislocations into equiaxed sub-grains with low dislocation density and coarsening of carbide precipitates attribute to the increased amount of softening in CGHAZ compared to the ICHAZ. The substructural changes in the form of ill-defined sub-grains with blocks of dislocation debris result in an extremely complex microstructure for the cyclically deformed specimens [19,28].

Half-life peak tensile stress and plastic strain values were determined from the hysteresis loops of LCF tests and depicted in Fig. 6.2 for all simulated ICHAZ, FGHAZ and CGHAZ and base metal, weld metal and cross-weld of P91 steel weld joint. A power-law equation is commonly used to represent the relationship for cyclic analysis of components and materials as follows:

$$\frac{\Delta\sigma}{2} = K' \left(\frac{\Delta\varepsilon_p}{2}\right)^{n'} \quad \text{----(6.1)}$$

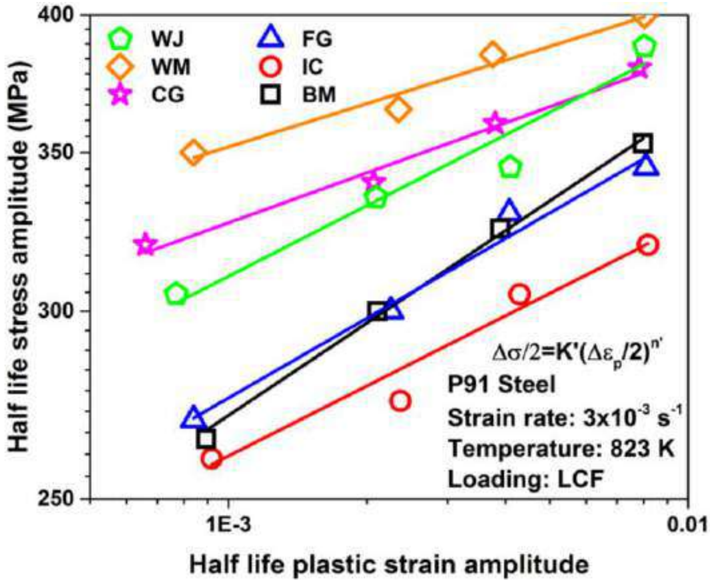

Fig. 6.2 Log-log cyclic stress-strain plots of base metal, simulated HAZs, weld metal and actual weld joint of P91 steel.

where K' and n' are the cyclic strength coefficient and cyclic strain hardening exponent, respectively. The highest half-life stress is that of weld metal followed by CGHAZ and weld joint. The half-life stress of ICHAZ is the lowest bound in the plot. The FGHAZ and base metal show similar hardening and are in between the plots of ICHAZ and weld joint. Also, the base metal, FGHAZ and ICHAZ microstructures exhibit higher slopes of cyclic stress-strain plots than the CGHAZ and weld metal microstructures thereby indicating therein higher hardening capabilities. The plot is a clear indication of the relation between the initial strength and the cyclic hardening nature. Thus, the initially softer microstructure such as ICHAZ undergoes cyclic hardening (Fig. 6.1).

6.3 FATIGUE LIFE

Fatigue lives of base metal, simulated microstructures of HAZs, weld metal and cross-weld of P91 steel weld joint for the applied total strain amplitudes between ±0.25% and ±1.0% at 823 K are depicted in Fig. 6.3(a) and (b). In general, irrespective of difference in the microstructures of the material fatigue lives decrease with the increasing of strain amplitudes.

Among the HAZ, the coarse grain exhibits better fatigue life at ±0.25% strain amplitude, whereas ICHAZ showed least fatigue lives at all applied strain amplitudes. In general, FGHAZ shows better fatigue lives among the simulated HAZs at all applied strain amplitudes. Though at ±1.0% strain amplitude the fatigue life of CGHAZ deteriorates significantly, considering the actual service conditions of the component, the strain amplitudes ≤ ±0.6% would be the most noteworthy parameters to take up for the analysis.

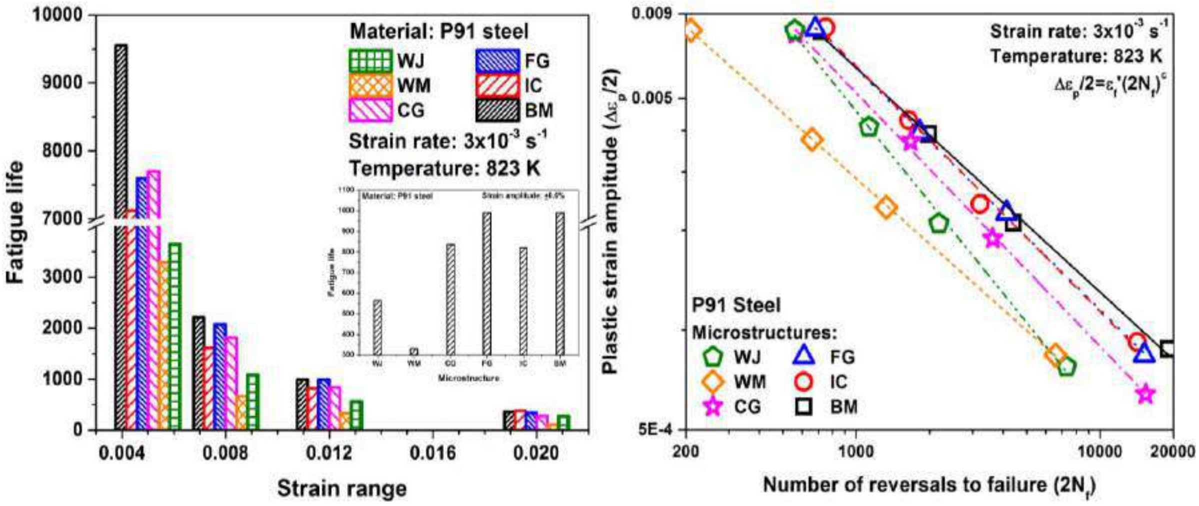

(a) (b)

Fig. 6.3 Fatigue life variations across the microstructures of P91 steel weld joint; (a) at the strain amplitudes ranges between ±0.25% and ±1.0% and (b) Coffin-Manson plots at 823 K.

The Fig. 6.3(a) shows the variations in the fatigue lives of the weld metal, the simulated microstructures of HAZ, base metal and the actual weld joint with respect to the applied strain ranges. The difference in the fatigue lives of the various microstructural regions is more pronounced at ±0.25% and to some extent at ±0.4%. The localization of cyclic deformation and creep are the important deformation mechanism for the large difference in the fatigue lives at the lower strain ranges. The increase in the intensity of gross deformation at the higher strain amplitudes shrinks the differences in the fatigue lives. However, the measurement scales associated with the fatigue lives at higher applied strain amplitudes are significantly low and hence even small amount of difference in the fatigue lives should be accountable.

In general, the Coffin-Manson plot is used to represent the relation between the accumulations of plastic strain and the fatigue lives of the material subject to the cyclic deformation at the plastic strain range. The Fig. 6.3(b) illustrates the fatigue lives of the various microstructural regions of P91 weld joint corresponding to the half-life plastic strain amplitude that they have accumulated/accommodated during cyclic deformation. The prior microstructure, amount of plastic strain accumulation with respect to the applied strain amplitude and the fatigue lives of the materials are inter-related. The initial high strength microstructure, CGHAZ experiences lower accumulation of plastic strain and exhibits better fatigue life at low applied total strain amplitude, ±0.25%. With the increase of applied strain amplitude, the plastic strain accumulation in the representative microstructural regions also increases and therefore the difference in the number of reversals also decreases. The fine grain region, which is a softer zone in the HAZs accumulates larger number of plastic strains during cyclic deformation and show better fatigue lives at all the applied strain amplitudes. The weld metal shows poor fatigue lives at all strain amplitudes and the inferiority is more pronounced at the higher applied strain amplitudes due to poor resistance against tensile strain, though it accommodates large amounts of plastic strain amplitude at half-life. The LCF parameters of base metal, the simulated microstructures of HAZ and weld metal and the actual weld joint are given in Table 6.1. The first cycles stress values of ICHAZ at the strain ranges of 1.2% and 2.0% are almost equal as observed between 0.5% and 0.8% (strain ranges). The variations in the first cycles stress values are within the experimental deviations.

At ±0.6%, the fatigue lives of FGHAZ and base metal are equal and higher than the CGHAZ, ICHAZ, weld metal and the actual weld joint. The fatigue lives are observed in the order of

(BM=FG)>(IC≈CG)>WJ>>WM. The fatigue life of the actual weld joint is however neither close to the fatigue lives of any of the constituent microstructures nor is equivalence to the average of the fatigue lives of all constituent microstructures, as seen in the insert of Fig. 6.3(a). This implies that the overall fatigue behavior of the actual weld joint is a synergistic effect of all microstructural constituents in a complex manner. The difference between the fatigue lives of the base metal and the weld joint is significantly large. The fatigue life reduction factor, which is defined as the ratio of fatigue life of base metal to the weld joint is found to be 1.75. Fatigue life reduction factor within a range of 1.5−2 have been reported on the weld joint of P91, P92 and E911 [278–280]. However, the determination of the reduction factor with respect to the base metal alone may not be sufficient to determine the fatigue behavior of its weld joint. Additionally, the weighted/contribution factors from the other microstructural zones, particularly from the heat-affected zone must also be taken into consideration for the fatigue life reduction of weld joint. In the previous Chapter it was concluded that the deformation weighted/contribution factors of the different regions towards the yield strength of actual weld joint vary with the microstructural gradient within the regions, which implies that the overall tensile behavior of the actual weld joint is dictated by the synergistic contributions of the hard and soft regions in the actual weld joint. The decrease in fatigue life of weld joint compared to base metal is attributed to the plastic strain localization in FGHAZ/ICHAZ and low rupture ductility of weld metal region [279].

Table 6.1 Low cycle fatigue parameters of P91 steel at 823 K.

Material	Strain range (%)	Fatigue life (N_f)	1st cycle stress (MPa)	Half life stress (MPa)	1st cycle plastic strain (%)	Half life plastic strain (%)
Weld joint	0.5	3650	330	310	0.106	0.150
	0.8	1090	380	335	0.354	0.418
	1.2	560	380	345	0.759	0.818
	2.0	280	445	390	1.550	1.606
Weld metal	0.5	3290	440	355	0.084	0.168
	0.8	665	480	370	0.312	0.465
	1.2	330	510	390	0.607	0.748
	2.0	105	520	400	1.440	1.608
CGHAZ	0.5	7700	348	318	0.045	0.131
	0.8	1755	456	348	0.244	0.413
	1.2	835	491	365	0.551	0.745
	2.0	280	520	395	1.413	1.563
FGHAZ	0.5	7600	335	290	0.493	0.170
	0.8	1660	375	320	0.348	0.465
	1.2	990	390	340	0.716	0.804
	2.0	340	415	360	1.413	1.563
ICHAZ	0.5	6900	320	276	0.146	0.187
	0.8	1610	320	294	0.467	0.474
	1.2	820	355	315	0.710	0.860
	2.0	375	350	335	1.578	1.636
BM	0.5	9550	338	289	0.083	0.175
	0.8	2210	391	317	0.324	0.422
	1.2	990	430	340	0.693	0.788
	2.0	360	450	370	1.459	1.591

The fatigue lives have been found to follow the strain-life relationship derived by Raske and Morrow [281] and Landgraf et al. [282] based on the relationship proposed by Basquin [140], Coffin [141] and Manson [142]. The strain-life relationship is given by,

$$\frac{\Delta\varepsilon}{2} = \frac{\Delta\varepsilon_e}{2} + \frac{\Delta\varepsilon_p}{2} = \frac{\sigma'_f}{E}(2N_f)^b + \varepsilon'_f(2N_f)^c \qquad \text{----(6.2)}$$

where $\frac{\Delta\varepsilon}{2}$ is the total strain amplitude, $\frac{\Delta\varepsilon_e}{2}$, the elastic strain amplitude, $\frac{\Delta\varepsilon_p}{2}$, the plastic strain amplitude, $2N_f$, the number of reversals to failure, σ'_f, the fatigue strength coefficient, b, the fatigue strength exponent, ε'_f, the fatigue ductility coefficient, c, the fatigue ductility exponent and E, the modulus of elasticity. The strain-life equation constants calculated from the Coffin-Manson plots by using least square fitting method (linear regression analysis) are summarized in Table 6.2. The constants for actual weld joint are also given for comparison.

Table 6.2 Constants in Coffin-Manson and Basquin and cyclic stress-strain relationships for different microstructures of P91 steel weld joint.

Microstructures	ε_f'	c	σ_f'/E	b	K	n′
Weld joint	2.5	−0.9	0.0028	−0.050	475	0.06
Weld metal	0.27	−0.65	0.0030	−0.066	530	0.05
CGHAZ	1.01	−0.76	0.0032	−0.052	530	0.07
FGHAZ	0.93	−0.73	0.0029	−0.056	596	0.11
ICHAZ	1.04	−0.74	0.0028	−0.047	510	0.10
Base metal	0.66	−0.68	0.0035	−0.074	660	0.13

6.4. HYSTERESIS STRESS−STRAIN BEHAVIOR

Figure 6.4 depicts the half-life stress-strain hysteresis loops of the weld metal, simulated CGHAZ, FGHAZ and ICHAZ and base metal and actual weld joint of P91 steel undergone LCF cycling at ±0.6% and 823 K. As shown in Fig. 6.4, the initial higher strength microstructures such as weld metal and CGHAZ display hysteresis loops with higher peak stresses and smaller widths at zero stress, whereas the hysteresis curve of soft ICHAZ exhibits the lowest peak stresses and larger width. The base metal, FGHAZ and ICHAZ exhibit serrated flows in the plastic portions of the hysteresis loops and the CGHAZ, weld metal and actual weld joint depict smooth stress-strain flow throughout the hysteresis loops. Serrated flow in the hysteresis loop, which is one of the manifestations of DSA phenomena at this test temperature is reported for modified 9Cr-1Mo steel [23,31]. In general, the difference in the serrated flow behavior is due to the difference in the solute content in the matrix depending upon the microstructural conditions. Dislocation-solute particles interactions appear in the form of serrated flow behavior in the hysteresis loops. Higher drag force to dislocation movement is expected in CGHAZ due to the presence of large amounts of slow diffusing solutes in the matrix. With the presence of considerable number of coarser precipitates at the lower temperature microstructures such as ICHAZ and FGHAZ the drag force on moving dislocations would be minimized. On the contrary, as shown in Fig. 6.4, serrated flow with higher magnitude discontinuous stress drops, one of the manifestations of DSA at 823 K, is observed for ICHAZ. This may be due to the difference in the dislocations movements through the matrixes of freshly formed fine tempered martensite and over tempered α-ferrite of the inter-critical zone. This however warrants more in-depth analysis as the scope of future study.

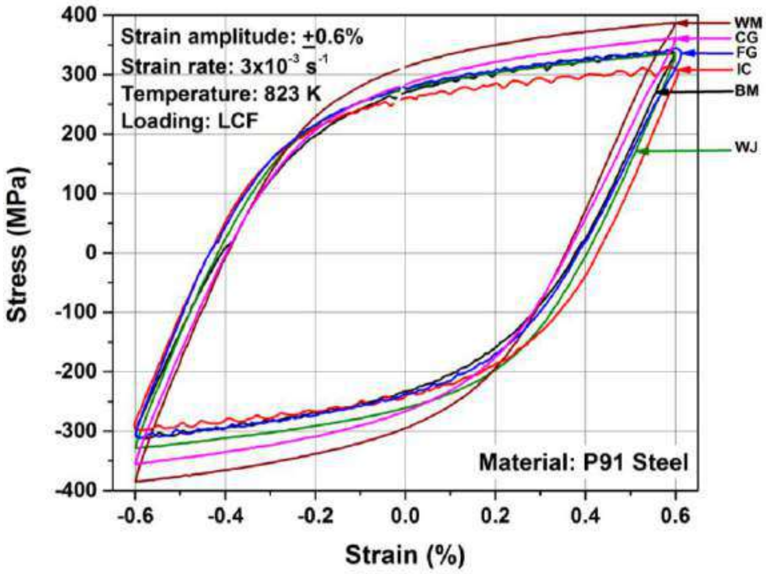

Fig. 6.4 Low cycle fatigue hysteresis loops of weld metal, simulated CGHAZ, FGHAZ and ICHAZ and base metal and actual weld joint of P91 steel at ±0.6% and 823 K.

6.5 YIELD STRENGTHS AND PLASTIC STRAIN ACCUMULATION UNDER CYCLIC LOADING

For an in-depth understanding of the underlying deformation behavior of each microstructural constituent and their effect on the overall fatigue performance of the actual weld joint, yield strength and the accumulated damaging plastic strain (obtained from the width of hysteresis loop) are compared at the same fatigue life fractions. The computed cyclic yield strength and accumulated cyclic plastic strain at 0 (cyclic plastic strain at 1st cycle), 5, 10, 30, and 50% of fatigue lives of the weld metal, simulated HAZs, base metal and actual weld joint are shown in Fig. 6.5(a) and (b), respectively. The yield strength at 0% fatigue life is obtained as the stress corresponding to 0.2% offset from the linear portion of the first cycle hysteresis loop obtained at the commencement of test. The plastic strain range is defined as the full width of the hysteresis loop at zero stress, i.e., the width between the hysteresis curves that intersect with the X-axis. The initial plastic strain range value is obtained from the hysteresis loop of 1st cycle (completed). The cyclic yield strengths for the remaining fatigue life fractions are obtained by drawing tangent lines on the slopes of the curves from the peak compressive stress of the hysteresis loops.

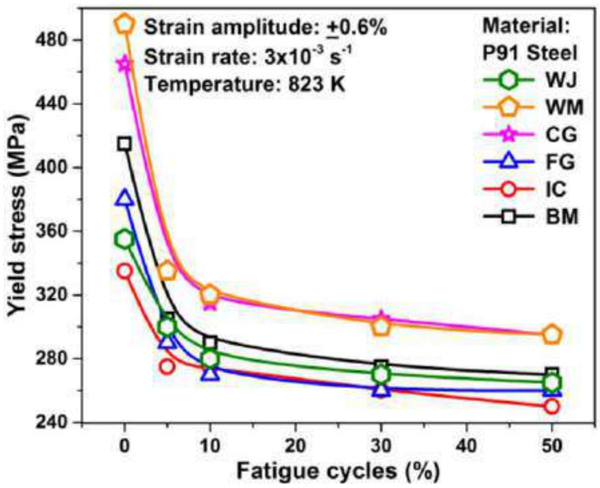

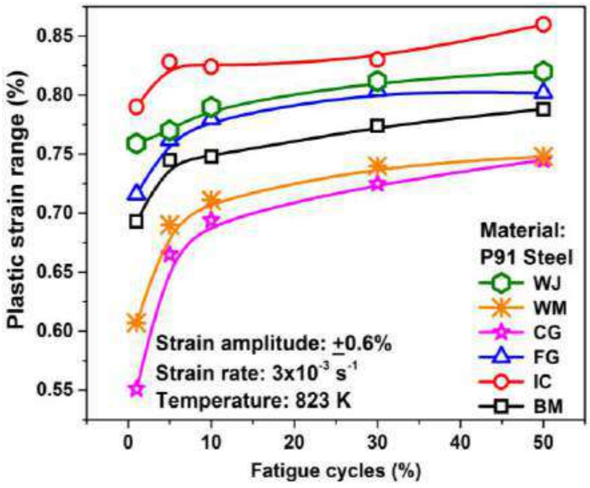

(a) (b)

Fig. 6.5 Variations of (a) cyclic yield strength and (b) cyclic plastic strain accumulation with the progressive cyclic deformation under LCF condition.

The extents of change in the yield strength and plastic strain accumulation depend upon the initial microstructure, though the nature of the changes in the yield strength and plastic strain remain identical. In general, two-slope behavior are observed for both yield strength and plastic strain (Fig. 6.5(a) and (b)) characterized by a rapid decrease/increase in yield strength/plastic strain within the initial 10% of fatigue life followed by gradual changes up to 50% of fatigue life. The similarity in the behavior also indicates that independent of the microstructural variations, the underlying deformation mechanisms for recovery may be the same, which is dislocation-controlled deformation. The amounts of reduction in the yield strength in the initial 10% of life are 125, 60, 105, 150, 180 and 75 MPa for base metal, ICHAZ, FGHAZ, CGHAZ, weld metal and actual weld joint respectively, whereas the yield strength reduction only ~20 MPa is observed between 10 to 50% of fatigue life. Similarly, the extent of cyclic plastic strain accumulation differs between the microstructures (Fig. 6.5(b)).

Whereas the base metal, ICHAZ, and FGHAZ exhibit only ~15% increase in plastic strain, the CGHAZ continuously accumulates the plastic strain about 35% with the progress of fatigue deformation up to 50% of fatigue life. Though the actual weld joint shows the same two-slope behavior, its value is not an average of all constituent microstructures. The decrease in yield strength associated with the substructural coarsening and the plastic strain depicting the strain accumulation capability of a microstructure thus clearly indicate a complex interplay of various factors resulting in the overall behavior of actual weld joint as the fatigue deformation progresses.

6.6 EFFECT OF MICROSTRUCTURES AND STRAIN AMPLITUDES ON CRACK PROPAGATION BEHAVIOR

The crack propagation in the weld metal, simulated CGHAZ, FGHAZ and ICHAZ and base metal during LCF loading at ±0.25% and 823 K are depicted in Fig. 6.6(a)-(e). It is observed that the cracks in all microstructural representative regions are thin, which could be due to the low applied strain amplitude. The islands of crack craters due to the deflections in the crack path are attributed to the presence of local heat-affected zones in the weld metal (Fig. 6.6(a)) that are deposited during multi-pass welding. The propagation and the branch diversions of cracks along the lath/block boundaries are discernible in the CGHAZ, as depicted in Fig. 6.6(b). The abundant grain boundaries, which offer the resistance to the extent of crack growth and the low applied strain amplitude, which is not enough to advance the crack led to the generation of multiple short cracks as observed in FGHAZ (Fig. 6.6(c)). The extents of the cracks through the dual phase microstructures of tempered martensite and over-tempered ferrite in the ICHAZ are diverted and exhibit branch propagations and are shown in Fig. 6.6(d).

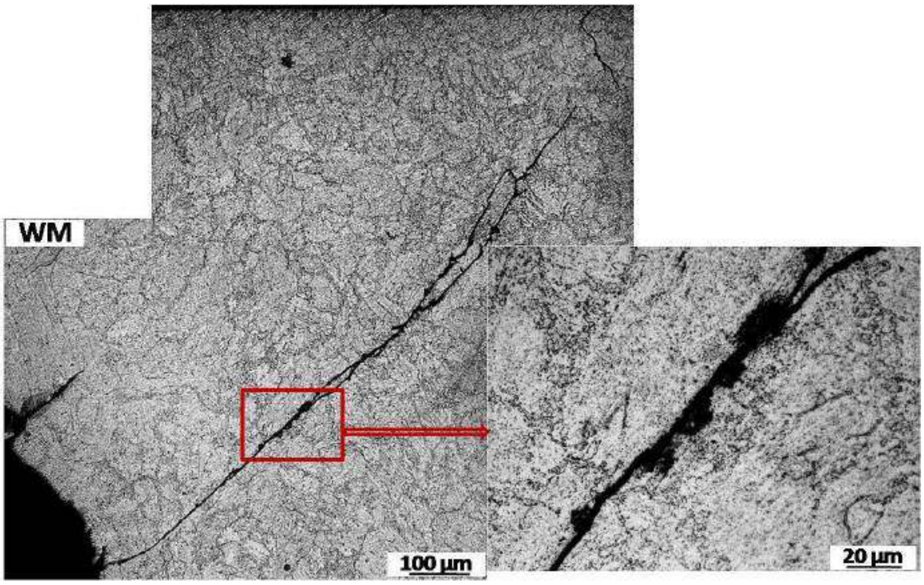

(a)

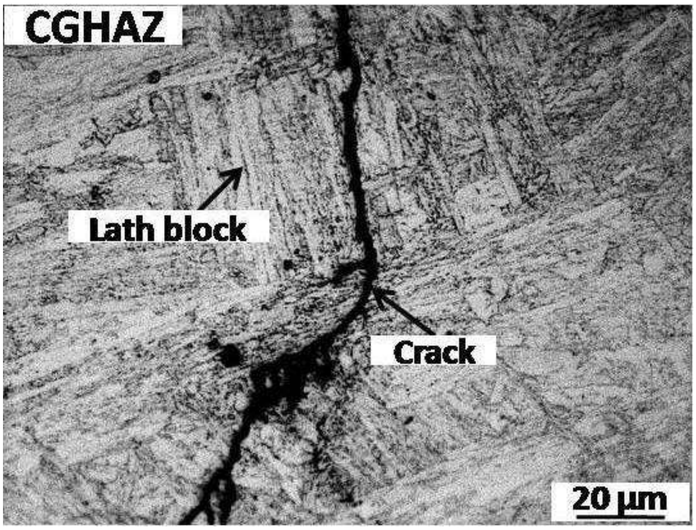

(b)

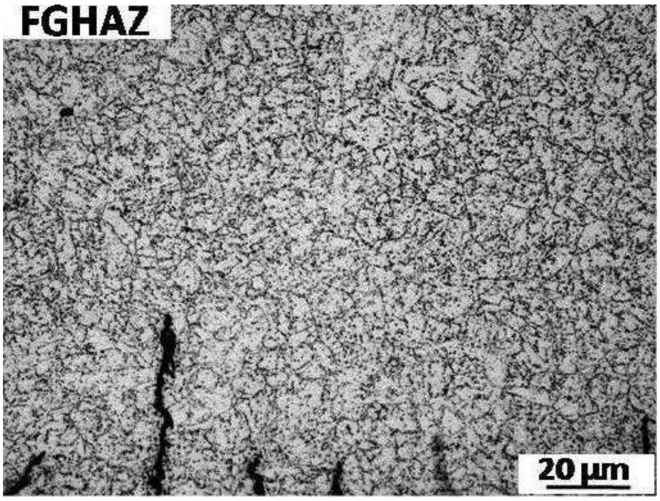

(c)

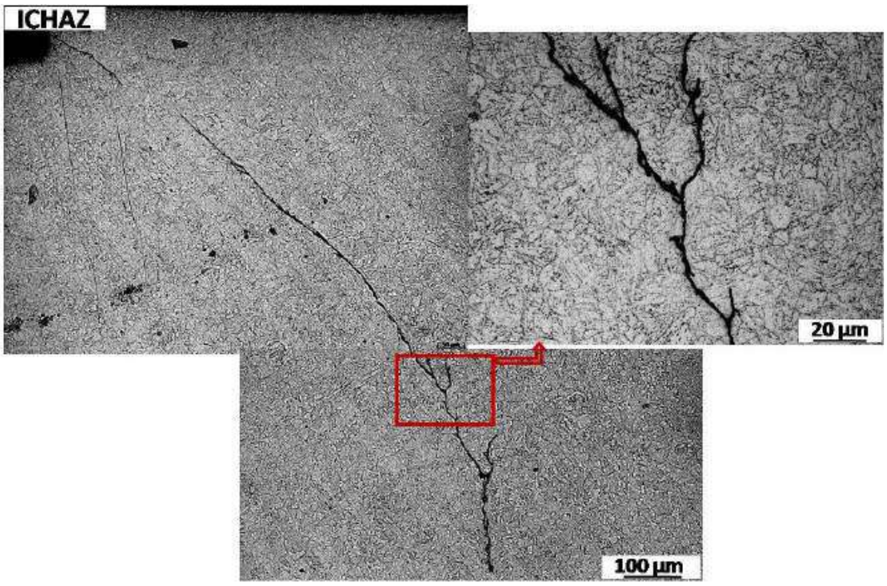

(d)

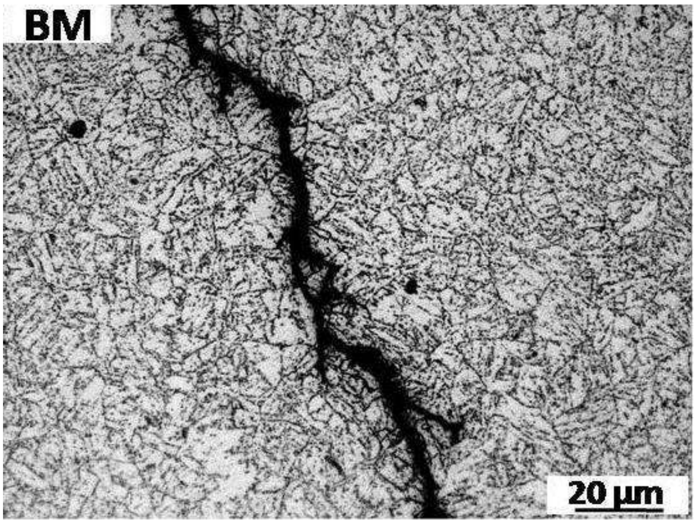

(e)

Fig. 6.6 Cracks propagations; (a) weld metal, simulated (b) CGHAZ, (c) FGHAZ and (d) ICHAZ and (e) base metal of P91 steel at ±0.25% and 823 K.

The representative optical micrographs, as shown in Fig. 6.7(a)-(f), illustrate the mode of crack propagation in the weld metal, simulated CGHAZ, FGHAZ and ICHAZ, and the base metal during LCF deformation at higher strain amplitude (±0.6%). Unlike the crack propagations behavior at lower strain amplitude of ±0.25%, extensive branching of transgranular cracks for all simulated and actual microstructural constituents of the weld joint are observed for the higher applied strain amplitude, ±0.6%. The PAGBs are reported to play an important role in the fatigue crack propagation [283]. In all microstructures, the network of cracks is characterized by deflections, presumably associated with the temporary arrest at the PAGBs or the lath/lath block boundaries with varying orientations.

The lower ductility of weld metal (Fig. 6.3(b)) reflects upon the formation of fewer but longer cracks (Fig. 6.7(a)) leading to catastrophic failure. A crack that is continuously propagated in the CGHAZ is depicted in Fig. 6.7(b). As mentioned earlier, the PAGBs and the substructure boundaries act as crack arresters and diverters. Thus, the lower number of boundaries per unit area in the CGHAZ translates into its reduced resistance to transgranular crack propagation under continuous cyclic deformation. It may be noted that the martensite lath boundaries are generally low-angle boundaries. Thus, the fatigue cracks are initiated and propagated, preferentially along the laths because of the weak crack propagation resistance as compared to high-angle block and PAG boundaries [283,284]. The preferential crack initiation and propagation along the lath boundaries, as shown in Fig. 6.7(c), cause the formation of many longer cracks, consequently leading to the early failure of CGHAZ. The easy crack propagation along the lengthy block/lath boundaries coupled with higher applied strain amplitude (±0.6%) decrease the fatigue life of CGHAZ compared to that of lower strain amplitude, ±0.25% (Fig. 6.3(a)). The uniform distribution of comparatively finer substructures of the FGHAZ served to cause more frequent crack arrests and deflections thereby improving the crack propagation resistance and fatigue life [283]. The initially soft ICHAZ is able to accommodate relatively larger amount of plastic strain during cyclic loading compared to all the other regions (Fig. 6.7(e)). Higher strain accumulation results in the formation of a greater number of crack initiation sites and eventually to the formation of greater amount of surface cracks. The numerous surface cracks and crack deflections resulting in the lowering of load bearing capacity of sample and reduced fatigue life of ICHAZ as compared to the base metal. This can be attributed to the presence of hard and fine tempered martensites along with over tempered soft ferrite consist of coarse carbides (~150 nm). The variation of mechanical properties of different phases within the ICHAZ (viz. coarse carbides, fine tempered martensites and over tempered ferrites) would have caused microcracking, decohesion and linkage about coarse carbides at various sites around them.

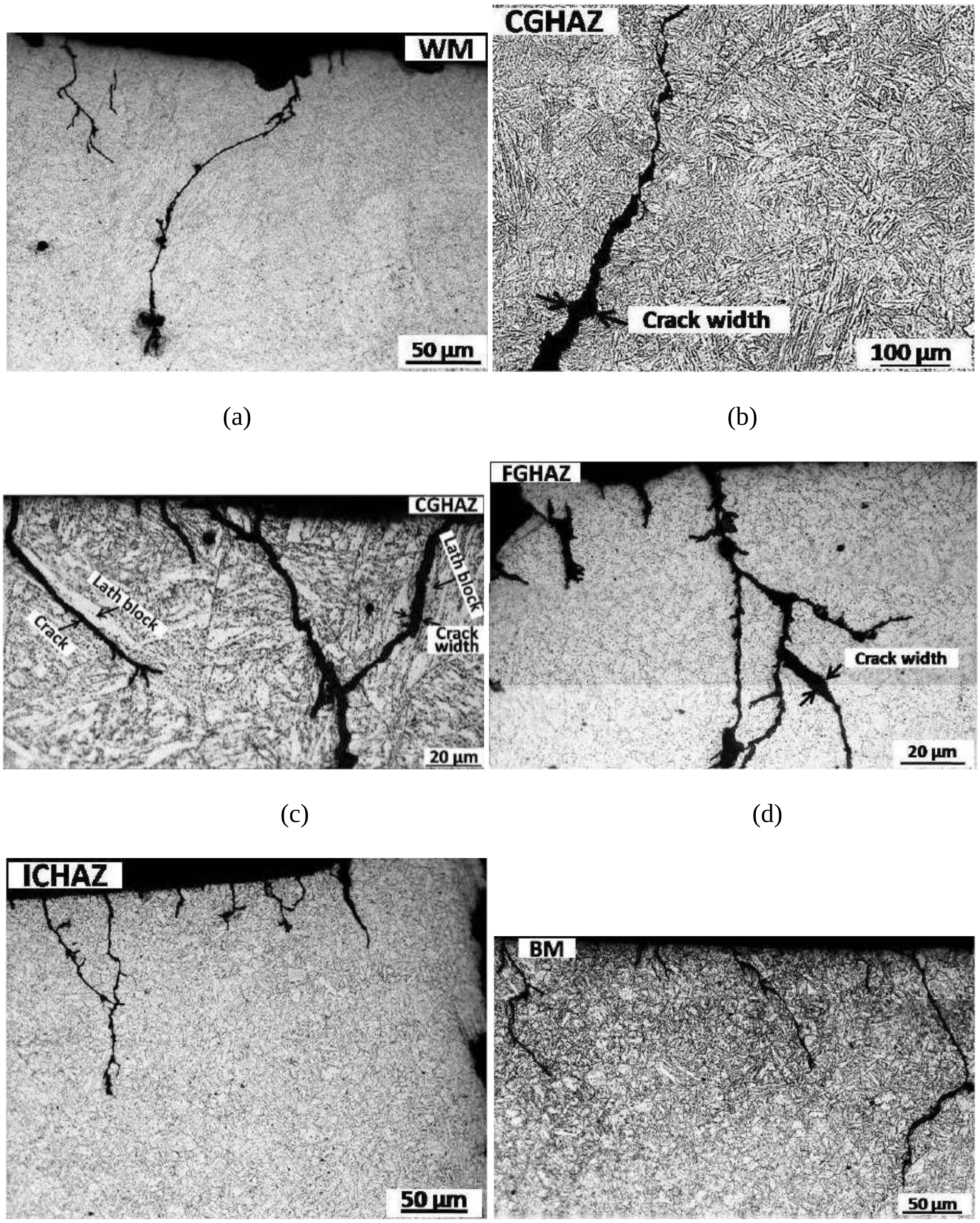

Fig. 6.7 Crack propagation; (a) weld metal, (b) and (c) CGHAZ, (d) FGHAZ, (e) ICHAZ and (f) base metal of P91 steel weld joint during LCF deformation at ±0.6% and 823 K.

A region with a long crack in the failed sample of simulated CGHAZ has been mapped using EBSD technique and the results are illustrated in Fig. 6.8(a)-(c). The microstructure consists of network of boundaries that have been broadly classified as low angle boundaries (denoted by red color) and high angle boundaries (denoted by black color) depending upon the local misoriention between the neighboring grains. In general, the crack path seems to follow the substructural boundaries rather than the prior austenite grain boundaries. Numerous low angle boundaries are present all along the crack propagation path that is also accompanied by large KAM strains. The KAM map indicate that all boundaries are associated with large strains (Fig. 6.8(c)), which are reported to be associated with the presence of geometrically necessary dislocations [285]. Also, some of the substructures are less strained as compared to the neighboring ones (indicated by arrows). Closer examination indicates that the substructures strained largely are associated within the same packets. This also confirms that the deformation in the microstructure is not homogeneous and contains regions of varying strains and dislocation densities.

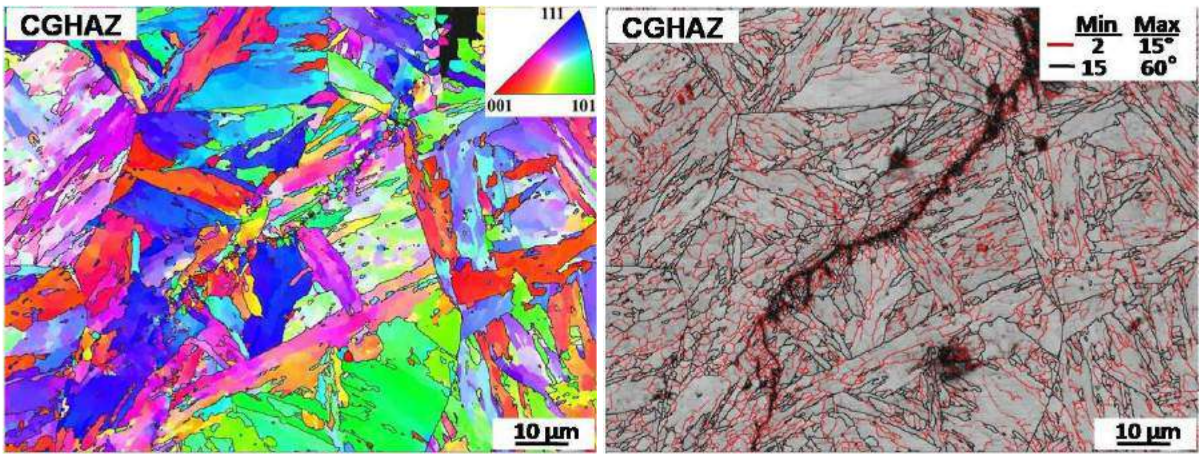

(a) (b)

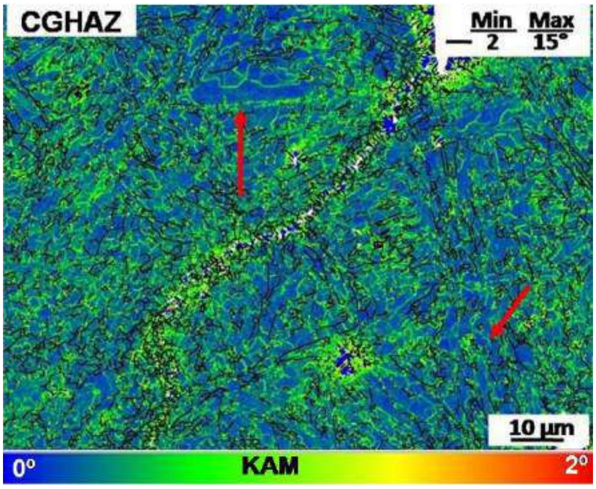

(c)

Fig. 6.8 Crack propagation detail in CGHAZ; (a) inverse pole figure (IPF) map, (b) grain boundary misorientation map and (c) KAM map with grain boundary misorientation distribution.

The cracks distribution against the crack length and width (width ─ maximum wide >1 µm in a crack) for all the simulated and actual microstructural constituents of the weld joint are depicted in Fig. 6.9 and 6.10. The number of cracks, crack lengths and crack widths are indirect indicators of strain/stress distribution and accommodation capability of the microstructural zones and that has an impact on the resultant fatigue life. As mentioned earlier, the simulated CGHAZ shows fewer but significantly longer and wider cracks than all other microstructures (Fig. 6.9) and its fatigue life is lower than the base metal but almost equal to simulated ICHAZ. The simulated ICHAZ depicts maximum number of short cracks of narrow widths (Fig. 6.9).

The comparatively longer and wider crack in the CGHAZ (Fig. 6.9) is related with the stronger matrix and its higher potential of strain accommodation coupled with the higher applied strain amplitude cyclic loading. Thus, the poor fatigue performance of CGHAZ is due to localized straining at fewer sites once the strain accommodation with the microstructure is exhausted. The presence of fine and hard tempered martensites and over tempered soft ferrites and the incompatibility of strain transfer among the heterogeneous microstructure in addition to the decohesion caused at comparatively coarser carbides lead to the generation of large number of cracks and attribute to the poor fatigue life of ICHAZ. Low ductility and high hardness of matrix due to both fine substructures and precipitates are the cause of the least fatigue life of the weld metal.

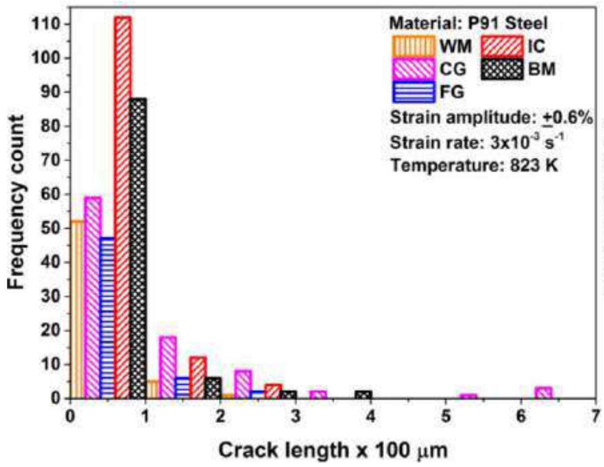

(a)

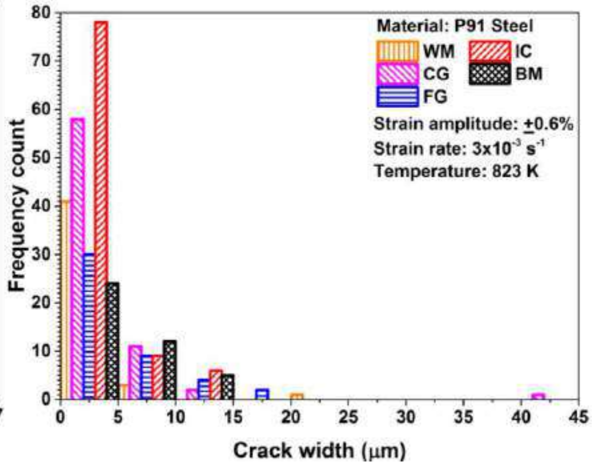

(b)

Fig. 6.9 Frequency distribution of cracks; (a) length and (b) width in weld metal, CGHAZ, FGHAZ, ICHAZ and base metal under LCF condition at 823 K.

Comparison of cracks in simulated and actual weld joint (Figs. 6.9 and 6.10) indicates that whereas for the simulated microstructures the number of cracks, crack length and width are in the order of IC>BM>CG>WM>FG, CG>BM>IC>FG>WM and CG>WM>FG>IC>BM respectively, for the actual weld joint they are in the order of BM>FG>IC, BM>IC>FG and IC>BM>FG respectively. The reason for this difference is due to the different volume fractions of the microstructures present in the actual weld joint and the evolution of strain accommodation capability of various constituting microstructures within the complex weld joint (Fig. 6.5(b)). For example, the weld metal and the base metal together occupy ~75% of the total volume in the weld joint as compared to a few grains of CGHAZ. On the contrary to the actual weld joint, the volumes of the samples are the same for all simulated microstructures. In the case of simulated microstructures, the higher strength base metal and FGHAZ exhibited better fatigue lives than others (ICHAZ, CGHAZ, weld joint, and weld metal). The higher number of comparatively short cracks (Fig. 6.9(a)) thereby indicating the load sharing and strain accommodation through cracking before final catastrophic failure. Though the initial strain accommodating capability (Fig. 6.5(b)) of CGHAZ is significant, the presence of longer and wider cracks indicates the concentration of strains in localized regions that is the cause of earlier catastrophic failure as compared to BM/FGHAZ. The same theory applies to the stronger weld metal as well. In the multi-component actual weld joint, the final failure is an aggregate of all these effects in addition to the shift of strains over the period depending upon local stress distributions.

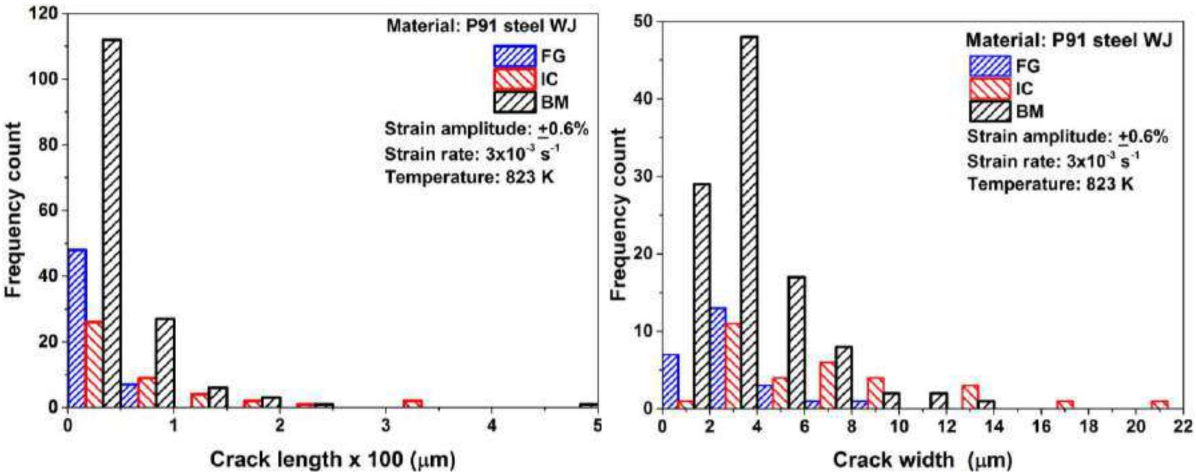

(a) (b)

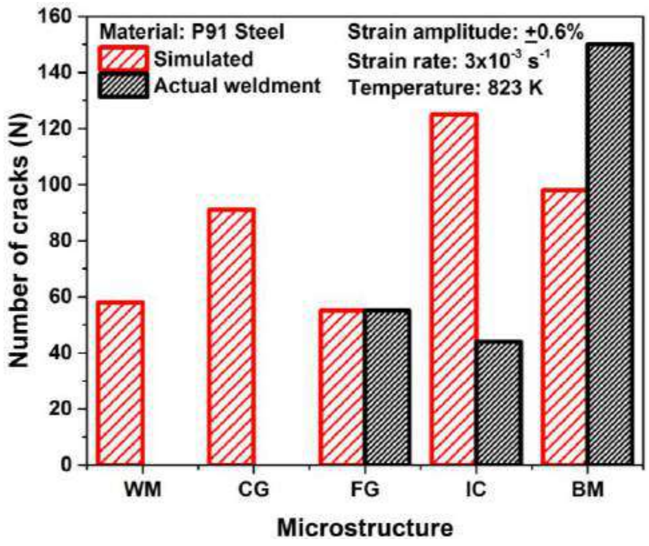

(c)

Fig. 6.10 Region-wise cracks distributions; (a) length and (b) width in the actual weld joint and (c) comparison of total number of cracks in the simulated and weld metal microstructures and microstructures of the actual P91 steel weld joint after the LCF test.

6.7 HARDNESS AND FAILURE LOCATION OF ACTUAL WELD JOINT

The changes in the hardness across the P91 weld joint after LCF tested is compared with the hardness after PWHT and is shown in Fig. 6.11. The gradient in the hardness profile of weld joint is due to the presence of thermally graded microstructure across the weld joint. A drastic drop in the hardness profile from CGHAZ to ICHAZ is attributed to the change in grain size distribution, coarsening of $M_{23}C_6$ carbide precipitates, increasing the mean inter-particle spacing and reduction in the solid solution hardening [8]. Further, a considerable amount of downward shift of the hardness profile of weld joint subjected to fatigue cycling as compared to PWHT is mainly due to the substructural recovery in the form of dislocation annihilation/attainment of lower energy configuration dislocation structure and to some extent the coarsening of the initially present carbides.

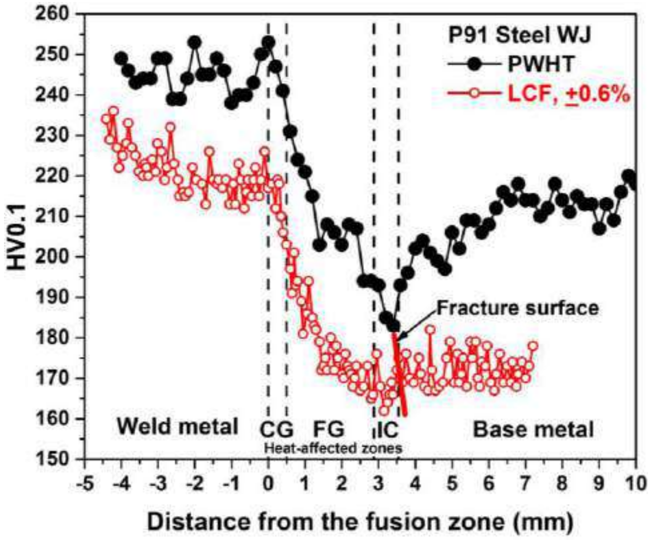

Fig. 6.11 Comparison of hardness profiles across the P91 steel weld joint after PWHT and LCF test.

The collaged optical micrograph of the failed actual weld joint under LCF loading is shown in Fig. 6.12. A few representative magnified images taken from various locations (marked by arrows, connecting with the collaged figure) are also depicted. The magnified image taken very close to the fractured surface indicates the failure location, which seems to be the microstructures of ICHAZ/base metal. This is also confirmed by the hardness values taken across the failed sample length and with the corresponding indentation locations (Fig. 6.12). From the Fig. 3.3(b), it is observed that the weld metal and the base metal together occupy ~75% volume in the gage section of the actual weld joint specimen. Nevertheless, the failure seems to initiate at the interface between the soft ICHAZ and the base metal.

The initial brief cyclic hardening of the soft ICHAZ due to the dislocations interactions, the small area fraction of CGHAZ (few grains), the comparatively stronger weld metal, CGHAZ, FGHAZ and base metal might have resulted the strain localization at the interface of ICHAZ and the base metal rather than within the soft ICHAZ. Under LCF, the crack initiation is known to take place within 5% of the total fatigue life of the material [169]. With the progressive cyclic deformation, the crack propagates normal to the loading axis, through both the soft ICHAZ and the base metal. Even though the simulated CGHAZ with a homogenous microstructural condition exhibited poor resistance to fatigue deformation, the failure of the actual weld joint did not take place at the CGHAZ. This could be because of the low volume fraction of the CGHAZ in the actual weld joint and its stronger microstructure and higher strain accommodating capability to shift the deformation from strain accommodation to strain localization.

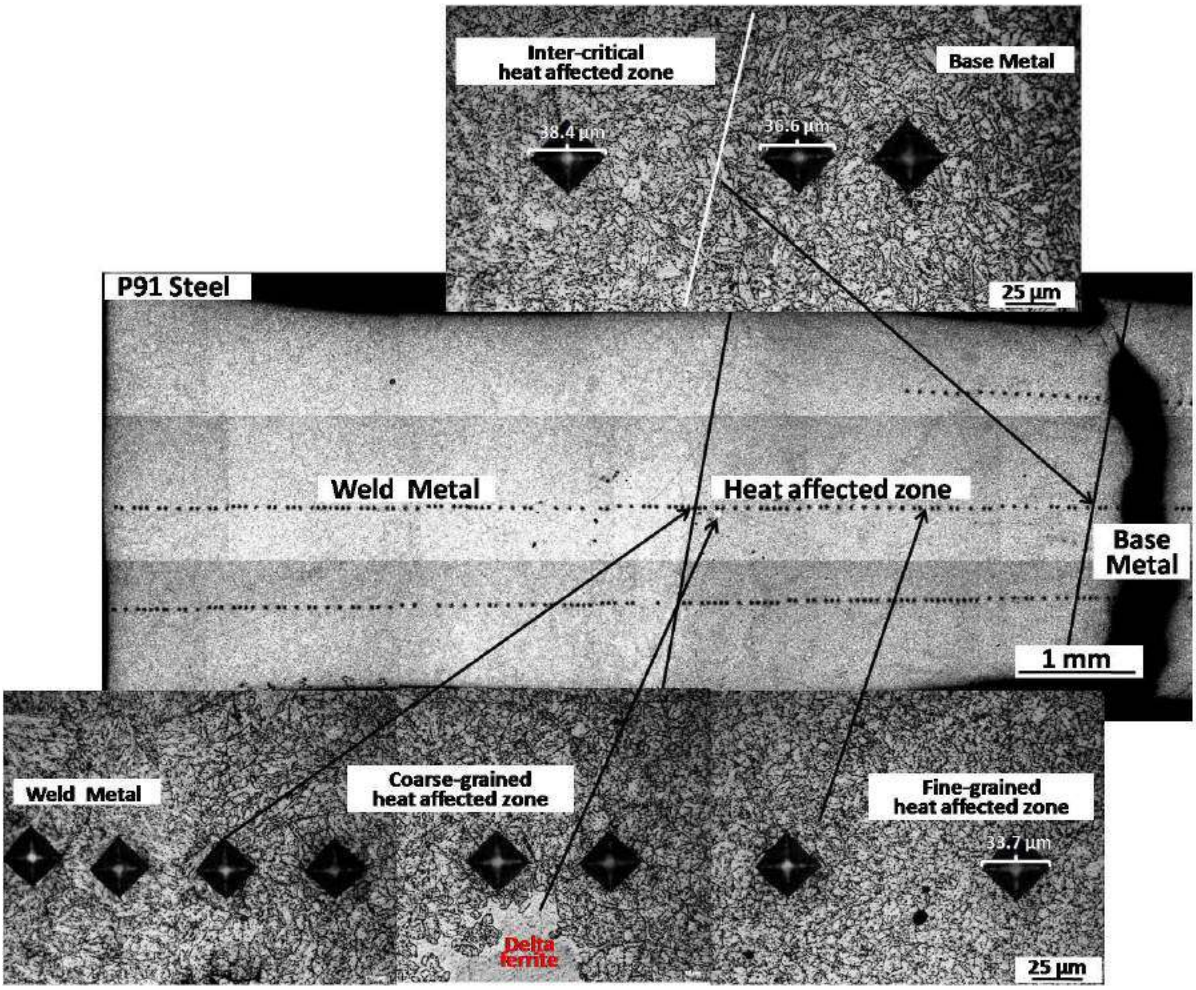

Fig. 6.12 Longitudinal image of failed sample of P91 steel weld joint subjected to LCF loading at 823 K; representative magnified images of weld metal, HAZs, and base metal are indicated.

6.8 FRACTURE ANALYSIS

The SEM fractographs of the weld metal and simulated CGHAZ, FGHAZ and ICHAZ, and base metal of P91 steel weld joint are presented in Fig. 6.13(a)-(e), respectively. The fractograph of weld joint specimen (Fig. 6.13(f)) reveals several crack initiations sites, ductile dimples, flat facets and overload ductile fracture. All microstructures exhibit typical transgranular crack propagation. Only a few microcracks are found along the lengthy columnar striations in the weld metal. Extensive transgranular/transverse cracks are observed in the CGHAZ. The fracture surface corresponding to the FGHAZ consists of fine striations, beach marks and flat facets, whereas the ICHAZ exhibits islands of striations and flat facets. The formation of fine striations and flat facets is attributed to the presence of freshly formed tempered martensite and untransformed ferrite in the dual phase matrix of the ICHAZ. Oxides are observed in the fracture surfaces of all microstructural constituents. The Fig. 6.13(e) depicts oxides formed on the fracture surface of the base metal. The variation of striations sizes between the various microstructural constituents is illustrated in Fig. 6.13(g). The average spacing between striations in the weld metal is ~ 32 μm, while the spacing between the striations of all other microstructures varies only between 1.5-6.0 μm. In most of the specimens the striations were annihilated due to the hammering effect by imperfect mating of surface during crack propagations.

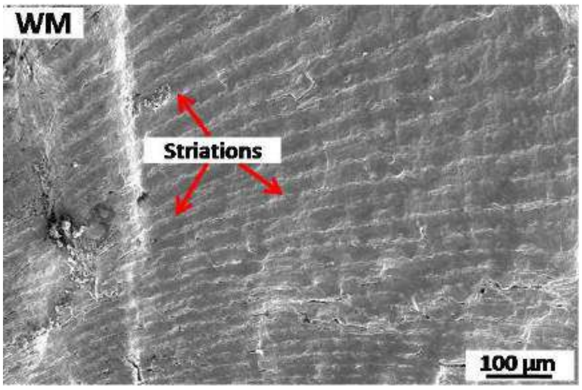
WM
Striations
100 µm

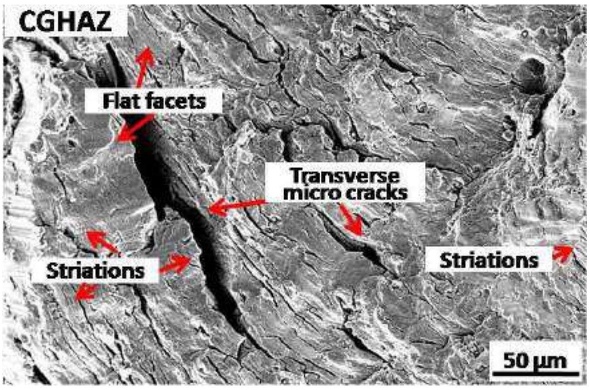
CGHAZ
Flat facets
Transverse micro cracks
Striations
Striations
50 µm

(a) (b)

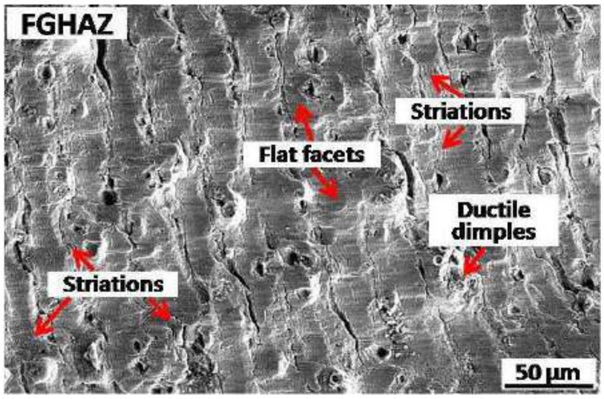
FGHAZ
Striations
Flat facets
Ductile dimples
Striations
50 µm

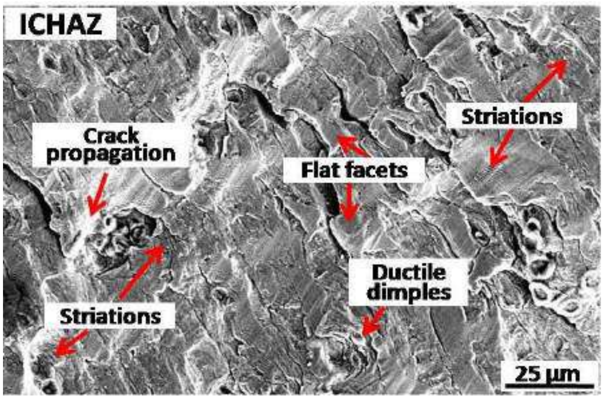
ICHAZ
Crack propagation
Striations
Flat facets
Ductile dimples
Striations
25 µm

(c) (d)

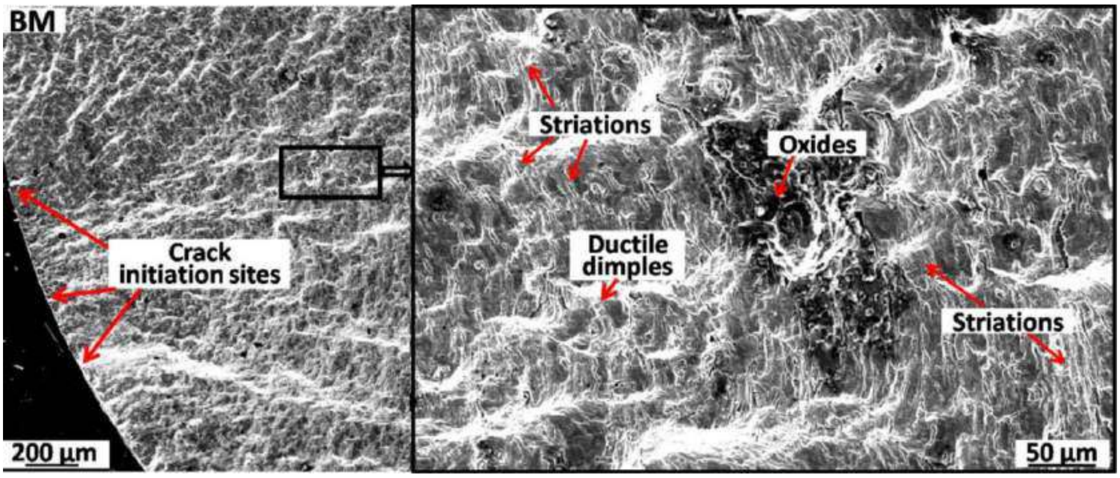
BM
Crack initiation sites
200 µm
Striations
Oxides
Ductile dimples
Striations
50 µm

(e)

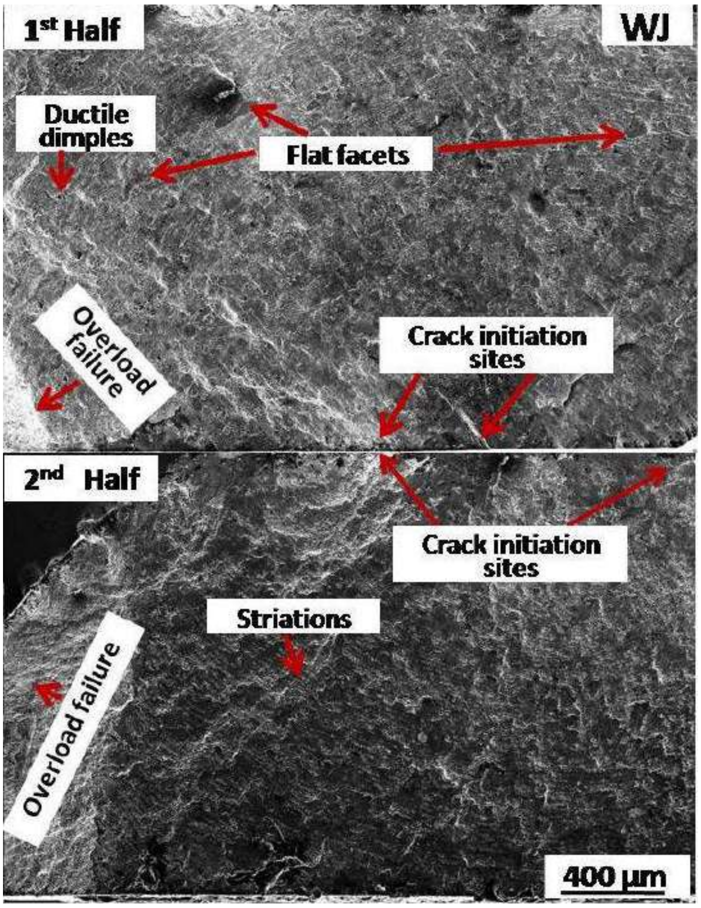

(f)

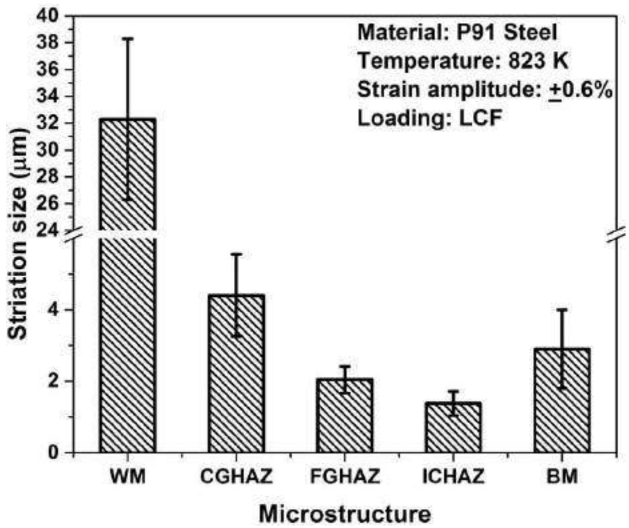

(g)

Fig. 6.13 Fracture surfaces of (a) weld metal, (b) CGHAZ, (c) FGHAZ, (d) ICHAZ, (e) base metal and (f) actual weld joint; (g) the bar charts of striations sizes with standard deviations for different microstructures of P91 steel after LCF deformation at ±0.6% and 823 K.

6.9 DEFORMATION MECHANISM ANALYSIS THROUGH EBSD TECHNIQUE

The inverse pole figures (IPFs), which signify the crystallographic orientations along rolling direction (RD) i.e., longitudinal direction of the planes observed in the specimens of weld metal, simulated CGHAZ, FGHAZ ad ICHAZ and base metal, are shown Fig. 6.14(a)-(e). The grain boundaries with the misorientations between 15° − 60º in the IPF maps are demarcated with black lines.

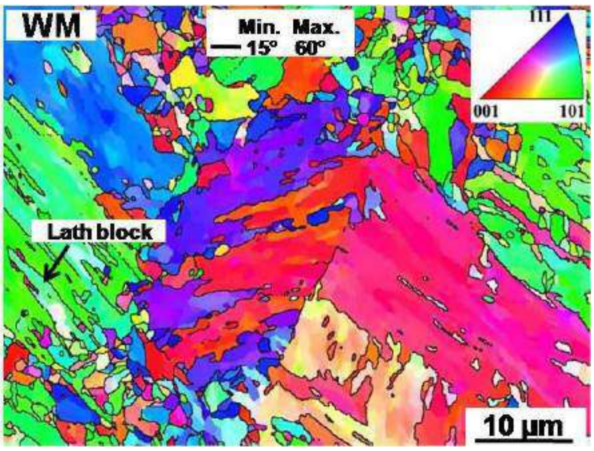

(a)

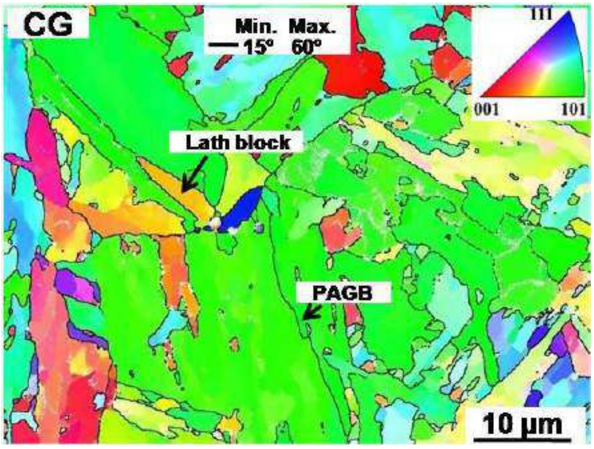

(b)

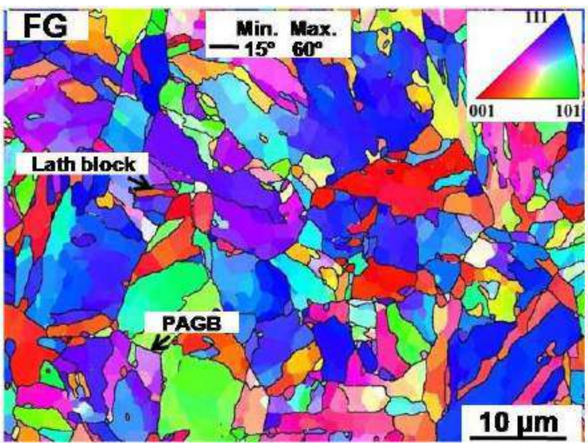

(c)

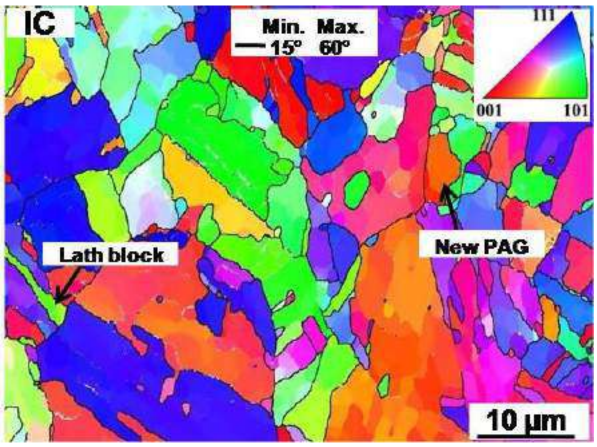

(d)

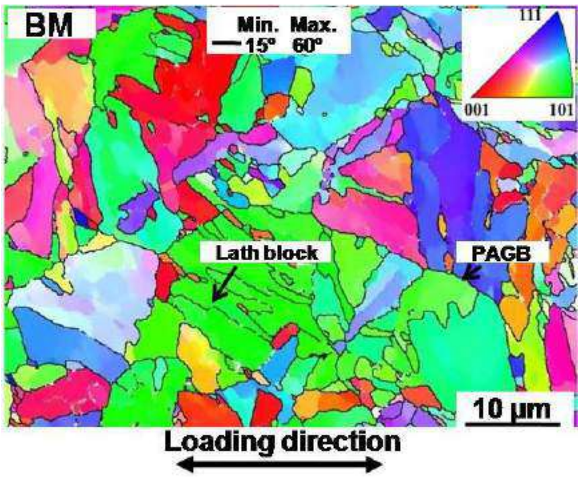

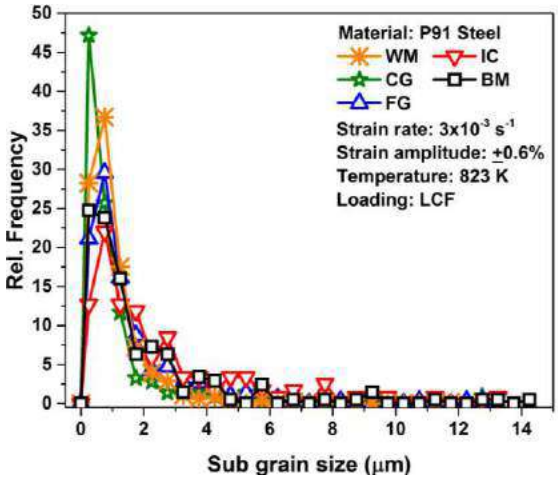

(e) (f)

Fig. 6.14 Substructural analysis; (a-e) IPF maps of various microstructural regions of P91 steel weld joint and (f) sub-grain size distribution after LCF test at 823 K.

Table 6.3 gives the quantification details of the low angle grain boundaries (LAGBs) and high angle grain boundaries (HAGBs) in the simulated CGHAZ, FGHAZ and ICHAZ after PWHT and LCF test. The formation of LAGBs in the CGHAZ and ICHAZ increases after LCF deformation. The sub-grain size evolution in the samples of fatigue deformed is depicted in Fig. 6.14(f) and the corresponding values are given in Table 6.3. The higher amount of finer sub-grains in the CGHAZ are due to the rearrangement of fine, lengthy lath martensite into cell structure due to cyclic deformation. The ICHAZ shows the increase in distribution of the sub-grain evolution than in other microstructures. This shows that both CGHAZ and ICHAZ accumulating/accommodating higher amount of plastic strain, which may lead to early crack initiation and lower fatigue lives.

The KAM maps for all simulated HAZs, base metal and weld metal are depicted in Fig. 6.15(a)-(e). The larger lath blocks in the CGHAZ show low misorientation distribution. Among the HAZ microstructures, the CGHAZ and ICHAZ depict higher amount of local misorientation distribution. The local strain as shown in KAM maps of CGHAZ and ICHAZ (Fig. 6.15(b) and (d)) are extensively distributed in the vicinity of LAGBs. The higher amount of local strain distributions in the ICHAZ and CGHAZ cause larger cracks generations (Fig. 6.13(b) and (d)) and associated decrease in the fatigue lives (Fig. 6.3(a)). The faster and limited grain growth in the FGHAZ is likely due to the large fraction of recrystallization sites provided by the increase in the number of HAGBs.

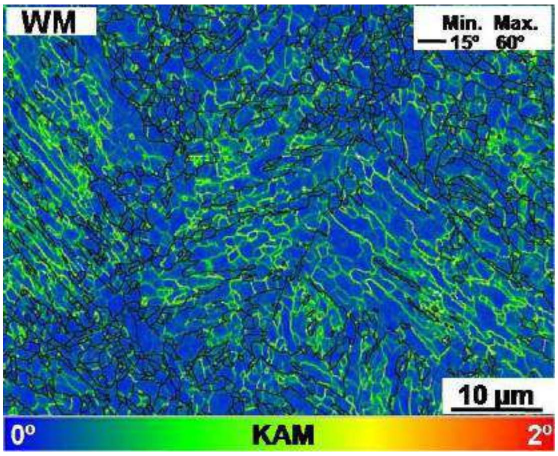

(a)

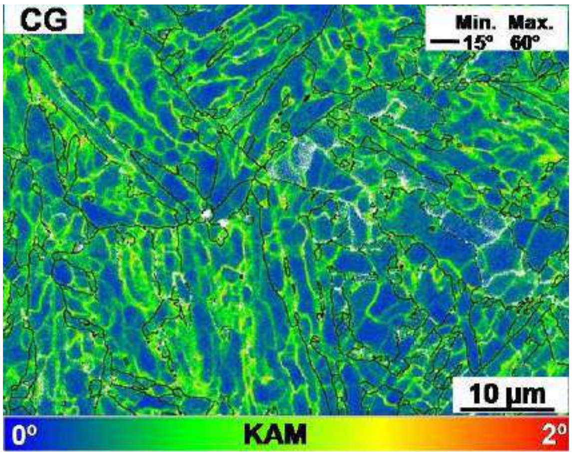

(b)

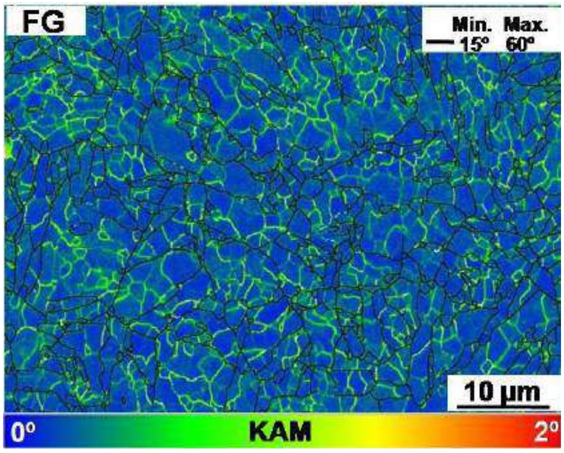

(c)

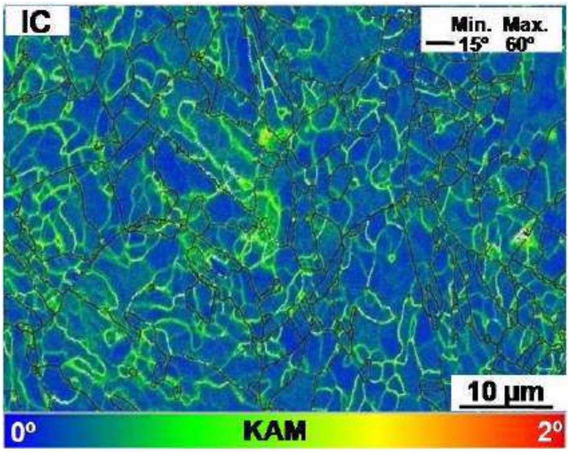

(d)

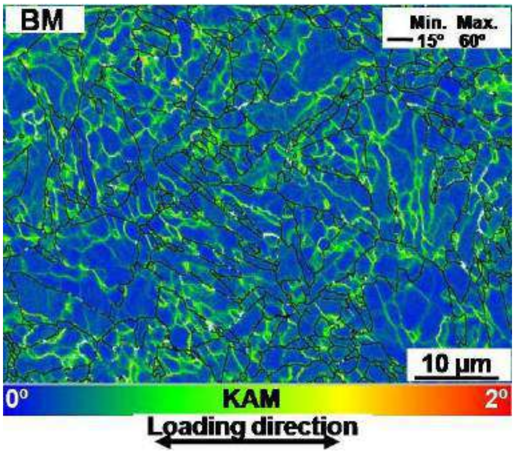

(e)

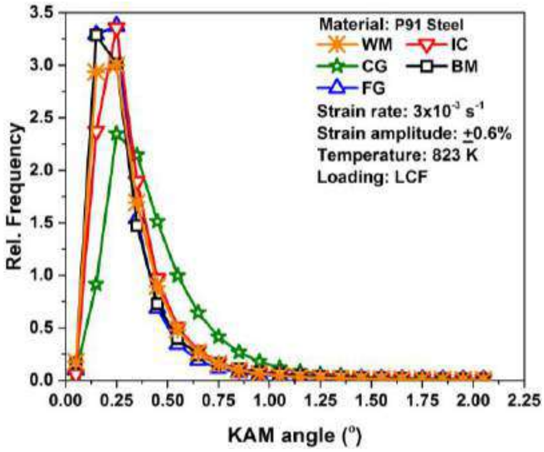

(f)

Fig. 6.15 Substructural analysis; (a-e) KAM maps and (f) local misorientation (KAM) distribution map of various microstructural regions of P91 steel weld joint after LCF test at 823 K.

Table 6.3 Comparison of EBSD results associated with microstructural changes in simulated microstructures of HAZ of P91 steel weld joint after PWHT and LCF test.

Microstructures		CGHAZ		FGHAZ		ICHAZ	
Conditions		PWHT	LCF	PWHT	LCF	PWHT	LCF
Grain boundaries fractions (%)	LAGB	74.1	78.5	61.2	53.1	58.6	63.8
	HAGB	25.9	21.5	39.8	46.9	41.4	36.2
	LAGB/HAGB	2.86	3.65	1.54	1.13	1.42	1.76
Sub-grain size$_{max}$ (Standard deviation, µm)		0.98 (±1.79)	1.07 (±1.67)	2.15 (±2.26)	1.74 (±2.14)	2.12 (±2.51)	2.47 (±2.49)
Max. frequency of KAM angle (°)		0.35	0.25	0.25	0.25	0.25	0.25
Microstructural changes	Substructured	96.8	90.7	92.1	65.2	89.4	83.6
	Recrystallized	2.11	7.8	7.6	34.4	10.3	15.9
	Deformed	1.07	1.5	0.3	0.4	0.3	0.5

6.10 DEFORMATION WEIGHTED/CONTRIBUTION FACTOR ANALYSIS UNDER LCF

In general, it has been reported that the fatigue life of P91 weld joint is inferior to the parent material. From the present study, it is found that at lower strain amplitude the difference in the fatigue lives between the parent metal and the weld joint is large. Hence the design criteria require applying of the weld strength reduction factor for safe life design. The estimation of reduction factor only with respect to the base metal may not be enough to evaluate the fatigue behavior of weld joint. Calculating the reduction factor of weld joint with reference to the heat-affected zones would be more crucial to understand the contribution of each constituent region for overall fatigue behavior of weld joint in actual service condition.

Therefore, in this study an attempt was made to determine the reduction factors of weld joint in accordance with all constituent regions of the weld joint rather only the use of base metal. Here, the Eq. 5.2 in which the yield strength parameter is replaced by fatigue life and is given below as

$$\mathbf{N}_{\mathbf{f}\,wj} = \mathbf{aN}_{\mathbf{f}\,bm} + \mathbf{bN}_{\mathbf{f}\,\mathbf{ic}} + \mathbf{cN}_{\mathbf{f}\,fg} + \mathbf{dN}_{\mathbf{f}\,cg} + \mathbf{eN}_{\mathbf{f}\,wm} \qquad \text{----(6.3)}$$

where a, b, c, d and e denote the fatigue lives weighted/contribution factors (WFs) of each constituent region of actual weld joint. The contribution factors are calculated using the equations as follows

$$\mathbf{WF}_{\mathbf{ind\ zone}} = \mathbf{1} - \frac{\mathbf{N}_{\mathbf{f\ wj}}}{\mathbf{N}_{\mathbf{f\ ind\ zone}}} \qquad \text{----(6.4)}$$

$$\mathbf{WF}_{\mathbf{wm}} = -\mathbf{1} - \frac{\mathbf{N}_{\mathbf{f\ wj}}}{\mathbf{N}_{\mathbf{f\ wm}}} \qquad \text{----(6.5)}$$

The negative sign given in Eq. 6.5 is associated with the reduced fatigue life of weld metal compared to that of the weld joint. The deduced fatigue life contribution factors against the corresponding microstructures are illustrated in Fig. 6.16. Though the difference between the values of weighted/contribution factors of HAZ microstructures is less, their influence on determining the fatigue life of actual weld joint is significant. As it is clear from Fig. 6.16, the damaging weighted/contribution factor of the weld metal has a major impact on deteriorating the fatigue life of the weld joint.

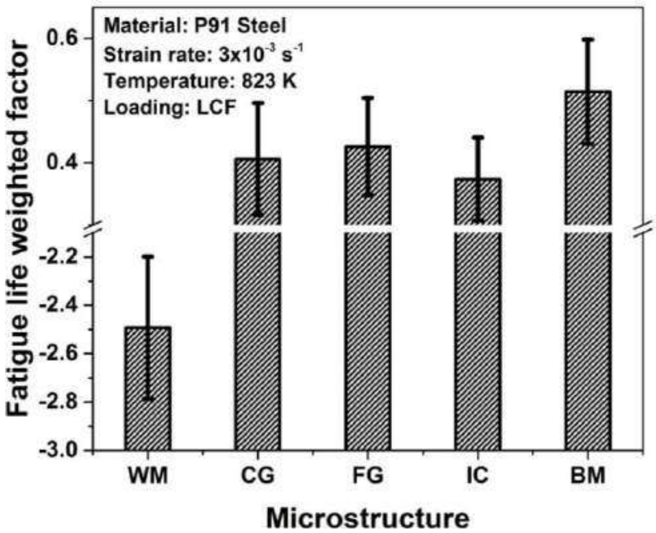

Fig. 6.16 Microstructure dependent weighted factor/weld strength reduction factors of P91 steel.

Therefore, the weighted/contribution factors of corresponding microstructural region are substituted in the Eq. 6.3 and is rewritten as Eq. 6.6, which is used for the estimation of fatigue life of actual weld joint for the strain amplitudes between ±0.25 and ±0.6% at 823 K;

$$N_{f\,wj} = 0.5N_{f\,bm} + 0.32N_{f\,ic} + 0.4N_{f\,fg} + 0.35N_{f\,cg} - 2.6N_{f\,wm} \quad \text{----(6.6)}$$

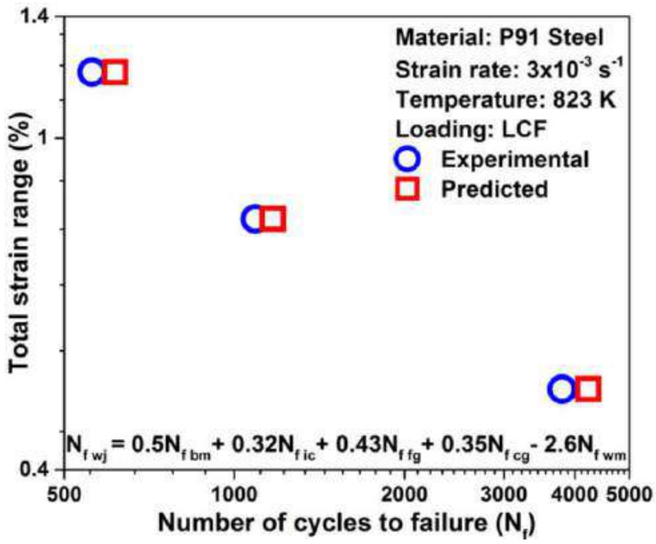

Fig. 6.17 Comparison of predicted and experimental fatigue lives of P91 weld joint under LCF condition at 823 K.

The comparison between predicted and experimental fatigue lives of P91 weld joint is presented in Fig. 6.17. The predicted fatigue life is comparable with the experimental fatigue life of the weld joint and the difference between the fatigue lives falls within ±10%. This implies that only the major constituent microstructures such as weld metal, CGHAZ, FGHAZ and ICHAZ and base metal significantly determine the fatigue life of the actual weld joint.

6.11 CONCLUSIONS

Study on the low cycle fatigue behavior of weld metal, simulated CGHAZ, FGHAZ and ICHAZ and base metal and the actual weld joint of P91 steel has drawn the following conclusions:

1 The CGHAZ and weld metal are the strongest and ICHAZ is the softest compared to FGHAZ, base metal and the actual weld joint, which showed intermediate strength or cyclic stress response. A common two-slope behavior of cyclic yield strength and plastic strain range for all the microstructures indicate that same underlying deformation mechanism is operative. The fatigue lives of base metal, simulated FGHAZ, ICHAZ and

CGHAZ, weld metal and actual weld joint are in the order as follows: (BM=FG)>(IC≈CG)>WJ>>WM. The fatigue life of the actual weld joint is not an average of the fatigue lives of the constituent microstructures and depends upon various factors.

2 Factors such as grain size (CG, FG), mechanical strength of various phases (fine tempered martensites and overtempered ferrite in ICHAZ), precipitate size (decohesion around coarsened carbides in ICHAZ), difference in the volume of microstructural regions in the actual weld joint, difference in plastic strain accommodation/accumulating capacity of individual microstructures and their evolution during fatigue deformation are identified for affecting cracking behavior and the resultant fatigue life. The weld joint failed at the interface between the ICHAZ and base metal. The initial brief cyclic hardening in the ICHAZ region causes the shift from initial strain accommodation within the stronger microstructures of CGHAZ to strain localization to the interface and leading to the crack initiation.

3 Low angle grain boundaries are increased after fatigue deformation than after PWHT due to the pronounced rearrangement of lath structure into sub-grain structure in CGHAZ and ICHAZ. The initial soft microstructure, ICHAZ exhibits increased sub-grain evolution after cyclic deformation. The higher amount of local strain distribution is due to the larger quantity of LAGBs formation. The extent of the local strain distributions in the vicinities of the LAGBs causes the generation of greater number of cracks and subsequent premature failure of CGHAZ and ICHAZ.

4 The predicted fatigue lives of P91 steel weld joint are comparable with the experimental and the difference falls within ±10%. The resultant fatigue life from empirical relationship means that all major constituent microstructures such as weld metal,

CGHAZ, FGHAZ, ICHAZ and base metal synergistically determine the fatigue life of P91 steel weld joint. The microstructural region, which has lower weighted factor fractions contribute towards the deterioration of fatigue life of actual weld joint of P91 steel.

CHAPTER 7 CREEP-FATIGUE INTERACTION BEHAVIOR

7.1 INTRODUCTION

In between the start-up and shut-down, the on-load service period in the power plant at elevated temperature (typically greater than 40% of the absolute melting temperature), changes the primary deformation and damage mode to creep or creep-fatigue interaction (CFI), respectively. Hence, the CFI behavior of structural components at elevated temperature is important design concern. Such important technological needs warrant an in-depth research on the material behavior under high temperature service conditions. The literature on the studies on the contribution of each constituent region towards the overall behavior of P91 steel weld joint under CFI conditions is yet to be documented. In the present work the study was carried out under various strain-hold durations viz. 1, 10 and 30 minutes at 823 K. However, the present chapter discusses the effect of longest hold duration i.e., 30-minute, on the fatigue behavior of the simulated HAZ and base metal to understand the failure mechanisms that are synergistically operative in the microstructurally heterogeneous actual weld joint of P91 steel. To the extent of the present work, an investigation was carried out on the change in tensile properties of P91 steel base metal subject to interrupted fatigue loading up to the various fractions of fatigue life (5, 10, 30 and 50%) under CFI condition at the accelerated test temperature of 873 K.

7.2 CYCLIC STRESS RESPONSE CURVES AND SOFTENING BEHAVIOR

The cyclic stress responses of base metal, simulated CGHAZ, FGHAZ and ICHAZ under hold time durations, viz. 1, 10 and 30 minutes are illustrated in Fig. 7.1(a)-(c). The overall trends of stress responses with the progressive cyclic deformation under creep-fatigue interaction are similar to the CSR observed for the same microstructures under continuous cycling (LCF) condition (Fig. 6.1). As observed in the LCF condition, under CFI condition the CGHAZ and ICHAZ exhibit the upper bound and lower bound stress responses respectively at all applied hold time durations. The dislocation annihilation and coarsening of lath structure and carbide precipitates ease the deformation process and subsequently lead to the cyclic softening of all microstructures under CFI. The macro crack growth results in large stress drops at the end of the CSR curves. Irrespective of the initial microstructure, the stress response decreases with increase in hold time (Fig. 7.1(a)-(c)). The effect of hold time on the CSRs of various microstructural zones and the actual weld joint is depicted in Fig. 7.1(c). All microstructures show lower stress responses under CFI than that of LCF. As noticed under LCF loading, the simulated ICHAZ and FGHAZ and the actual weld joint also exhibit initial brief (up to 5 cycles) cyclic hardening behavior under CFI loading. The higher stress response of actual weld joint in the initial loading under CFI is due to the localized cyclic hardening behavior of soft ICHAZ.

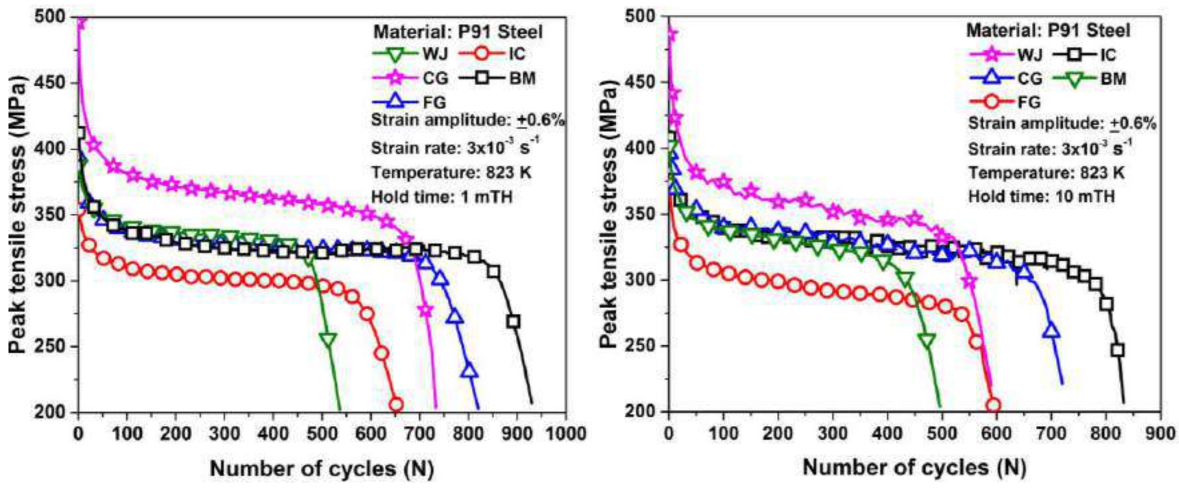

(a) (b)

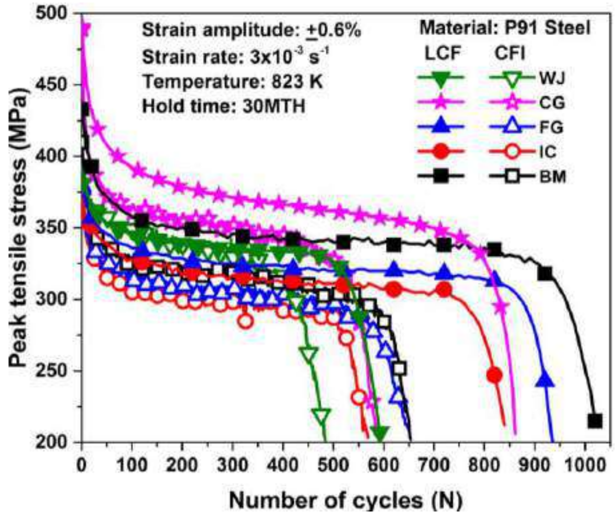

(c)

Fig. 7.1 Cyclic stress response curves of base metal and simulated CGHAZ, FGHAZ and ICHAZ and actual weld joint of P91 steel tested under CFI condition; (a) 1 MTH, (b) 10 MTH and (c) 30 MTH.

During mechanical strain cycling at elevated temperature, the initial lath structure is converted to cell structure or sub-grains with low energy configuration due to the dislocation rearrangement due to shuttling motion [286]**.** Even though the cycle numbers of the stress responses are much lower under CFI, the total duration of the test is an order magnitude longer than the time taken for completing tests under LCF condition at the same test temperature. The extent of duration due to hold application provides sufficient time for the dislocations to get rearranged into completely developed sub-grains or cell structures. With increase in hold duration the sizes of cells or sub-grains also increases [28]. During the strain hold, stress relaxations take place due to the progressive conversion of elastic strain into inelastic strain. The hold duration, size of the sub-grains, the precipitate size and the plastic strain accumulated are interrelated.

Precipitate size analysis was carried out from the scanning electron micrographs of the simulated CGHAZ, FGHAZ and ICHAZ deformed under CFI condition (Fig. 7.2(a)-(c)). The SEM micrographs of CGHAZ, FGHAZ and ICHAZ after loading under CFI condition illustrate tempered martensite microstructures with the hierarchy of PAGs, packets/blocks and lath martensite decorated with the $M_{23}C_6$ at the boundaries and the evenly distributed MX type precipitates in the intra-lath region. The precipitate coarsening is discernible at the grain boundaries than the matrix. Further, it is observed that in the CGHAZ, FGHAZ and ICHAZ, micro voids/cavities appear close to the fracture surface and many of them exist in the boundaries as seen in Fig. 7.2 (a)-(c).

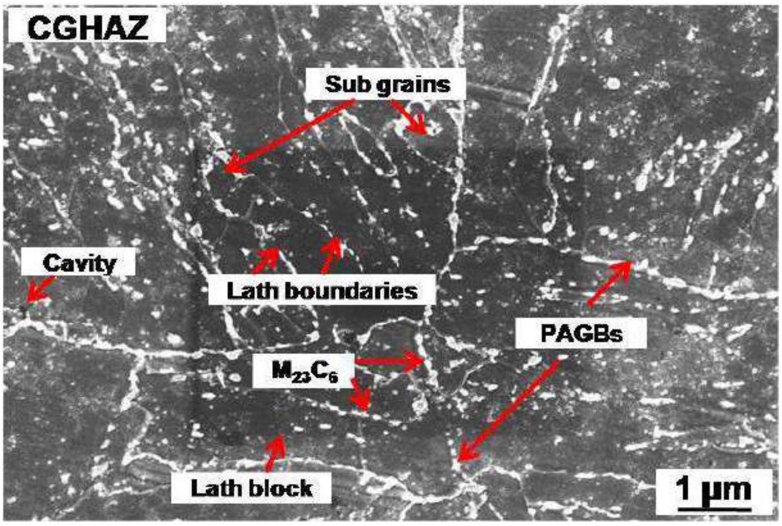

(a)

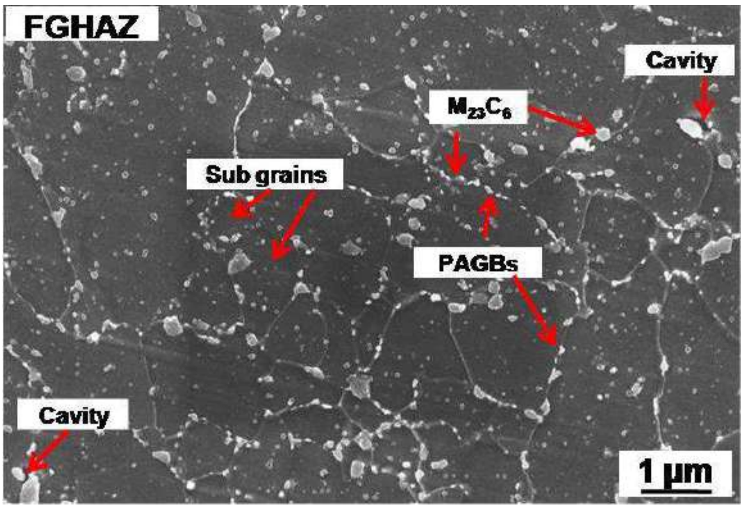

(b)

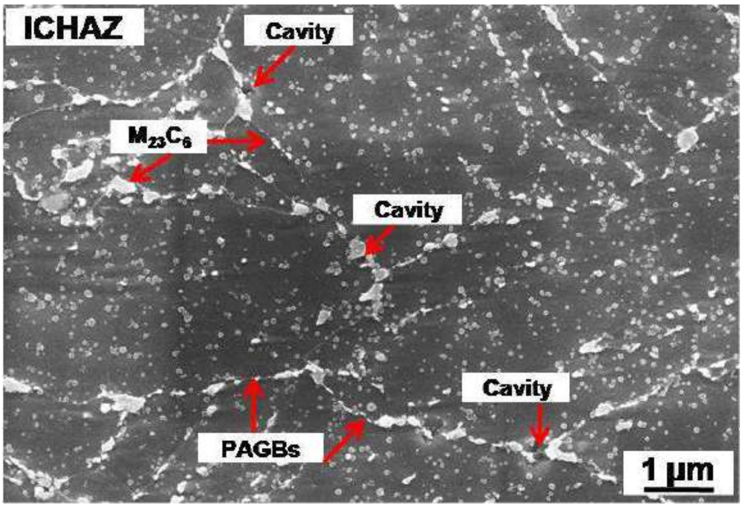

(c)

Fig.7.2 Scanning electron micrographs of simulated (a) CGHAZ, (b) FGHAZ and (c) ICHAZ under 30MTH-CFI at 823 K.

In the ICHAZ the cavities formation is due to the unequal deformation between the differently strengthened freshly formed martensite and the over-tempered ferrite. Considerable amounts of coarsening of sub-grains, carbide precipitates and lath structures are found for all microstructures under CFI condition. Figure 7.3(a) illustrates the precipitate size distributions in the simulated CGHAZ, FGHAZ and ICHAZ after creep-fatigue interaction deformation. The precipitate size in CGHAZ and FGHAZ exhibited a single Gaussian distribution, whereas the ICHAZ exhibited a double Gaussian distribution due to dual phase microstructures comprising both fresh tempered martensite and over-tempered ferrite. The average precipitate sizes of various simulated microstructures of HAZ after creep-fatigue deformation are compared with that of after PWHT (Fig. 7.3(b)). It is found that the difference in the average precipitate sizes between PWHT and CFI tested conditions i.e., precipitate coarsening due to creep-fatigue deformation is higher in the case of CGHAZ than the FGHAZ and ICHAZ. The precipitate coarsening analysis for the continuous cycling is not performed presuming negligible coarsening due to shorter test duration.

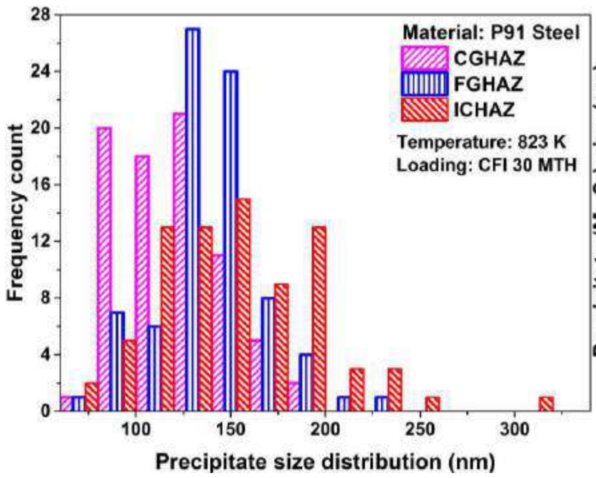

(a)

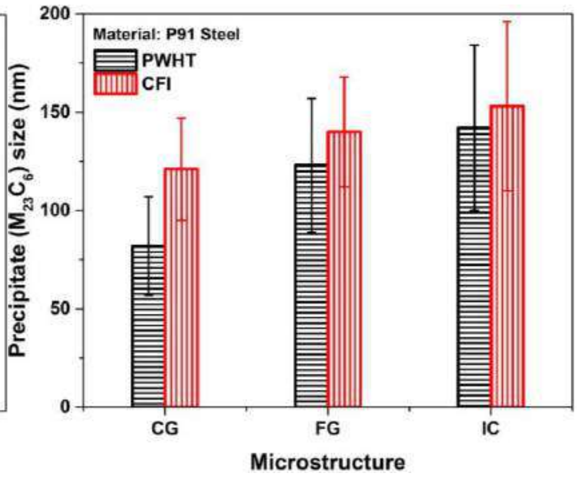

(b)

Fig. 7.3 Plots of (a) precipitate sizes distribution and (b) comparison between average precipitate sizes of simulated CGHAZ, FGHAZ and ICHAZ under CFI and tempering conditions.

A comparison of change in cyclic yield strength and plastic strain accumulations during fatigue deformation with or without strain-hold application is depicted in Fig. 7.4(a) and (b) respectively. Under both the LCF and CFI loadings all microstructures exhibit two-slope behavior in terms of variations in the yield strength and plastic strain. In general, the extent of the decrease in cyclic yield strength with the progressive cyclic deformation under CFI is more pronounced compared to that under LCF. Under CFI loading condition the amount of decrease in yield strengths of CGHAZ, base metal, FGHAZ, ICHAZ and weld joint within the initial 10% of fatigue lives are 182, 176, 139, 110 and 68 MPa respectively, whereas the reduction in the yield strength due to LCF loading are 150, 125, 105, 60 and 75 MPa respectively. The difference of decrease in yield strengths of CGHAZ, FGHAZ between LCF and CFI deformation is 30 MPa, whereas the difference of that for the ICHAZ and base metal is 50 MPa. The decrease in yield strength in case of the ICHAZ during CFI is comparatively higher. This is because even in the PWHT condition, the precipitate size in the ICHAZ is considerably larger than other constituent regions. Exposure to additional time duration in the holding regimes during CFI tests further enhances the sizes of precipitates in this region and results in degradation of strength in the ICHAZ region. As found in the LCF, larger reduction in yield strength under CFI takes place within the initial 10% of fatigue life and only about 20% decrease in yield strength is observed during the remaining deformation up to 50% of fatigue life. It is further interesting that the difference in the yield strength reduction for the actual weld joint between the CFI and LCF condition is insignificant, while there are significant number of differences in the yield strengths of the simulated microstructures and base metal between the fatigue deformation under CFI and LCF conditions. The low amounts of change in yield strength of actual weld joint with the progressive fatigue deformation under CFI and LCF is due to the synergistic effect of localized strain accumulation and deformation constraint between the low volume fraction of soft and large volume fraction of higher strength microstructural regions. The influence of strain-hold application on the plastic strain accumulation after 5% of fatigue life is almost negligible unlike that of continuous cyclic deformation (Fig. 7.4(b)). But the amount of plastic strain accumulated within the 5% of fatigue life under CFI is remarkably higher than even the accumulation of plastic strain up to 50% of fatigue life under LCF. The overall downward shifts of yield strength and upward shifts of plastic strain (Fig. 7.4(a) and (b)) are attributed to the creep during the strain-hold.

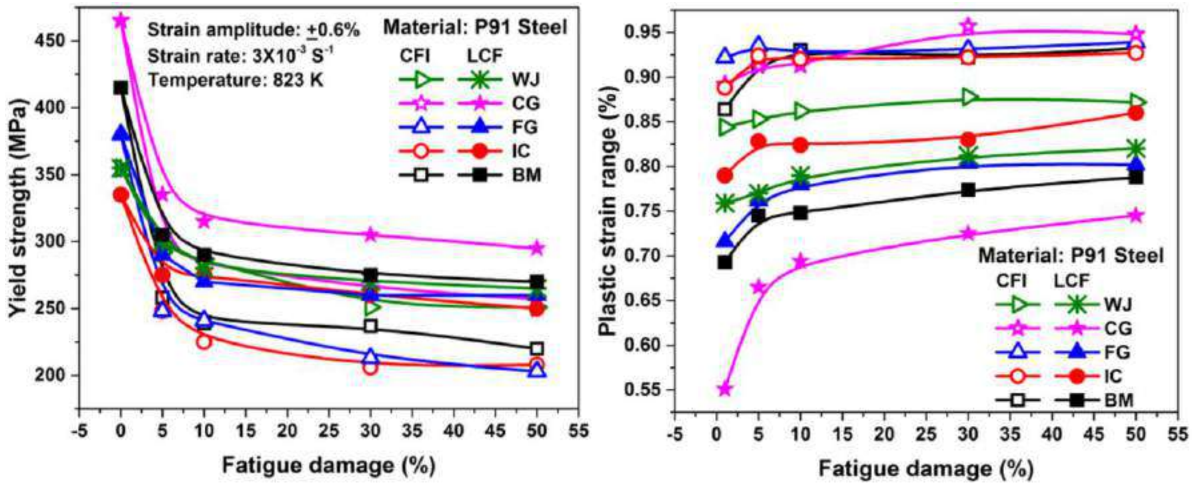

(a) (b)

Fig. 7.4 Comparison of variations of (a) cyclic yield strengths and (b) plastic strain accumulations with the progressive fatigue damage under LCF and 30MTH-CFI conditions at 823 K.

7.3 FATIGUE LIFE AND FRACTURE BEHAVIOR

The hold time effect on the fatigue lives of various constituent microstructures and actual weld joint of P91 steel is shown in Fig. 7.5(a). The fatigue lives of CGHAZ and ICHAZ exponentially decreases with increase in hold duration. Though the base metal and FGHAZ exhibit higher fatigue lives under both the LCF and CFI conditions, their fatigue lives gradually decrease with increase in the hold duration than the saturation in the fatigue lives of CGHAZ, ICHAZ under CFI as shown in Fig. 7.5(a). The actual weld joint shows inferior fatigue lives than the individual, homogenous microstructural regions under both LCF and CFI loadings and it didn't display significant amount of dwell sensitivity (Fig. 7.5(b)). The dwell sensitivity is a parameter that is used to measure the fatigue resistance of a material against the strain/stress-hold fatigue loading and is calculated as the ratio of the number of cycles to failure under CFI loading to the number of cycles to failure under continuous cyclic (LCF) loading. The continuous increases of dwell sensitivities of base metal and FGHAZ with increase of hold time are of concern though their fatigue lives are better than the CGHAZ, ICHAZ and the actual weld joint of P91 steel up to 30 minutes tensile hold.

Figure 7.5(c) illustrates the correlation between the stress relaxation and fatigue lives of base metal, simulated CGHAZ, FGHAZ and ICHAZ of P91 steel under CFI condition at 823 K. From the Fig. 7.5(b), it is observed that the base metal and the simulated CGHAZ and FGHAZ exhibit inverse relationship between the fatigue life and stress relaxation, whereas ICHAZ and the actual weld joint of P91 steel do not show such relations. This implies that the homogenous microstructural regions such as CGHAZ, FGHAZ and base metal show the simple relations while the ICHAZ, which has dual phase microstructure with freshly formed martensite and over-tempered ferrite and actual weld joint, which has complex microstructures do not follow the same.

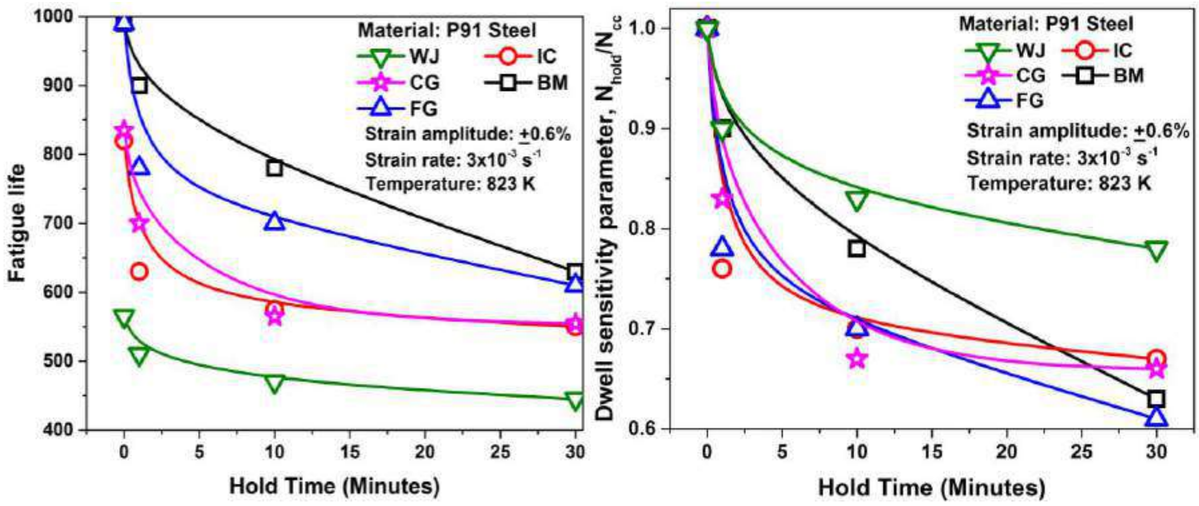

(a) (b)

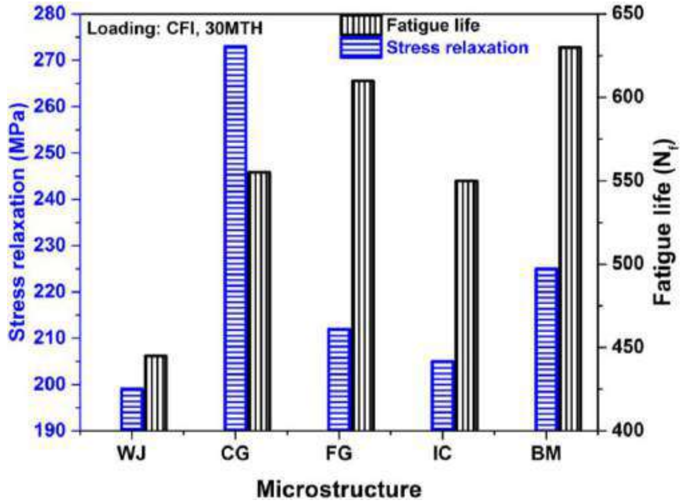

(c)

Fig. 7.5 Hold time effect on (a) fatigue life and (b) dwell sensitivity and (c) correlation between fatigue life and stress relaxation of simulated microstructures and actual weld joint of P91 steel at 823 K.

Representative fractographs of the simulated CGHAZ, FGHAZ and ICHAZ after fatigue tests with the application of 30-minute tensile strain-hold at 823 K are provided in Fig. 7.6(a)-(c). The magnified image of the fractograph of CGHAZ shows (Fig. 7.6(a)) the oxides, which completely masked the fracture surface matrix and striations. The crack propagation marked by fatigue striations are not observed in the fracture surface of CGHAZ under CFI unlike the striations observed in the fracture surface of CGHAZ under continuous cycling. It is found that all microstructural specimens fracture surfaces show multiple crack initiations and subsequent mixed mode of crack propagations. By comparing Fig. 7.6(a) through (c), it is clear that the apparent number density of the crack initiation sites is more in the simulated FGHAZ and could be attributed to the greater number of grain boundaries, which restrict the crack propagations.

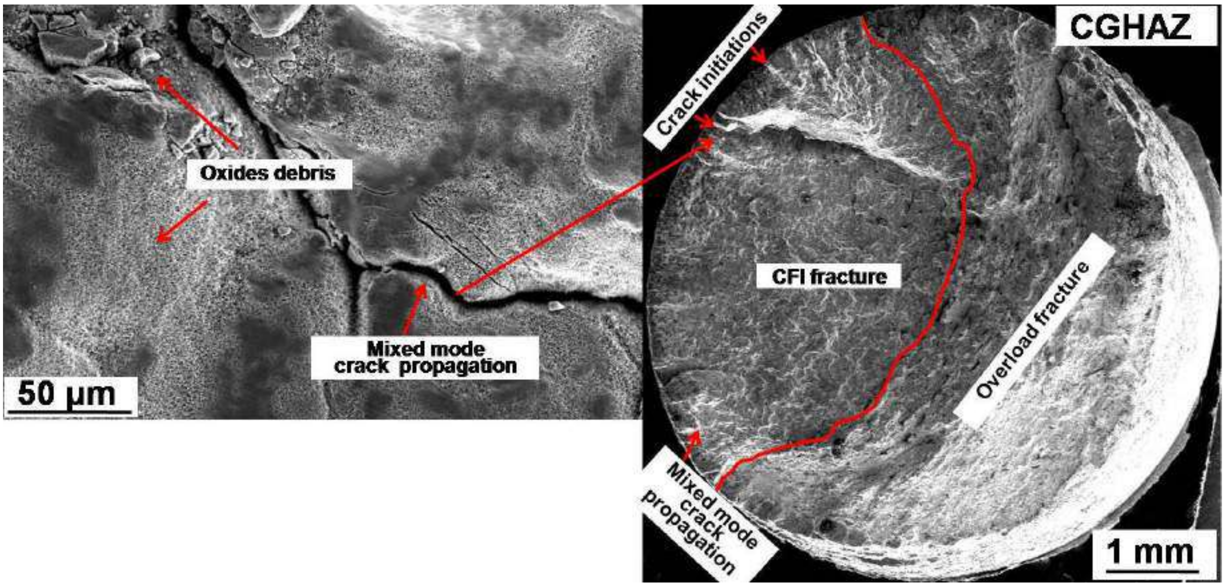
CGHAZ
Crack initiations
Oxides debris
CFI fracture
Overload fracture
Mixed mode
crack propagation
50 µm
Mixed mode
crack
propagation
1 mm

(a)

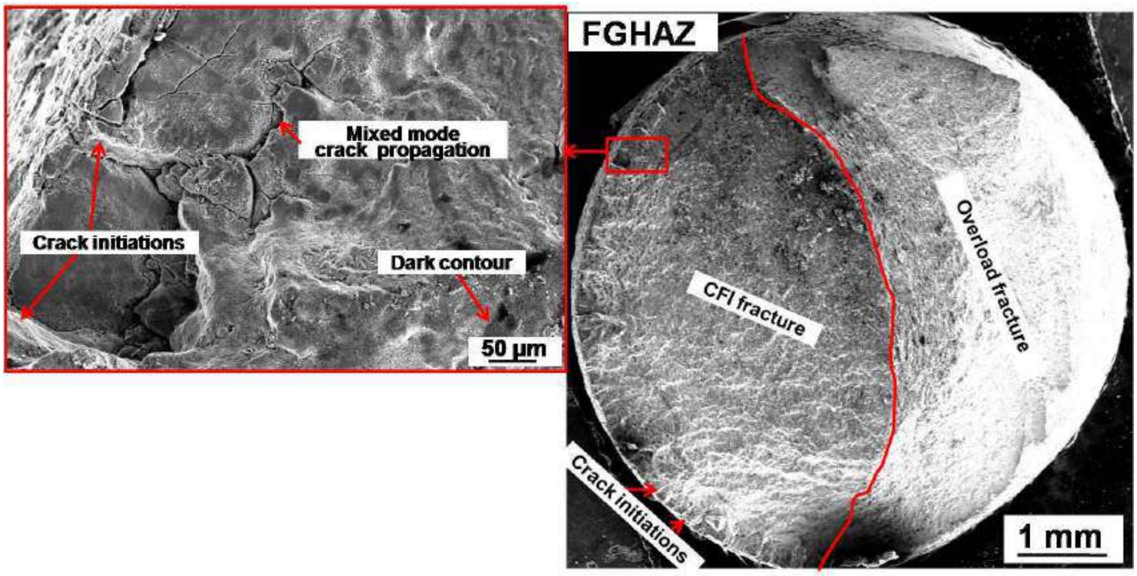
FGHAZ
Mixed mode
crack propagation
Crack initiations
Dark contour
50 µm
CFI fracture
Overload fracture
Crack initiations
1 mm

(b)

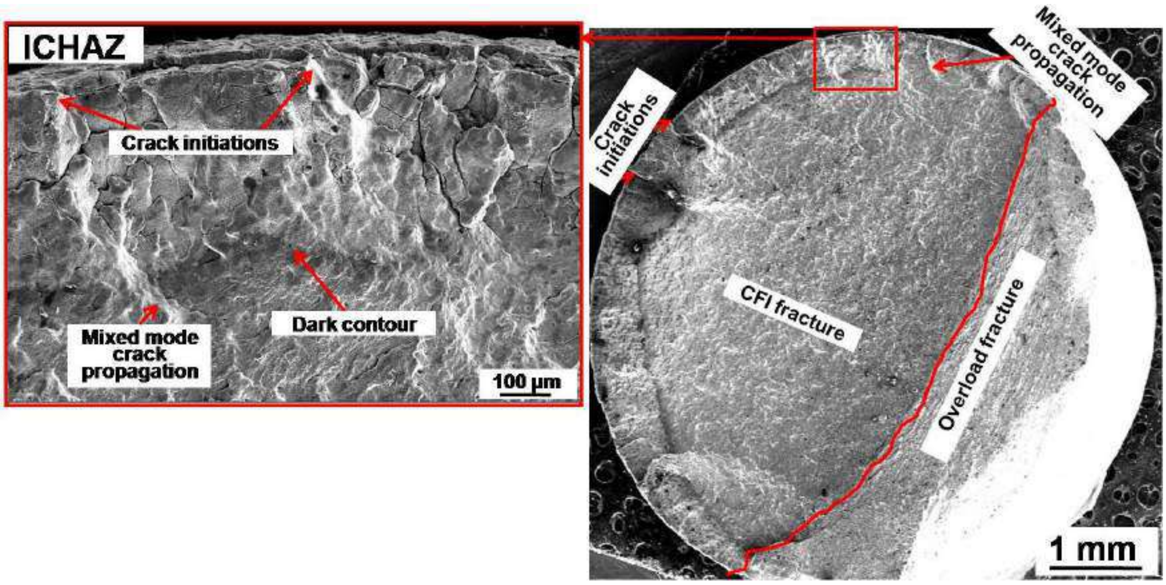

(c)

Fig. 7.6 Fracture surface morphologies of the simulated microstructures of (a) CGHAZ, (b) FGHAZ and (c) ICHAZ of P91 steel under 30MTH-CFI condition at 823 K.

Dark contours in the topography of the fracture surfaces periphery (just 0.75 mm below) in the FGHAZ and ICHAZ are observed as illustrated in Fig. 7.6(b) and (c) respectively. A similar observation in the P91 weld joint has been reported by Vani Shankar et al.[32]. The authors [32] have stated that the dark contour in the periphery of the fracture surface is the indication of cracking due to the linkage of numerous creep cavities, separate or coalesced in these localized regions.

7.4 CRACK PROPAGATION BEHAVIOR

The observation of fatigue performances and the fracture surface features reveals that clear differences exist in fatigue crack growth behavior for the various regions of the weld joint, particularly in the CGHAZ, FGHAZ and ICHAZ. This result is associated with the changes in crack path and the mode of fracture due to microstructural sensitivity of fatigue crack propagation. Figure 7.7(a)-(d) provides the details of the crack propagation path in the simulated HAZs and the base metal during 30-minute strain-hold creep-fatigue deformation. Cracks observed in the P91 steel due to creep-fatigue loading are straight, widely open and filled with oxides [287]. Figure 7.7 presents some of these observations.

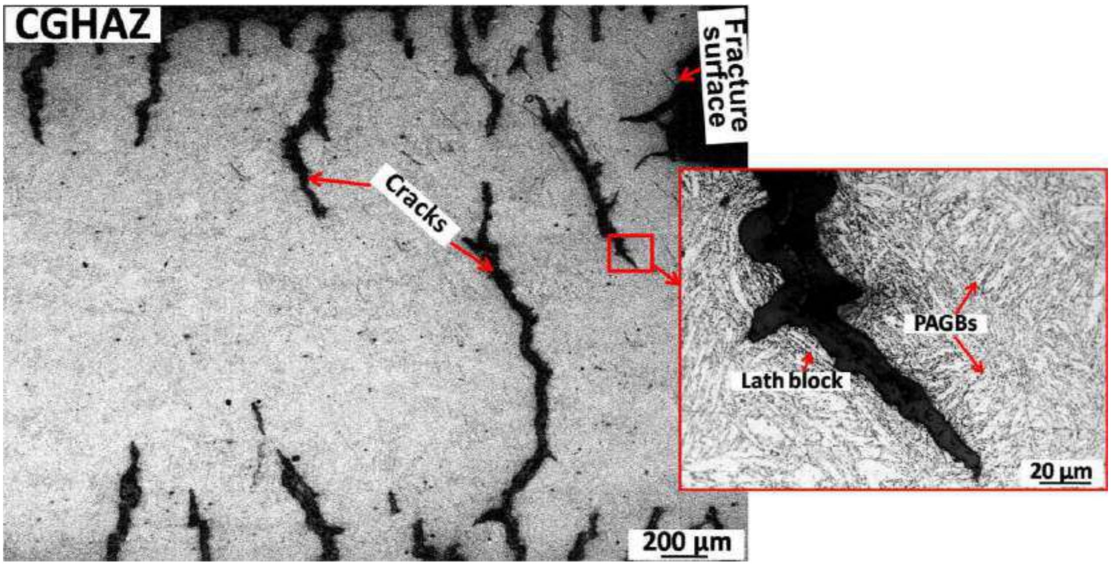

(a)

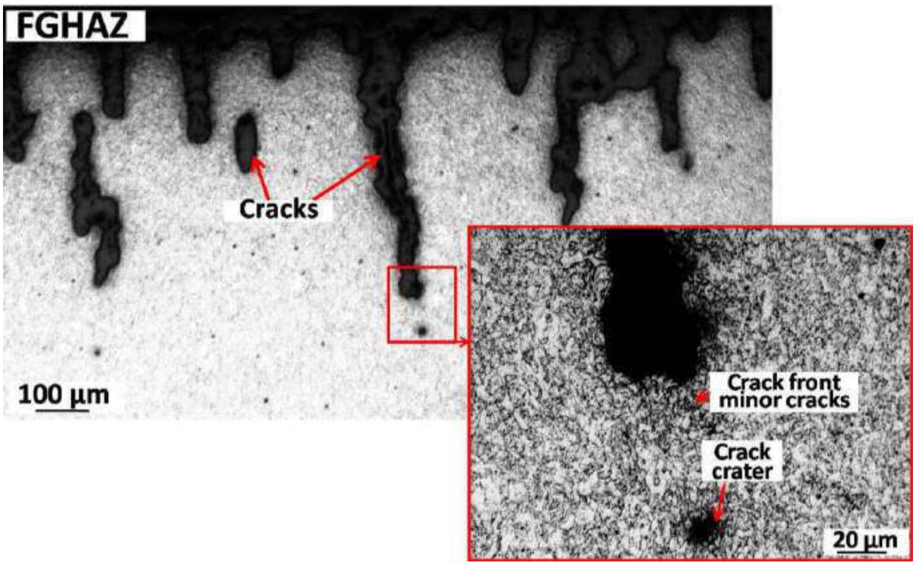

(b)

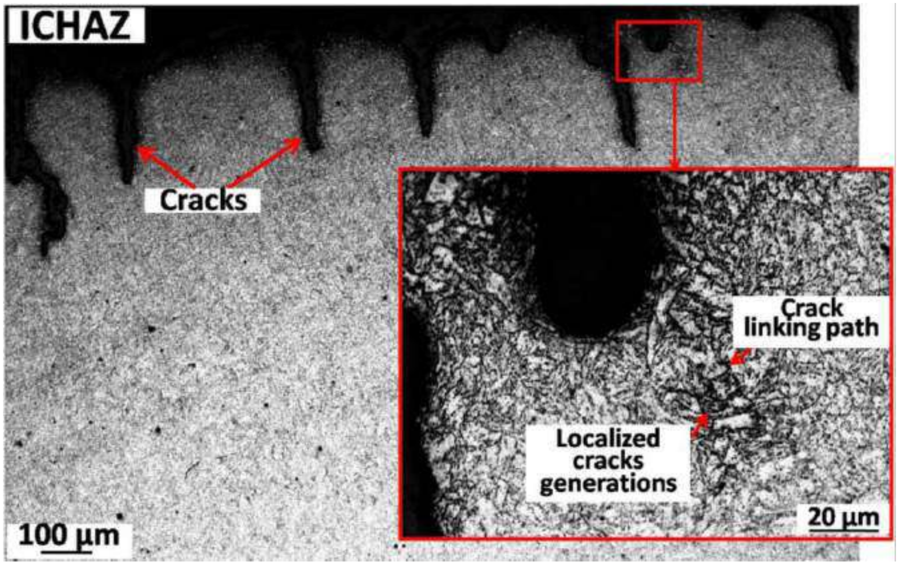

(c)

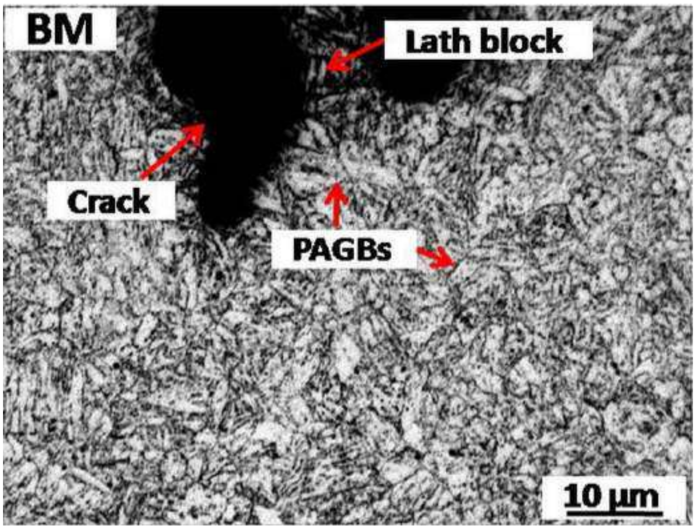

(a)

Fig. 7.7 Optical micrographs of simulated (a) CGHAZ, (b) FGHAZ and (c) ICHAZ and (d) base metal and under 30MTH-CFI condition at 823 K.

As presented in Fig. 7.7(a) multiple long cracks are seen in the specimen of CGHAZ. Crack deflections along the directions of block or lath boundaries are visible. Longer and wider cracks are found in the CGHAZ. More than 50 cracks were observed and measured on one half of the fractured specimen. In the FGHAZ, ICHAZ and base metal, the minor cracks at the crack front get linked and eventually join the major crack. The FGHAZ shows a localized development of crack crater almost equal to a PAG size (Fig. 7.7(b)). Initiations of minor cracks along the lath/block and PAG boundaries and linkage to the major cracks are discernible in the ICHAZ (Fig. 7.7(c)).

The distributions of lengths and widths of cracks in the simulated CGHAZ, FGHAZ and ICHAZ and base metal are depicted in Fig. 7.8(a) and (b). As shown in Fig. 7.8(a) and (b) CGHAZ exhibit longer and wider cracks, which may be due to the presence of lengthy and finer lath boundaries. The thick cracks in CGHAZ could also be due to the applied higher cyclic strain amplitude coupled with longer hold duration. The higher amounts of, comparatively, lower crack widths observed in the ICHAZ may be attributed to the presence of islands of soft over-tempered α-ferrite.

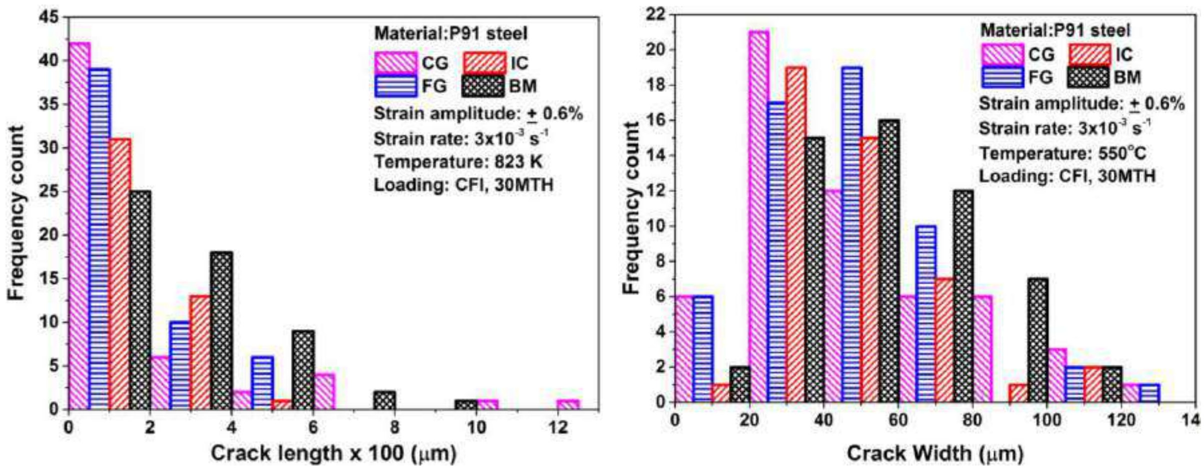

(a) (b)

Fig. 7.8 Cracks distributions under 30 MTH at 823 K; (a) length and (b) width.

7.5 HARDNESS VARIATION AND FAILURE LOCATION IN THE ACTUAL WELD JOINT

Analysis was carried out on the failed sample of actual weld joint of P91 steel to understand the deformation and damage mechanism under 30-minute strain-hold fatigue condition. It is well known that the hardness values of precipitation/solid solution strengthened steel decreases during mechanical loading due to substructural recovery and coarsening of strengthening carbides. Hence, hardness profiles across the weld joint after PWHT and LCF and CFI tests are compared. It is clear from Fig. 7.9 that there are overall downward shifts of the hardness profiles of the samples under LCF and CFI loadings compared to after PWHT. The decrease in the hardness profile across the weld joint due to continuous cycling (LCF) reiterate here. Under CFI, further decrease in the hardness values across the weld joint indicates the occurrence of time dependent processes such as substructural and carbide coarsening due to the application of strain-hold in the cyclic deformation.

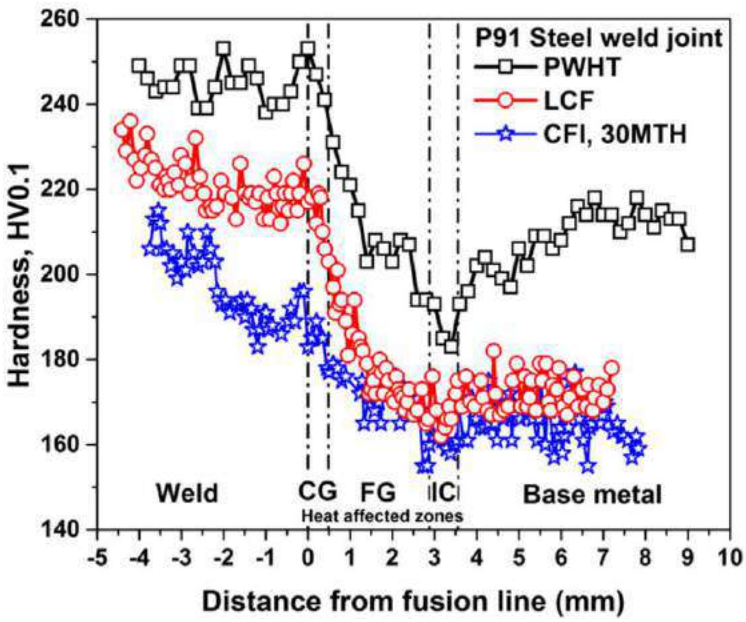

Fig. 7.9 Variation of hardness profiles across the weld joint microstructures after PWHT and LCF and CFI tests.

The optical micrographs of longitudinal section of full-length actual weld joint specimen failed due to creep-fatigue loading were collaged as shown in Fig. 7.10. This single collaged micrograph assists to identify the origin of main crack that might have led to final fracture. The distance of the fracture from the fusion line, as illustrated in Fig. 7.10, clearly indicates that the weld joint failed at the interface between ICHAZ and FGHAZ, which is typically known as Type IV cracking. From the microstructure viewpoint, the occurrence of Type IV cracking is due to the creep-vulnerability of small grains and coarse precipitates. Occurrence of high frequency HAGBs and the highest fraction of recrystallized grains and the largest precipitate-distribution heterogeneity are some observations that are in line with occurrence of Type IV cracking [71]. As has been already discussed in Chapter 6 about the failure location in the actual weld joint due to continuous cycling (LCF), under the CFI loading condition the initial cyclic hardening behavior of soft ICHAZ causes the shift of the strain localization towards the other regions of the weld joint. Brief cyclic hardenings are clearly observed in the CSRs of simulated ICHAZ and actual weld joint (Fig. 7.1(c)). Unlike during LCF, where the strain localization is shifted towards the base metal region, under CFI the strain localization is shifted towards the FGHAZ. In the previous Chapters it has been reported that the failure locations under monotonic tensile (test is completed within few minutes) and continuous cyclic loadings (test duration is 2 to 3 h) are well within the base metal (Fig. 5.4) and the interface between the base metal and ICHAZ (Fig. 6.12) respectively. Further, under the creep-fatigue interaction loading (test duration is about 2 weeks) the failure location of the weld joint is identified at the interface of ICHAZ and FGHAZ. This clearly implies that the failure location in the P91 weld joint directly related to the time dependent deformation processes. But it does not mean that the failure location in the weld joint shifts from the base metal towards the weld metal with the increase of test duration. However, it may be concluded that the longer hold (creep) duration and low applied strain range may provide the possibility of creep strain concentration at the weak inter-critical zone though it exhibits the initial hardening behavior. Overall, from the present observation, it is further concluded that the factors such as initial hardening behavior, low volume fraction and inadequate total hold (creep) time synergistically defer the strain localization and subsequent failure at the ICHAZ of the P91 steel weld joint.

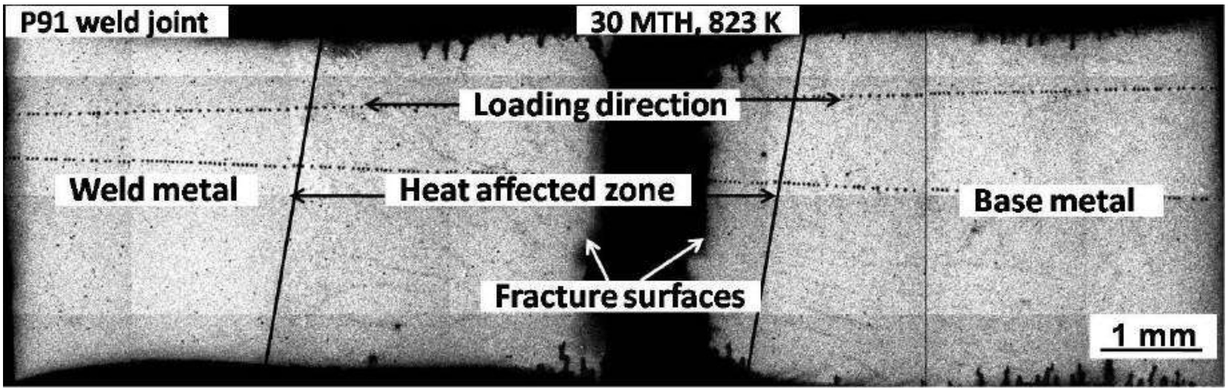

Fig. 7.10 Collaged optical micrograph of actual weld joint of P91 steel failed under 30MTH-CFI condition at 823 K.

The region wise formation of cracks in the actual weld joint, as appeared in Fig. 7.10, is validated through the cracks distribution measurement as shown in Fig. 7.11(a)-(c). More than 50% of the total number of cracks in the actual weld joint is generated in the base metal region and the remaining cracks are shared between the weld metal, FGHAZ and ICHAZ regions. The uneven crack distribution depends upon the volume fraction of each region and their plastic strain accommodating capability. The greater number of strain reversals under continuous cycling (LCF) attributes to the generation of larger number of cracks (Fig. 7.11(c)). The creep strain accumulation in the base metal region, which occupies the larger volume fraction of actual weld joint increases the number fraction of cracks under CFI. Overall, the stronger regions such as weld metal and CGHAZ do not show cracks generation due to their self-resistance to the plastic deformation under both LCF and CFI conditions.

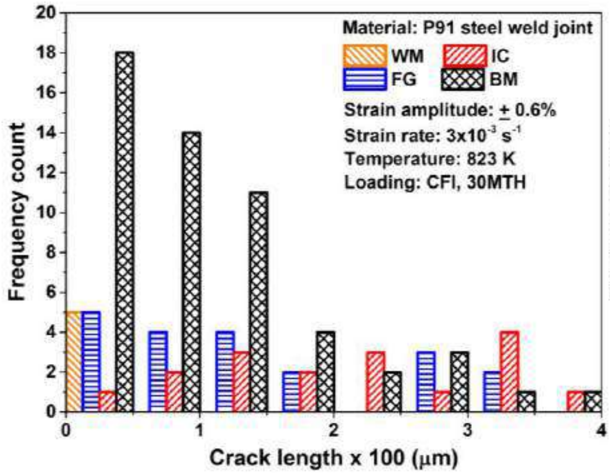

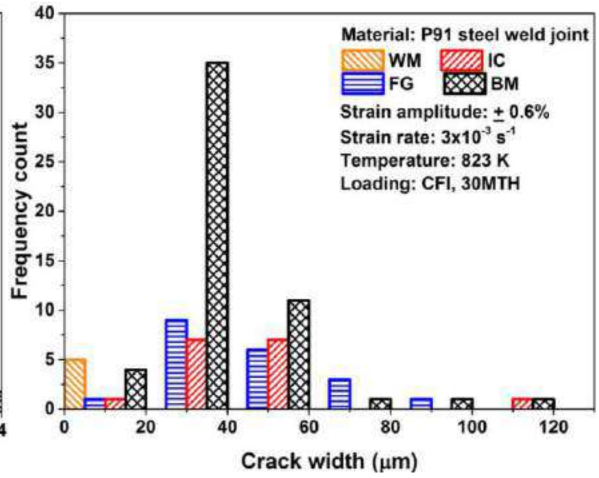

(a) (b)

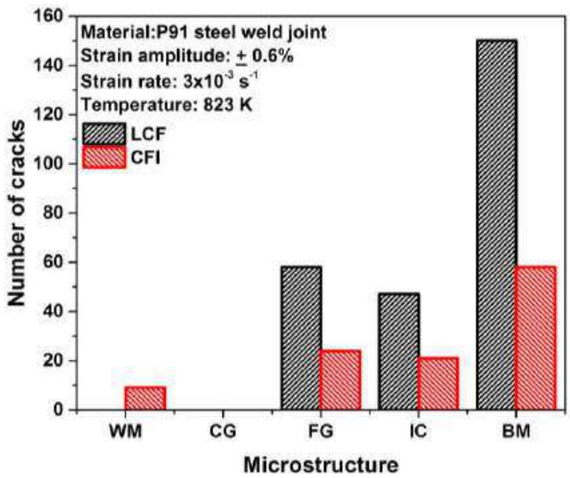

(c)

Fig. 7.11 Cracks distributions; (a) length and (b) width and (c) comparison of total number of cracks in the actual weld joint tested under LCF and CFI conditions at 823 K.

7.6 SUBSTRUCTURE EVOLUTION AND PROPERTY CORRELATION

The grain boundary maps in Fig. 7.12(a)-(h) illustrate a two-scale boundary structures in base metal and simulated CGHAZ, FGHAZ and ICHAZ after PWHT and creep-fatigue deformation. After PWHT the base metal and the CGHAZ microstructures consist of more LAGBs compared to the microstructures of FGHAZ and ICHAZ. This means that soaking at the temperatures higher than 1273 K generates a greater number of LAGBs. Irrespective of the initial microstructures the deformation induces the formation of LAGBs extensively, which is discernible in the representative Fig. 7.12 (right column) of samples tested under CFI. The relative frequencies of HAGBs and the LAGBs for the base metal, simulated CGHAZ, FGHAZ and ICHAZ are calculated and given in Table 7.1. The ratio of LAGBs/HAGBs for the CGHAZ and ICHAZ decreases after CFI deformation, while it increases due to LCF (without strain-hold). The ratio of LAGBs/HAGBs in FGHAZ continuously decreases under both the LCF and CFI loadings. The considerable amount of decrease in ratio of LAGBs to HAGBs from 1.54 to 0.89 in FGHAZ signifies the decline of the stability of lath structure during exposed to the high creep temperature and strain. This attributes to the continuous decrease of fatigue life of FGHAZ under CFI compared to CGHAZ and ICHAZ that exhibit the saturation in the fatigue lives after 10-minute hold duration (Fig. 7.5(a)).

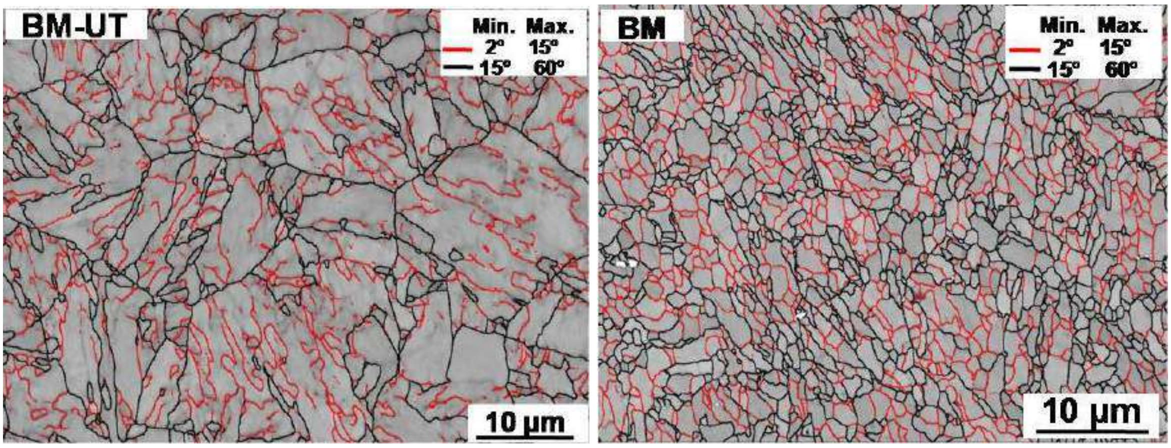

(a) (b)

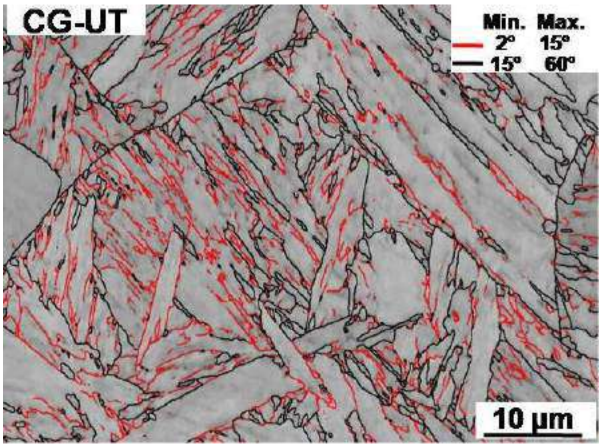
CG-UT
Min. Max.
2° 15°
15° 60°
10 µm

(c)

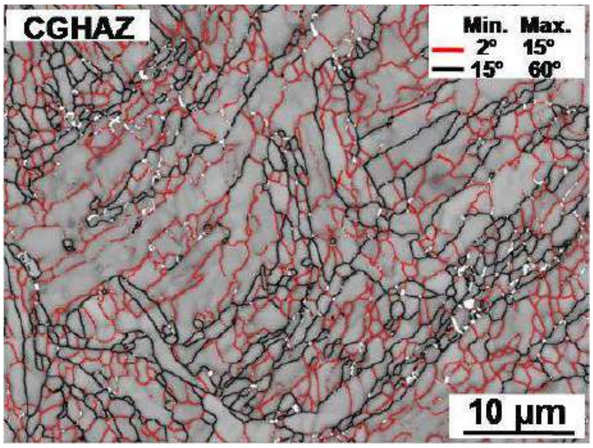
CGHAZ
Min. Max.
2° 15°
15° 60°
10 µm

(d)

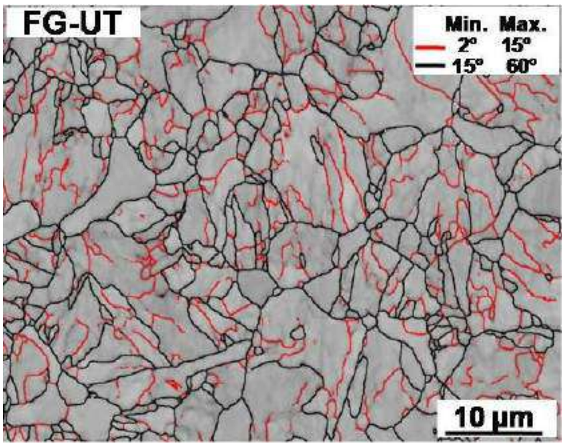
FG-UT
Min. Max.
2° 15°
15° 60°
10 µm

(e)

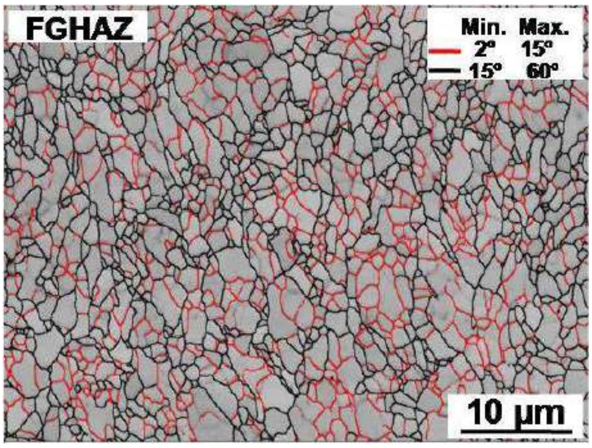
FGHAZ
Min. Max.
2° 15°
15° 60°
10 µm

(f)

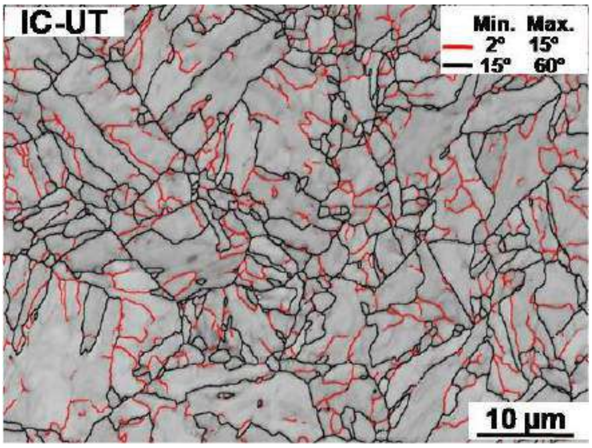

(g)

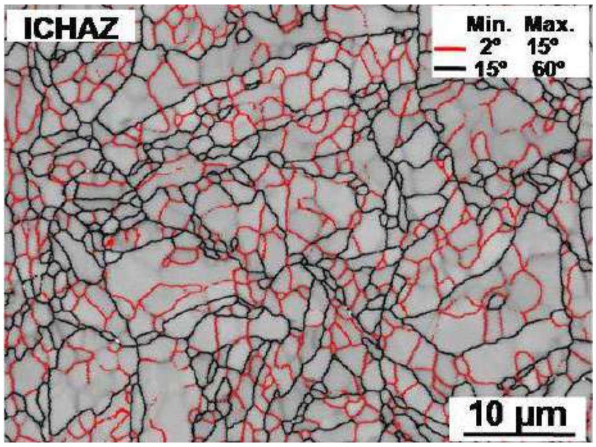

(h)

Fig. 7.12 Grain boundary misorientations maps of (a and b) base metal and simulated (c and d) CGHAZ, (e and f) FGHAZ and (g and h) ICHAZ after PWHT (left) and 30MTH-CFI deformation (right) at 823 K.

Substructural distributions in the simulated CGHAZ, FGHAZ and ICHAZ and base metal after creep-fatigue deformation are illustrated in Fig. 7.13(a). The sub-grain size was measured employing the misorientation angle between 15 to 2°. In general, the following main contributors lead to the non-equilibrium substructures formation in the HAZ: (1) the evolutions of dominant structure attributable to the heat treatment temperatures and (2) the variations of local structure arising from the structural inhomogeneities in the as-received base metal [71]. As shown in Fig. 7.13(a), the base metal and CGHAZ exhibit higher frequency formation of low size sub-grains (< 2μm). The higher range of substructures coarsening is observed in the CGHAZ and ICHAZ. The sub-grain sizes of each region measured from EBSD grain boundary maps are listed in Table 7.1.

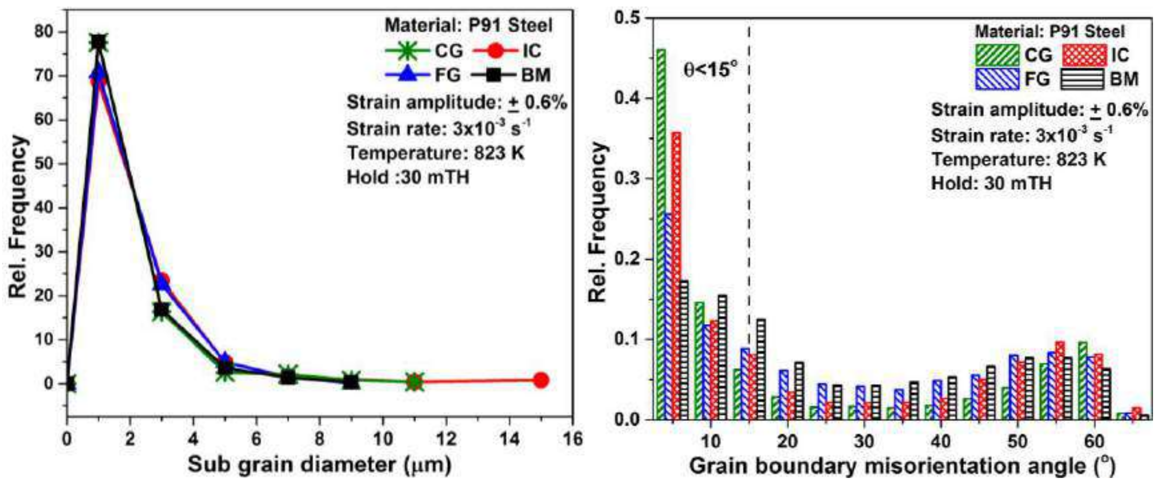

(a) (b)

Fig. 7.13 Plots of (a) substructures sizes and (b) grain boundary misorientations distributions.

Misorientation distributions of grain boundaries in base metal, simulated CGHAZ, FGHAZ and ICHAZ due to creep-fatigue deformation are shown in Fig. 7.13(b). Among the HAZ microstructures, the FGHAZ shows the uniform higher frequency distributions of HAGBs. On the other hand, the CGHAZ maintains the higher number of LAGBs even after creep-fatigue deformation. The ICHAZ exhibits significant amount of formation of both LAGBs and HAGBs after creep-fatigue deformation. This is due to the difference in the initial density fraction of PAGs in the dual phase structures such as tempered martensite and over-tempered α-ferrite. Whereas the initial soft ferrite leads to the formation of HAGBs the fresh martensite transformed to tempered martensite on tempering account for the formation of LAGBs on deformation.

Figure 7.14(a)-(d) illustrates the maps of the deformed, substructured and recrystallized grains in base metal, simulated CGHAZ, FGHAZ and ICHAZ due to creep-fatigue deformation. The percentage of area fraction for each of the three kinds of matrix grains is calculated and given in Table 7.1. Among the HAZ microstructures, the FGHAZ exhibit the highest amount of recrystallization (64.1%) followed by ICHAZ (46.6%) and CGHAZ (25.5%). But the increase in the recrystallization fraction in CGHAZ due to creep is significantly high, i.e., ~10 times compared to ~3 times due to pure LCF from the PWHT condition. On the contrary, the FGHAZ, due to creep-fatigue deformation, depicts the lowest fraction of substructured (34.1%). The highest substructured observed in the CGHAZ (73.5%), while the ICHAZ has the substructured grain matrix of 53.1%. There is no substantial variation in the fraction of deformed matrixes of grains for all microstructures including base metal even after the LCF and CFI deformations.

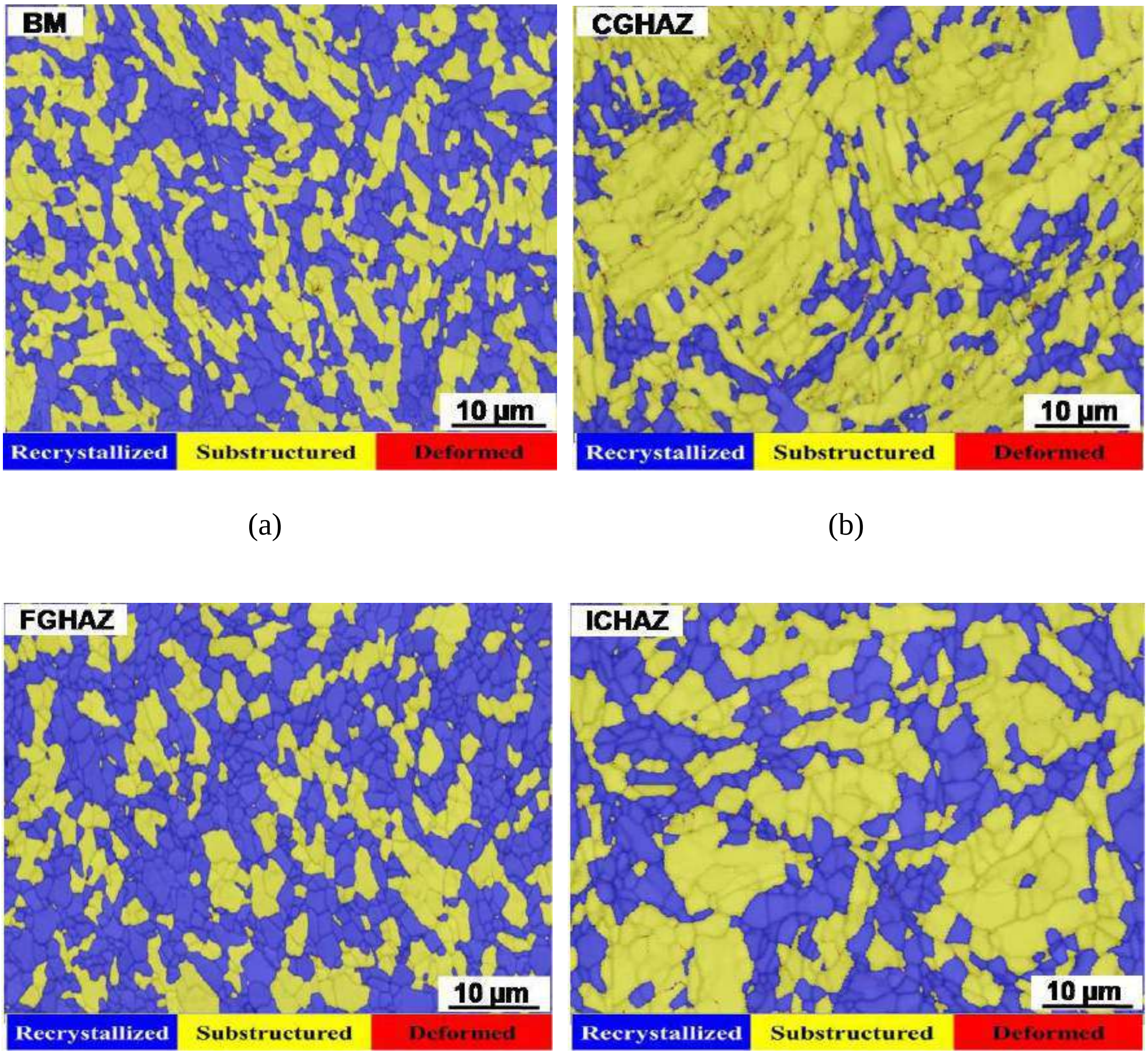

(a) (b)

(c) (d)

Fig. 7.14 Microstructural changes in terms of substructured, recrystallization and deformed fractions in the specimens of (a) base metal, simulated (b) CGHAZ, (c) FGHAZ and (d) ICHAZ of P91 steel weld joint tested under 30MTH-CFI condition at 823 K.

Correlation between fatigue life against the microstructural changes in terms of substructured and recrystallization due to CFI deformation is shown in Fig. 7.15. In general, it is clear that the fatigue lives of CGHAZ and ICHAZ decreases with the increase of substructural coarsening and decrease of recrystallization. Conversely, higher rate of recrystallization and low amount of substructural coarsening occur in FGHAZ and base metal during creep-fatigue deformation. Though the fatigue life of ICHAZ is lower than the CGHAZ the extent of substructural coarsening is not as in the case of CGHAZ due to the dual-phase complex microstructure in the ICHAZ.

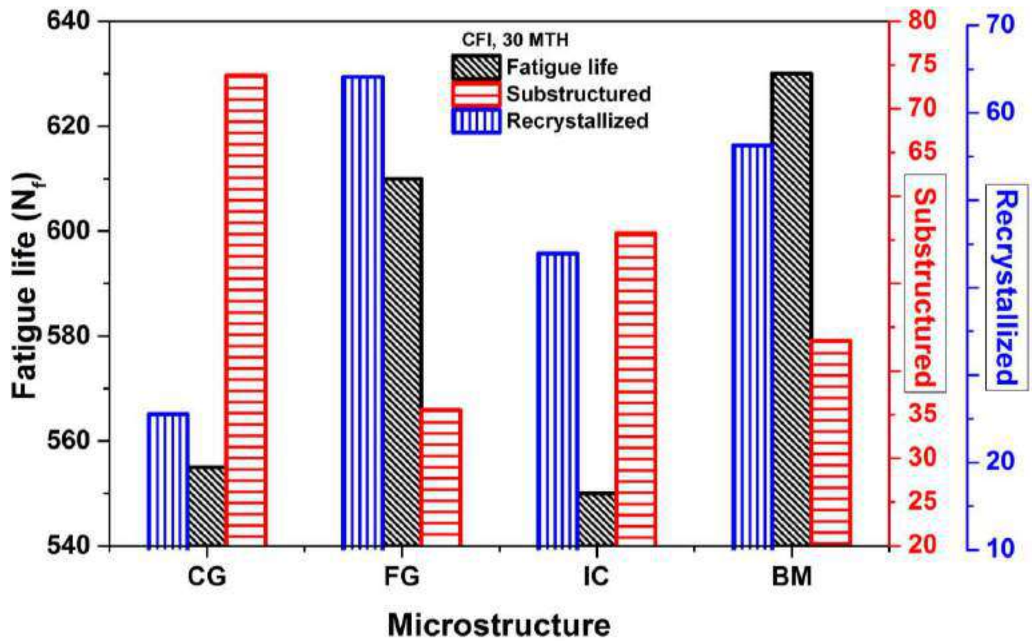

Fig. 7.15 Fatigue lives variations with the microstructural changes in the simulated CGHAZ, FGHAZ and ICHAZ and base metal of P91 steel weld joint tested under 30MTH-CFI condition at 823 K.

Table 7.1 Comparison of EBSD results associated with microstructural changes in simulated microstructures of P91 steel HAZ after PWHT and LCF and CFI tests.

Microstructures		CGHAZ			FGHAZ			ICHAZ		
Conditions		PWHT	LCF	CFI	PWHT	LCF	CFI	PWHT	LCF	CFI
Grain boundaries fractions (%)	LAGB	74.1	78.5	67.7	61.2	53.1	47.0	58.6	63.8	57.5
	HAGB	25.9	21.5	32.3	39.8	46.9	53.0	41.6	36.2	42.5
	LAGB/HAGB	2.86	3.65	2.10	1.54	1.13	0.89	1.41	1.76	1.35
Sub-grain size$_{avg}$ (Standard deviation, μm)		0.98 (±1.79)	1.07 (±1.67)	1.54 (±1.61)	2.15 (±2.26)	1.74 (±2.14)	1.70 (±1.36)	2.12 (±2.51)	2.47 (±2.49)	2.02 (±1.97)
Max. frequency of KAM angle (°)		0.35	0.25	0.15	0.25	0.25	0.25	0.25	0.25	0.25
Microstructural changes	Substructured	96.8	90.7	73.5	92.1	65.2	35.6	89.4	83.6	53.1
	Recrystallized	2.11	7.8	25.5	7.6	34.4	64.1	10.3	15.9	46.6
	Deformed	1.07	1.5	0.65	0.3	0.4	0.3	0.3	0.5	0.3

7.7 OPTIMIZATION OF WEIGHTED/CONTRIBUTION FACTORS OF EACH CONSTITUENT REGION FOR ESTIMATING THE FATIGUE LIFE OF ACTUAL WELD JOINT

The fatigue life weighted/contribution factors for each region to estimate the overall fatigue lives of actual weld joint under LCF and CFI conditions are illustrated in Fig. 7.16(a). The fatigue life weighted factors of the CGHAZ, FGHAZ and FGHAZ and base metal under CFI are derived from the Eq. 6.4. The Fig. 7.16(a) also shows the optimized weighted factors of each microstructural region that can be used to estimate the fatigue lives of actual weld joint under both LCF and CFI loading conditions. The optimized factors for each constituent region of weld joint were derived with the adjustment of the factors values within the standard deviations. Due to the limitation in the specimen fabrication experiments are not carried out for the weld metal under CFI condition. The fatigue lives of weld metal under CFI for 1, 10 and 30-minute hold are estimated using the empirical relation (Eq. 7.1). The predicated fatigue lives of weld metal as shown in Fig. 7.16(b) are following the similar trends of other microstructures. The predicted fatigue lives of actual weld joint of P91 steel using Eq. 7.1, with the applying of the optimized weighted factors of individual microstructural region are comparable with that of experimental under both LCF and CFI conditions (Fig.7.16(c) and (d)). The fatigue lives weighted/contribution factors of the regions of weld joint for LCF and CFI alone and the optimized factors for both the conditions are given in Table 7.2. Among the microstructures of HAZ, ICHAZ exhibits low weighted/contribution factor, which means that it substantially contributes in the decrease of fatigue life of actual weld joint. Presence of micro defects and complex multi layers microstructures due to the repeated heating and cooling during welding, consequent poor ductility account for the extremely low value of weighted/contributing factor of weld metal.

$$N_{f\,wj} = 0.45N_{f\,bm} + 0.29N_{f\,ic} + 0.37N_{f\,fg} + 0.31N_{f\,cg} - 2.3N_{f\,wm} \qquad \text{----(7.1)}$$

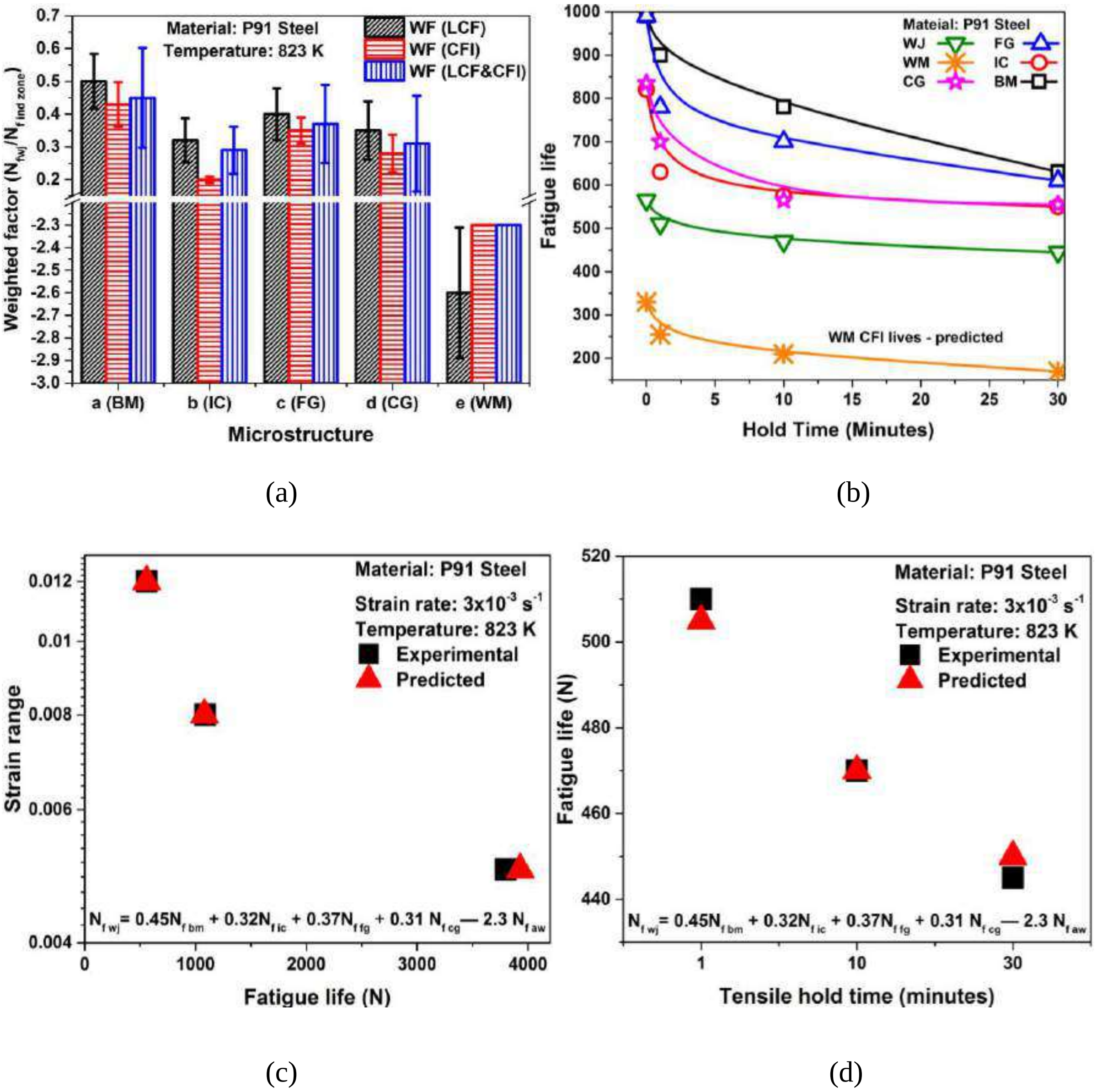

Fig. 7.16 Plots of (a) fatigue life weighted/contribution factors for individual mirostructural region, (b) predicted CFI lives of weld metal and comparison of fatigue lives between predicted and experimental results (c) LCF and (d) CFI at 823 K.

Table 7.2 Weighted/contribution factors indicating the amount of contribution of the individual microstructural region for the fatigue lives of P91 weld joint under LCF and CFI conditions at 823 K.

Notation (Microstucture)	LCF		CFI		Both (LCF&CFI)	
	WF/DF	SD (±)	WF/DF	SD (±)	WF/DF	SD (±)
a (BM)	0.5	0.084	0.43	0.068	0.45	0.1
b (IC)	0.4	0.079	0.35	0.04	0.37	0.08
c (FG)	0.35	0.089	0.28	0.057	0.31	0.12
c (CG)	0.32	0.067	0.2	0.01	0.29	0.1
d (WM)	-2.6	0.29	-2.3		-2.3	

7.8 PRIOR CREEP−FATIGUE INTERACTION DAMAGE ON TENSILE PROPERTIES OF P91 STEEL BASE METAL

When the welded components are put into service involving complex loading conditions, the mechanical properties of the component decline steadily with service [288,289]. Thus, the deprivation of the mechanical properties has serious implications on the safety of structures or components thus warranting attention from the viewpoint of design. Since, the same component is evaluated for service under various modes of loading like fatigue, creep or monotonous loading, it is essential to understand how these test conditions influence each other during actual service condition. This knowledge is essential for guarding against failures and for remnant life assessment. In these components as failure due to fatigue is most dominant, knowledge of the effect of prior fatigue loading on the tensile properties of the material used in structures can be an important design input. Therefore, the present investigation is extended to evaluate the prior fatigue damage on the tensile properties of base metal under CFI condition at 873 K.

The variation of the tensile properties such as yield strength (YS), ultimate tensile strength (UTS), total and uniform elongations with the amount of prior strain cycling under both LCF and CFI conditions is depicted in Fig. 7.17(a)-(d) for base metal of P91 steel. It is evident that under both LCF and CFI conditions, the yield strength/UTS decreases with respect to the as-received steel (Fig. 7.17(a) and (b)). As discussed above in the Section 7.2, a two-slope behavior is observed in the plot of yield strength versus life fractions; in the initial up to 10% of fatigue life the yield strengths of the specimens subjected to the prior LCF and CFI damages are almost equal. The change in yield strength from 10 to 50% of fatigue life, under LCF is almost saturated as compared to that of under CFI condition. The initial yield strength is 389 MPa. During the initial 10% of the fatigue life, the decrease of yield strength is about 80 MPa under both LCF and CFI. During the damage from 10 to 50% of fatigue life, under LCF, a further decrease of only 25 MPa is observed, whereas under CFI, the yield strength considerably decreases about ~115 MPa. The significant decrease in yield strength has a large practical implication since the overall performance of a component might get affected due to the cyclic softening due to LCF and CFI loadings. The change in total elongation/uniform elongation under LCF is between 2 to 3% and that under CFI it is between 5 to 9% (Fig. 7.17(c) and (d)). This implies that whereas the yield strength/UTS are quite sensitive, the ductility is not significantly affected due to the prior fatigue loadings under LCF and CFI conditions.

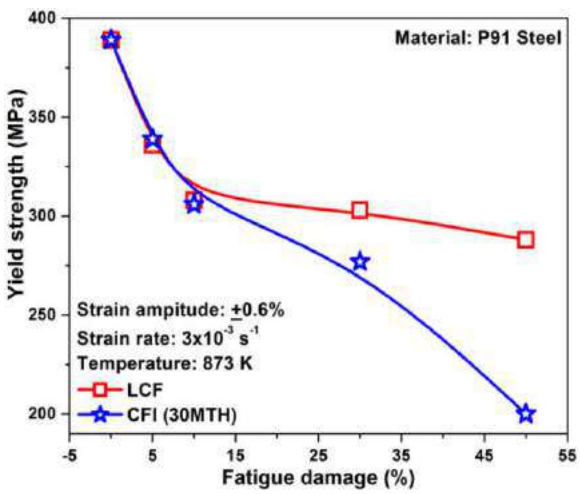

(a)

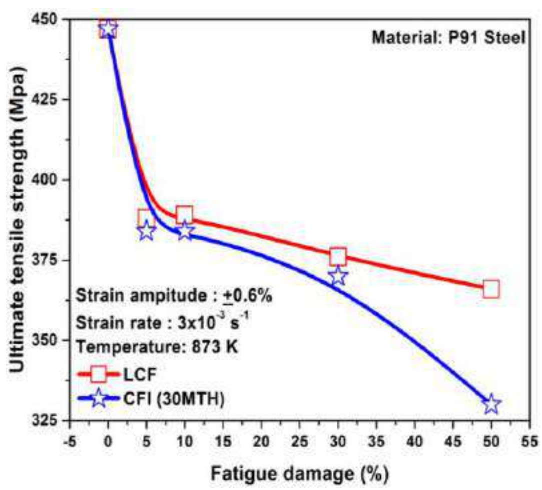

(b)

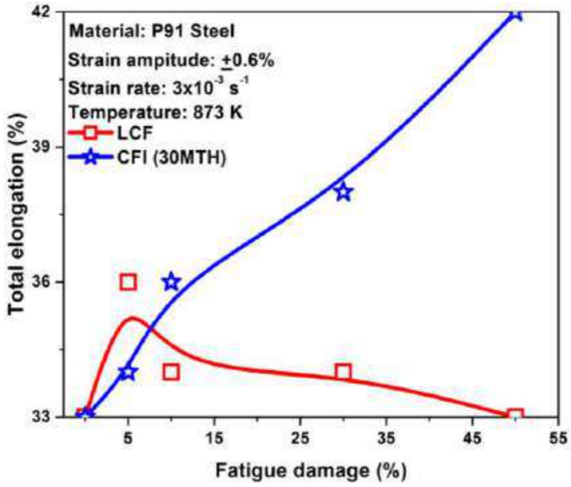

(c)

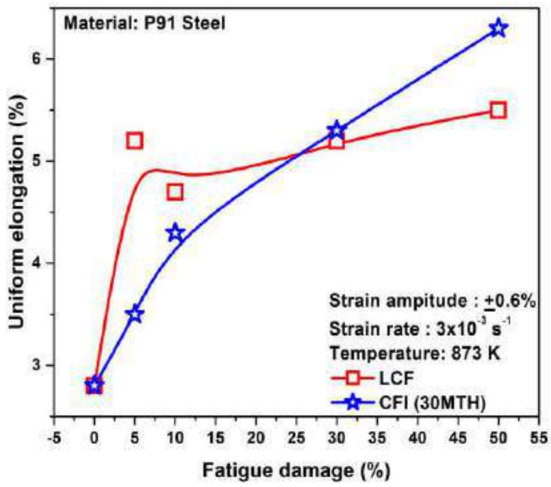

(d)

Fig. 7.17 Change in tensile properties; (a) yield strength, (b) tensile strength, (c) total elongation and (d) uniform elongation of P91 steel base metal due to fatigue damage at 873 K.

The yield strength reduction and the extent of stress relaxation with progressive fatigue deformation under CFI condition at 873 K is illustrated in Fig. 7.18. The yield strength is inversely related to the stress relaxation. The creep in the CFI loading increases the plastic strain accumulation and thereby increases the stress relaxation. The decrease in yield strength has been related to the microstructural coarsening due to the fatigue deformation under CFI. However, the strength loss due to fatigue damage beyond 30% of fatigue life has also been associated with the oxidation at this test temperature. Therefore, the higher amount of stress relaxation than the yield strength beyond 30% of fatigue life is likely to be related with the oxidation assisted surface cracks in addition to the coarsening of substructures and precipitates.

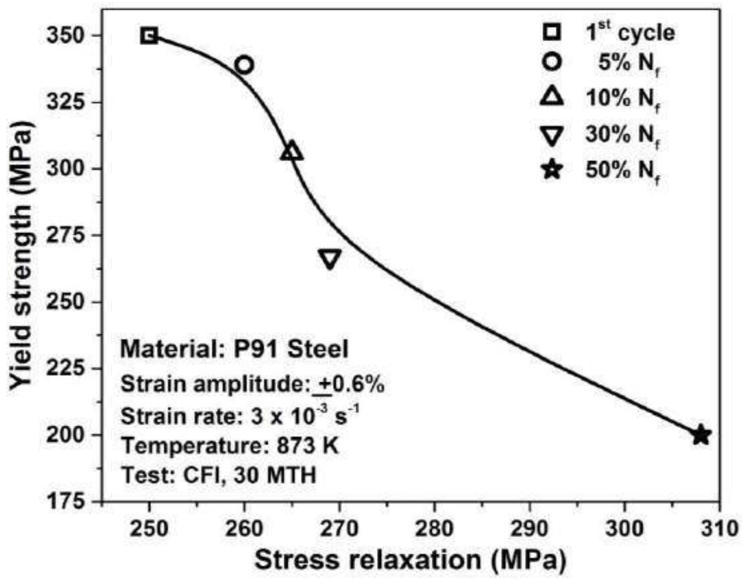

Fig. 7.18 Correlation between yield strength changes and stress relaxation during the progressive of CFI deformation at 873 K.

Specimens with the conditions of as-fabricated and subjected to fatigue cycling up to 5, 30 and 50% of fatigue life were used for the EBSD analyses. In each test condition, at least two regions on the surface of the sample were selected to quantify the substructure. Inverse pole figure (IPF) maps, as shown in Fig. 7.19(a)-(d), of the samples of as-heat treated and subjected to strain-hold fatigue deformation up to 5, 30 and 50% of fatigue life illustrate that the substructures of the samples for all conditions appear to be similar and heterogeneous. As depicted in Fig. 7.19(e), the increase of average substructural size (μm) against fatigue damage fractions (%) clearly indicates the continuous coarsening of the substructures with the extent of fatigue deformation under CFI.

The variation in yield strength with grain boundaries/grain was observed to be following the Hall-Petch relationship in martensitic steel [290]. Thus, the growth of substructural size with the progressive fatigue damage attributes to the decrease in the yield strength values up to 50% of fatigue life. Larger substructural coarsening under creep-fatigue interaction as compared to low cycle fatigue loading is expected to occur during the extended period of creep/application of hold time [121].

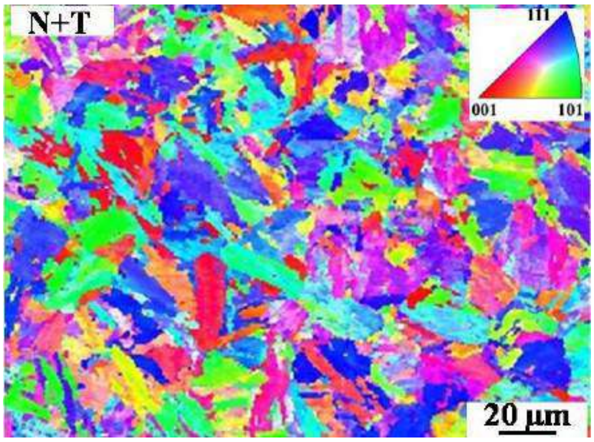

(a)

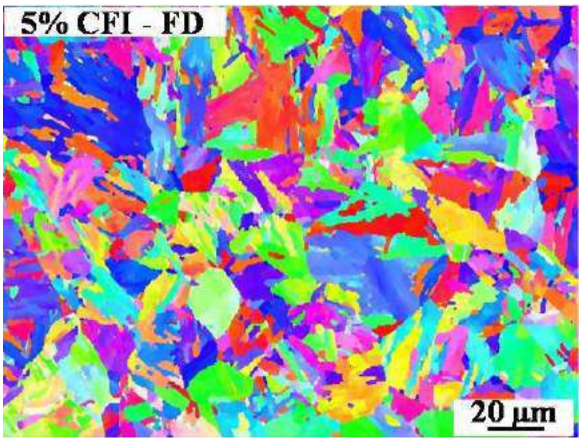

(b)

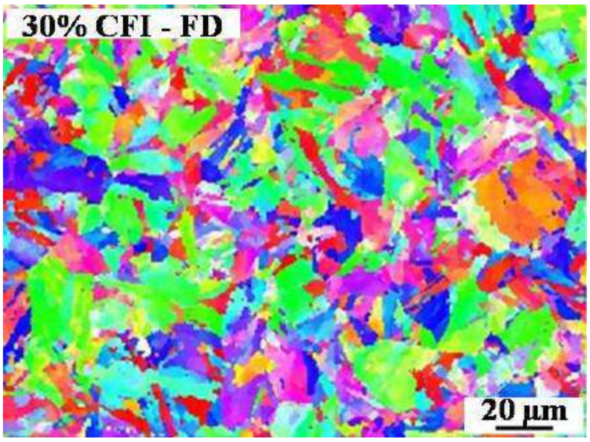

(b)

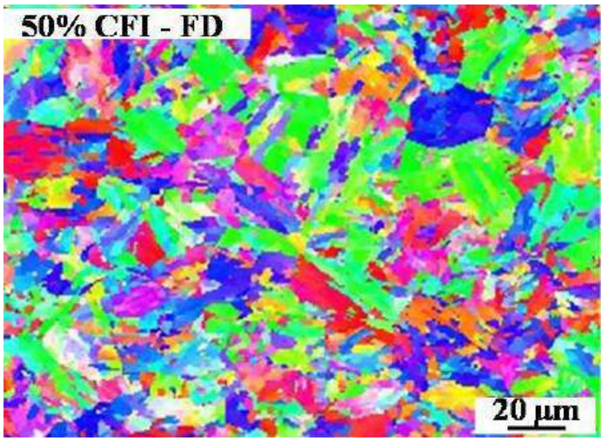

(d)

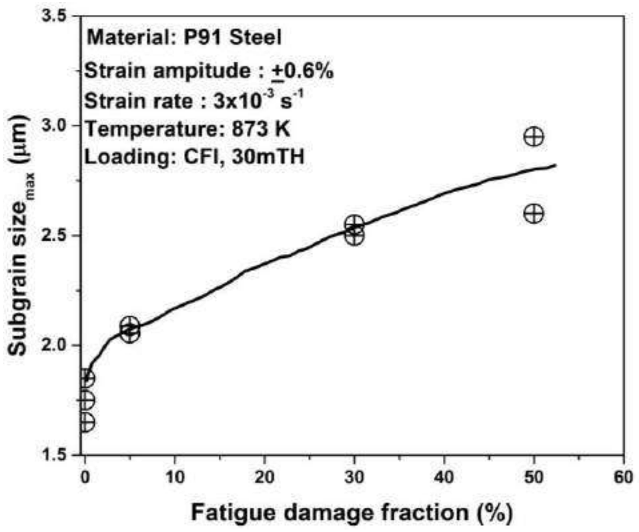

(e)

Fig. 7.19 Inverse pole figure maps of the specimens after (a) normalizing and tempering and fatigue deformation up to (b) 5%, (c) 30% and (d) 50% of fatigue life and (e) plot of sub-grain size evolution with the progressive fatigue damage under CFI condition at 873 K. Step size is 0.2 µm.

In addition to the substructural coarsening, the formation of oxidation induced micro cracks results in a decrease in the load-bearing cross-sectional area of the specimen is also reported as one of the important reasons for strength loss due to cyclic deformation [158]. The decrease in the yield strengths with the extent of prior cyclic deformation have been related to the initiation of microcracking in SS 304LN and P92 steel [291,292]. Figure 7.20 shows the surface replicas taken on the samples interrupted after various fatigue life fractions under CFI condition. As shown in Fig. 7.20(a), apparently, no surface damage is observed in the specimen undergone 10% fatigue damage at 873 K. Owing to the fatigue damage up to 50% many white patches/islands (probably oxides) are visible on the surface. As P91 steel is prone to oxidation, the slip bands are masked by the oxides (shown in Fig. 7.20(c)) formed on the specimen surface during the extended period of hold application under CFI loading condition.

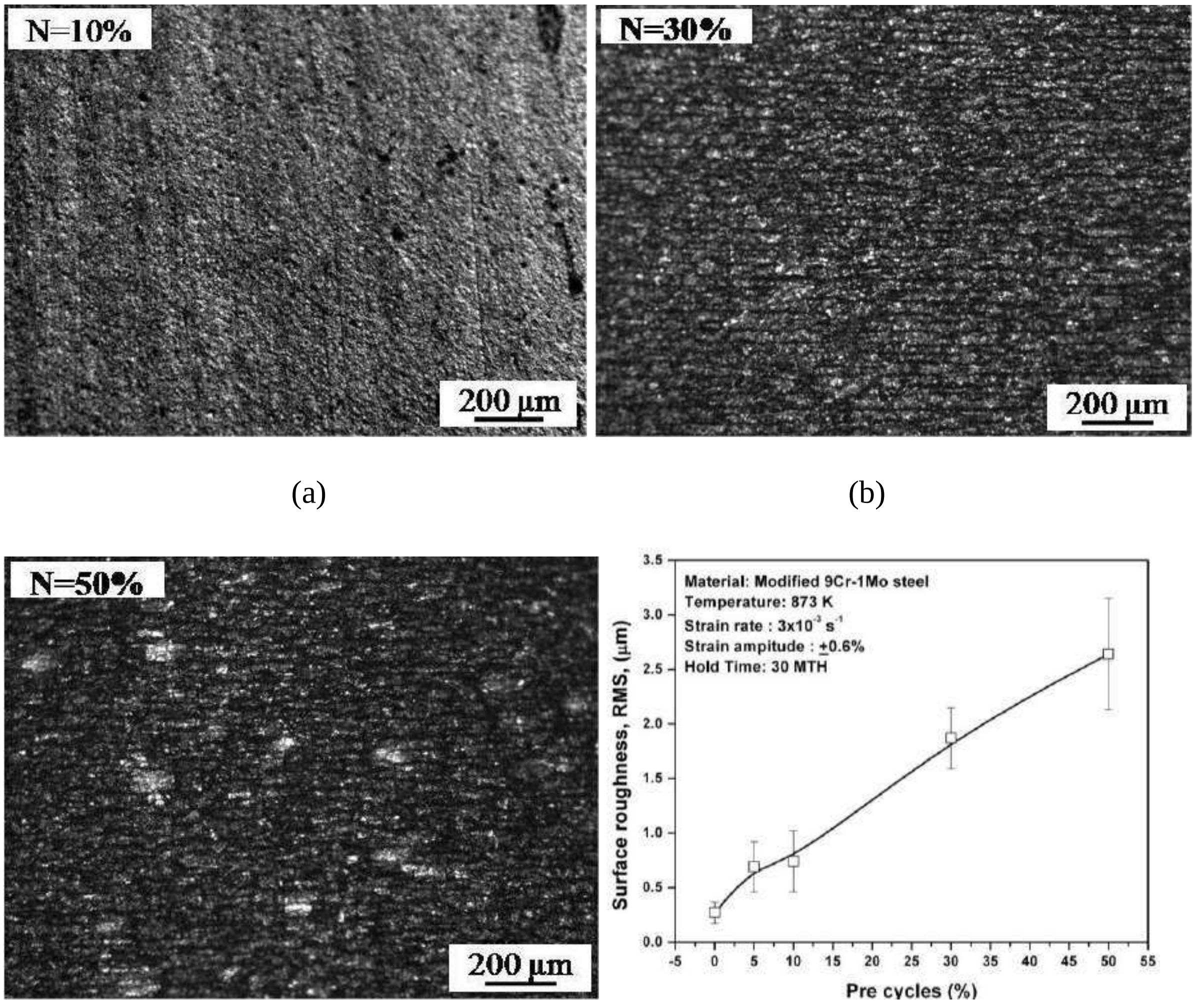

(a) (b)

(c) (d)

Fig. 7.20 Oxidation in P91 steel base metal subject to fatigue loadings up to (a) 10%, (b) 30% and (c) 50% of fatigue life and (d) surface roughness versus fatigue cycles under CFI condition at 873 K.

Surface roughness continuously increases with the progress of CFI damage, as illustrated in Fig. 7.20(d). There is more than one factor contributing to the change in the surface roughness. Those are microstructural features such as slip band formation, crack initiation near slip bands and subsequent widening/deepening of the cracks and surface oxidation. Oxidation requires an incubation period to grow to a detectable thickness/size. It may be hypothesized that the initial changes in the surface roughness (Fig. 7.20(d)) is due to microstructural changes such as formation of slip bands. Further changes may be essentially attributed to the parabolic growth [293] of oxide layers. Wang et al.[294] have reported that the surface roughness increases with the increase in fatigue cycles and the slip band formation mainly contributes to the increase in the surface roughness in the early stages of the fatigue damage.

7.9 CONCLUSIONS

1. Irrespective of the initial microstructure, the cyclic stress responses decrease with increase in hold time. All simulated CGHAZ, FGHAZ and ICHAZ show lower stress responses under CFI than that of LCF. Like under the LCF, the simulated ICHAZ and the actual weld joint exhibit brief (up to 5 cycles) cyclic hardening behavior under CFI also. The higher stress response of actual weld joint in the initial loading under CFI is due to the localized cyclic hardening behavior of soft ICHAZ. The coarsening of precipitates and substructures eases the deformation process and results in higher softening under CFI. Increase in hold time decreases the fatigue lives. The CGHAZ and ICHAZ exhibit lower fatigue lives under CFI. The actual weld joint failed in the interface between FGHAZ and ICHAZ due to the shifting of strain localization due to the initial hardening behavior of soft ICHAZ.

2. The ratios of LAGBs/HAGBs for the simulated CGHAZ and ICHAZ decrease after CFI deformation compared to that of PWHT, while they increase due to LCF. The ratio of LAGBs/HAGBs in FGHAZ continuously decreases under both the LCF and CFI loadings. The decrease in the ratio of LAGBs/HAGBs signifies the decline of the stability of lath structure due to exposure of high temperature and creep strain. Among the HAZ microstructures, the FGHAZ exhibits the highest fraction of recrystallization. The higher number of grain boundaries attributes to the increase in recrystallization in FGHAZ and the recrystallization of partially austenitized region accounts the moderate

level in ICHAZ due to CFI deformation. The highest substructural changes were observed in the CGHAZ. The fine, lengthy martensite laths in CGHAZ enhanced the substructural changes.

3 A common empirical relationship was established to estimate the fatigue life of weld joint using the sum of product of weighted factors and the fatigue lives of constituent regions under LCF and CFI loadings. Among the microstructures of HAZ, ICHAZ exhibits low weighted factor, which means that it substantially contributes in the decrease of fatigue life of weld joint. The presence of micro defects and complex multi layered microstructures due to the repeated heating and cooling during welding, results in poor ductility and extremely low value of weighted/contribution factor of weld metal.

4 The decrease in yield strength has been related to microstructural coarsening as the fatigue damage progresses under CFI loading conditions. However, the strength loss due to fatigue damage beyond 30% of fatigue life has also been associated with the oxidation at this test temperature. Therefore, in addition to the substructural coarsening, the formation of oxidation induced micro cracks results in a decrease in the load-bearing cross-sectional area of the specimen, which is also one of the many reasons for strength loss due to cyclic deformation.

CHAPTER 8 SUMMARY AND CONCLUSIONS

Study on the hardness, tensile, low cycle fatigue and creep-fatigue interaction behavior of various microstructural constituents such as weld metal, simulated CGHAZ, FGHAZ and ICHAZ and base metal of P91 steel weld joint and correlating them with the actual weld joint has drawn the following conclusions:

1 A comparative study on the microstructures of constituent regions of simulated and actual weld joint using prior austenite grain size, precipitate size and hardness determinations and differential scanning calorimetry method established that the soaking temperatures of 1473 K, 1208 K and 1138 K are adequate to simulate the corresponding microstructures of CGHAZ, FGHAZ and ICHAZ of P91 steel weld joint. Thus, the grain size, precipitate size and hardness analyses validate the simulations of microstructures of HAZ of P91 weld joint through heat treatments.

2 The higher amount of LAGBs distribution in the HAZ microstructures of actual weld joint compared to the simulated HAZ's is due to large temperature gradient across the weld joint HAZ during welding. The larger LAGBs distribution gives rise to the higher amount of KAM distribution in the actual weld joint HAZ as the LAGBs are the potential source of strain localization. The significant recovery and recrystallisation during PWHT accredited to the higher amount of HAGBs in simulated homogenous FGHAZ and ICHAZ.

3 Significant variation (~150 MPa) in yield strengths and trivial difference in ductility (2-9%) among the various microstructural regions of P91 weld joint confirmed that strength dictated the tensile behavior of weld joint and not the ductility at a strain rate of 3×10^{-3} s^{-1} and temperature of 823 K.

4 The variations in the hardness across the weld joint before and after tensile test indicate strain/work hardening of ICHAZ and softening of comparatively harder microstructural regions such as CGHAZ and weld metal during monotonic tensile deformation. Among the microstructural constituents of the weld joint, the ICHAZ exhibits the minimum yield strength and the lowest hardness. However, the actual P91 weld joint failed in the base metal due to tensile deformation. The strain/work hardening of the soft ICHAZ and the strain incompatibility among the strength contributing zones causes the shifts of the strain localization towards the base metal of the weld joint.

5 The higher local strain (KAM) distribution in the ICHAZ after tensile deformation compared to after PWHT validates the strain/work hardening behavior in P91 steel weld joint during monotonic tensile deformation. This is due to the numerous interactions between the dislocations, depending upon the local microstructure and stress states during tensile deformation.

6 The deformation weighted/contribution factors of the simulated/individual microstructures, predicted that higher contribution towards the failure of the actual weld joint would be from the low strength and high ductility microstructures. The complex and synergistic role of microstructure, strain accommodating capability of individual microstructure and the volume fractions of various regions cause the final failure of the weld joint in the relatively higher strength base metal rather than in the soft inter-critical or FGHAZ.

7 The CGHAZ and weld metal are the strongest and ICHAZ is the softest, whereas the FGHAZ and base metal and the actual weld joint exhibit intermediate strength or cyclic stress response. A common two-slope behavior of cyclic yield strength and plastic strain range for all microstructures indicate that same underlying deformation mechanism is

operative. The fatigue lives of base metal, simulated ICHAZ, FGHAZ and CGHAZ, weld metal and actual weld joint are in the order as follows: (BM=FG)>(IC≈CG)>WJ>>WM. The fatigue life of the actual weld joint is not an average of the fatigue lives of the constituent microstructures and depends upon various factors.

8 Factors such as grain size (CG, FG), mechanical strength of various phases (fine tempered martensites and over-tempered ferrite in ICHAZ), precipitate size (de-cohesion around coarsened carbides in ICHAZ), difference in the volume of microstructural regions in the actual weld joint, difference in plastic strain accommodation/accumulating capacity of individual microstructures and their evolution during fatigue deformation are identified for affecting cracking behavior and the resultant fatigue life. The weld joint specimen failed at the interface between the ICHAZ and base metal under LCF loading. The initial brief cyclic hardening in the ICHAZ region causes the shifts of initial strain localization to the interface and leading to the crack initiation.

9 The formation of LAGBs is increased due to fatigue deformation compared to after PWHT due to the pronounced generation of dislocation and the rearrangement of lath structure into sub-grain structure in CGHAZ and ICHAZ. The initial soft ICHAZ exhibits increased sub-grain evolution after cyclic deformation. The higher amount of local strain distribution is due to the greater number of LAGBs formation. The local strain distributions in the vicinity of the LAGBs results in the generation of micro cracks subsequently leading to earlier failure of CGHAZ and ICHAZ under LCF loading.

10 The predicted fatigue life using weighted factor of each constituent region is comparable with the experimental fatigue life of weld joint and the differences fall within ±10%. The predicted fatigue life from empirical relation means that all major constituent regions such as base metal, weld metal, CGHAZ, FGHAZ and ICHAZ synergistically affect the overall

fatigue life of P91 steel weld joint. The constituent region, which has lower factor fraction contribute towards the deterioration of fatigue life of actual weld joint of P91 steel.

11 Irrespective of the initial microstructure, the cyclic stress responses decrease with increase in hold time. All simulated CGHAZ, FGHAZ and ICHAZ show lower stress responses under CFI than that of LCF. The coarsening of precipitates and substructures eases the deformation process and result in higher softening under CFI. The CGHAZ and ICHAZ exhibit lower fatigue lives than FGHAZ and base metal under CFI. The continuous increase of dwell sensitivities of base metal and FGHAZ with increase of hold time are of concern though their fatigue lives are better than the other microstructures. The actual weld joint failed at the interface between FGHAZ and ICHAZ due to the shift of strain localization towards the interface due to initial hardening behavior of soft ICHAZ.

12 The ratios of LAGBs/HAGBs for the simulated CGHAZ and ICHAZ decrease after CFI deformation compared to that of PWHT, while they increase due to LCF. The ratio of LAGBs/HAGBs in FGHAZ continuously decreases under both the LCF and CFI loadings. The decrease in the ratio of LAGBs/HAGBs signifies the decline of the stability of lath structure due to exposure of high temperature and creep strain. Among the HAZ microstructures, the FGHAZ exhibits the highest fraction of recrystallization. The higher number of grain boundaries attributes to the increase in recrystallization in FGHAZ and the recrystallization of partially austenitized region accounts the moderate level in ICHAZ under CFI loading. The highest substructural changes were observed in the CGHAZ. The fine, lengthy martensite laths in CGHAZ enhanced the substructural changes.

13 A common empirical relationship was established to estimate the fatigue life of actual weld joint using the sum of the product of weighted factors and the fatigue lives of constituent regions under LCF and CFI loadings. Among the HAZ microstructures,

ICHAZ exhibits low weighted factor, which means that it substantially contributes in the decrease of fatigue life of actual weld joint. The presence of micro defects and complex multi layered microstructures due to the repeated heating and cooling during welding, results in poor ductility and extremely low value of weighted/contribution factor of weld metal.

14 The decrease in yield strength has been related to microstructural coarsening as the fatigue damage progresses under CFI loading condition. In addition to the substructural coarsening, the formation of oxidation induced micro cracks results in a decrease in the load-bearing cross-sectional area of the specimen, which is also one of the many reasons for strength loss due to cyclic deformation under CFI condition.

CHAPTER 9 FUTURE DIRECTIONS

The investigation on the fatigue behavior of simulated heat-affected zones of P91 steel weld joint has enhanced the scope for further investigation in the related area:

1 In the present study the mechanical behavior such as hardness, tensile, low cycle fatigue and creep-fatigue interaction were characterized for the simulated microstructures of heat-affected zone of P91 steel weld joint that are generated through heat treatment. In order to strengthen the reliability of the present data, a comparative study may be carried out on the same heat-affected zone microstructures replicated through heating/cooling using GLEEBLE simulator.

2 The fatigue behavior of various constituent regions of P91 steel weld joint have been discussed from the experimental results of the strain amplitude of ±0.6% and 823 K under LCF and CFI conditions. The CGHAZ and ICHAZ exhibited poor fatigue performances at such higher strain amplitudes. The applied higher strain amplitude might have not given the credit to the microstructural contribution especially in the dual phase microstructures of ICHAZ and multi complex microstructures in the actual weld joint. This effect will be more pronounced and distinguished when creep component is introduced in the cyclic loading. Therefore, decreasing the applied strain amplitude to ±0.25% would be more suitable to study such localized behavior under the CFI condition. Additionally, employing lower strain rate of 1×10^{-5} s^{-1} would also assist to understand the material behavior at the operating rate of heating and cooling during start-ups and shut-downs of the steam generator.

3 The new finding of lower fatigue life of CGHAZ under CFI condition in the current study is quite surprising although the literature reports that the CGHAZ shows longer creep life. Therefore, decoupling the fatigue and creep components, i.e., through sequential loading

of both components would provide further insight of failure mechanism operative in the fatigue and creep components individually. The same study shall be extended to other microstructural zones of the weld joint.

4 As discussed in the present study low angle boundaries (LAGBs) and coarsening of $M_{23}C_6$ precipitates play important roles in the deformation behavior and the resultant fatigue lives of all constituent regions of weld joint. But it is suspected that the coarsening of primary carbides such as NbC and V(C,N) may significantly contribute for the poor fatigue lives of all microstructures due to the involvement of time dependent processes under 30-minute CFI loading. Therefore, extensive TEM analysis may be carried out to evaluate the coarsening of primary carbides and dislocation density evolution under such loadings. Additionally, partitioning of strain accumulation in the LAGBs and HAGBs using EBSD technique would further assist to understand the crack initiation and the resultant failure mechanism in the P91 steel.

5 Deformation weighted/contribution factor of each constituent region of weld joint at various temperatures may be established to evaluate the actual weld joint behavior under the wide spectrum of service conditions. This study would help to improve the welding technology to mitigate the Type IV cracking.

REFERENCES:

[1] V.K. Sikka, C.T. Ward, K.C. Thomas, Modified 9 Cr-1 Mo Steel - An Improved Alloy for Steam Generator Application, in: A.K. Khare (Ed.), Int. Conf. Ferritic Steels High Temp. Appl., ASM, Metals Park, OH, 1983: pp. 65–84.

[2] R. Blum, R.W. Vanstone, C. Messelier-Gouze, Materials Development for Boilers and Steam Turbines Operating at 700 °C, in: 4th Int. Conf. Adv. Mater. Technol. Foss. Power Plants (ASM Int. Hilt. Head Island, 2005)., 2005: p. 116.

[3] M. Basirat, T. Shrestha, G.P. Potirniche, I. Charit, K. Rink, A study of the creep behavior of modified 9Cr-1Mo steel using continuum-damage modeling, Int. J. Plast. 37 (2012) 95–107.

[4] N. Sivai Bharasi, K. Thyagarajan, H. Shaikh, M. Radhika, A.K. Balamurugan, S. Venugopal, A. Moitra, S. Kalavathy, S. Chandramouli, A.K. Tyagi, R.K. Dayal, K.K. Rajan, Evaluation of microstructural, mechanical properties and corrosion behavior of AISI type 316LN stainless steel and modified 9Cr-1Mo steel exposed in a dynamic bimetallic sodium loop at 798 K (525 °c) for 16,000 hours, Metall. Mater. Trans. A Phys. Metall. Mater. Sci. 43 (2012) 561–571.

[5] P. Bocquet, P. Bourges, A. Cheviet, Properties of heavy components of steel grade 91 and their welds, Nucl. Eng. Des. 144 (1993) 149–154.

[6] R. Blume, K.E. Leich, H. Heuser, F.W. Meyer, Welding of modified 9%Cr steel, Stainl. Steel Eur. (1995) 449–453.

[7] M. Sireesha, S.K. Albert, S. Sundaresan, Microstructure and mechanical properties of weld fusion zones in modified 9Cr-1Mo steel, J. Mater. Eng. Perform. 10 (2001) 320–330.

[8] M. Taneike, K. Sawada, F. Abe, Effect of carbon concentration on precipitation behavior of M23C6 carbides and MX carbonitrides in martensitic 9Cr steel during heat treatment, Metall. Mater. Trans. A Phys. Metall. Mater. Sci. 35 A (2004) 1255–1262.

[9] Y.Z. Shen, S.H. Kim, H.D. Cho, C.H. Han, W.S. Ryu, Identification of precipitate phases in a 11Cr ferritic/martensitic steel using electron micro-diffraction, J. Nucl. Mater. 400 (2010) 64–68.

[10] U. Ceyhan, B. Dogan, Deformation and fracture behaviour of P91 steel weldments at high temperatures, Sci. Technol. Weld. Join. 11 (2006) 538–543.

[11] H. Ghassemi-Armaki, R. Maaß, S.P. Bhat, S. Sriram, J.R. Greer, K.S. Kumar, Deformation response of ferrite and martensite in a dual-phase steel, Acta Mater. 62 (2014) 197–211.

[12] Q. Jia, W. Guo, W. Li, Y. Zhu, P. Peng, G. Zou, Microstructure and tensile behavior of fiber laser-welded blanks of DP600 and DP980 steels, J. Mater. Process. Technol. 236 (2016) 73–83.

[13] H. Ashrafi, M. Shamanian, R. Emadi, M. Ahl Sarmadi, Comparison of Microstructure and Tensile Properties of Dual Phase Steel Welded Using Friction Stir Welding and Gas Tungsten Arc Welding, Steel Res. Int. 89 (2018) 1–8.

[14] Y. Tsuchida, K. Okamoto, Y. Tokunaga, Study of creep rupture strength in heat affected zone of 9Cr-1Mo-V-Nb-N steel by welding thermal cycle simulation, Weld. Int. 10 (1996) 454–460.

[15] K. Laha, Tensile and creep behavior of similar and dissimilar weld joints of Cr-Mo steels, PhD Thesis, Ind. Inst. Sci. Bangalore, India, 1998.

[16] K.S. Chandravathi, K. Laha, K. Bhanu Sankara Rao, S.L. Mannan, Microstructure and tensile properties of modified 9Cr-1Mo steel (grade 91), Mater. Sci. Technol. 17 (2001) 559–565.

[17] A.F. Armas, M. Avalos, I. Alvarez-Armas, C. Petersen, R. Schmitt, Dynamic strain ageing evidences during low cycle fatigue deformation in ferritic-martensitic stainless steels, J. Nucl. Mater. 258–263 (1998) 1204–1208.

[18] W.B. Jones, C.R. Hills, D.H. Polonis, Microstructural evolution of modified 9Cr-1Mo steel, Metall. Trans. A. 22 (1991) 1049–1058.

[19] G. Ebi, A.J. McEvily, Effect of processing on the high temperture low cycle fatigue properties of modified 9Cr-1Mo ferritic steel, Fat. Fract. Eng. Mater. Struct. 7 (1984) 299–314.

[20] R.W. Swindman, Cyclic Stress-Strain-Time Response of a 9Cr-1Mo-V-Nb Pressure

Vessel at High Temperature, in: S.D. Solomon, G.R. Halford, L.R. Kaisand, B.N. Leis (Eds.), Low Cycle Fatigue, ASTM STP 942, 1988: pp. 107–122.

[21] Y. Asada, K. Dozaki, M. Ueta, M. Ichimiya, K. Mori, K. Taguchi, M. Kitagawa, T. Nishida, T. Sakon, M. Sukekawa, Exploratory research on creep and fatigue properties of 9Cr-steels for the steam generator of an FBR, Nucl. Eng. Des. 139 (1993) 269–275.

[22] W.B.Jones, Effects of mechanical cycling on the substructure of 9Cr-1Mo ferritic steel, in: A.K. Khare (Ed.), Ferritic Steels High Temp. Appl., ASM International, Metals Park, Ohio, 1981: pp. 221–235.

[23] A. Nagesha, M. Valsan, R. Kannan, K. Bhanu Sankara Rao, S.L. Mannan, Influence of temperature on the low cycle fatigue behaviour of a modified 9Cr-1Mo ferritic steel, Int. J. Fatigue. 24 (2002) 1285–1293.

[24] D. Eifler, D. Rottger, High temperature low cycle fatigue behavior of X20CrMoV121 and 2145 X10CrMoVNb91 under total strain control, in: Z.-G.W. Xue-Ren Wu (Ed.), Fatigue '99 Proc. Seventh Int. Fatigue Congr., Beijing, China, 1999: pp. 2145–2152.

[25] S. Nishino, K. Shiozawa, K. Takahashi, S. Seo, Y. Yamamoto, Low-cycle-fatigue property of forged Mod. 9Cr-lMo steel at elevated temperature., in: Z.-G.W. Xue-Ren Wu (Ed.), Fatigue '99 Proc. Seventh Int. Fatigue Congr. 8-12 June 1999, Beijing, China, 1999: pp. 2177–2182.

[26] Y. Furuya, H. Nishikawa, H. Hirukawa, N. Nagashima, E. Takeuchi, Data sheets on elevated-temperature, time-dependent low-cycle fatigue properties of ASTM A387 grade 91 (9Cr-1Mo) steel plate for pressure vessels, NRIM Fatigue Data Sheet. (1993) 78.

[27] Vani Shankar, Low cycle fatigue and creep-fatigue interaction behavior of modified 9Cr-1Mo ferritic steel and its weld joint., PhD Thesis, IIT Madras , India, 2007.

[28] Vani Shankar, M. Valsan, K. Bhanu Sankara Rao, R. Kannan, S.L. Mannan, S.D. Pathak, Low cycle fatigue behavior and microstructural evolution of modified 9Cr – 1Mo ferritic steel, Mater. Sci. Eng. A. 437 (2006) 413–422.

[29] K. Guguloth, S. Sivaprasad, D. Chakrabarti, S. Tarafder, Low-cyclic fatigue behavior of modified 9Cr-1Mo steel at elevated temperature, Mater. Sci. Eng. A. 604 (2014)

196–206.

[30] Preeti Verma, N.. Santhi Srinivas, V. Singh, Low Cycle Fatigue Behaviour of Modified 9Cr–1Mo Steel at 600 °C, Indian Inst. Met. 69 (2016) 331–335.

[31] K. Mariappan, Vani Shankar, R. Sandhya, G. V. Prasad Reddy, M.D. Mathew, Dynamic strain aging behavior of modified 9Cr-1Mo and reduced activation ferritic martensitic steels under low cycle fatigue, J. Nucl. Mater. 435 (2013) 207–213.

[32] Vani Shankar, K. Mariappan, R. Sandhya, M.D. Mathew, Evaluation of Low Cycle Fatigue Damage in Grade 91 Steel Weld Joints for High Temperature Applications, Procedia Eng. 55 (2013) 128–135.

[33] H.C. Yang, Y. Tu, M.M. Yu, J. Zhao, Investigation of the low-cycle fatigue and fatigue crack growth behaviors of P91 base metal and weld joints, Acta Metall. Sin. (English Lett. 17 (2004) 597–600.

[34] Y. Takahashi, Study on Type-IV Damage Prevention in High-Temperature Welded Structures of Next-Generation Reactor Plants: Part I — Fatigue and Creep-Fatigue Behavior of Welded Joints of Modified 9Cr-1Mo Steel, in: ASME 2006 Press. Vessel. Piping/ICPVT-11 Conf., 2006: pp. 937–944.

[35] T.P. Farragher, S. Scully, N.P. O'Dowd, C.J. Hyde, S.B. Leen, High temperature, low cycle fatigue characterization of P91 weld and heat affected zone material, J. Press. Vessel Technol. Trans. ASME. 136 (2014) 1–10.

[36] Vani Shankar, K. Mariappan, R. Sandhya, M.D. Mathew, T. Jayakumar, Effect of application of short and long holds on fatigue life of modified 9Cr-1Mo steel weld joint, Metall. Mater. Trans. A. 45 (2014) 1390–1400.

[37] Dong-Feng Li, R.A. Barrett, P.E. O'Donoghue, N.P. O'Dowd, S.B. Leen, A multi-scale crystal plasticity model for cyclic plasticity and low-cycle fatigue in a precipitate-strengthened steel at elevated temperature, J. Mech. Phys. Solids. 101 (2017) 44–62.

[38] Dong-Feng Li, R.A. Barrett, P.E. O'Donoghue, C.J. Hyde, N.P. O'Dowd, S.B. Leen, Micromechanical finite element modelling of thermo-mechanical fatigue for P91 steels, Int. J. Fatigue. 87 (2016) 192–202.

[39] F.V. Ellis, R. Viswanathan., Review of Type IV cracking in piping welds, in: Integr. High Temp. Welds, Prof. Publishing Ltd, London, 1998: pp. 125–134.

[40] K. Sawada, M. Tabuchi, K. Kimura, Degradation Mechanism of Creep Strength Enhanced Ferritic Steels for Power Plants, in: M.K. T. Bollinghaus, J. Lexow, T. Kishi (Ed.), Mater. Challenges Test. Supply Energy Resour., Springer, 2012: pp. 35–43.

[41] H. Cerjak, E. Letofsky, The effect of welding on the properties of advanced 9–12% Cr steels, Sci. Tech. Weld Join. 1 (1996) 36–42.

[42] K. Laha, K.S. Chandravathi, P. Parameswaran, K. Bhanu Sankara Rao, S.L. Mannan, Characterization of microstructures across the heat-affected zone of the modified 9Cr-1Mo weld joint to understand its role in promoting type IV cracking, Metall. Mater. Trans. A Phys. Metall. Mater. Sci. 38 (2007) 58–68.

[43] Ljubica Milović, Microstructural investigations of the simulated heat affected zone of the creep resistant steel P91, Mater. High Temp. 27 (2010) 233–242.

[44] V. Kalyanasundaram, Creep, fatigue and creep-fatigue interactions in modified 9% Chromium-1% Molybdenum (P91) steels, PhD Thesis, University of Arkansas, Fayetteville, 2013.

[45] Tyler K Payton, On the improvement of creep-fatigue behavior of grade 91 steel weldments, MS Thesis, The Ohio State University, 2017.

[46] S.L. Mannan, S.C. Chetal, Baldev Raj, S.B. Bhoje, Selection of materials for Prototype fast breeder reactor, Trans. Inst. Met. 56 (2003) 155–178.

[47] V.K. Sikka, Development of modified 9Cr-1Mo steel for elevated temperature service, in: J.W. Davis, D.J. Michel (Eds.), Ferritic Alloy. Use Nucl. Energy Technol., TMS-AIME Warrendale, Pennsylvania, USA, 1984: pp. 317–324.

[48] K. Kimura, H. Kushima, F. Abe, K. Yagi, H. Iries, Assessment of creep strength properties of 9–12%Cr steels, in: A. Strang, W.M. Banks, R.D. Conroy, M.J. Goulette (Eds.), Adv. Turbine Mater. Des. Manuf. 4th Int. Charles Parsons Turbine Conf., London, UK, 1997: pp. 257–269.

[49] Baldev Raj, P. Chellapandi, P. Vasudeva Rao, Sodium fast reactors with closed fuel

cycle, CRC Press. (2015).

[50] J.M. Vitek, R.L. Klueh, Precipitation Reactions during the Heat Treatment of Ferritic Steels, Metall. Trans. A. 14 (1983) 1047–1055.

[51] S.J. Brett, Identification of weak thick section modified 9 chrome forgings in Service, in: R. Viswanathan, Et.al (Eds.), EPRI Conf. Adv. Mater. Technol. Foss. Power Plants, University of Wales, Swansea, Wales, 2001: pp. 343–351.

[52] P.J. Alberry, W.K.C. Jones, Diagram for the prediction of weld heat-affected zone microstructure, Met. Technol. 4 (1977) 360–364.

[53] Z. Briggs, T.D. Parker, The Super 12% Cr Steels, in: Mater. Corros., New York, USA, 1965: pp. 642–642.

[54] Anon, Super 12% Cr Steels-An Update, Climax Molybdenum Company, New York, USA, 1983.

[55] C. Willby, J. Walters., Material choice for the commercial fast breeder steam generator, in: Int. Conf. Ferritic Steels Fast React. Steam Gener., British Nuclear Energy Society, London, 1977: pp. 40–49.

[56] J. Orr, F.R. Beckitt, G.D. Fawkes, The Physical Metallurgy of chromium-molybdenum steels for reactor boilers, in: Int. Conf. Ferritic Steels Fast React. Stream Gener. Br. Nucl. Energy Soc. London, British Nuclear Energy Society, London, 1977: pp. 91–109.

[57] L. Egnell, High temperature properties of steel, Iron Steel Inst., London, Publ. 97. (1967) 153.

[58] Taisuke Hayashi, K. Ito, M. Takamoto, K. Tanaka, The effect of Nb and W alloying additions to the thermal expansion anisotropy and elastic properties of Mo5Si3, Metall. Mater. Trans. A Phys. Metall. Mater. Sci. 36 (2005) 533–538.

[59] R. Blum, J. Hald, Benefit Of Advanced Steam Power Plants, Mater. Adv. Power Eng. Ed. by Lacomte-Becker (European Comm. Univ. Liége 21 Part II, 2002). (2002) 1007–1015.

[60] P.J. Ennis, Czyrska-Filemonowicz, Recent Advances In Creep-Resistant Steels For

Power Plant Applications, Sādhanā. 28 (2003) 709–730.

[61] R. Viswanathan, W. Bakker, Materials for ultrasupercritical coal power plants - boiler materials: Part 1, J. Mater. Eng. Perform. 10 (2001) 81–95.

[62] K. H. Mayer, Final Report of the European COST 522 Project, (2000).

[63] F. Masuyama, Advance power plant developments and materials experience in Japan, in: J Lecompte-Beckers et al. (Ed.), 8th Liege Conf. Sept. 2006, Liege, Belgium, Res. Cent. Julich, 2006, Research Centre Julich, Liege, Belgium, 2006: pp. 175–187.

[64] F. Abe, T.U. Kern, R. Viswanathan, Creep-resistant Steels, Woodhead Publishing, CRC Press, Cambridge, England, 2008.

[65] R.L. Klueh, Elevated – Temperature Ferritic and Martensitic Steels and their Application to Future Nuclear Reactors, Int. Mater. Rev. 50 (2005) 287–310.

[66] K.H.J. Buschow, Encyclopedia of Materials: Science and Technology, Elsevier, Amsterdam, The Netherlands, 2001.

[67] R.W. Cahn, P. Haasen, Physical Metallurgy, North-Holland Physics Publication: Elsevier Science Publishing Company, New York, USA, 1983.

[68] R.W. Cahn, P. Haasen, E.J. Kramer, H.E.H. Meijer, Materials Science and Technology: A Comprehensive Treatment, Wiley-VCH, Weinheim, Germany, 1998.

[69] F. Abe, T. Horiuchi, M. Taneike, K. Sawada, Stabilization of martensitic microstructure in advanced 9Cr steel during creep at high temperature, Mater. Sci. Eng. A. 378 (2004) 299–303.

[70] Z. Nishiyama, Martensitic Transformation, Academic Press INC, New York, United States, 1978.

[71] Y. Wang, Microstructure and Creep Behavior of Heat-Affected Zone in Grade 91 Steel Weldments, PhD Thesis, University of Alberta, 2017.

[72] T. Fujita, Advanced High-Chromium Ferritic Steels For High-Temperatures, Met. Prog. 130. (1986) 33–40.

[73] J.C. Vaillant, B. Vandenberghe, B. Hahn, H. Heuser, C. Jochum, T/P23, 24, 911 and

92: New grades for advanced coal-fired power plants-Properties and experience, Int. J. Press. Vessel. Pip. 85 (2008) 38–46.

[74] J. Baker, R. G. & Nutting, The Tempering of 2.25Cr-1Mo Steel after Quenching and Normalizing, J. Iron Steel Inst. 192. (1959) 257–268.

[75] K. Miyata, Y. Sawaragi, Effect of Mo and W on the phase stability of precipitates in low Cr heat resistant steels, ISIJ Int. 41 (2001) 281–289.

[76] T. Onizawa, T. Wakai, M. Ando, K. Aoto, Effect of V and Nb on precipitation behavior and mechanical properties of high Cr steel, Nucl. Eng. Des. 238 (2008) 408–416.

[77] M. Taneike, F. Abe, K. Sawada, Creep-strengthening of Steel at High Temperatures using nano-sized Carbonitride Dispersions, Nature. 424 (2003) 294–296.

[78] T. Fujita, N. Takahashi, Effects of V and Nb on the long period creep rupture strength of 12% Cr Heat resisting steel containing Mo and B, Trans Iron Steel Inst Jpn. 18 (1978) 269–278.

[79] K. Miyata, M. Igarashi, Y. Sawaragi, Effect of Trace Elements on Creep Properties ot 0.06C-2.25Cr-1.6W-0.1Mo-0.25V-0.05Nb Steel, ISIJ Int. 39 (1999) 947–954.

[80] B.S. Ku, J. Yu, Effects of Cu addition on the creep rupture properties of a 12% Cr steel, Scr. Mater. 45 (2001) 205–211.

[81] T. Fujita, Development of High Chromium Ferritic Heat Resistant Steels for Power Plant, J. Therm. Nucl. Power 42. (1991) 1485–1496.

[82] A.M. Huntz, V. Bague, G. Beauplé, C. Haut, C. Sévérac, P. Lecour, X. Longaygue, F. Ropital, Effect of silicon on the oxidation resistance of 9% Cr steels, Appl. Surf. Sci. 207 (2003) 255–275.

[83] N. Fujitsuna, M. Igarashi, F. Abe, Acceleration of Fe2W precipitation and its effect on creep deformation behavior of 8.5Cr-2W-VNb steels with Si, Key Eng. Mater. 171–174 (2000) 469–476.

[84] A. Aghajani, F. Richter, C. Somsen, S.G. Fries, I. Steinbach, G. Eggeler, On the formation and growth of Mo-rich Laves phase particles during long-term creep of a

12% chromium tempered martensite ferritic steel, Scr. Mater. 61 (2009) 1068–1071.

[85] J.H. Woodhead, A.G. Quarrel, Role of Carbides in Low-alloy Creep Resisting Steels, J. Iron Steel Inst. 203. (1965) 605–620.

[86] Y. Liu, S. Tsukamoto, K. Sawada, F. Abe, Role of boundary strengthening on prevention of type IV failure in high Cr ferritic heat-resistant steels, Metall. Mater. Trans. A Phys. Metall. Mater. Sci. 45 (2014) 1306–1314.

[87] F. Abe, M. Tabuchi, S. Tsukamoto, T. Shirane, Microstructure evolution in HAZ and suppression of Type IV fracture in advanced ferritic power plant steels, Int. J. Press. Vessel. Pip. 87 (2010) 598–604.

[88] J. Parker, J. Siefert, J. Shingledecker, The benefits of improved control of composition fo creep strength enhanced ferritic steel Grade 91, EPRI Rep. 3002003472. (2014).

[89] S.J. Sanderson, Mechanical properties and metallurgy of 9%Cr-1%Mo steel, in: A.K. Khare (Ed.), Ferritic Steels High Temp. Appl., ASM International, Metals Park, Ohio, 1981: pp. 85–99.

[90] K.J. Irwin, D.J. Crowe, F.B. Pickering, The physical metallurgy of 12% Chromium steels, J Iron Steel Inst. (1960) 386–405.

[91] P. Patriarca, S.D. Harkness, J.M. Duke, L.R. Cooper, U.S. Advanced Materials Development Program for Steam Generators, Nucl. Technol. 28 (1976) 516–536.

[92] S.J. Sanderson, Interrelationships between mechanical properties and microstructure in 9%Cr-1%Mo steel, in: Int. Conf. Ferritic Steel Fast React. Steam Gener. Br. Nucl. Energy Soc. London, 1977: pp. 120–127.

[93] S.J. Sanderson, Secondary hardening and tempering processes for 9%Cr-1%Mo steel austenitized in the phase fielditle, Met. Sci. 11 (1977) 490–492.

[94] J. Orr, S.J. Sanderson, An examination of the potential for 9%Cr-1%Mo steel as thick section tube plate in fast reactors, in: Top. Conf. Ferritic Alloy. Use Nucl. Energy Technol. AIME, New York, 1983.

[95] M. Atkins, Atlas of continuous cooling transformation diagrams for engineering steels, Metals Park, Ohio : American Society for Metals ; Sheffield, Eng. : British Steel Corp.,

©1980., n.d.

[96] F.B. Pickering, Microstructural Development and Stability in High Chromium Ferritic Power Plant Steels, Institute of Materials, London, 1997.

[97] J. Hald, Metallurgy and creep properties of new 9-12%Cr steels, Steel Res. 67 (1996) 369–374.

[98] T.C. Totemeier, H. Tian, J.. Simpson, Effect of Normalization Temperature on the Creep Strength of Modified 9Cr-1Mo Steel, Metall. Mater. Trans. A Phys. Metall. Mater. Sci. (2006) 1519–1525.

[99] J. Hald, Long-term Stability of 9- to 12 % Cr Steels, VGB PowerTech. 84 (2004) 74–79.

[100] P. Gocmen, A., Uggowitzer, P. J., Solenthaler, C., Speidel, M. O. Ernst, Alloy design for creep resistant martensitic 9-12% chromium steels, in: Int. Conf. Microstruct. Stab. Creep Resist. Alloy. High Temp. Plant Appl. London, Inst. Mater., 1998: pp. 311–322.

[101] H.K. Danielsen, Z-phase in 9-12 % Cr Steels, PhD Thesis, Technical Univeristy of Denmark, 2007.

[102] P.R. Jemian, J.R. Weertman, G.G. Long, R.D. Spal, Characterization of 9Cr-1MoVNb steel by anomalous small-angle X-ray scattering, Acta Metall. Mater. 39 (1991) 2477–2487.

[103] A. Orlová, J. Buršík, K. Kuchařová, V. Sklenička, Microstructural development during high temperature creep of 9% Cr steel, Mater. Sci. Eng. A. 245 (1998) 39–48.

[104] K. Tokuno, K. Hamada, R. Uemori, T. Takeda, K. Itoh, A complex carbonitride of niobium and vanadium in 9% Cr ferritic steels, Scr. Metall. Mater. 25 (1991) 871–876.

[105] F. Abe, Bainitic and martensitic creep-resistant steels, Curr. Opin. Solid State Mater. Sci. 8 (2004) 305–311.

[106] K. Maruyama, K. Sawada, J. Koike, Strengthening mechanisms of creep resistant tempered martensitic steel, ISIJ Int. 41 (2001) 641–653.

[107] R.E. Reed-Hill, Physical Metallurgy Principles, D.Van Nostrand Company Inc.,

Princeton, N.J., 1964.

[108] R.C. Thomson, H.K.D.H. Bhadeshia, Carbide precipitation in 12Cr1MoV power plant steel, Metall. Trans. A. 23 (1992) 1171–1179.

[109] F. Abe, Creep rates and strengthening mechanisms in tungsten-strengthened 9Cr steels, Mater. Sci. Eng. A. 319–321 (2001) 770–773.

[110] P.J. Ennis, A. Zielinska-Lipiec, O. Wachter, A. Czyrska-Filemonowicz, Microstructural stability and creep rupture strength of the martensitic steel P92 for advanced power plant, Acta Mater. 45 (1997) 4901–4907.

[111] N. Ridley, S. Maropoulos, J.D.H. Paul, Effects of heat treatment on microstructure and mechanical properties of Cr–Mo–3·5Ni–V steel, Mater. Sci. Technol. (United Kingdom). 10 (1994) 239–249.

[112] S. Takeuchi, A.S. Argon, Steady-state creep of single-phase crystalline matter at high temperature, J. Mater. Sci. 11 (1976) 1542–1566.

[113] F. Masuyama, Creep degradation in welds of Mod.9Cr1Mo steel, Int. J. Press. Vessel. Pip. 83 (2006) 819–825.

[114] A. Kimura, R. Kasada, A. Kohyama, H. Tanigawa, T. Hirose, K. Shiba, S. Jitsukawa, S. Ohtsuka, S. Ukai, M.A. Sokolov, R.L. Klueh, T. Yamamoto, G.R. Odette, Recent progress in US-Japan collaborative research on ferritic steels R&D, J. Nucl. Mater. 367-370 A (2007) 60–67.

[115] P.F. Giroux, F. Dalle, M. Sauzay, J. Malaplate, B. Fournier, A.F. Gourgues-Lorenzon, Mechanical and microstructural stability of P92 steel under uniaxial tension at high temperature, Mater. Sci. Eng. A. 527 (2010) 3984–3993.

[116] D. Rojas, J. Garcia, O. Prat, C. Carrasco, G. Sauthoff, A.R. Kaysser-Pyzalla, Design and characterization of microstructure evolution during creep of 12% Cr heat resistant steels, Mater. Sci. Eng. A. 527 (2010) 3864–3876.

[117] V. Sklenička, K. Kuchařová, M. Svoboda, L. Kloc, J. Buršík, A. Kroupa, Long-term creep behavior of 9-12%Cr power plant steels, Mater. Charact. 51 (2003) 35–48.

[118] J. Hald, L. Korcakova, Precipitate stability in creep resistant ferritic steels -

Experimental investigations and modelling, ISIJ Int. 43 (2003) 420–427.

[119] Y. Kadoya, B.F. Dyson, M. McLean, Microstructural stability during creep of Mo- or W-bearing 12Cr steels, Metall. Mater. Trans. A Phys. Metall. Mater. Sci. 33 (2002) 2549–2557.

[120] Y. Qin, G. Götz, W. Blum, Subgrain structure during annealing and creep of the cast martensitic Cr-steel G-X12CrMoWVNbN 10-1-1, Mater. Sci. Eng. A. 341 (2003) 211–215.

[121] J.S. Dubey, H. Chilukuru, J.K. Chakravartty, M. Schwienheer, A. Scholz, W. Blum, Effects of cyclic deformation on subgrain evolution and creep in 9 – 12 % Cr-steels, Mater. Sci. Eng. A. 406 (2005) 152–159.

[122] D. Rojas, J. Garcia, O. Prat, L. Agudo, C. Carrasco, G. Sauthoff, A.R. Kaysser-Pyzalla, Effect of processing parameters on the evolution of dislocation density and sub-grain size of a 12%Cr heat resistant steel during creep at 650°C, Mater. Sci. Eng. A. 528 (2011) 1372–1381.

[123] J. Hald, Microstructure and long-term creep properties of 9-12% Cr steels, Int. J. Press. Vessel. Pip. 85 (2008) 30–37.

[124] P.W. Voorhees, The Theory of Ostwald Ripening, J. Stat. Phys. 38 (1985) 231–252.

[125] A.A. Bazazi, Evolution of Microstructure during Long term Creep of a Tempered Martensite Ferritic Steel, PhD Thesis, Ruhr University Bochum, Germany, 2009.

[126] G. Eggeler, N. Nilsvang, B. Ilschner, Microstructural changes in a 12% chromium steel during creep, Steel Res. 58 (1987) 97–103.

[127] F. Abe, H. Araki, T. Noda, Microstructural evolution in bainite, martensite, and δ ferrite of low activation Cr–2W ferritic steels, Mater. Sci. Technol. (United Kingdom). 6 (1990) 714–723.

[128] A. Dronhofer, J. Pešicka, A. Dlouhý, G. Eggeler, On the nature of internal interfaces in tempered martensite ferritic steels, Zeitschrift Fuer Met. Res. Adv. Tech. 94 (2003) 511–520.

[129] W. Blum, G. Götz, Evolution of dislocation structure in martensitic steels: The

subgrain size as a sensor for creep strain and residual creep life, Steel Res. 70 (1999) 274–278.

[130] W. Blum, P. Eisenlohr, Dislocation mechanics of creep, Mater. Sci. Eng. A. 510–511 (2009) 7–13.

[131] W.D. Callister Jr., Fundamentals of Materials Science and Engineering An Interactive, 5th ed., John Wiley & Sons, Inc., New York, United States, 2001.

[132] Norman E. Dowling, Mechanical Behavior of Materials, 4th ed., Pearson Education Limited, 1993.

[133] G.E. Dieter, Mechanical Metallurgy, SI Metric, McGraw-Hill, 1988.

[134] ASTM Standard, E1823-11 - Standard Terminology Relating to Fatigue and Fracture Testing, ASTM Int. (2011) 1–24.

[135] R. Viswanathan, Damage Mechanisms and Life Assessment of High Temperature Components, ASM Int. Met. Park. (1989) 497.

[136] R. P. Skelton, Crack initiation and growth in simple metal components during thermal cycling Fatigue at High Temperature, Appl. Sci. Publ. (1983) 1–63.

[137] L. F. Coffin, Fatigue at High Temperature, ASTM Int. (1973) 5–34.

[138] K. Pohl, P. Mayr, E. Macherauch, Cyclic deformation behavior of a low carbon steel in the temperature range between room temperature and 850 K, Int. J. Fract. 17 (1981) 221–233.

[139] E.A. Starke Jr, Fatigue and Microstructure, ASM, Ohio,. (1978) 205.

[140] O.H. Basquin, The exponential law of endurance test, ASTM Int. 10 (1910) 625–630.

[141] L.F.Coffin Jr., A Study of effects of Cyclic thermal Stresses on a ductile metal., ASME. 76 (1954) 931–950.

[142] S.S.Manson, Behavior of Materials under conditions of Thermal Stress, Natl. Advis. Comm. Aeronaut. 14 (1953) 399.

[143] H.Mughrabi, Fatigue life and cyclic stress - strain behavior, in: Encycl. Mater. Sci.

Technol., Elsevier Science Ltd., 2001: pp. 2919–2933.

[144] S. Suresh, Fatigue of Materials, 2nd ed., Cambridge University press, 1998.

[145] Todd S. Gross, Micromechanisms of Monotonic and Cyclic Crack Growth, in: Fatigue Fract., 1996: pp. 42–60.

[146] A. Pineau, High temperature fatigue behaviour of engineering materials in relation to microstructure, in: R.P. Skelton (Ed.), Fatigue High Temp., Applied Science Publishers, London, UK, 1983: pp. 305–364.

[147] J. Bressers, Fatigue and microstructures, in: J. B. Marriott, M. Merz, J. Niboul, J. Ward (Eds.), Int. Conf. High Temp. Alloy Their Exploit. Potential, Elsevier Applied Science, 1985: pp. 385–410.

[148] M. Gell, G.. Leverant, Mechanisms of high temperature fatigue, fatigue at elevated temperatures, ASTM STP. 520 (1973) 37–67.

[149] J.C. Grosskruetz, Strengthening and Fracture in Fatigue. (Approaches for Achieving High Fatigue Strength)., Met. Trans. 3 (1972) 1255–1262.

[150] C. Laird, C.E. Feltner, the Coffin-Manson law in relation to slip character, Trans. Met. Soc. AIME. 239 (1967) 1074–1083.

[151] A. Saxena, S.D. Antolovich, Low cycle fatigue, fatigue crack propagation and substructures in a series of polycrystalline Cu-Al alloys, Metall. Trans. A. 6 (1975) 1809–1828.

[152] J.O. Nilsson, The Effect of Slip behavior in the low cycle fatigue behavior of two austenitic stainless steels, Scr. Met. 17 (1983) 593–596.

[153] M. Abd El-Azim Metwally, Mechanical properties of some high temperature alloys (Alloy 800 H and Alloy 617), PhD Thesis, Cairo University, 1986.

[154] K. Bhanu Sankara Rao, M. Valsan, R. Sandhya, S.L. Mannan, P. Rodriguez, Manifestations of DSA during Low Cycle Fatigue of type 304 Stainless steel, Met. Mater. Process. 2 (1990) 17.

[155] K. Bhanu Sankara Rao, Time dependent low cycle fatigue behavior of high

temperature alloys, Trans. Indian. Inst. Met. 42 (Suppl. (1989) 61–82.

[156] L.F.Coffin Jr., Corrosion Fatigue, in: Int. Conf. Fatigue, Chem. Math. Microstruct. Nat. Ass.Corr.Engrs, Houst., 1972: pp. 590–600.

[157] B.A. Kschinka, J.F. Stubbins, Creep-fatigue-environment interaction in a bainitic 2.25wt.%Cr-1wt.%Mo steel forging, Mater. Sci. Eng. A. 110 (1989) 89–102.

[158] S. Kim, J.R. Weertman, Investigation of Microstructural Changes in a Ferritic Steel Caused By High Temperature Fatigue., Metall. Trans. A. 19 A (1988) 999–1007.

[159] J.C. Earthman, G. Eggeler, B. Ilschner, Deformation and damage processes in a 12%CrMoV steel under high temperature low cycle fatigue conditions in air and vacuum, Mater. Sci. Eng. A. 110 (1989) 103–114.

[160] L.F.Coffin, Damage Process in Time-Dependent fatigue-A Review, in: Creep-Fatigue Environ. Interact., AIME, Warendale, 1980: pp. 1–23.

[161] D.S. Wood, G. Slatteru, J. Wynn, Preliminary results of effects of environment on the LCF of type 316 nand 9Cr-1Mo steels, Influ. Environ. Fatigue, I.M.E., London. (1977) 1–20.

[162] L.F. Coffin, The effect of high vacuum on the low cycle fatigue law, Metall. Trans. 3 (1972) 1777–1788.

[163] L.F. Coffin, Environmental effects on high-temperature, low-cycle fatigue, in: Low-Cycle Fatigue Strength Elasto-Plastic Behav. Mater., 1979: pp. 9–24.

[164] J.R. Haigh, R.P. Skelton, C.E. Richards, Oxidation-assisted crack growth during high cycle fatigue of a 1%CrMoV steel at 550°C, Mater. Sci. Eng. 26 (1976) 167–174.

[165] R.P. Skelton, J.I. Bucklow, Cyclic oxidation and crack growth during high strain fatigue of low alloy steel, Met. Sci. 12 (1978) 64–70.

[166] P. J. Cotterill and J. F. Knott, Effects of temperature and Environment on Fatigue growth mechanisms in 9Cr-1Mo steel, Acta Met. Mater. 40 (1992) 2752–2764.

[167] J. Wareing, Creep-fatigue behaviour of four casts of Type 316 stainless steel., Fatigue Eng. Mater. Struct. 4 (1981) 131–145.

[168] E.G.Ellison, A.J.E.Patterson, Creep fatigue interaction in a 1 Cr Mo V steel - 1, Inst Mech Eng Proc. 190 (1976) 321–332.

[169] K. Mariappan, Vani Shankar, R. Sandhya, M.D. Mathew, A.K. Bhaduri, Influence of Prior Fatigue Damage on Tensile Properties of 316L(N) Stainless Steel and Modified 9Cr-1Mo Steel, Metall. Mater. Trans. A. 46 (2015) 989–1003.

[170] B. Fournier, M. Sauzay, F. Barcelo, E. Rauch, A. Renault, T. Cozzika, L. Dupuy, A. Pineau, Creep-fatigue interactions in a 9 Pct Cr-1 Pct Mo martensitic steel: Part II. Microstructural evolutions, Metall. Mater. Trans. A Phys. Metall. Mater. Sci. 40 (2009) 330–341.

[171] P. Rodriguez, S.L. Mannan, High temperature low cycle fatigue, Sadhana. 20 (1995) 123–164.

[172] Tarun Goswami, Development of generic creep-fatigue life prediction models, Mater. Des. 25 (2004) 277–288.

[173] C.R. Brinkman, High-temperature time-dependent fatigue behaviour of several engineering structural alloys, Int. Met. Rev. 30 (1985) 235–258.

[174] Vani Shankar, K. Mariappan, R. Sandhya, K. Laha, Understanding low cycle fatigue and creep-fatigue interaction behavior of 316 L(N) stainless steel weld joint, Int. J. Fatigue. 82 (2016) 487–496.

[175] P. Rodriguez, K. Bhanu Sankara Rao, Nucleation and growth of cracks and cavities under creep-fatigue interaction, Prog. Mater. Sci. 37 (1993) 403–480.

[176] R. Hales, A Quantitative Metallographic Assessment of Structural Degradation of Type 316 Stainless Steel During Creep-Fatigue, Fatigue Fract. Eng. Mater. Struct. 3 (1980) 339–356.

[177] C.Y. Cheng, D.R. Diercks, Effecs of hold time on Low cycle fatigue behavior of AISI type 304 stainless steel at 593 degree C, Met. Trans. 4 (1973) 615–617.

[178] H. Teranishi, A.J. McEvily, On Fatigue Crack Initiation and Propagation at Elevated Temperature, in: D. Francois (Ed.), Adv. Fract. Res. (Fracture 81). Cannes, Fr., Pergamon Press, Cannes, France, 1981: pp. 2439–2447.

[179] J. Wareing, Creep-fatigue interaction in austenitic stainless steels, Metall. Trans. A. 8 (1977) 711–721.

[180] Stuart Holdsworth, Creep-fatigue failure diagnosis, Materials (Basel). 8 (2015) 7757–7769.

[181] K. Bhanu Sankara Rao, Influence of metallurgical variables on low cycle fatigue behaviour of type 304 stainless steel; grain size, cold work and thermal ageing effects, University of madras, India, 1989.

[182] L.A. James, R.L. Knecht, Fatigue-crack propagation behavior of type 304 stainless steel in a liquid sodium environment, Metall. Trans. A. 6 (1975) 109–116.

[183] M.W. Mahoney, N.E. Paton, The influence of gas environments on fatigue crack growth rates in types 316 and 321 stainless steel, Nucl. Technol. 23 (1974) 290–297.

[184] S.D. Antolovich, N. Jayaraman, Effects of Environment and Structural Stability on the Low Cycle Fatigue Behaviour of Nickel-Base Superalloys., High Temp. Technol. 2 (1984) 3–13.

[185] D.J. Duquette, M. Gell, The Effects of Environment on the Elevated Temperature Fatigue Behavior of Nickel-Base Superalloy Single Crystals, Metall. Trans. 3 (1972).

[186] M. Gell, G.R. Leverant, Effect of temperature on fatigue fracture in a directionally-solidified nickel-base superalloy, in: Second Internat. Conf. Fract. Chapman Hell ltd., London, 1969: pp. 565–575.

[187] D.J. Duquette, M. Gell, The effect of environment on the mechanism of Stage I fatigue fracture, Metall. Trans. 2 (1971) 1325–1331.

[188] C.J. McMahon, L.F. Coffin, Mechanisms of damage and fracture in high-temperature, low-cycle fatigue of a cast nickel-based superalloy, Metall. Trans. 1 (1970) 3443–3450.

[189] K.D. Challenger, A.K. Miller, C.R. Brinkman, An explanation for the effects of hold periods on the elevated temperature fatigue behavior of 2¼Cr-1Mo steel, J. Eng. Mater. Technol. Trans. ASME. 103 (1981) 7–14.

[190] K.D. Challenger, A.K. Miller, R.L. Langdon, Elevated temperature fatigue with hold

time in a low alloy steel: A predictive correlation, J. Mater. Energy Syst. 3 (1981) 51–61.

[191] H. Teranishi, A.J. McEvily, The Effect of Oxidation on Hold Time Fatigue Behavior of 2.25Cr-1Mo Steel, Met. Trans. A. 10 (1979) 1806–1808.

[192] K. Aoto, R. Komine, F. Ueno, H. Kawasaki, Y. Wada, Creep-fatigue evaluation of normalized and tempered modified 9Cr1Mo, Nucl. Eng. Des. 153 (1994) 97–110.

[193] Vani Shankar, V. Bauer, R. Sandhya, M.D. Mathew, H.J. Christ, Low cycle fatigue and thermo-mechanical fatigue behavior of modified 9Cr-1Mo ferritic steel at elevated temperatures, J. Nucl. Mater. 420 (2012) 23–30.

[194] T. Ogata, A. Nitta, Environment and strain waveform effect~ on creep-fatigue life of mod. 9Cr I Mo steel, in: Proc. 30th Symp. Struct. Mater. High Temp., 1992: p. 149.

[195] R. Townsend, Electricity Beyond 2000, Electr. Power Res. Inst. (1991) 251–281.

[196] I.A. Shibli, Performance of P91 steel under steady and cyclic loading conditions-Research and power plant experience, in: A. Strang, R.D. Conroy, W.M. Banks, M. Blacker, J. Leggett, G.M. McColvin, S. Simpson, M. Smith, F. Star, R.W. Vanstone (Eds.), Parsons 2003, Eng. Issues Turbine Mach. Power Plant Renewable, Proc. Sixth Int. Charles Parson Turbine Conf., Dublin, Ireland, 2003: pp. 261–279.

[197] M. Tabuchi, T. Watanabe, K. Kubo, M. Matsui, J. Kinugawa, F. Abe, Creep crack growth behavior in the HAZ of weldments of W containing high Cr steel, Int. J. Press. Vessel. Pip. 78 (2001) 779–784.

[198] D.J. Gooch, S.T. Kimmins, type IV cracking in 0.5Cr 0.5 Mo 0.25V/ 2.25Cr 1Mo weldments, in: B. Wileshire, R. W. Evans (Eds.), Third Int. Confrence Creep Fatigue Eng. Mater. Struct. Swansea, 1987.

[199] T. Sakthivel, K. Laha, M. Vasudevan, M. Koteswara Rao, S. Panneer Selvi, Type IV cracking behaviour of modified 9Cr-1Mo steel weld joints, Mater. High Temp. 3409 (2016) 1–17.

[200] T. Sakthivel, S.M. Nandeswarudu, P. Shruti, G.V.S. Nageswara Rao, K. Laha, G. Sasikala, T. Srinivasa Rao, An improvement in creep strength of thermo-mechanical

treated modified 9Cr-1Mo steel weld joint, Mater. High Temp. 36 (2019) 76–86.

[201] J. Xu, X. Zhong, T. Shoji, T. Tatsuki, Y. Matsumura, M. Nakashima, Characterizations of the Microstructure of 9Cr-1Mo Steel Weld Joint After Long-Term Service in a Supercritical Fossil Power Plant, Metall. Mater. Trans. A Phys. Metall. Mater. Sci. 49 (2018) 4700–4709.

[202] T. Sakthivel, G. Sasikala, M. Vasudevan, Role of microstructures on heterogeneous creep behavior across P91 steel weld joint assessed by impression creep testing, Mater. Charact. (2019) 109988.

[203] W.F. Newell Jr., Welding and PWHT of P91 steels, Weld. J. (2010) 33–36.

[204] K. Haarmann, J.C. Vaillant, B. Vandenberghe, W. Bendick, A. Arbab, The T91/P91 book, 2nd ed., Boulogne, Vallourec-Mannesmann Tubes, 2002.

[205] Y.M. Samir, A review of effect of welding and post weld heat treatment properties of grade 91 steel, Int. J Res. Eng. Tech. 4 (2015) 574–581.

[206] J.A. Francis, W. Mazur, H.K.D.H. Bhadeshia, Type IV cracking in ferritic power plant steels, Mater. Sci. Technol. 22 (2006) 1387–1395.

[207] D. Richardot, J.C. Vaillant, A. Arbab, W. Bendick, The T92/P92 book, 1st ed., Boulogne: Vallourec-Mannesmann tubes, 2000.

[208] E.L. Bergquist, Consumables and welding modified 9Cr1Mo steel, Svetsaren. 54 (1999) 22–25.

[209] M. Tabuchi, M. Matsui, T. Watanabe, H. Hongo, K. Kubo, F. Abe, Creep Fracture Analysis of W Strengthened High Cr Steel Weldment, Mater. Sci. Res. Int. 9 (2003) 23–28.

[210] S.K. Albert, M. Tabuchi, H. Hongo, T. Watanabe, K. Kubo, M. Matsui, Effect of welding process and groove angle on type IV cracking behaviour of weld joints of a ferritic steel, Sci. Technol. Weld. Join. 10 (2005) 149–157.

[211] H. Cerjak, P. Mayr, Creep strength of welded joints of ferritic steels, Woodhead Publishing, 2008.

[212] M. Li, F.W. Sun, R.A. Barrett, E. Meade, D.F. Li, P.E. O'Donoghue, S.B. Leen, N.P. O'Dowd, Influence of material inhomogeneity on the mechanical response of a tempered martensite steel, Proc. Inst. Mech. Eng. Part L J. Mater. Des. Appl. 231 (2017) 14–22.

[213] M. Li, F. Sun, D.F. Li, P.E. O'Donoghue, S.B. Leen, N.P. O'Dowd, The effect of ferrite phases on the micromechanical response and crack initiation in the intercritical heat-affected zone of a welded 9Cr martensitic steel, Fatigue Fract. Eng. Mater. Struct. 41 (2018) 1245–1259.

[214] S.J. Brett, D.L. Oates, C. Johnston, In-service type IV cracking in a modified 9Cr (Grade 91) header., in: I.A. Shibli, et.al (Eds.), ECCC Creep Conf., DEStech Publications Incorporated, London, 2005: pp. 563–575.

[215] G. Potirniche, Prediction and Monitoring Systems of Creep-Fracture Behavior of 9Cr-1Mo Steels for Reactor Pressure Vessels, 2013.

[216] E. Barker, G.J. Lloyd, R. Pilkington, Creep fracture of a 9Cr1Mo steel, Mater. Sci. Eng. 84 (1986) 49–64.

[217] S.A. David, T. DebRoy, Current issues and problems in welding science, Science (80-.). 257 (1992) 497–502.

[218] M. Regev, S. Berger, B.Z. Weiss, Investigation of microstructure mechanical and creep properties of weldments between T91 and T22 steels, Weld. Res. Suppl. 75 (1996) 260s-268s.

[219] H.J. Schuller, L. Haigh, A. Woitscheck, Cracking in the weld region of shaped components in hot steam lines – materials investigations, Der Maschinenschaden. 47 (1974) 1–13.

[220] J.M. Brear, A. Fleming, Prediction of P91 life under plant operating conditions, in: Int. Conf. 'High Temp. Plant Integr. Life Extension,' Cambridge, UK, 2004.

[221] F. Abe, M. Tabuchi, Microstructure and creep strength of welds in advanced ferritic power plant steels, Sci. Technol. Weld. Join. 9 (2004) 22–30.

[222] D.J. Abson, J.S. Rothwell, Review of type IV cracking of weldments in 9- 12%Cr

creep strength enhanced ferritic steels, Int. Mater. Rev. 58 (2013) 437–473.

[223] F. Abe, Precipitate design for creep strengthening of 9% Cr tempered martensitic steel for ultra-supercritical power plants, Sci. Technol. Adv. Mater. 9 (2008).

[224] R.P. Chen, H.G. Armaki, K. Maruyama, Y. Minami, M. Igarashi, Microstructural Degradation During High Temperature Exposure Up To 105 H And Its Effects On Creep Of Gr . 91 Steel, in: Sixth Int. Conf. Adv. Mater. Technol. Foss. Power Plants, 2010: pp. 654–665.

[225] H. Hirata, K. Ogawa, Metallurgical investigation and modelling of deterioration of creep rupture strength in heat affected zone of heat resistant ferritic steel, Mater. High Temp. 27 (2010) 219–226.

[226] S.-H. Ryu, Y.-S. Lee, B.-O. Kong, J.-T. Kim, Low cycle fatigue behaviors of the welded joints of 9 to 12% Cr ferritic heat resistant steels for boiler of fossil power plants, Super-High Strength Steels. (2005).

[227] N.Z. Gutiérrez, J.V. Alvarado, H. de Cicco, A. Danón, Microstructural Study of Welded Joints in a High Temperature Martensitic-ferritic ASTM A335 P91 Steel, Procedia Mater. Sci. 8 (2015) 1140–1149.

[228] Triratna Shrestha, S.F. Alsagabi, I. Charit, G.P. Potirniche, M. V Glazoff, Effect of Heat Treatment on Microstructure and Hardness of Grade 91 Steel, (2015) 131–149.

[229] C.R. Das, S.K. Albert, J. Swaminathan, A.K. Bhaduri, B.S. Murty, Effect of boron on creep behaviour of inter-critically annealed modified 9Cr-1Mo steel, Procedia Eng. 55 (2013) 402–407.

[230] R. Celin, J. Burja, G. Kosec, A comparison of as-welded and simulated heat affected zone (HAZ) microstructures, Mater. Tehnol. 50 (2016) 455–460.

[231] G. Taniguchi, K. Yamashita, Effects of Post Weld Heat Treatment (PWHT) Temperature on Mechanical Properties of Weld Metals for High-Cr, Kobelco Technol. Rev. (2013) 33–39.

[232] B. Silwal, L. Li, A. Deceuster, B. Griffiths, Effect of postweld heat treatment on the toughness of heat-affected zone for grade 91 steel, Weld. J. 92 (2013) 80–87.

[233] N. Newell, Guideline for Welding Creep Strength-Enhanced Ferritic Alloys, EPRI. (2007).

[234] G. Eggeler, A. Ramteke, M. Coleman, B. Chew, G. Peter, A. Burblies, J. Hald, C. Jefferey, J. Rantala, M. DeWitte, R. Mohrmann, Analysis of creep in a welded "P91" pressure vessel, Int. J. Press. Vessel. Pip. 60 (1994) 237–257.

[235] L. Li, R. Wright, S. Lesica, Effect of Post-Weld Heat Treatment on Creep Rupture Properties of Grade 91 Steel Heavy Section Welds, U.S. Dep. Energy. (2012).

[236] D.P. Singh, M. Sharma, J.S. Gill, Effect of Post Weld Heat Treatment on the Impact Toughness and Microstructural Property of P-91 Steel Weldment, Int. J. Res. Mech. Eng. Technol. 3 (2013) 216–219.

[237] A. Khajuria, R. Kumar, R. Bedi, J. Swaminanthan, D.K. Shukla, Impression creep studies on simulated reheated haz of P91 and P91b steels, Int. J. Mod. Manuf. Technol. 10 (2018) 50–56.

[238] A. Khajuria, R. Kumar, R. Bedi, Characterizing Creep Behaviour of Modified 9Cr1Mo Steel by using Small Punch Impression Technique for Thermal Powerplants, J. Mech. Mech. Eng. 4 (2018) 47–61.

[239] R. Nandakumar, S. Athmalingam, V. Balasubramaniyan, S.C. Chetal, Steam Generators for Future Fast Breeder Reactors, Energy Procedia. 7 (2011) 351–358.

[240] V. Shankar, R. Sandhya, M.D. Mathew, Creep – fatigue-oxidation interaction in Grade 91 steel weld joints for high temperature applications, Mater. Sci. Eng. A. 528 (2011) 8428–8437.

[241] R. Kannan, V. Ganesan, K. Mariappan, G. Sukumaran, R. Sandhya, M.D. Mathew, K.B. Sankara, Influence of dynamic sodium environment on the creep – fatigue behaviour of Modified 9Cr – 1Mo ferritic – martensitic steel, 241 (2011) 2807–2812.

[242] ASTM E606-92, Standard Practice for Strain-Controlled Fatigue Testing, Annu. B. ASTM Stand. 2004. (2004).

[243] ASTM E2714, Standard Test Method for Creep-Fatigue Testing, ASTM Stand. i (2013) 1–15.

[244] K. Bhanu Sankara Rao, M. Valsan, R. Sandhya, S.K. Ray, S.L. Mannan, P. Rodriguez, On the failure condition in strain-controlled low cycle fatigue, Int. J. Fatigue. 7 (1985) 141–147.

[245] Peter J. Goodhew, Specimen Preparation for Transmission Electron Microscopy of Materials, Royal Micr, Thomson West, New York, United States, 1984.

[246] K. Sawada, T. Hara, M. Tabuchi, K. Kimura, K. Kubushiro, Microstructure characterization of heat affected zone after welding in Mod.9Cr-1Mo steel, Mater. Charact. 101 (2015) 106–113.

[247] H. Kitahara, R. Ueji, N. Tsuji, Y. Minamino, Crystallographic features of lath martensite in low-carbon steel, Acta Mater. 54 (2006) 1279–1288.

[248] K. Fujiyama, K. Mori, T. Matsunaga, H. Kimachi, T. Saito, T. Hino, R. Ishii, Creep-damage assessment of high chromium heat resistant steels and weldments, Mater. Sci. Eng. A. 510–511 (2009) 195–201.

[249] Y. Wang, L. Li, Microstructure evolution of fine-grained heat-affected zone in type IV failure of P91 welds, Weld. J. 95 (2016) 27s-36s.

[250] R.L. Klueh, D.R. Harries, High-chromium ferritic and martensitic steels for nuclear applications, ASTM International, 2001, West Conshohocken, USA, 2001.

[251] A.L. Marzocca, M.I. Luppo, M. Zalazar, Identification of Precipitates in Weldments Performed in an ASTM A335 Gr P91 Steel by the FCAW Process, Procedia Mater. Sci. 8 (2015) 894–903.

[252] J. Hald, Metallurgy and creep properties of new 9-12%Cr steel, Steel Res. Int. 67 (1996) 369–374.

[253] C. Pandey, M.M. Mahapatra, P. Kumar, N. Saini, Homogenization of P91 weldments using varying normalizing and tempering treatment, Mater. Sci. Eng. A. 710 (2018) 86–101.

[254] P. Mayr, C. Schlacher, S. Mitsche, Critical issues with creep-exposed ferritic-martensitic welded joints for thermal power plants, in: D. V. Kulkarni, M. Samant, S. Krishnan, A. De, J. Krishnan, H.D. Patel, A.K. Bhaduri (Eds.), Int. Con. Glob. Trends

Joining, Cut. Surf. Technol., Narosa Publishing House Pvt. Ltd, 2011: pp. 417–425.

[255] T. Vuherer, M. Dunder, L.J. Milović, M. Zrilić, I. Samardžić, Microstructural investigation of the heat-affected zone of simulated welded joint of P91 steel, Metalurgija. 52 (2013) 317–320.

[256] X.. Wang, Y.. Tsai, J.. Yang, Z.. Wang, X.. Li, C.. Shang, R.D.. Misra, Effect of interpass temperature on the microstructure and mechanical properties of multi-pass weld metal in a 550-MPa-grade offshore engineering steel, (2017) 1155–1168.

[257] J. Guo, X. Xu, A.E. Mark Jepson, R.C. Thomson, Influence of weld thermal cycle and post weld heat treatment on the microstructure of MarBN steel, Int. J. Press. Vessel. Pip. 174 (2019) 13–24.

[258] L. Cipolla, D. Gianfrancesci, S. Caminada, G. Cumino, Production experience of Tenaris Dalmine Grades 91 and 23: microstructure, mechanical properties and creep behaviour, in: New Mater. Semin. Organ. by ETD, London, London, 2007: pp. P06-S01.

[259] R.C. MacLachlan, J.J. Sanchez-Hanton, R.C. Thomson, The effect of simulated post weld heat treatment temperature overshoot on microstructural evolution in P91 and P92 power plant steels, in: Adv. Mater. Technol. Foss. Power Plants - Proc. from 6th Int. Conf., 2011: pp. 787–799.

[260] V. Gaffard, A.F. Gourgues-Lorenzon, J. Besson, High temperature creep flow and damage properties of the weakest area of 9Cr1Mo-NbV martensitic steel weldments, ISIJ Int. 45 (2005) 1915–1924.

[261] M. Ramini, E. Surian, M. Zalazar, Characterization of circumferencial welds of 9CrMo advanced steels, in: XXXVII Congr. Nac. Soldag., Natal, RN, Brasil, 2011.

[262] S. Sulaiman, D. Dunne, Microstructural and Hardness Investigations on Simulated Heat Affected Zone (HAZ) in P91 Creep Resisting Steel, Solid State Sci. Technol. 15 (2007) 102–107.

[263] Y. Wang, R. Kannan, L. Li, Characterization of as-welded microstructure of heat-affected zone in modified 9Cr-1Mo-V-Nb steel weldment, Mater. Charact. 118 (2016) 225–234.

[264] M. Yanet, Z. Mónica, Microstructure Characterization of Heat Affected Zone in Single Pass Welding in 9Cr-1Mo Steels, Procedia Mater. Sci. 8 (2015) 904–913.

[265] N. Isasti, D. Jorge-Badiola, J. Alkorta, P. Uranga, Analysis of Complex Steel Microstructures by High-Resolution EBSD, Jom. 68 (2016) 215–223. https://doi.org/10.1007/s11837-015-1677-0.

[266] X. Yu, Multi-Scale Characterization of Heat-Affected Zone in Martensitic Steels, The Ohio State University, 2012.

[267] S. Paddea, J.A. Francis, A.M. Paradowska, P.J. Bouchard, I.A. Shibli, Residual stress distributions in a P91 steel-pipe girth weld before and after post weld heat treatment, Mater. Sci. Eng. A. 534 (2012) 663–672.

[268] A.J. Schwartz, M. Kumar, B.L. Adams, D.P. Field, Electron backscatter diffraction in materials science, Springer US, 2009.

[269] S.I. Wright, M.M. Nowell, D.P. Field, A review of strain analysis using electron backscatter diffraction, Microsc. Microanal. 17 (2011) 316–329.

[270] J.H. Cho, A.D. Rollett, J.S. Cho, Y.J. Park, J.T. Moon, K.H. Oh, Investigation of recrystallization and grain growth of copper and gold bonding wires, Metall. Mater. Trans. A Phys. Metall. Mater. Sci. 37 (2006) 3085–3097.

[271] K. Sawada, T. Ohba, H. Kushima, K. Kimura, Effect of microstructure on elastic property at high temperatures in ferritic heat resistant steels, 394 (2005) 36–42.

[272] T. Otomo, H. Matsumoto, N. Nomura, A. Chiba, Influence of Cold-Working and Subsequent Heat-Treatment on Young’s Modulus and Strength of Co-Ni-Cr-Mo Alloy * 1, 51 (2010) 434–441.

[273] S. Montecinos, S. Tognana, W. Salgueiro, Influence of microstructure on the Young’s modulus in a Cu-2Be (wt%) alloy, J. Alloys Compd. 729 (2017) 43–48.

[274] M.E. Abd El-Azim, O.E. El-Desoky, H. Ruoff, F. Kauffmann, E. Roos, Creep fracture mechanism in welded joints of P91 steel, Mater. Sci. Technol. (United Kingdom). 29 (2013) 1027–1033.

[275] T. Sakthivel, M. Vasudevan, K. Laha, P. Parameswaran, K.S. Chandravathi, S.

Panneer Selvi, V. Maduraimuthu, M.D. Mathew, Creep rupture behavior of 9Cr-1.8W-0.5Mo-VNb (ASME grade 92) ferritic steel weld joint, Mater. Sci. Eng. A. 591 (2014) 111–120.

[276] S.R. Mediratta, V. Ramaswamy, P.R. Rao, Influence of ferrite-martensite microstructural morphology on the low cycle fatigue of a dual-phase steel, Int. J. Fatigue. 7 (1985) 107–115. https://doi.org/10.1016/0142-1123(85)90041-6.

[277] S.K. Paul, N. Stanford, T. Hilditch, Effect of martensite volume fraction on low cycle fatigue behaviour of dual phase steels: Experimental and microstructural investigation, Mater. Sci. Eng. A. 638 (2015) 296–304. https://doi.org/10.1016/j.msea.2015.04.059.

[278] R. Mohrmann, T. Hollstein, R. Westerheide, Modelling of Low cycle fatigue Behavior of the steel E911, in: Mater Adv Power Eng , Proc. 6th Liege Conf., 1998.

[279] I.A. Shibli, LeMatHamata Ian, U. Gampe, Nikbin, The Effect of low Frequency cycling on creep crack growth in welded P22 and P91 pipe tests, in: Int. HIDA Conf. Adv. Defect Assess. High Temp. Plant, MPA, Stuttgart, Germany, 2000.

[280] Vani Shankar, M. Valsan, K. Bhanu Sankara Rao, S.D. Pathak, Low cycle fatigue and creep-fatigue interaction behavior of modified 9Cr-1Mo ferritic steel and its weld joint, Trans. Indian Inst. Met. 63 (2010) 622–628.

[281] D.T. Raske, J.D. Morrow, Manual on Low Cycle Fatigue Testing, Am. Soc. Test. Mater. STP 465. (1969) 1–26.

[282] R.W. Landgraf, J.D. Morrow, T. Endo, Determination of the cyclic stress–strain curve, J. Mater. 4 (1969) 176–188.

[283] Z. Zhao, P. Xu, H. Cheng, J. Miao, F. Xiao, Characterization of Microstructures and Fatigue Properties for Dual-Phase Pipeline Steels by Gleeble Simulation of Heat-Affected Zone, Materials (Basel). 12 (2019) 1989.

[284] M.N. Batista, S. Hereñú, I. Alvarez-armas, The role of microstructure in fatigue crack initiation and propagation in 9-12Cr ferritic-martensitic steels, Procedia Eng. 74 (2014) 228–231.

[285] V.D. Vijayanand, J. Vanaja, C.R. Das, K. Mariappan, A. Thakur, S. Hussain, G.V.P.

Reddy, G. Sasikala, S.K. Albert, An investigation of microstructural evolution in electron beam welded RAFM steel and 316LN SS dissimilar joint under creep loading conditions, Mater. Sci. Eng. A. 742 (2019) 432–441.

[286] W.B. Jones, J.A. Van Den Avyle, Substructure and strengthening mechanisms in 2.25 Cr-1 Mo steel at elevated temperatures, Metall. Trans. A. 11 (1980) 1275–1286.

[287] B. Fournier, M. Sauzay, C. Caës, M. Noblecourt, M. Mottot, A. Bougault, V. Rabeau, A. Pineau, Creep-fatigue-oxidation interactions in a 9Cr-1Mo martensitic steel. Part I: Effect of tensile holding period on fatigue lifetime, Int. J. Fatigue. 30 (2008) 649–662.

[288] P.K. Liaw, A. Saxena, J. Schaefer, Estimating remaining life of elevated-temperature steam pipes-Part I. Materials properties, Eng. Fract. Mech. 32 (1989) 675–708. https://doi.org/10.1016/0013-7944(89)90166-5.

[289] X.H. Yang, W.Z. Dui, Study of steam turbine blade degradation Part 1 - Degradation of mechanical properties of blade during service, Mater. Sci. Technol. 17 (2001) 551–555. https://doi.org/10.1179/026708301101510195.

[290] R.K. Islamgaliev, M.A. Nikitina, A. V. Ganeev, M. V. Karavaeva, Effect of grain refinement on mechanical properties of martensitic steel, IOP Conf. Ser. Mater. Sci. Eng. 194 (2017).

[291] S.K. Paul, S. Sivaprasad, S. Dhar, S. Tarafder, Cyclic plastic deformation and cyclic hardening / softening behavior in 304LN stainless steel, Theor. Appl. Fract. Mech. 54 (2010) 63–70.

[292] W. Zhang, X. Wang, H. Chen, T. Zhang, J. Gong, Evaluation of the effect of various prior creep-fatigue interaction damages on subsequent tensile and creep properties of 9 % Cr steel, Int. J. Fatigue. 125 (2019) 440–453.

[293] M. Saito, Y. Ishikawa, K. Ikeda, H. Furuya, Oxidation behavior of stainless steel for fast breeder reactor fuel cladding, J. Nucl. Sci. Technol. 21 (1984) 356–365.

[294] Y. Wang, E.I. Meletis, H. Huang, Quantitative study of surface roughness evolution during low-cycle fatigue of 316L stainless steel using Scanning Whitelight Interferometric (SWLI) Microscopy, Int. J. Fatigue. 48 (2013) 280–288.